# The 60 GHz Indoor Radio Channel - Overcoming the Challenges of Human Blockage

Von der Fakultät für Elektrotechnik, Informationstechnik, Physik
der Technischen Universität Carolo-Wilhelmina zu Braunschweig

zur Erlangung der Würde eines Doktor-Ingenieurs (Dr.-Ing.)

genehmigte

Dissertation

von

Dipl.-Ing. Martin Jacob

aus Bielefeld

Eingereicht am: 26.07.2013
Mündliche Prüfung: 03.12.2013

Referenten: Prof. Dr.-Ing. Thomas Kürner (Technische Universität Braunschweig)
Prof. Dr.-Ing. habil. Reiner S. Thomä (Technische Universität Ilmenau)
Vorsitzender: Prof. Dr.-Ing. Jörg Schöbel (Technische Universität Braunschweig)

2014

Mitteilungen aus dem Institut für Nachrichtentechnik der
Technischen Universität Braunschweig

Band 34

**Martin Jacob**

# The 60 GHz Indoor Radio Channel – Overcoming the Challenges of Human Blockage

Shaker Verlag
Aachen 2014

**Bibliographic information published by the Deutsche Nationalbibliothek**
The Deutsche Nationalbibliothek lists this publication in the Deutsche Nationalbibliografie; detailed bibliographic data are available in the Internet at http://dnb.d-nb.de.

Zugl.: Braunschweig, Techn. Univ., Diss., 2013



Printed in Germany.

ISBN 978-3-8440-2714-3
ISSN 1865-2484

Shaker Verlag GmbH • P.O. BOX 101818 • D-52018 Aachen
Phone: 0049/2407/9596-0 • Telefax: 0049/2407/9596-9
Internet: www.shaker.de • e-mail: info@shaker.de

*Für Nicole.*

# Vorwort

Eine Arbeit wie diese ist nicht denkbar ohne die Unterstützung von Kollegen, Freunden und Familie. Ich freue mich deshalb an dieser Stelle all denen danken zu können, die zum erfolgreichen Gelingen dieser Dissertation unerlässlich gewesen sind. Die Arbeit entstand in meiner Zeit als wissenschaftlicher Mitarbeiter am Institut für Nachrichtentechnik der Technischen Universität Braunschweig. Sie basiert zu einem Großteil auf Forschungsergebnissen, die ich im Rahmen des europäischen Qstream-Projektes und der Standardisierung innerhalb der IEEE 802.11 Arbeitsgruppe erarbeitet habe.

Eine Dissertation soll die Befähigung zu vertiefter und selbständiger wissenschaftlicher Arbeit nachweisen. Mein aufrichtiger Dank gilt deshalb an erster Stelle meinem Doktorvater Prof. Thomas Kürner, der dafür einen überaus professionellen und angenehmen Rahmen geschaffen hat. Seine fachliche Unterstützung und sein großer Erfahrungsschatz im Bereich der Wellenausbreitung haben mir sehr geholfen die eine oder andere Hürde auf dem Weg zur Promotion zu überspringen. Der Freiraum, den Prof. Kürner mir dabei gelassen hat spiegelt sein Vertrauen in meine Fähigkeiten wider, für das ich ihm sehr dankbar bin. Abschließend möchte ich mich noch ganz besonders für den immer fairen und menschlichen Umgang bedanken, der sehr wichtig für mich war und mich immer wieder aufs Neue motiviert hat. Mein weiterer Dank gilt Prof. Reiner Thomä für die Übernahme des Zweitgutachtens der Dissertation und Prof. Jörg Schöbel, der nicht nur den Vorsitz der Prüfungskommission übernommen hat, sondern auch im Qstream-Projekt ein verlässlicher Partner war und mir oft mit Rat und Tat zur Seite stand.

Einen wesentlichen Anteil am Gelingen der Promotion hat Sebastian Priebe, der mich bereits als Student unterstützt hat. Unsere gemeinsamen Zeit als wissenschaftliche Mitarbeiter hat er durch die unzähligen fachlichen Diskussionen, die Zusammenarbeit an Veröffentlichungen und den immer unterhaltsamen Büro-Alltag außerordentlich bereichert. Des weiteren möchte ich mich bei Moritz Schack bedanken, auf dessen Arbeiten ich aufbauen konnte. Gleiches gilt für Radoslaw Piesiewicz, von dem ich zu Beginn meiner wissenschaftlichen Tätigkeit sehr viel lernen konnte. Unterstützt wurde ich ebenfalls von den Studenten Aleksandra Malko, Ludmila Kirchkesner und Christian Mbianke, aus dessen Diplomarbeit auch eine gemeinsame Veröffentlichung resultierte. Uwe Hellrung, Klaus Moullion und dem gesamten Team der mechanischen Werkstatt des IfN spreche ich meinen Dank für die Planung und Anfertigung von unterschiedlichen Messaufbauten aus, ohne die die durchgeführten Ausbreitungsmessungen nicht in der erreichten Präzision möglich gewesen wären.

Für die gute Kooperation möchte ich allen Partnern des Qstream-Projektes danken. Hervorzuheben sind hierbei Pablo Herrero Tomás vom IHF in Braunschweig und Anton de Graauw und Maristella Spella von NXP in Eindhoven, die sehr eng mit mir zusammengearbeitet haben. Mein Beitrag zur Standardisierung wurde erst durch die Unterstützung von Alexander Maltsev und Artyom Lomayev von Intel und Vinko Erceg von Broadcom möglich. Für die Einführung in die IEEE 802.11ad Standardisierungsgruppe

danke ich Philipe Chambelin, der zu meinem größten Bedauern viel zu früh verstorben ist.

Zwei weitere erfolgreich verlaufende Kooperationen, die zu mehreren Veröffentlichungen geführt haben, sollen nicht unerwähnt bleiben. Michael Peter und Robert Felbecker vom HHI in Berlin danke ich für den intensiven fachlichen Austausch und die Bereitstellung von Messdaten. Thomas Kleine-Ostmann und Robert Dickhoff gilt mein Dank für die Unterstützung bei den Diffraktionsmessungen, die ich gemeinsam mit ihnen an der PTB durchgeführt habe.

Bedanken möchte ich mich bei allen Kollegen für die tolle Atmosphäre am IfN, die von Institutsleiter Prof. Ulrich Reimers stark gefördert und letztlich erst ermöglicht wird. Ganz besonders danke ich Alexander Fricke für seine Emotio und Thomas Jansen, Dennis Rose und Huajun Yu für die vielen gemeinsamen Aktivitäten innerhalb und außerhalb der Dienstzeit. Für seine Hilfsbereitschaft in allen Belangen danke ich Rudolf Görke, der "guten Seele" des Instituts, mit dem mich die Begeisterung für Großbritannien im Allgemeinen und für England im speziellen verbindet. Darüber hinaus danke ich Petra Beyer für das Korrekturlesen meiner Veröffentlichungen und Andreas Gudat für seine stets charmante Art, mit der er meine unzähligen elektronischen Sonderwünsche erfüllt hat.

Meinen Eltern Rolf und Gudrun Jacob danke ich für den Rückhalt, den sie mir bereits während des Studiums immer gegeben haben. Abschließend sei gesagt, dass der wichtigste Mensch in der Zeit der Promotion ohne Zweifel meine Frau Nicole gewesen ist. Ich bin mir sicher, dass ich ohne sie nicht so weit gekommen wäre. Vielen Dank.

Braunschweig, im März 2014

*Martin Jacob*

# Kurzfassung

Wegen seiner großen verfügbaren Bandbreite und der hohen erlaubten Sendeleistung erweist sich der unlizensierte Frequenzbereich um 60 GHz als hervorragend geeignet für die Realisierung drahtloser Multi-Gigabit-Kommunikationssysteme. Während des Entwicklungsprozesses solcher Systeme ist eine detaillierte Kenntnis des Funkkanals unerlässlich. Unter Berücksichtigung offener Fragestellungen leistet die vorliegende Dissertation einen wesentlichen Beitrag zum Wissensstand auf dem Gebiet der 60-GHz-Kanalcharakterisierung. Im Vordergrund steht dabei die Abschattung durch Personen, die bei Trägerfrequenzen um 60 GHz zu einer hohen und gleichzeitig zeitvarianten Funkfelddämpfung führt.

Um realistische Ergebnisse zu liefern, sind im 60-GHz-Bereich komplexe Funkkanalmodelle erforderlich, die insbesondere Winkelinformationen am Sender und Empfänger enthalten und die zeitvariante Abschattung durch Personen berücksichtigen sollten. Beides ist notwendig, um intelligente Antennensysteme evaluieren zu können. Solche umfassenden Modelle sind bisher nicht verfügbar und stellen deshalb ein wesentliches Ziel dieser Dissertation dar. In der Arbeit werden verschiedene Szenarien untersucht, die alle stationäre Sender und Empfänger enthalten. Die zeitinvarianten Eigenschaften werden dabei mit einem deterministischen Ray-Tracing-Tool modelliert. Zur Validierung und Kalibrierung des Tools werden aufwändige breitbandige Kanalmessungen durchgeführt. Diese Messungen liefern gleichzeitig Aufschluss über die Beschaffenheit des Kanals hinsichtlich der Verteilung von Angle-of-Arrival und Angle-of-Departure. Darüber hinaus wird die Relevanz von Beugungseffekten im mm-Wellenbereich untersucht, basierend sowohl auf Ausbreitungsmessungen als auch auf Ray-Tracing-Simulationen.

Zudem werden in der Arbeit verschiedene elektromagnetische Modelle zur Beschreibung der menschlichen Abschattung in einer vergleichenden Studie analysiert und messtechnisch validiert. Hierbei ist insbesondere ein auf Knife-Edge-Beugung basierendes selbst entwickeltes Abschattungsmodell zu nennen, das aufgrund seiner guten Übereinstimmung mit den Messungen bei gleichzeitiger geringer Rechenzeit im weiteren Verlauf der Arbeit genutzt wird. Zusammen mit dem Ray-Tracing-Simulator stellt es ein breitbandiges zeitvariantes deterministisches Kanalmodell dar.

Um anderen Nutzern die Möglichkeit zu geben die Ergebnisse direkt und in einfacher Art und Weise zu verwenden, werden in der Dissertation zwei stochastische Modelle entwickelt, und zwar ein semi-statischer und ein vollständig zeitvarianter Ansatz. Das erst genannte Modell basiert vollkommen auf Simulationsdaten des oben genannten deterministischen Ansatzes. Das zweite Modell verbindet empirisch gewonnene Daten über die Abschattung mit Ray-Tracing-Simulation in einem hybriden Ansatz. Beide Modelle sind in das Clusterbasierte *IEEE802.11ad*-Funkkanalmodell eingeflossen. Die Modelle reproduzieren den Einfluss menschlicher Aktivität und berücksichtigen bis zu zehn Personen. Insbesondere das zeitvariante Modell ist das erste breitbandige Modell seiner Art im 60-GHz-Bereich.

Neben den Funkkanaluntersuchungen werden Antennenkonzepte zur Verminderung der Beeinträchtigung durch Personen analysiert. Als Grundlage wird das in der Arbeit entwickelte deterministische Funkkanalmodell genutzt. Unter Berücksichtigung der Anforderungen an das Gesamt-Übertragungssystem wird dabei abschließend gezeigt, dass Makrodiversität und Beamforming eine wirksame Maßnahme gegen Abschattung durch Personen darstellt.

# Abstract

Driven by the ever increasing capacity of storage devices and HD video streaming applications, there will be a strong demand for wireless multi-Gbps consumer applications soon. Due to its large available bandwidth and the high allowed transmit power, the unlicensed frequency range around 60 GHz is proving ideal for the realization of such systems. During the development process of 60 GHz multi-gigabit wireless systems, a detailed knowledge of the radio channel is essential. Taking into account research gaps, this dissertation makes a significant contribution to knowledge in the field of 60 GHz channel characterization. The focus is on human shadowing and its influence on the channel characteristics, which leads to a high and time-variant path loss.

In order to provide realistic results, sophisticated radio channel models are required for the 60 GHz range. In particular, they should include information in the spatial domain at the receiver and the transmitter as well as take into account time-varying human shadowing. The angular information is necessary in this case to evaluate smart antenna systems. Such comprehensive models are not yet available and therefore represent a major outcome of this dissertation. Various propagation scenarios with stationary transmitters and receivers are analyzed. The time-invariant properties are modeled utilizing a deterministic ray tracing tool. In order to validate and calibrate the tool extensive broadband channel measurements are performed. at the same time, these measurements provide information about the radio channel with respect to the angle of arrival and angle of departure properties. In addition, the relevance of diffraction effects in the mm-wave range is studied, based on both propagation measurements as well as ray tracing simulations. Furthermore, different electromagnetic models to describe the human shadowing are analyzed in a comparative study as well as validated by measurements. Here, a self developed model should be highlighted, which is based on knife edge diffraction. It is characterized by a good agreement with measurement results and a very low computational effort. Together with the ray tracing simulator it provides a broadband time-variant deterministic channel model.

In order to make the results directly applicable for future research, stochastic models are developed in the thesis, namely a semi-static and a fully time-variant approach. The first-mentioned model is based entirely on simulation data of the above deterministic approach. The second model combines empirically obtained data from shadowing measurements with ray tracing simulation in a hybrid approach. Both complement the time-invariant cluster-based IEEE802.11ad radio channel model. The models reproduce the influence of human activity and consider up to ten people. Especially the time-variant model is the first wideband model of its kind in the 60 GHz range.

In addition to the radio channel investigations, antenna diversity concepts reducing the impairments of human shadowing are analyzed. For this purpose, the validated deterministic approach mentioned above is utilized. Finally, taking into consideration the requirements of the overall transmission system, it is demonstrated that macro diversity and beamforming is an effective countermeasure to human shadowing.

# Contents

# 1 Introduction

Wireless local area networks (WLANs) and wireless personal area networks (WPANs) have become indispensable and integral parts of our everyday lives, either in the home environment or at public places like hotels, restaurants and office buildings. Nevertheless, the ever increasing demand for higher transmission rates will soon reach the limits of the established systems. These systems, typically use frequency bands at 2.4 GHz and 5 GHz with available channel bandwidths of up to 40 MHz. Besides the possibility to increase the spectral efficency at these bands, one solution to reach higher data rates is a shift to higher carrier frequencies, where larger bandwidths are available [Laska07]. Here, the mm-wave frequency range is of special interest, as the 60 GHz band (57 - 66 GHz) offers a continuous bandwidth of at least 5 GHz in many countries worldwide. In combination with the relatively high allowed transmit power of up to 40 dBm EIRP (equivalent isotropically radiated power), multi-gigabit transmission generally becomes feasible without high requirements to the spectral efficiency [Yong11]. However, due to the small wavelength of mm-waves, the free space loss is inherently much higher than at 2.4 and 5 GHz. Furthermore, the presence of moving people may cause an additional signal attenuation, which is also higher than that at microwave frequencies. For these reasons, potential 60 GHz systems will be limited to operate in single rooms and at distances of less than 10 meters [Smuld95]. Even for the coverage of single rooms, antenna diversity and beamforming techniques will have to enhance the link budget by realizing high antenna gains in order to countermeasure the high propagation losses [Yong11]. Accordingly, a huge development effort is necessary to make the band accessible for wireless communication applications, as partly totally new technologies have to be used.

In the development process of modern wireless communication systems, computer simulations play a key role. They support the design process already at a very early stage. For link level simulations, a precise knowledge of the radio channel is essential. This thesis contributes to this knowledge and is dedicated to support the development and optimization of wireless indoor communication systems at millimeter-wave frequencies. It addresses basic propagation mechanisms at mm-wave frequencies, the holistic characterization of the time-variant 60 GHz radio channel and the evaluation of antenna diversity

techniques and beamforming. As it is a severe problem at 60 GHz, a special interest is always devoted to the impact of human activity.

## 1.1 Current Wireless Multi-Gigabit Indoor Communication Systems at 60 GHz

Using the mm-wave band for broadband indoor wireless communication systems has been already proposed around 1990 [Thare88,Smuld95]. However, it was to take about 20 years before the first commercial products have been available. This has only become possible, since silicon process technologies and low-cost integration solutions suitable for mass production have arisen in recent years [Yong11]. Besides the possibility to realize such high-rate systems, nowadays there is also an actual need for them. The maximum data rates of established technologies like *IEEE802.11n* (240 Mbps) [IEEE809a] or *Bluetooth* (2.1 Mbps) [IEEE805] will soon become insufficient for several applications. The following list compiles some of these applications:

- The replacement of *HDMI (High-Definition Multimedia Interface) [HDMI12]* or *DisplayPort [Kobay12]* cables, which offer a throughput of up to 10.2 Gbps and 21.4 Gbps respectively (see Fig. 1.1a).
- High quality video streaming solutions similar to today's *DLNA (Digital Living Network Alliance), AirPlay or Miracast [DLNA12, AirP13, WiFi12].*
- Typical WLAN applications and Gigabit Ethernet cable replacement.
- Kiosk download applications for ultra fast file transfers (see Fig. 1.1b).
- The ultra short range connection between data storage devices.

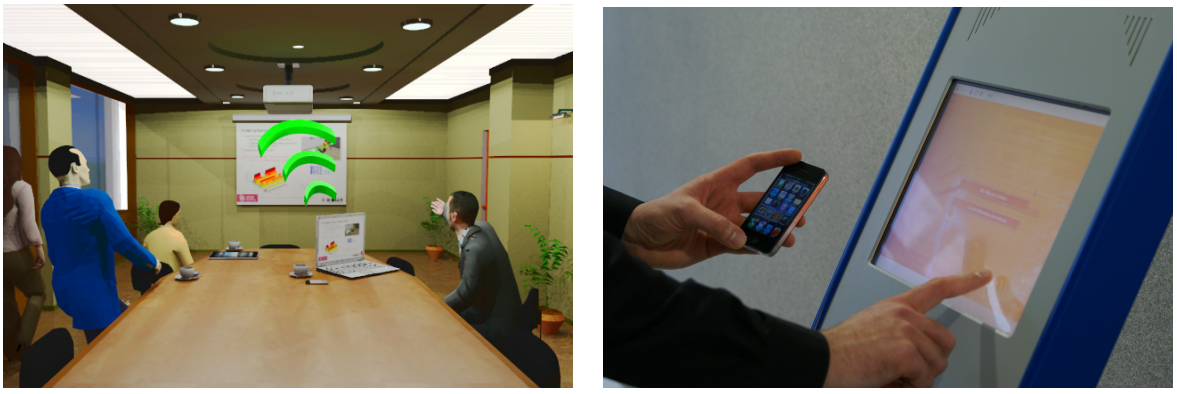

**(a)** Wireless HDMI replacement. **(b)** Kiosk download application.

**Figure 1.1:** Exemplary application scenarios.

As it can be seen, the main technology drivers are high definition video applications and the growing storage capacities of electronic devices. Upon publication of this thesis, five 60 GHz standards are available, addressing these applications. Table 1.1 compares the data rates of the standards with that of *IEEE802.11n* and *Bluetooth*.

The *Ecma-387* standard specifies a physical layer (PHY), distributed medium access control (MAC) sublayer, and an HDMI protocol adaptation layer (PAL) for bulk data transfer as well as video streaming applications [ECMA08]. The standard distinguishes between three types of devices with trainable and non trainable antennas. They mainly differ in their use cases, namely 10 meter line-of-sight/non-line-of-sight (LOS/NLOS) multipath environments, short range (1-3 meter) LOS links and point-to-point links at less than 1 meter range. The *Ecma* standard defines a maximum data rate of 6.35 Gbps for a single channel and 25.41 Gbps for four bonded channels.

The *IEEE802.15.3c Task Group (TG3c)* was formed in March 2005 to develop a mm-wave-based alternative PHY for the existing 802.15.3 wireless personal area network (WPAN) Standard 802.15.3-2003 [IEEE803]. In [Sadri07], five usage models have been defined ranging from uncompressed video streaming to kiosk file-downloading. The standard has been completed in 2009 and provides data rates of up to 5.67 Gbps [IEEE809b].

The *WirelessHD* consortium, an industry-led association, has published their first specification in 2007 and made it available for adoption in January 2008 [Wirel07]. This specification is based on parts of the *IEEE802.15.3c* standard and focuses on high definition (HD) audio and video streaming for a typical range of 10 meters. It distinguishes between eleven use cases with different data rates, e.g. a use case with three different streams for HD video, compressed A/V signals or pure audio signals. Here, the defined layers (PHY, MAC and adaption sublayer) are similar to the ones defined in the *Ecma-387* standard. The specification defines two different methods of beamforming, depending on the type of device used. In the current version of the specification, the data rates, which are adapted to the video streaming application, can amount to up to 7.1 Gbps supporting 3D TV and 4K resolution [Wirel10].

Another industry led consortium is the *Wireless Gigabit Alliance (WiGig)*, which focuses on *connectivity among PCs, consumer electronics and handheld devices* [WiGig12]. It

**Table 1.1:** Overview of 60 GHz standards and comparison with established systems.

| System | Frequency Band | Ch. Bandwidth | Max. Data Rate | Published |
|---|---|---|---|---|
| *Bluetooth* | 2.4 GHz | 1 MHz | 2.1 Mbps | 2005 |
| *IEEE802.11n* | 2.4/5 GHz | 40 MHz | 600 Mbps | 2009 |
| *Ecma-387* | 60 GHz | 2 GHz | 6.35 Gbps | 2008 |
| *IEEE802.15.3c* | | | 5.67 Gbps | 2009 |
| *WirelessHD* | | | 7.1 Gbps | 2010 |
| *WiGig* | | | 7 Gbps | 2010 |
| *IEEE802.11ad* | | | 6.8 Gbps | 2012 |

has been formed in May 2009 by several companies from different industrial sectors ranging from semiconductor manufacturers to software developers. The group finalized their specifications in 2010 which define data rates of up to 7 Gbps [WiGig12].

The *WiGig* specifications in turn have served as a standard draft for the *IEEE802.11ad Task Group (TGad)*. Similar to *TG3c*, *TGad* was formed in 2009 as an amendment to the existing IEEE802.11 standards. [Perah08] summarizes the goal of this group as follows: *This amendment defines standardized modifications to both the 802.11 physical layers (PHY) and the 802.11 Medium Access Control Layer (MAC) to enable operation in the 60 GHz frequency band (typically 57-66 GHz) capable of very high throughput.* The final specifications have been published in 2012 and support data rates of up to 6.76 Gbps [IEEE812]. The standard also defines beamforming protocols in which the general framework and messaging are defined [Corde10]. It is noteworthy that this thesis is connected to the *IEEE802.11ad* standardization process, as the author actively participated in the development of the radio channel model in the early phase of *TGad* .

Upon the publication of this thesis, *WirelessHD*-conformal chipsets are available on the market and *IEEE802.11ad*-conformal chips are announced by several manufacturers [Ahler12]. While *WirelessHD* devices are intended for A/V applications, the focus of the *IEEE802.11ad* is broader and adresses all of the applications mentioned above. The *Ecma-387* standard seems to play no further role. The same holds for *IEEE802.15.3c* as *WirelessHD* already provides a further development of this standard. As mentioned above, the *WiGig* specifications are quasi-identical to *IEEE802.11ad*.

## 1.2 State of the Art of Relevant Research Topics

Although 60 GHz multi-gigabit devices are already available, there is still a demand for research, even on fundamental topics like propagation and channel modeling, as they are not fully explored yet. In this section, the state of the art of research fields which are relevant for this thesis are given, namely propagation and channel modeling and the performance evaluation of antenna diversity techniques and beamforming as a countermeasure to human blockage. Please note that the focus lies on 60 GHz indoor applications only. The section is meant to briefly review the evolution of research from early work to the very recent work. On this base, the section identifies research gaps and puts the thesis into a context by pointing out its relationship to other work.

### 1.2.1 60 GHz Radio Channel Modeling

The fundamental propagation mechanisms like reflection or scattering at typical indoor building materials as well as transmission through objects have been thoroughly studied at 60 GHz [Sato97, Lange02, Coche05, Rappa11]. The only exception is the diffraction at

objects like partition walls or other furniture, which will be adressed in this thesis. Until now, only rudimentary studies exist [Thare88, Malts10b].

Typically, the relevant radio channel properties are divided into large-scale and small-scale effects. The large-scale properties (path loss and shadowing) have been subject to many investigations reaching back to the 1990s (see e.g. [Bense91, Xu02, Kyro12]). The path loss is commonly modeled by a log-distance dependency together with log-normal distributed shadowing. Usually, a distinction is drawn between LOS and NLOS situations. Most of the models are based on measurements, some are based on simulations like ray tracing (RT). Extensive overviews about path loss models with data for several different indoor environments can be found in [Smuld09, Yong11]. In addition, it is noteworthy that, although the atmospheric attenuation at 60 GHz is significantly higher than at microwave frequencies, it has virtually no influence on indoor short range applications [Yong11].

The small-scale effects in indoor environments have been characterized experimentally as well as theoretically (see e.g. [Smuld97, Xu02, Yang08b, Geng09]). In order to model the small-scale properties of broadband radio channels, channel impulse response (CIR) models are typically used. Deterministic models are mainly based on RT techniques, which have been proven valid in the 60 GHz range [Smuld94, Youss94, Peter07, Garci11]. Stochastic models give other researchers the possibility to use them without a high implementation effort. They are based on measurement or RT data, where also hybrid approaches can be found. A variety of stochastic models exist for different environments, namely corridors, conference and office rooms, living rooms and even hospitals. [Smuld95, Hubne97, Zwick05, Kyro12] are examples for stochastic models, which generate CIR realizations in time domain only for a specific antenna configuration. However, in order to evaluate systems that employ beamforming techniques, double directional channel models are needed [Stein01]. Here, in addition to the time domain, the spatial domain has to be considered also. A variety of experimental investigations considering the spatial domain can be found in literature. However, mostly, they are limited to angle of arrival (AoA) measurements, e.g. [Xu02, Sarri07, Morai10]. For this reason, measurements are conducted and analyzed in the framework of this thesis, which focus on the spatial channel properties, namely the angular dispersion of AoA as well as angle of departure (AoD). Only few similar measurement results have been shown just recently at 60 GHz and in parallel to this thesis [Malts09, Malts10b, Sawad09].

Stochastic channel models including the angular domain do also exist. For instance, such a model has been developed in 2006, in the framework of *IEEE802.15.3c* [Yong06]. This model adopts the Saleh-Valenzuela-cluster-approach [Saleh87] with added AoA information. It is based on measurements in different environments and has been extensively used for the evaluation of 60 GHz transmission techniques. However, it lacks information about AoD and the polarimetric properties of the modeled multipath components (MPCs). The first stochastic 60 GHz channel model including information about AoA as well as AoD was not available until 2010, when *TGad* finished its work on channel modeling [Malts10d]. The statistics in this model are based on hybrid data from both measurements and RT respectively. Although polarization has been analyzed be-

fore [Manab96, Manab95, Zhao03, Yıldı08], the *TGad* model is also the first fully polarimetric stochastic 60 GHz model. The author of this thesis has contributed to the *TGad* model, by introducing human blockage. Therefore a basic knowledge of this model will be required for a better understanding of this thesis. For this purpose, an overview about the model can be found in Appendix A.

In an environment with stationary devices like in typical indoor scenarios, non-stationarity of the 60 GHz channel mainly results from moving people. Measurements have shown that at 60 GHz MPCs are not fully blocked by persons, but rather attenuated by a certain amount. In literature, it has been reported that in the 60 GHz frequency band people may attenuate the received signal by more than 20 dB [Sato98, Flame00, Collo03a, Collo03b, Collo04, Garci10c, Garci10b]. The duration of shadowing events was found to be wide spread. As a key figure, 300 to 550 ms can be found in [Collo04, Collo03a, Collo03b]. Other important parameters such as amplitude, rising time and occurrence rate of fading events were investigated experimentally. This has been done e.g. in typical indoor environments [Sato98, Flame00, Collo03a], in a kiosk scenario [Garci11] and even in an airplane [Garci10c, Garci10b].

Besides the sole description of human blockage, deterministic channel models taking into account human shadowing do also exist. However, they make very rough assumptions. They model the body either as fully absorbing obstacles [Obaya98, Pollo09, An09, Genc10, Sawad12] or as reflecting objects [Khafa08, Saada09]. In this thesis, the interaction between electromagnetic waves and the human body is modeled more accurately, by taking into account diffraction around the body. Similar approaches have arisen mainly just recently [Villa00, Singh09, Ali10, Gusta12, Genc12], in the context of the emerging standards and in parallel to this thesis. There, the human body or parts of the body are also modelled under more accurate assumptions by using different diffraction theories. In addition, complete stochastic wideband channel models including the influence of moving persons are available (e.g. [Zwick02, Pagan06]). However, they are not suitable for the evaluation of 60 GHz WLANs, since they have been developed for frequencies below 10 GHz. For this reason, such a model is developed in this thesis, based on the *TGad* channel model. Thereby, it is the first stochastic 60 GHz CIR model taking into account time-variant human activity.

### 1.2.2 Performance Evaluation of Diversity Techniques and Beamforming to Overcome Human Blockage at 60 GHz

During the development of broadband 60 GHz devices, one main objective is the choice of an optimum antenna configuration. For instance, the *IEEE802.11ad* standards only define beamforming protocols, which specify a general framework and the messaging between devices. The choice of actual beamforming algorithms and the antenna specifications itself are left to the developer [Corde10]. The receiving and transmitting antennas of a wireless communication system are inseparably tied to the radio channel. The antenna characteristics, especially the beamwidth, has a strong influence on the channel conditions and hence

also on the data transmission [Yang08a]. In addition, human shadowing introduces time-variance and partly high attenuation the 60 GHz propagation channel. On the one hand, adaptive antenna systems can be used to countermeasure human blockage problems. On the other hand, they introduce additional time-variance, as their antenna characteristics may fundamentally change with time. It is evident, that the performance evaluation of such dynamic systems is more complex than that for systems with conventional antennas.

In literature, a few studies about the impact of antennas on the 60 GHz propagation conditions can be found. However, they do not account for human shadowing, e.g. [Manab96, Yang08a, Dong12], or only use rough assumptions for the modeling of humans as mentioned already above, e.g. [An09, Pollo09, Pan10, Genc10, Sawad12]. In this thesis, diversity techniques and beamforming are evaluated based on RT in realistic scenarios and the self-developed, diffraction-based human blockage model. Upon the publication of this thesis, the work in [Singh09, Genc12] can be seen as the only comparable analyses of diversity and beamforming based on realistic deterministic human blockage models. The only stochastic approach to evaluate beamforming has been used in [Tsang11a, Tsang11b, Tsang11c]. This methodology is based on the *TGad* channel model [Malts10d] and the models from [Collo04]. Experimental and simulative work can also be found, focusing on macro-diversity including human shadowing effects [Garci09, Garci10c, Garci10a, Schul11, Flame02]. Remarkably, some authors already use the stochastic time-variant channel model, considering human activity, developed by the author of this thesis for the analysis of diversity techniques [Nguye11, Lan11, Park12].

## 1.3 Approach of the Work

The compilation of the state of the art has revealed that the topics related to this thesis have been subject to investigations already since the 1990s. In the context of the emerging multi-gigabit standards, the propagation related 60 GHz research experiences an ongoing renaissance, which started in 2006 with the *TG3c* channel model. Up to that point, the existing scientific work on channel modeling had lacked two important things. First, comprehensive propagation measurements were missing for the spatial characterization of the double directional 60 GHz radio channel. Second, stochastic channel models including human shadowing, which could be used for the system and antenna design, were not available. The thesis addresses both issues following a three step approach:

1. Extensive measurement campaigns in order to verify the deterministic human blockage models and ray tracing.

2. Simulation of a large number of realistic dynamic environments using the verified electromagnetic models.

3. Derivation of stochastic channel models based on the simulation data.

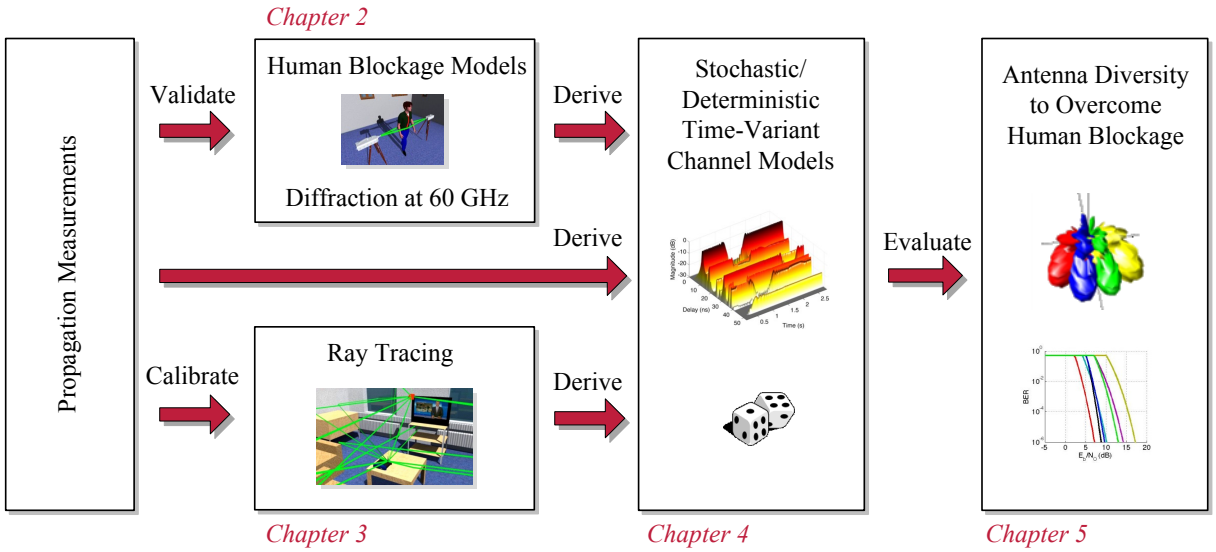


**Figure 1.2:** Methodology and structure of the thesis.

Based on the illustration in Fig. 1.2, the approach will now be discussed in detail. In Chapter 2, different possibilities of modeling human blockage at 60 GHz are analyzed. The focus lies on the choice of a fundamental model, which should be easily integrateable into ray tracing simulations. Chapter 2 additionally includes a study about the relevance of diffraction in indoor scenarios. Both analyses have in common that the considered electromagnetic models are validated by propagation measurements.

The main goal of Chapter 3 is to set up a deterministic spatio-temporal channel modeling tool and relevant reference scenarios for 60 GHz indoor applications. Therefore, RT simulations are calibrated based on extensive channel measurements. These measurements give also insight into the spatial characteristics of the 60 GHz radio channel.

Based on the preceding chapters, a deterministic channel modeling methodology is presented in Chapter 4, which includes human induced time-variance. For this purpose, the chosen human blockage model is combined with the ray tracing simulations. Based on this approach, two kinds of stochastic models are derived. The first one is semi-static and based on simulations only. The second is a fully time-variant model based on simulations and measurements. These models are then used in Chapter 5 to realistically evaluate spatial diversity and beamforming in order to assess their ability to overcome the challenges of human blockage.

# 2

# Fundamental Analyses of Diffraction Mechanisms at mm-Wave Frequencies

Relevant interaction mechanisms between electromagnetic waves and objects in an indoor scenario are manifold at mm-wave frequencies. As they were largely studied in detail before, the fundamental propagation mechanisms are not the main objective of this thesis. Hence, this chapter is not meant to provide a complete picture of all relevant mechanisms. Specific open issues are rather addressed and contributions beyond the current state of research are focussed on.

Chosen interaction mechanisms with corresponding measurements and models are presented, namely diffraction and human blockage. Other propagation mechanisms like reflection, transmission, scattering at rough surfaces or atmospheric attenuation are not treated here, because they have been thoroughly studied before in the mm-wave region (see e.g. [Jacob09f, Coche05, Sato97, Piesi07, Giann99, Rappa11]).

Diffraction at obstacles like partioning screens or other furniture is analyzed in Section 2.1. A variety of diffraction studies exist for lower frequencies and different environments, e.g. [Erceg02,Berna04]. However, currently no methodic study about diffraction at 60 GHz exists. The motivation for carrying out such a study is to provide a quantitative measure in order to judge the relevance of diffraction effects in 60 GHz indoor radio channels.

The main focus of this thesis is to study the influence of human blockage on the 60 GHz radio channel and ways to overcome the arising problems. For this reason, human blockage is treated separately in this chapter in Section 2.2, although strictly speaking it is rather a combination of reflection and diffraction than an individual phenomenon. The intention of this section is to select one model for the implementation into a ray tracing environment and to give the reader the theoretical background necessary to understand the following chapters.

Please note, that parts of the work presented in this chapter have been already published by the author in [Czink12, Jacob12, Jacob10c, Jacob11a, Peter12, Klein12, Jacob13c, Jacob09b, Jacob09g, Jacob10e]. Additionally, it is noteworthy that the diffraction related

investigations presented in Section 2.1 have been performed in close cooperation with Dr.-Ing. Sebastian Priebe. Thereby, Dr. Priebe has focussed on frequencies beyond 300 GHz and the implementation of the diffraction models in ray tracing simulations. In contrast, the focus of this thesis lies on the measurement based validation of the diffraction models at 60 GHz.

## 2.1 Diffraction

The shadowing of electromagnetic waves by obstructions commonly is described by diffraction for both cellular as well as wireless indoor networks. In the indoor case, electromagnetic waves may be diffracted at edge or wedge like obstacles like bookshelves, closets or any other home furnishings. In addition other shapes may be important as they occur in reality. As an example the diffraction around a circular cylinder will be analyzed additionally. First experimental investigations have been presented for the 60 GHz range in [Malts10b]. However, a methodic study analyzing proper diffraction models for indoor usage and the influence of diffraction effects on the 60 GHz radio channel so far does not exist.

At first, the diffraction theories used in the investigations are shortly reviewed. Then, measurements are presented with the main goal of validating the models in the mm-wave region. An exemplary study employing ray tracing simulations analyzes the quantitative impact of diffraction at 60 GHz, which concludes this section.

### 2.1.1 Theories

#### 2.1.1.1 Knife Edge Diffraction (KED)

In the following, the knife edge diffraction model is reviewed. Although it is well-known, this is done, because it also contributes to the understanding of the human blockage model presented in Section 2.2.1.4. The derivation of the diffraction loss of an absorbing half-plane, the knife edge, is based on the Huygens' principle. An electromagnetic wave impinges the absorbing half plane and the wave behind the half plane becomes then the summation of all the wave fronts that are not absorbed. This summation can be calculated by the Fresnel integral [Saund07]:

$$F(\nu) = \frac{1+j}{2} \int_{\nu}^{\infty} e^{-\frac{j\pi\tau^2}{2}} d\tau \tag{2-1}$$

This so called transition function describes the relationship between received and emitted field strength and hence the diffraction loss:

$$L_{D,KED}|_{dB} = -20 \cdot \log_{10} \left| \frac{E_{RX}}{E_{TX}} \right| = -20 \cdot \log_{10} |F(\nu)| . \tag{2-2}$$

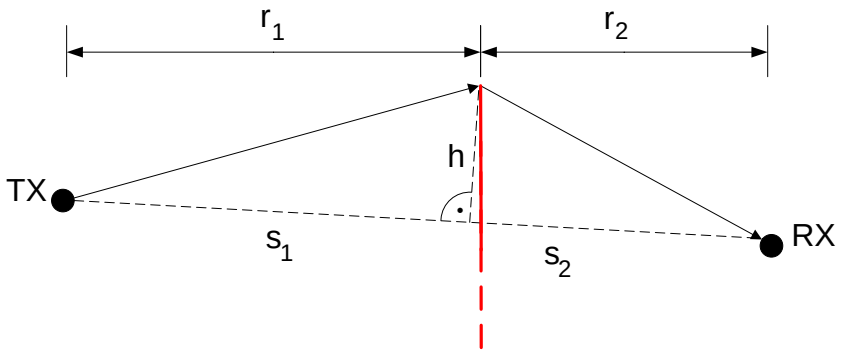


**Figure 2.1:** Geometry for the calculation of the diffraction attenuation at a single knife edge.

An interpretation of the given function is only possible with the determination of $\nu$ for a given geometry. The corresponding general structure is shown in Fig. 2.1 schematically with all relevant parameters. Assuming these parameters and a wavelength $\lambda$, the parameter $\nu$ can be determined by

$$\nu = h \cdot \sqrt{\frac{2}{\lambda} \cdot \left( \frac{s_1 + s_2}{r_1 \cdot r_2} \right)} \tag{2-3}$$

For $\nu = 0$, the knife edge just blocks the direct path between TX and RX and shadows half of the incoming wave ($L_D = 6$ dB). For $\nu > 0$, the receiver lies in the shadow region. Here, only the diffracted part of the wave exists, and an increased shadowing leads to an increased diffraction loss. In the area $\nu < 0$, in contrast, both the direct and the diffracted beam are received, resulting in sections of constructive or destructive interference with partly negative diffraction attenuation. It is also noteworthy that the diffraction loss is negligible for large negative values of $\nu$.

#### 2.1.1.2 UTD Solution for a Dielectric Wedge

Another useful method, which can be applied in a much wider range of situations than the KED model, is the uniform theory of diffraction (UTD). Unlike the KED, it is a ray based method and hence takes into account polarization [Hall03]. Here, complex diffraction coefficients applied to the diffracted rays account for all diffraction effects. As this modeling approach will be treated only marginally in this thesis the reader is referred to the literature for a detailed description of the theory [Hall03, Kouyo74, Vaugh03]. The definite advantage of the UTD is its assumption of diffracted rays, which makes it easy to implement in ray tracing and to also account antenna patterns.

#### 2.1.1.3 UTD solution for a Conducting Cylinder

In this section, the UTD has been chosen to model the diffraction at a cylindrical obstacle [McNam90, Patha80] due to its lower computational effort compared to the analytical solution. Like the wedge diffraction UTD, this theory is ray based. In the following a description of the theory from [Patha80] will be given. This is done in more detail, as the cylinder UTD is rather uncommon and rarely treated compared to the wedge diffraction UTD. The solution for the present scattering problem is given in terms of certain special functions, namely Fock and Fresnel integral functions [McNam90]. In order to have a consistent glossary throughout the thesis, the nomenclature of Pathak et al. [Patha80] has been slightly changed.

The lit region is the region where the receiver position has a direct LOS connection with the transmitter. The geometry of this problem with all required geometric quantities is depicted in Fig. 2.2a. In this region, the resulting field at the receiver point $RX$ is a superposition of the direct field $E^i$, the surface diffracted field $E^r$, which is a reflected field and the field $E^d$ diffracted around the cylinder:

$$E\left(RX\right) = E^i\left(RX\right) + E^r\left(RX\right) + E^d\left(RX\right) \tag{2-4}$$

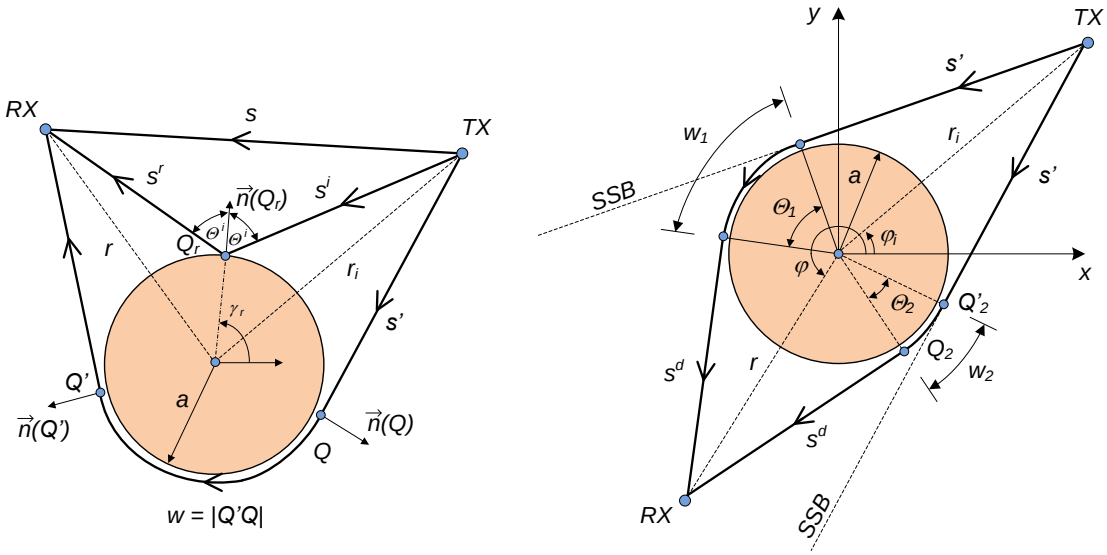


**(a)** Receiver in the lit region.

**(b)** Receiver in the shadow region.

**Figure 2.2:** Geometry for the ray interpretation of the scattering by an infinitely long circular cylinder.

The calculation of the direct field strength $E^i$ can be done according to free space propagation. The UTD expression for the reflected field at the observation point is

$$E^r\left(RX\right) = E^i\left(Q_r\right) R_{TE,TM} \sqrt{\frac{\rho^r}{\rho^r + s^r}} e^{-jks^r}, \tag{2-5}$$

where $k$ is the wave number. The incident field $E^i$ at reflection point $Q_r$ is only depending on the distance $s^i$ and again can be calculated according to free space propagation. The parameter $\rho^r$ is the so called *caustic distance*, i.e. the wave's radius of curvature at its reference point $Q_r$. It is obtained from:

$$\frac{1}{\rho^r} = \frac{1}{s^i} + \frac{2}{a\ cos\left(\theta^i\right)}. \tag{2-6}$$

The determination of the location of the specular point $Q_r$ and hence $\theta^i$ is not trivial. $Q_r$ has to satisfy the law of reflection

$$\vec{n}\left(Q_r\right) \cdot \vec{s^i}\left(Q_r\right) = -\vec{n}\left(Q_r\right) \cdot \vec{s^r}\left(Q_r\right). \tag{2-7}$$

Points on the circle can be described by an angle $\gamma$ and the radius $a$. In order to find the specular point, the angle $\gamma_r$ is determined numerically, for which (2-7) is fulfilled. It is noteworthy to mention, that this is the most extensive part of the entire field calculation.

The actual core of the UTD is the generalized reflection coefficient for TE and TM polarization:

$$\begin{bmatrix} R_{TE} \\ R_{TM} \end{bmatrix} = -\sqrt{\frac{-4}{\xi_p}} e^{-j\xi_p^3/12} e^{-j\pi/4} \left[ \frac{-1}{2\xi_p\sqrt{\pi}} F\left(X_p\right) \begin{cases} p^*\left(\xi_p\right) \\ q^*\left(\xi_p\right) \end{cases} \right], \tag{2-8}$$

with $\xi_p$ being the *Fock parameter*:

$$\xi_p = -\left(4ka\right)^{\frac{1}{3}} cos\left(\theta^i\right). \tag{2-9}$$

For the sake of briefness, the so called *Fock scattering functions* $p^*\left(x\right)$ and $q^*\left(x\right)$ will not be discussed here in detail. The calculation rules for this integral equations can be found in [McNam90]. The argument of the transition function is

$$X_p = 2kcos^2\left(\theta^i\right) \frac{s^r s^i}{s^r + s^i}. \tag{2-10}$$

In the shadow region, where the LOS path is blocked by the cylinder, the total field is composed by contributions from two so-called surface diffracted rays. One is traveling clockwise and the other one counterclockwise around the cylinder (see Fig. 2.2b). Each of these diffracted fields is given by

$$E^d\left(RX\right) = E^i\left(Q'\right) T_{TE,TM} \frac{e^{-jks^d}}{\sqrt{s^d}}, \tag{2-11}$$

with $E^i(Q')$ being the field at the attachment point $Q'$ according to geometrical optics. This formulation is also valid for the calculation of the diffracted field in equation (2-4). Similar to the lit region case, here the UTD surface diffraction coefficient $T_{TE,TM}$ can be calculated by the Fock and transition functions:

$$\begin{bmatrix} T_{TE} \\ T_{TM} \end{bmatrix} = -\left(\frac{ka}{2}\right)^{\frac{1}{3}} \sqrt{\frac{2}{k}} e^{-jkw} e^{-j\pi/4} \left[ \frac{-1}{2\xi_d\sqrt{\pi}} F(X_d) + \begin{Bmatrix} p^*(\xi_d) \\ q^*(\xi_d) \end{Bmatrix} \right], \tag{2-12}$$

where $w$ is the arc length traversed by the surface ray between $Q'$ and $Q$. The *Fock parameter* in this case amounts to:

$$\xi_d = -w \cdot \left(\frac{k}{2a^2}\right)^{\frac{1}{3}}, \tag{2-13}$$

and the argument of the transition function amounts to:

$$X_d = \frac{kw^2}{2a^2} \frac{s^d s'}{s^d + s}. \tag{2-14}$$

As the calculation of the integral equations is computationally extensive, polynomial approximations have been used for the implementation [McNam90, Smith98].

## 2.1.2 Measurements

The motivation for the diffraction measurements described in this section is twofold. On the one hand, we use them to validate the theoretical models presented at mm-wave frequencies. On the other hand, the basic differences between the diffraction at distinct objects will be highlighted.

All measurements have been carried out with a Rohde & Schwarz ZVA50 vector network analyzer (VNA) in combination with external transmitting and receiving test heads. As measurement antennas, 20 dBi WR-15 fed standard gain horns (SGHs) have been used. Measurements have been taken in both horizontal (HH) and vertical (VV) polarization.

Two types of measurements were performed in order to analyze individual aspects, namely the angular dependence of diffraction and diffraction at closed objects positioned on a translation stage. The different measurement setups will be described along with the results in the following subsections.

### 2.1.2.1 Angular Dependent Diffraction Loss

The first measurement setup is shown in Fig. 2.3. Here the angular dependent diffraction loss is analyzed. For that purpose, the transmitting and receiving test heads are mounted on rotatable arms, pointing always towards the direction of the rotation axis $z$. The

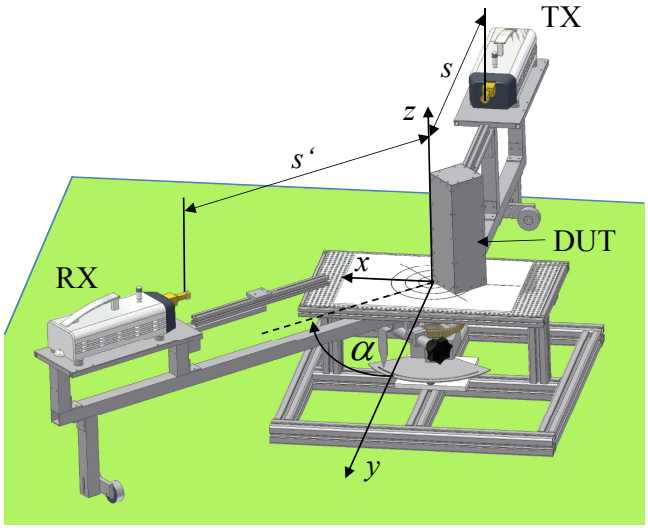


**Figure 2.3:** Setup for the angular-dependent measurements (setup 1).

transmitter is kept fixed in order to always illuminate the discontinuity of the object, i.e. the corner of the edge or the wedge under the same angle. The measurement object (DUT) is positioned endwise vertically at $x = 0$, resulting in a shadow boundary for $\alpha = 0°$. The receiver is rotated, with positive angles $\alpha$ corresponding to the lit region and negative angles to the shadow region. With this manual setup a maximum angular resolution of 1° is achieved . The distances $s$ and $s'$ are fixed to a value of 0.47 m. Due to the narrow beamwidth of the antennas, the direct signal in the LOS case as well as a possible signal transmitted through the object in the NLOS case is highly attenuated mostly except for the area around the shadow boundary.

Please note that the definitions of horizontal and vertical polarization throughout the whole thesis is based on the antenna polarization and its relation to the ground plane. Here, for instancethe term VV belongs to an electrical field strength vector parallel to the z-axis in Fig. 2.3.

The total received electrical field strength $E^{tot}$ is a superposition of different contributions. In case of the first measurement setup, the electrical field strength can be calculated according to:

$$E^{tot} = \begin{cases} g_{TX}(0) \cdot g_{RX}(0) \cdot E^{r} \\ \quad + g_{TX}(\Phi_{AoD}) \cdot g_{RX}(\Phi_{AoA}) \cdot E^{LOS}, \quad \alpha \geq 0 \\ \\ g_{TX}(0) \cdot g_{RX}(0) \cdot E^{d} \\ \quad + g_{TX}(\Phi_{AoD}) \cdot g_{RX}(\Phi_{AoA}) \cdot tE^{LOS}, \quad \alpha < 0, \end{cases} \tag{2-15}$$

where $E^{d}$ is the diffracted field, $E^{r}$ is the reflected field and $E^{LOS}$ is the field propagating on the shortest geometric path from TX to RX either directly or through the material.

$g_{TX}(\Phi_{AoD})$ and $g_{RX}(\Phi_{AoA})$ are the antenna gains for the corresponding angle of arrival and angle of departure at the antennas. In case of dielectric materials, an attenuated direct field component does also exist in the shadow region. Hence, $E^{LOS}$ has to be multiplied by a transmission coefficient $t$. For metal, the parameter $t$ is assumed to be 0, and for wood it is calculated according to the Fresnel equations. Please note that in case of $t \neq 0$ the UTD diffraction coefficients have to be corrected according to [Burns83], taking into account the actual value of $t$.

In a setup like this, the correct consideration of the antenna patterns is essential. In principal, the radiation pattern ought to be included in the derivation of the diffraction theory [Vaugh03], but the comparison between measurements and theory in the analysis will show that it is sufficient to assume the field components as rays weighted with the antenna gains $g_{TX}$ and $g_{RX}$. The angles $\Phi_{AoD}$ and $\Phi_{AoA}$ change with $\alpha$, whereas the diffracted component $E_D$ is always amplified by the maximum gain of the antennas. For the correct consideration, the SGH patterns have been simulated with Ansoft HFSS [HFSS13].

Complex transfer functions with frequency bandwidths of 20 GHz and a center frequency of 60 GHz have been measured. Afterwards they have been transformed to the time domain via inverse Fourier transform. Here, a rectangular time gating was performed in order to suppress undesired signal components, i.e. multipath reflections. After transformation to the frequency domain, the diffraction losses are calculated as the ratio of the received power with the diffracting object and the power under unobstructed conditions for $\alpha = 0$. The results are analyzed for a single frequency only, because the dispersive behavior is marginal in the frequency range of interest. All measurements can be reduced to a planar problem due to the invariant shape of the objects in $z$-dimension. In addition, objects are illuminated in a way that the antenna footprint does not excite diffraction over the object. TX and RX are always in a horizontal plane and hence the polarization of the radiated waves will not change during propagation.

Fig. 2.4 depicts the results of the diffraction measurements and the comparison with the UTD for the angular-dependent diffraction. The measurements have been performed for a metal edge, a wooden edge and a metal wedge with a wedge angle of 90°. The angular range is limited to $\alpha = -45° \ldots 30°$, because only here the influence of diffraction is significant. Fig. 2.4a illustrates the measurement results for the metal edge. In the shadow region ($\alpha < 0$) the loss characteristics correspond to the diffracted field $E^d$ only, because a transmitted signal does not exist ($t_{metal} = 0$). The loss in the shadow region is higher for vertical polarization. In the lit region, a general increase of losses due to the filtering of the direct path by the antenna pattern is observed as the RX remains fixed. The oscillations are caused by interference between $E^{LOS}$ and $E^r$. Unfortunately, the measurement resolution in the lit region is not high enough to reproduce the oscillations. However, the general trend of the measurement agrees well with the prediction in all cases. Regarding the wooden edge (Fig. 2.4b), the characteristic in the lit region is in principle equal to the characteristic of the metal edge. It is steeper only close to $\alpha = 0°$.

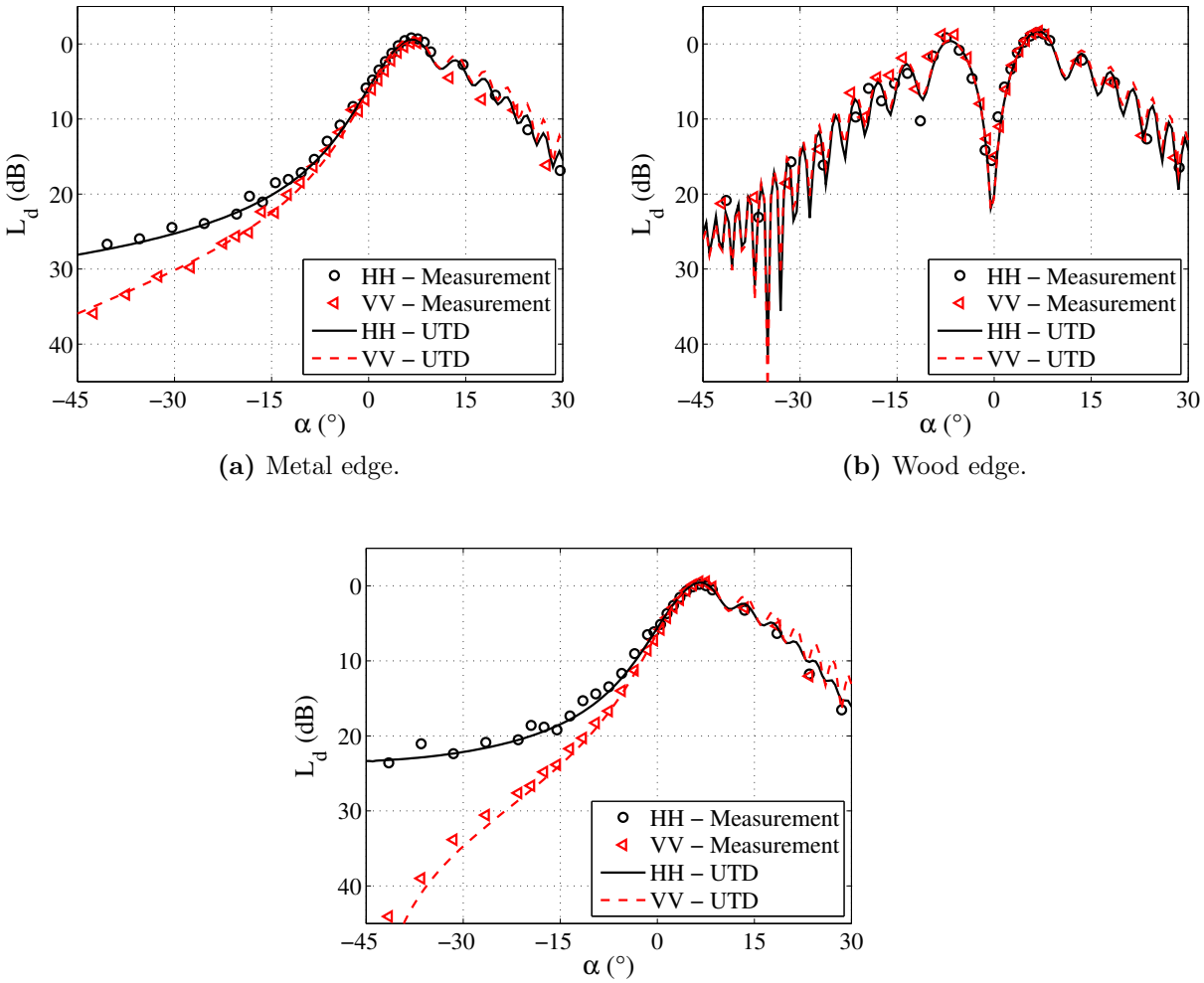


**(a)** Metal edge.

**(b)** Wood edge.

**(c)** Metal wedge.

**Figure 2.4:** Comparison of angular-dependent diffraction measurements and UTD.

In contrast to the metal edge, the behavior in the shadow region is almost identical to that in the lit region, because here the diffracted field interferes with the transmitted field, which is not present in the the case of the metal edge. A dielectric permittivity of $\varepsilon_r = 1.82 - j0.051$ has been determined for the wood by a transmission experiment as described in [Jacob10c]. The parameter $t$ is then calculated according to the transfer matrix method (see [Jacob10c]). The transmission losses are almost independent of the angle and amount to about 1.8 dB for the used thickness of 7.6 mm. This is much lower than the diffraction loss. Nevertheless, the total loss increases with more negative angles due to the radiation characteristics of the transmitting antenna. The agreement between measurement and model is very good around $\alpha = 0°$, however, for larger absolute angles the measurement resolution is not high enough to reproduce the oscillations. There, the exact location of the oscillation minima and maxima strongly depends on a perfect knowledge of the dielectric properties of the wood. Deviations between measurement and

model can be caused by unavoidable small inaccuracies during the determination of these properties. As expected from theory no significant differences could be observed regarding the polarization.

Regarding the results of the metal wedge measurements (Fig. 2.4c), the main difference compared to the metal edge is that the losses for horizontal polarization are lower and the losses for vertical polarization are higher in the shadow region. In the lit region, the characteristics are almost identical.

#### 2.1.2.2 Translation Stage Measurements

In the second setup, both the TX and the RX are kept fixed. The measurement object is positioned on a translation stage and moved in x-direction in steps of 1 mm (see Fig. 2.5). The measurements were taken for a single frequency of 60 GHz. Like for the angular dependent measurements, standard gain horns have been used as transmitting and receiving antennas. The unobstructed case always serves as a reference. Closed objects have been used, namely the circular cylinder mentioned above and a metallic cuboid with quadratic cross section (80 x 80 mm$^2$). In this setup, the interference between diffracted field components around both sides of the object is of interest, because the interference leads to a different diffraction characteristic, especially in the shadow region.

As TX and RX are kept fixed and the objects are moved, the total field must be calculated in a different way than for the first setup. On the one hand, the field component $E_{LOS}$ is constant, on the other hand we are dealing with closed objects here. In the lit region, the total field is modeled according to

$$\begin{aligned} E_{tot} &= g_{TX}(0) \cdot g_{RX}(0) \cdot E_{LOS} \\ &+ g_{TX}(\Phi_{AoD,1}) \cdot g_{RX}(\Phi_{AoA,1}) \cdot E_{D,1} \\ &+ g_{TX}(\Phi_{AoD,2}) \cdot g_{RX}(\Phi_{AoA,2}) \cdot E_{D,2}, \end{aligned} \tag{2-16}$$

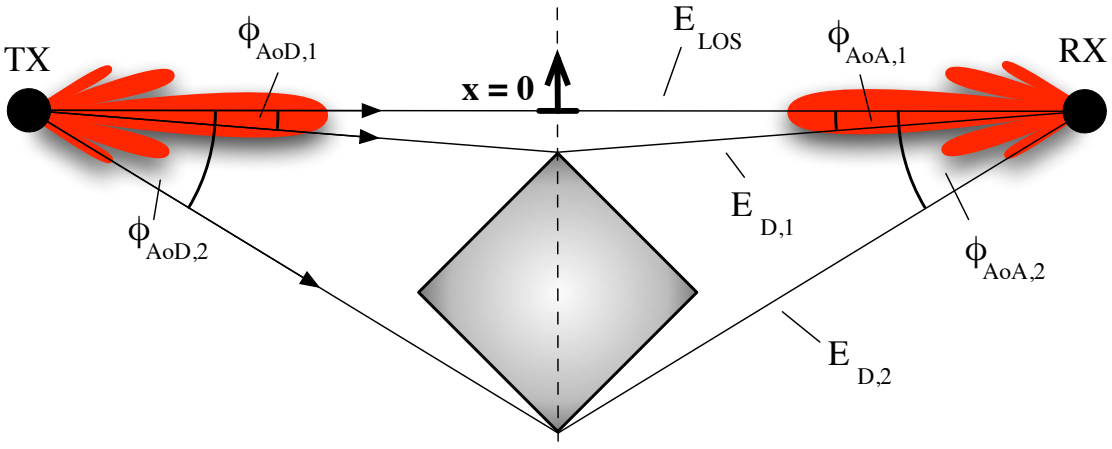


**Figure 2.5:** Translation stage measurement setup (setup 2).

where $E_{D,1/2}$ are the diffracted field components around both sides of the object (see Fig. 2.5), weighted with the corresponding antenna gain values $g_{TX}\left(\Phi_{AoD,1/2}\right)$ and $g_{RX}\left(\Phi_{AoA,1/2}\right)$. The individual terms $E_{D,1}$ and $E_{D,2}$ are calculated assuming two single edges (cf. section 2.2.1.4) or wedges at the front and the back of the cuboid. Please note that the cylinder UTD already accounts for both components inherently. It is noteworthy to mention that here only metal objects are analyzed and hence $E_{LOS} = 0$ in the shadow region.

The results for the longitudinal movement of the objects are shown in Fig. 2.6. Again, the range is limited to the relevant area from $x$ = -9 cm to $x = 5$ cm. The position, where the object reaches the LOS connection between TX and RX defines the point of origin $x = 0$ (see Fig. 2.5). For symmetry reasons, the characteristics are mirrored for larger

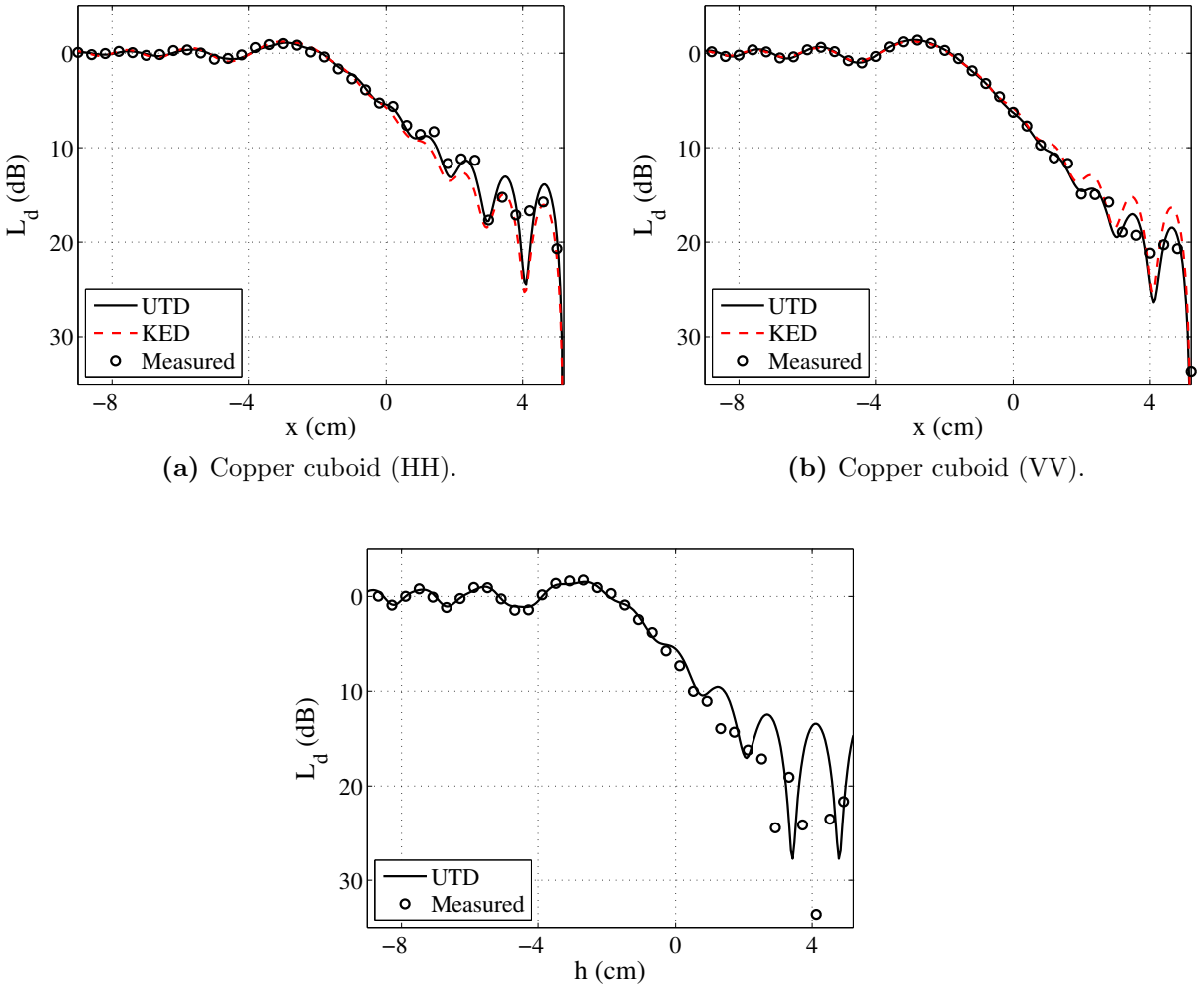


**(a)** Copper cuboid (HH).

**(b)** Copper cuboid (VV).

**(c)** Metal cylinder (VV).

**Figure 2.6:** Comparison of diffraction measurements and modeling results of metal objects.

$x$-values. Due to the relatively narrow antenna pattern, mostly one of the diffracted field components $E_{D,1}$ or $E_{D,1}$ dominates. The other component is suppressed by the antenna diagram. Only in the deep shadow region, where the components have a similar magnitude and experience similar antenna gains, the interference of both parts causes oscillations.

Figs. 2.6a and 2.6b depict the results for the copper cuboid. In addition to the UTD, here the KED results are also shown. In the lit region, the loss oscillates around 0 dB, whereas it decreases in the shadow region. As expected, the losses amount to 6 dB at $x = 0$ in any case. Comparing the horizontal and vertical polarization, small differences can be recognized, which is also expected in the case of metallic objects. The interference between $E_{D,1}$ and $E_{D,2}$ is clearly visible in the shadow region for both polarizations. Although the measured objects are not edge-shaped, KED and measurements are also in good agreement. The RMS modeling error amounts to about 1.7 dB compared to 0.8 dB for the UTD. This shows that even this simple model provides a sufficient and pragmatic solution for commonly encountered diffraction problems. Considering the metal cylinder measurements (Fig. 2.6c), only slight differences can be recognized compared to the cuboid. Measurements and UTD again agree well, except for cases in the deep shadow region where the theory overestimates the diffraction losses.

### 2.1.3 Impact on the 60 GHz Radio Propagation Channel

Based on the validated diffraction theories, the impact of diffraction at obstacles on the 60 GHz radio channel is investigated. Therefore ray tracing simulations (see Chapter 3) for an office scenario including reflection, transmission and diffraction is performed in order to get channel impulse responses. A schematic of the scenario is depicted in Fig. 2.7a, wheras a detailed description of the scenario can be found in [Jacob12]. The transmitter

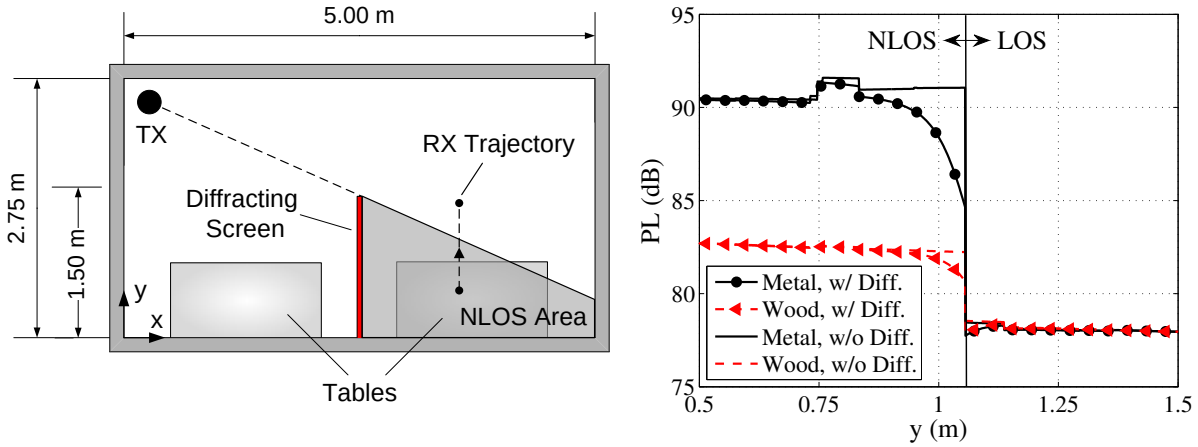


**(a)** Scheme of the scenario in top view.

**(b)** Path loss along trajectory.

**Figure 2.7:** Impact of the diffraction at a screen evaluated in terms of the path loss.

is positioned in the upper left corner of the roof under the ceiling emulating a WLAN access point. A vertical screen partitioning two cubicle-like workplaces is included in the scenario in order to investigate the sole influence of one major diffracting object on the channel characteristics. A one meter long trajectory (1 mm resolution) representing the transition between LOS and NLOS area behind the screen is used for the evaluation.

Fig. 2.7b depicts the path loss along the trajectory with and without taking diffraction into account. The path loss is determined by a power addition of all received rays in order to eliminate small scale fading and focus on the path loss only. The influence on the small scale fading can be found in [Jacob12]. Two cases are considered, a metallic and a wooden screen. In the LOS area the path loss is clearly dominated by the direct connection of TX and RX and diffraction does not play a significant role. In the NLOS area the received power is supported by reflected multipath components in case of the impenetrable metallic screen. In the case of the wooden partition, the path loss is about 8 dB lower, because here the LOS ray is not fully blocked, but just attenuated and hence contributes to the overall received power. At the transition (y = 1.05 m), a drop of path loss occurs. This drop is very abrupt when the diffracted wave is not taken into account and rather smooth with the diffracted wave. The influence of diffraction is lower for the wooden screen due to the relatively strong transmitted ray. Concluding the study, the diffraction at the screen can be neglected everywhere but in the close vicinity to the transition between LOS and NLOS area. The most significant factor is that the path loss in the shadow region is slightly lower due to the diffracted wave portion. Please note that the given analysis is part of a more detailed study, including additional examinations of the implications on the 60 GHz radio channel or a comparison between 60 GHz and 300 GHz [Jacob12].

## 2.2 Human Blockage

In this thesis, suitable models for the mm-wave range are proposed. Therefore, in this chapter different potential models accounting for the interaction between electromagnetic waves and the human body are developed or adapted to this application and compared. In Section 2.2.1, the different models are presented and their theory is shortly reviewed. Then, in Section 2.2.2 the models are compared in order to choose the best one to be included into ray tracing simulations (see Chapter 4). The focus here lies on human shadowing and not on reflection at the human body.

### 2.2.1 Theories

In this section, different human blockage models are presented. This is done in order to choose a model which can be used best to describe the interaction of the electromagnetic waves with the human body. There are three main requirements for such a model:

1. It should accurately reproduce the empirically observed shadowing characteristic due to human blockage.

2. Since the model should be used in extensive simulations to generate data sets for the development of statistical models, the computational effort must be manageable.

3. Additionally, the model must be easy to implement into ray tracing simulations.

Three different geometric models have been considered, namely the circular cylinder, the elliptic cylinder and the multiple knife edge model (see Fig. 2.8). In [Ghadd04, Ghadd07], the UTD for a conducting circular cylinder has been proven to be valid for modeling the presence of a human body at 10.5 GHz. In this thesis, the approach is extended to a dielectric cylinder model and a dielectric-coated conducting cylinder in order to account for human skin and clothing. Taking into account the actual shape of the human body, a dielectric elliptic cylinder is a better physical representation of a person. For this reason, the elliptic cylinder is also considered. Kunisch and Pamp have shown that it is sufficient to describe a human blockage event in the upper microwave region by knife edge diffraction [Kunis08]. A further development of this model is proposed in this thesis. This multiple knife edge model is described in more detail than the other models, as it is self developed and plays a key role in Chapter 4 and 5. The list below summarizes the models:

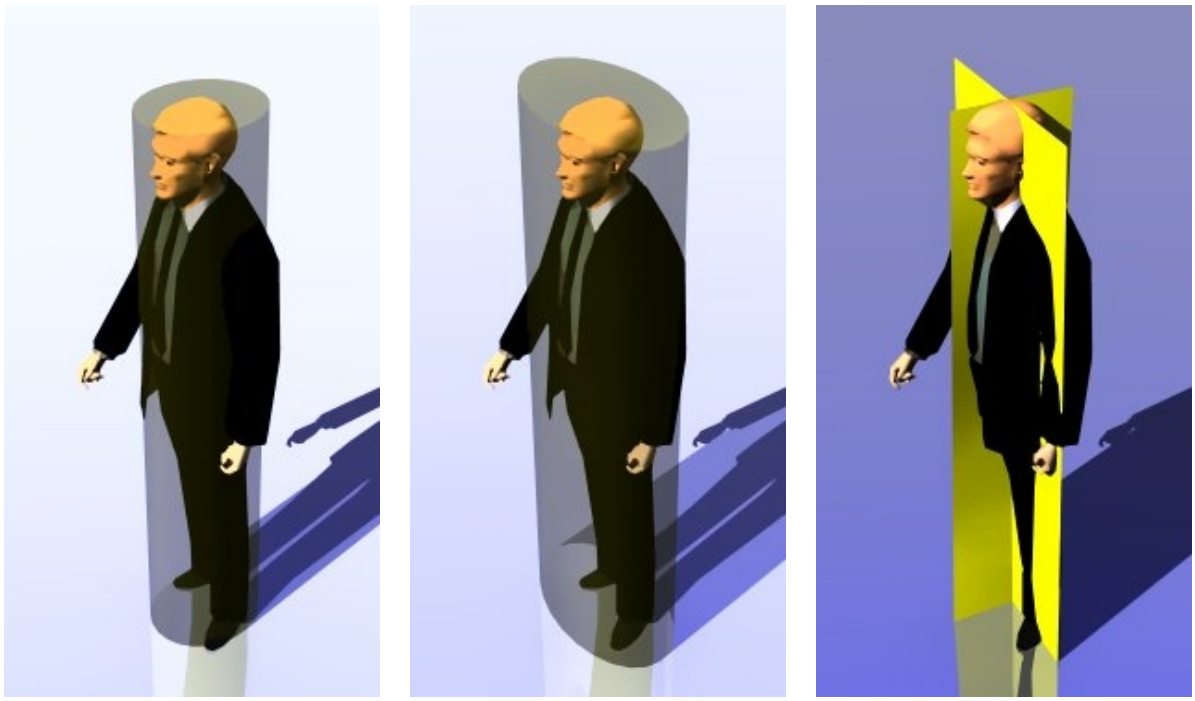

**(a)** Circular cylinder. **(b)** Elliptic cylinder. **(c)** Multiple knife edges.

**Figure 2.8:** Considered geometric models for the human body.

1a) *Perfectly conducting circular cylinder.*

1b) *Dielectric circular cylinder*, taking into account the permittivity of the human skin.

1c) *Dielectric-coated conducting circular cylinder*, taking into account clothing.

2) *Dielectric elliptic cylinder* as a better geometric representation of the human body.

3) *Multiple knife edge diffraction*, proposed as a new computationally efficient model.

For the sake of briefness, the theories as well as the comparison are predominantly shown for TE polarized waves.

#### 2.2.1.1 Exact Solution for a Dielectric Circular Cylinder

For the scattering by an infinitely long circular cylinder, exact solutions for different kinds of incident waves exist [Bowma87, Van B07, Wait59, Harri01, Balan89]. The most general case would be the solution for the scattered field assuming a point source as transmitter. Nevertheless, the problem of a line source parallel to a cylinder as shown in Fig. 2.9 is sufficient to model the two-dimensional case which is used for the comparison in Section 2.2.2. The fully three-dimensional solutions can be found in literature and have a structure very similar to that given in the following. As it is used only once in this section, the solution for the field within the human body is not given here, because it is irrelevant for the application in WLAN/WPAN channel models. The solution for this case can be found in the given literature. In the following, the calculation instructions for this special case will be reviewed briefly based on [Balan89]. The incident wave at the RX is assumed to be z-polarized of the form

$$E_z^i = E_0 H_0^{(1)} \left( k \left| \vec{r} - \vec{r_i} \right| \right), \tag{2-17}$$

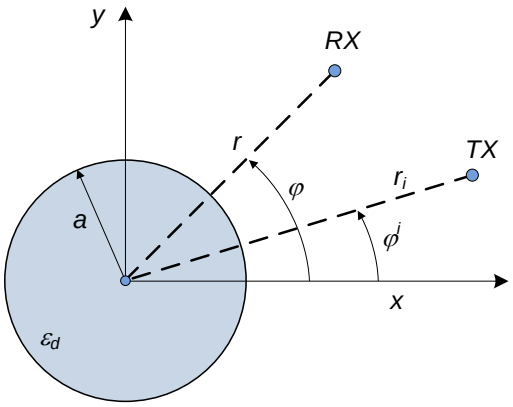


**Figure 2.9:** Geometry for the scattering by a dielectric cylinder.

which is the representation of a cylindrical wave with its origin at the TX as shown in Fig. 2.9. Here, $H_0^{(1)}$ is the Hankel function of the first kind and zero$^{th}$ order. The total field at the RX is determined by inserting this ansatz into Helmholtz' equation, to satisfy Bessel's equation under the special boundary conditions for this problem [Balan89]. The total field is a superposition of the incident and scattered fields:

$$E_z = E_z^i + E_z^s \tag{2-18}$$

After solving Bessel's equation the total field reads:

$$E_z = E_0 \left[ 1 - \sum_{n=-\infty}^{\infty} a_n \frac{H_n^{(1)}(kr)\, H_n^{(1)}(kr_i)}{H_0^{(1)}(k\,|\vec{r} - \vec{r_i}|)} e^{jn\left(\varphi - \varphi^i\right)} \right] \tag{2-19}$$

where $a_n$ is the scattering coefficient

$$a_n = \frac{J_n^{'}(ka)\, J_n(k_d a) - \sqrt{\varepsilon_d} J_n^{'}(k_d a)\, J_n(ka)}{\sqrt{\varepsilon_d} J_n^{'}(k_d a)\, H_n^{(2)}(ka) - J_n(k_d a)\, H_n^{'(2)}(ka)}. \tag{2-20}$$

Here $J_n$ and $J_n^{'}$ are the Bessel functions of the first kind and the $n^{th}$ order as well as the corresponding derivative, $\varepsilon_d$ is the complex permittivity and $a$ the radius of the cylinder. The wavenumber within the cylinder is calculated as $k_d = k\sqrt{\varepsilon_d}$. For the perfectly electric conducting (PEC) cylinder, the scattering coefficient reduces to

$$a_n = -\frac{J_n(ka)}{H_n^{(2)}(ka)}, \tag{2-21}$$

because $\varepsilon_d \to \infty$. Please note, that in contrast to the cylinder UTD in Section 2.1.1.3, no distinction of cases between lit and shadow region is necessary here. The disadvantage of the analytical solution clearly is the fact, that it is not ray based and hence one cannot distinguish between the different field components. This would be a problem, if the different field components should be weighed by an antenna diagram.

#### 2.2.1.2 Exact Solution for a Dielectric-Coated Conducting Cylinder

The solution for the scattering from a dielectric-coated, perfectly conducting cylinder (see Fig. 2.10a) can be derived in a similar manner like the solution for the dielectric cylinder. For the calculation of the electrical field, only the scattering coefficient has to be adapted [Tang57]:

$$a_n = \frac{A_n k_d J_n(kb) - B_n k J_n^{'}(kb)}{-A_n k_d H_n^{(1)}(kb) + B_n k H_n^{'(1)}(kb)}, \quad \text{with} \tag{2-22a}$$

$$A_n = \left[ H_n^{'(1)}(k_d b)\, H_n^{(2)}(k_d a) - H_n^{'(2)}(k_d b)\, H_n^{(1)}(k_d a) \right] \tag{2-22b}$$

$$B_n = \left[ H_n^{(1)}(k_d b)\, H_n^{(2)}(k_d a) - H_n^{(2)}(k_d b)\, H_n^{(1)}(k_d a) \right] \tag{2-22c}$$

The total field again can be calculated by (2-19).

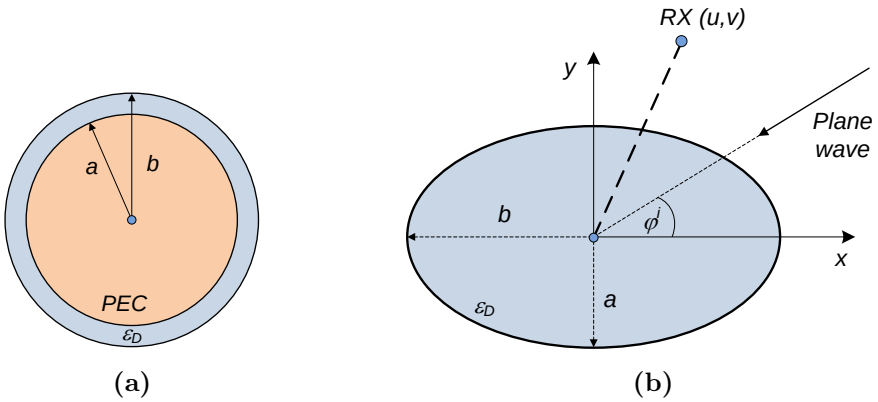


**Figure 2.10:** Geometry of the dielectric-coated conducting (a) and the elliptic (b) cylinder.

#### 2.2.1.3 Exact Solution for a Dielectric Elliptic Cylinder

For the comparison in Section 2.2.2, the solution for scattering of an elliptic cylinder illuminated by a plane wave will be used (see Fig. 2.10b). The exact solution can be derived by solving the wave equation in elliptic cylindrical coordinates. These coordinates $(u, v, z)$ are defined by the relations [Cojoc08]:

$$u = \text{real}\left(\text{acosh}\left(\frac{x+jy}{f}\right)\right) \tag{2-23}$$

$$v = \text{imag}\left(\text{acosh}\left(\frac{x+jy}{f}\right)\right) \tag{2-24}$$

$$z = z, \tag{2-25}$$

with $0 \leq u \leq \infty$ and $0 \leq v \leq 2\pi$ and $f = \sqrt{a^2 - b^2}$ being the semifocal length of the ellipse. The contours of constant $u$ are confocal ellipses and those of constant $v$ are confocal hyperbolas [Cojoc13].

The scattering solution is given in terms of sums of the so called Mathieu functions $J_{pm}, N_{pm}, H_{pm1}$ and $S_{pm}$. The total field is a superposition of the plane wave and the scattered field $E_z^s$ [Strat41]:

$$E_z^s = \sum_{n=0}^{\infty} i^n \alpha_{pm}^{sc}(n)\, H_{pm1}(q_0, u, n)\, S_{pm}(q_0, v, n)\, S_{pm}\left(q_0, \varphi^i, n\right), \tag{2-26a}$$

$$\alpha_{pm}^{sc}(n) = \frac{J_{pm}(q_0, u_1, n)}{N_{pm}(q_0, n)\, H_{pm1}(q_0, u_1, n)} \frac{\mathcal{J}_{pm}(q_0, u_1, n) - \mathcal{J}_{pm}(q_1, u_1, n)}{\mathcal{J}_{pm}(q_1, u_1, n) - \mathcal{H}_{pm1}(q_0, u_1, n)}, \tag{2-26b}$$

with $q_0 = \frac{f^2 k^2}{4}$, $q_1 = \frac{f^2 k_d^2}{4}$, $u_1 = \text{acosh}(\frac{a}{f})$ and $\mathcal{F} = F'/F$ being the log-derivative of the Mathieu functions with respect to $u$. Please note that the nomenclature of [Cojoc08] is

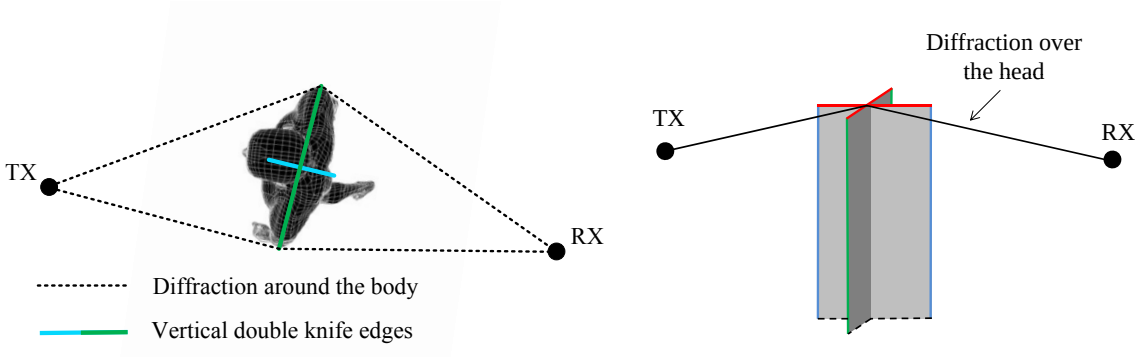


**(a)** Movement of the person. **(b)** Diffraction over the person's head.

**Figure 2.11:** Multiple knife edge model. (a) Movement of the person according to the extended double knife edge model (top view). (b) Vertical double knife edges around the body and two horizontal single knife edges for diffraction over the person's head.

used here.[1] For more detailed information about the Mathieu functions and the derivation of the scattering solution, the reader is referred to the given literature.

#### 2.2.1.4 Multiple Knife Edge Diffraction Model (MKE)

In this thesis, the double knife edge model (DKE model) from Kunisch and Pamp is extended to a multiple knife edge model as their model disregards diffraction over a person's head and according DKE model [Kunis08], the total field at a receiver is the superposition of diffracted components from two knife edges. An example of the application of the DKE model to the shadowing by a person is shown in bird view in Fig. 2.11a. This way, the shadowing around the human body is taken into account. In the original DKE model only the blue plane representing the sagittal body plane, i.e. between back and chest exist. Here the fields are determined for each knife edge separately according to the Fresnel integral in Eq. (2-1) and are summed up coherently afterwards:

$$E_{DKE} = F(\nu_1) + F(\nu_2), \tag{2-27}$$

Here, $\nu_1$ and $\nu_1$ have to be determined for the diffraction around both sides of the human body. The advantage of the DKE model is the very low computational effort compared to any other model discussed in this thesis. However, in [Kunis08] only one double knife edge is proposed along the body's main axis, whereas a constant motion along a straight line almost perpendicular to the ray is assumed. This model proves to be insufficient in the case of a motion nearly parallel to the ray, as the ray does not intersect the double knife edge, but the body still shadows the ray. Therefore, the proposed extended DKE

[1] In addition, a freely available MATLAB toolbox [Cojoc13] has been used for the implementation of the Mathieu functions.

model includes an additional double knife edge parallel to the body's axis as shown green in Fig. 2.11a. Furthermore, the conventional double knife edge model is limited to two-dimensional geometries. This would disregard a possible diffraction by the person's head. However, this is expected for certain positions in a realistic indoor scenario, so the introduction of two more horizontally oriented knife edges on top of the body is required (see Fig. 2.11b). The adoption of two double knife edges would be incorrect as diffraction under the feet is implausible due to the ground.

For the determination of the resulting diffraction loss different geometry parameters have to be derived for each double knife edge first. The total loss is then a superposition of the relevant DKE and the diffraction over the head. A detailed description of the geometrical calculations is given in Appendix B on page 139ff.

## 2.2.2 Suitability of the Different Models for Human Blockage

In the following, the presented models are analyzed regarding their suitability to model the human blockage at 60 GHz. This is done in order to choose the most appropriate model which will be applied together with ray tracing in Chapter 4 to derive stochastic channel models regarding human blockage. Therefore, at first the influence of the human skin, the kind of object shape and the influence of clothing is analyzed. Then, in the end of the section, the models are compared to measurements in order to judge the accuracy.

### 2.2.2.1 Influence of the Human Skin

The circular cylinder has been used to model human blockage before [Ghadd04, Ghadd07, Khafa08]. Here, it will be now discussed, whether a cylinder with the dielectric properties of human skin is a better assumption than the PEC cylinder. Therefore the scattering of a plane wave is compared for both cases (see Fig. 2.12). A variety of simulated and measured electrical properties of the skin at 60 GHz is available. A relative permittivity of $\varepsilon_d = 8.05 - j4.13$ has been adopted for the human skin [Zhado11]. This value has been chosen because the imaginary part representing the conductivity of the skin is comparatively low and hence is a worst case compared to the infinite conductivity of the PEC cylinder. Please note that the influence of clothing will be analyzed separately subsequently in this chapter.

Fig. 2.12a and 2.12b show the loss in relation to the case without cylinder, which would be the lossless propagation of a z-polarized plane wave propagating along the $x$-direction. The loss is shown in the z = 0 plane. The cylinder diameter is chosen to be 25 cm according to the typical width of the human body. In both cases, the expected behavior can be observed. Directly behind the cylinder obstacle in the deep shadow region, very high losses occur, whereas the diffracted power increases at larger distances. At first glance no significant difference between the two cases is observed, which denotes that the

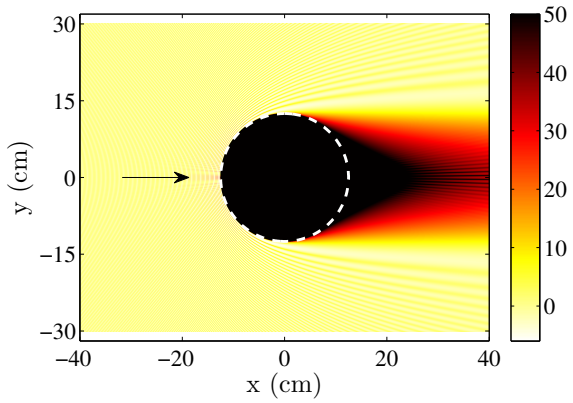


**(a)** Shadow attenuation (dB) of a metallic cylinder.

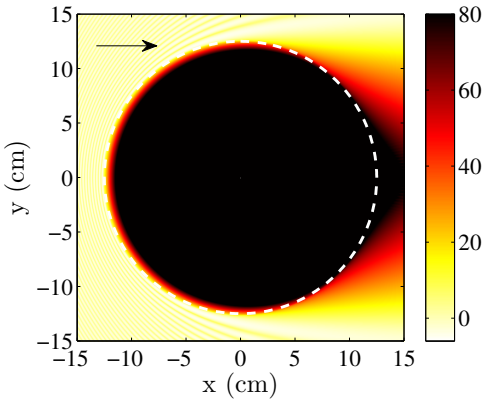


**(b)** Shadow attenuation (dB) of a dielectric (skin) cylinder.

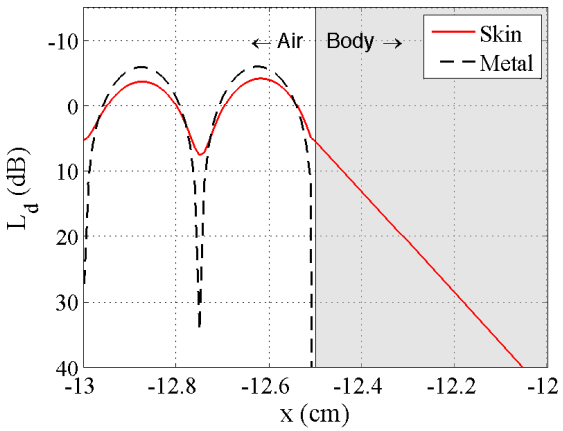


**(c)** Attenuation characteristics at the skin-air interface ($y = 0$).

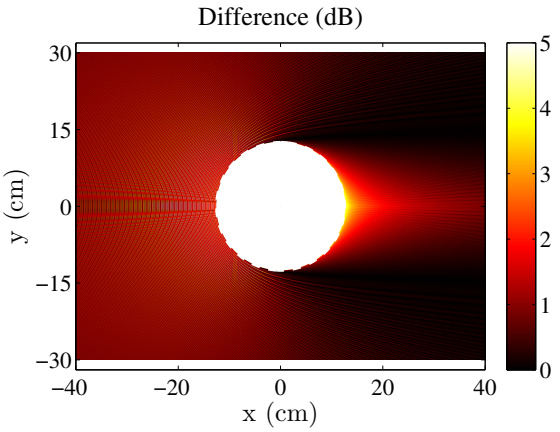


**(d)** Difference between attenuation for metallic and dielectric (skin) cylinder

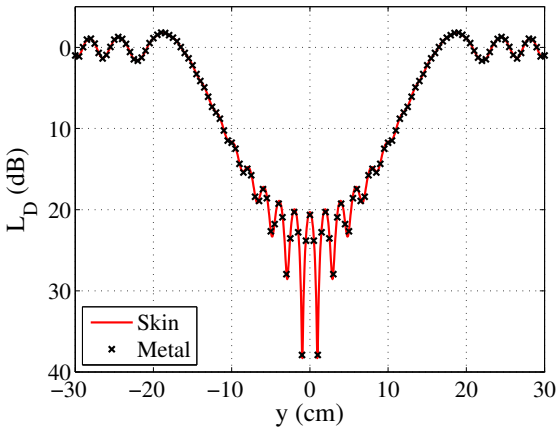


**(e)** Shadowing characteristic for a metallic and a dielectric (skin) cylinder at $x = 1.0$ m.

**Figure 2.12:** Comparison of the field strength for a metallic and a dielectric (skin) cylinder. The arrows mark the direction of an assumed plane wave.

conductivity of the human skin is sufficiently high enough to assume it approximately as a PEC. This will be analyzed in more detail in the following. Fig. 2.12c shows a cut-out of the loss characteristics at the skin-air interface for y = 0 and -13 cm $\leq$ x $\leq$ -12 cm. As already pointed out, the field inside the cylinder is of minor interest, because it is irrelevant for WLAN channel models. Nevertheless it is shown here, as it contributes to the understanding of the diffraction mechanism. Inside the PEC cylinder the loss is infinitely high as the field does not penetrate the cylinder. This is different for the dielectric (skin) cylinder, where the electromagnetic field is highly attenuated with a factor of more than 70 dB/cm. This can be also seen in Fig. 2.12b, where the loss distribution within the cylinder is shown as an enlargement. The losses quickly exceed values of 80 dB moving away from the air-skin interface.

In front of the cylinder fading can be observed due to the interference between scattered and incident field. The fading characteristics are more pronounced with higher maxima and lower minima for the metal cylinder as here the reflectivity is higher than than for the dielectric cylinder. This holds for the entire area in front of the object (see Fig. 2.12d). In this Figure, the absolute difference between the loss distributions in the $z = 0$ plane is depicted. Besides the different behavior inside the cylinders, the area behind the cylinder is of main interest. Directly behind the cylinder, the field strength is up to 5 dB higher for the dielectric (skin) cylinder. It is noteworthy to mention, that in both cases the wave is attenuated by more than 50 dB (see Fig. 2.12a). Besides the general trend, interference patterns in the order of several millimeters can be observed in the whole plane for the absolute loss as well as the loss differences. This can be traced back to the short wavelength. Fig. 2.12e completes the comparison between PEC and skin. Here, the loss characteristic is shown behind the cylinder for x = 1.0 m and -0.3 cm $\leq$ y $\leq$ 0.3 cm. This illustration clearly shows that in the area far behind the cylinder there is no difference between the scattering by a PEC and the dielectric (skin) cylinder at all.

#### 2.2.2.2 Influence of the Object Shape

The influence of the model geometry is compared for the human arm. This is done, because there is a need for models not only for the whole human body but also for the extremities [Gusta12]. Obviously, the elliptic cylinder is also a better physical representation of the human body compared to the circular cylinder, as it approximates the cross section of the human torso more appropriately. Nevertheless, the investigation for the human torso is left out intentionally here for the sake of briefness. In order to model the human arm, the minor radius $a$ and major radius $b$ of the elliptic cylinder are chosen to be 2.75 and 3.5 cm, which are typical values. Two cases are analyzed, a plane wave propagating along the major axis and the minor axis of the elliptic cross section (see Fig. 2.13a and 2.13b respectively). In addition to the elliptical cylinder model, the results for the circular cylinder and a MKE is shown. The cylinder diameter as well as the width of the MKE is chosen equivalent to the relevant axes of the elliptical cylinder, i.e. 5.5 cm in Fig. 2.13a and 7 cm in Fig. 2.13b. This comparison is done for the shadow region 0.2 m behind

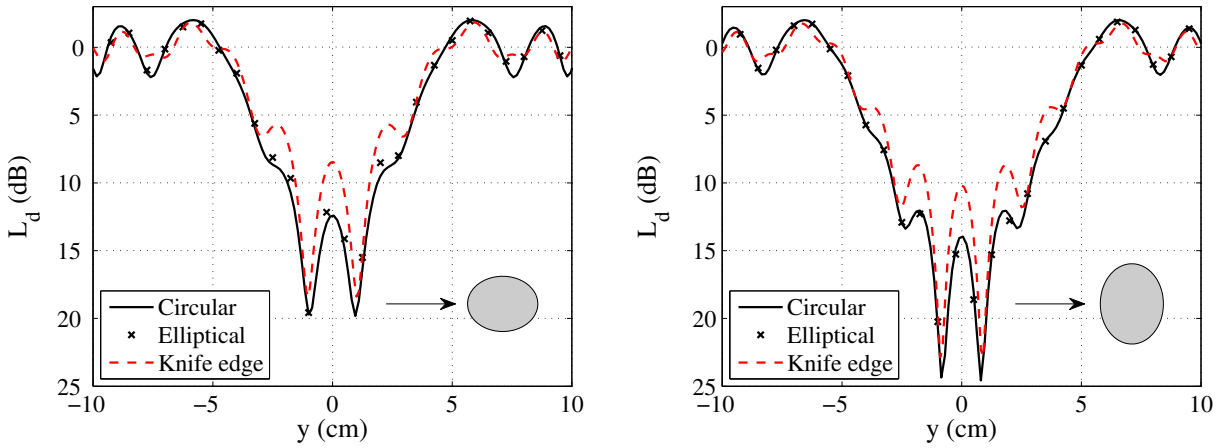


**(a)** Propagation along major axis.

**(b)** Propagation along minor axis.

**Figure 2.13:** Shadowing characteristic for an elliptic cylinder compared to the circular cylinder and the MKE model

the cylinder and the transition to the lit region. In both cases, almost no difference between circular and elliptical cylinder model is visible. Regarding the MKE solution, the interference maxima are higher and the characteristic in the lit region also slightly deviates from the other models.

#### 2.2.2.3 Influence of Clothing

In order to analyze the influence of clothing further, additional measurements of a brass cylinder have been performed. These measurements have been carried out at a single frequency of 69 GHz using setup 1 as described in Section 2.1. A cylinder with a radius of 4 cm has been measured barely and covered with 5 mm of cotton (see Fig. 2.14). The results presented above have shown that the human skin can be assumed to be a PEC because no significant difference could be observed. Hence, the covered metallic cylinder is a sufficient approximation for clothing on skin. Fig. 2.14c depicts the angular dependent results for vertical (VV) and horizontal (HH) polarization. Again, negative angles corresponds to the shadowing region. In the metallic case, the characteristic is steeper and the absolute loss is higher for the vertical polarization compared to horizontal polarization, which is expected. Interestingly, in case of vertically polarized waves, the clothing leads to losses, *lower* by up to 20 dB in the shadowing region. This does not hold for the horizontal polarization. Here, the maximum difference amounts to only 6.9 dB, however, mostly the metal cylinder case shows the lower losses. It is noteworthy that the diffraction behavior is highly sensitive to the layer thickness and the dielectric properties of the clothing. This will also be analyzed in the next section.

**(a)** Bare.

**(b)** Covered with cotton.

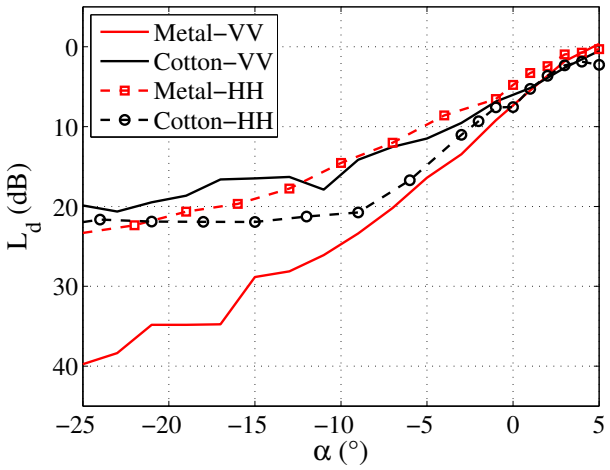


**(c)** Shadow attenuation for a cylinder with and without clothing.

**Figure 2.14:** Cylinders used for measurements and measurement results.

#### 2.2.2.4 Validation with Measurements

In order to validate the human blockage models, its simulation results have been compared to human blockage measurements. This comparison has been carried out for the MKE model, the metal cylinder (UTD) as well as the coated cylinder. The UTD and the MKE model have been chosen because of their low computational effort, as well as the fact that the previous analysis has shown that assuming metal instead of human skin is sufficient. In order to study the impact of clothes, the coated cylinder model is also considered here. Two different cases are considered here. A 5 mm and a 10 mm thick dielectric coating is assumed to emulate a fleece layer with $\varepsilon_d = 1.25 + j0.042$ [Zhado11, Hertl07].

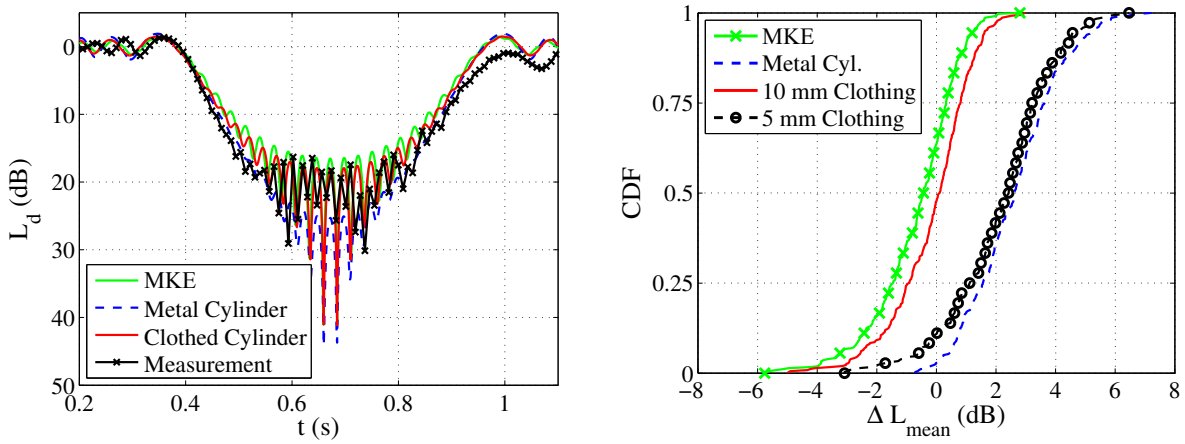


**(a)** Exemplary shadowing event.

**(b)** CDF of differences between averaged measured and simulated shadowing attenuation.

**Figure 2.15:** Comparison of human blockage models and measurements.

The measurement results used for the validation were kindly provided the Heinrich-Hertz-Institut in Berlin. The measurements have been performed with a 60 GHz real time 2×2 MIMO channel sounder. At this point, the sole LOS MPC is considered. During the measurements a clothed person has crossed the LOS link nearly perpendicularly. A detailed description of the measurement setup can be found in [Peter12]. In the reference, also a comparison of measurements and models with a slightly different focus is given and also supports the findings presented in this thesis.

All three models have three degrees of freedom, namely the starting point $x_0$ of the person, the walking speed $v$ and the depth $2a$ of the person. These parameters have been extracted from the measurements taking into consideration the geometry of the measurement scenario. For the parameter extraction, the person is assumed as a double knife edge. The time where one knife edge reaches the connection line between TX and RX corresponds to an attenuation of 6 dB, because approximately half of the field strength is shadowed by the person. This holds true for the 6 dB level crossings of the falling edge as well as the rising edge of the shadowing event. By exploiting this fact and the exact knowledge of the position of the different MIMO antennas all degrees of freedom can be determined. On average, the walking speed was $\mathrm{v} = 0.51\,\frac{\mathrm{m}}{\mathrm{s}}$ and the body depth was 0.23 m.

Fig. 2.15a shows a typical temporal characteristic of a shadowing event. One can observe oscillations before the actual event and interference during the deep shadow phase. The event has a duration of about 600 ms. A qualitative comparison reveals that all models show deviations compared to the measurement. In general, the cylinder UTD mostly overestimates the attenuation in the deep shadowing zone, whereas the other models sometimes underestimate and sometimes overestimates it. The deviations can be explained by the facts that a constant walking speed is assumed and the actual body shape deviates

from the model geometries. In addition, the small wavelength makes the fading behavior extremely sensitive to the walking speed of the person and a possible inaccuracy of the determined antenna positions. Hence, a perfect alignment of measured and simulated interference pattern is not expected in any case. Another fact is that the models produce symmetrical shadowing events, which is not the case for the measurements. The reason for this is the asymmetrical shape of the body as well as a varying walking speed. Nevertheless, the trend including the general fading characteristics is well modeled especially with MKE and coated cylinder model.

Besides this qualitative comparison, a quantitative comparison in terms of the fading statistics is carried out. Here, the results for a 5 mm thick fleece layer are considered additionally. In principle, all models show a good agreement with the experimentally observed shadowing events. Fig. 2.15b shows the CDFs of the differences between measured and simulated shadowing loss. As a basis for this statistic, for every shadowing event the mean value of the attenuation higher than 10 dB has been taken into account. The averaging is done as already slight temporal displacements between measured and simulated interference patterns would lead to very high differences. Altogether, the CDF is derived from 360 different shadowing events with distances between RX and TX ranging from 2 to 10 meters. The CDFs reflects the behavior already observed in Fig. 2.15a. The metal cylinder model tends to overestimate the attenuation by up to 6 dB, whereas MKE and coated cylinder model (10 mm coating) in principle show better performance with average deviations of 0.1 and 0.4 dB respectively. In case of the MKE model, this is quite surprising, as the metal cylinder definitely provides a better approximation of the human body than knife edges. In case of the coated cylinder it is also an interesting result, that obviously the consideration of clothing can lead to a significantly higher model accuracy. Nevertheless, the accuracy is very sensitive to the coating parameters, i.e. thickness and dielectric properties. The modeling error for the 5 mm coating is for example almost as high as for the bare metal cylinder. The dielectric properties as well as the layer thickness of the clothing, which have been worn during the measurements, are not known. Nevertheless, the results suggests that it is possible to enhance the modeling accuracy by taking into account clothing.

Up to this point, the mere amplitude of shadowing events has been considered. However, measurements have revealed that the phase of a signal rapidly changes during an event. This is especially important for the modeling of time-variant channel impulse response (cf. Section 4.3). Fig. 2.16 illustrates the phase behavior of an exemplary measured shadowing event and the corresponding MKE simulation results. The figure shows the amplitude as well as the phase. The amplitude characteristic is given here as a reference only because the amplitude have been discussed thoroughly above. The shown shadowing event is almost symmetrical. The phase remains nearly constant up to the instant of time, when the loss reaches 6 dB. This corresponds to the position where the person just shadows the LOS connection. Before this point, the loss characteristic is dominated by the LOS link, which possesses a constant phase. In the shadow region behind this point, the diffracted components dominate. Compared to the small wavelength, these components

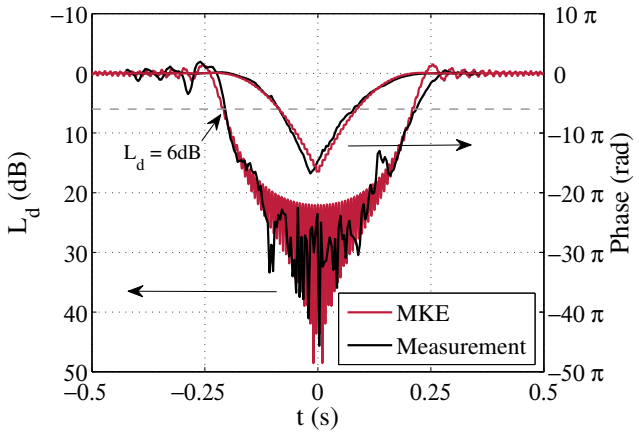


**Figure 2.16:** Comparison of MKE and measurements.

change their length and hence the phases very fast. The phase decreases by $16\,\pi$ until in the first half of the event and increases afterwards. This can be explained by the fact that the component diffracted around the front of the body, which gets longer with time, dominates first. Then, in the second half of the event, the component diffracted at the back dominates, which gets shorter with time. Despite a small time shift, which can be explained by a varying walking speed in the measurements, the agreement of the measured and the simulated phase is very good.

Table 2.1 summarizes the comparison in terms of accuracy. For the elliptic cylinder model, the evaluation was not possible due to a slow convergence of the terms of sums and a hence a too high computational time for cylinder dimensions much larger than the wavelength. Nevertheless, the results for the modeling of the human arm suggests that the accuracy of this model would be high. Despite the similar modeling errors, the MKE performance is rated worse than the dielectric-coated cylinder model in the table since it does account for polarization. As shown before, the consideration of the dielectric properties of human skin does not lead to a higher accuracy compared to the PEC case. The computational effort and the analysis of implementation aspects will be discussed in the next subsection.

#### 2.2.2.5 Computational Effort and Implementation Aspects

Like stated in the beginning of the section, a manageable computational effort as well as the implementability into a ray tracing tool is an important criterion for the choice of a proper human blockage model.

The computational effort is analyzed by comparing the average simulation time for the validation with measurements presented in the last subsection. The simulation time is normalized to the value for the MKE model as this is the most efficient algorithm (see Table 2.1). All other models are at least nine times slower. The analytical solutions all exhibit the summation of Bessel or Mathieu functions. For the dimensions of a human

**Table 2.1:** Comparison between different human blockage models.

| | **Accuracy** | **Computational Effort** | **Implementation Effort** |
|---|---|---|---|
| PEC cylinder (UTD/Analytical) | +/+ | 9/40 | ++/+ |
| Dielectric cylinder | + | 300 | + |
| Dielectric-coated cylinder | ++ | 220 | + |
| Elliptic cylinder | [1] | 70000 | + |
| MKE | + | 1 | ++ |

[1] Evaluation not possible due to convergence problems for cylinder dimensions much larger than the wavelength.

body, which are much larger than the wavelength in our case, the calculation of a few hundred summands is necessary. This leads to an effort, which is 40 - 70000 times higher than for the MKE.

Regarding the implementability into ray tracing simulations, the UTD is the model suited best, as it is inherently ray based. For all the analytical solutions a separation of different diffracted field components is not possible. This leads to errors if directive antennas are used as the different components arrives under different AoAs (cf. Fig. 2.5, page 18). The MKE model is also technically not ray based, but here, at least the different field components are calculated separately (cf. Eq. (2-27), page 26). The AoAs can be estimated from the position of the single knife edges (cf. Fig. 2.11a), which is definitely an advantage over the analytical solutions.

Based on the comparison, the MKE has been chosen as the model which is best suited for the aimed application, as it combines a very low computational effort with very good implementability and despite some disadvantages a good accuracy.

## 2.3 Concluding Remarks

In this chapter, measurement and simulation results for different propagation mechanisms in the mm-wave range have been presented.

- ▷ Measurement and ray tracing based investigations of the diffraction in 60 GHz propagation channels have been presented. The conducted analysis is the first methodical study in this frequency range. Diffraction at an edge, at a wedge and at a cylinder has been measured. Those shapes are representative for typical objects in indoor environments like screens, corners or furniture. The measurement results have been compared to simulations according to the knife edge model and the uniform geometrical theory of diffraction. Realistic antenna patterns have been considered and good

agreements have been achieved. Apart from metal, also wooden objects have been investigated. In the latter case, it has been observed that the transmission has a much higher influence than diffraction. Furthermore, the high impact of the antenna pattern on the received diffracted power were proven. This is especially important for systems employing directive antennas, e.g. in case of potential beamforming.

The impact of diffraction on the 60 GHz radio channel properties has been analyzed exemplarily for a specific situation. From the ray tracing simulations, it can be concluded that diffraction plays a minor role in the 60 GHz frequency range. It has been shown that only under NLOS conditions and in a very small region close to the transition to the LOS area the path loss is affected by diffracted waves. Everywhere else, diffraction at obstacles like partioning screens can be neglected. This is especially true for thin penetrable edges, where transmission effects reduce the impact of diffraction even further.

For the reasons mentioned above it can be concluded, that diffraction at obstacles like furniture will not have to be respected in the following chapters. Especially for higher order diffraction the computational effort is out of all proportion to the benefit in terms of higher accuracy.

- The main focus of this thesis is to study the influence of human blockage on the 60 GHz radio channel and ways to overcome the arising problems. For the geometrical modeling of the human body, different cylindrical structures have been analyzed in this chapter. In addition, the multiple knife edge model is introduced as a new alternative approach. The analysis in this chapter had the main goal to choose or develop a suitable human blockage description for further use in deterministic channel models. At first, the theories for the scattering by dielectric circular and elliptical cylinders have been reviewed and the theory of the multiple knife edge diffraction model have been given. Based on these theories, the suitability of the approaches for the application in deterministic radio channel modeling has been investigated. It has been shown that it is not necessary to consider the dielectric properties of the human skin, as its conductivity is high enough to be assumed as a perfectly electrical conductor instead of a dielectric material. Regarding the model geometry, the elliptical cylinder as well as the MKE model provide the advantage over the circular cylinder that they account for the width and the depth of the human torso. Finally, the model results have been validated by measurements, which lead to two interesting results. The agreement between the knife edge diffraction simulations and the human blockage measurements is quite good. In addition, clothing can have a significant influence on the attenuation under certain circumstances. Compared to the human blockage measurements the cylinder model accuracy could be increased by more than 2 dB taking into account clothing. On the other hand, this model is very sensitive to the thickness and the material of the clothing.

  In summary, appropriate approaches could be found to model the human induced shadowing even under consideration of clothing. Although the multiple knife edge diffraction does not take into account polarization, it has been chosen to be used

in the remaining part of this thesis as its computational effort is very low and the results still show a high accuracy.

To generally conclude, the findings of this chapter on the one hand provide quantitative statements about the considered propagation mechanisms. On the other hand they lay the foundation for the next chapters, where the presented models of separate propagation mechanisms are used to analyze the 60 GHz radio channel in a holistic way. In the following chapter e.g. the spatio-temporal channel characteristics will be investigated.

# 3

# Spatio-Temporal Channel Models and Measurements

Radio channel models combine relevant individual propagation mechanisms in order to provide a complete and realistic picture of the propagation channel. They serve different purposes like the evaluation or optimization of link and system level performance. Due to the high propagation losses, 60 GHz indoor systems will have to incorporate smart antennas in order to achieve multi-gigabit data rates. These antennas will be able to provide adaptive radiation characteristics ranging from omnidirectional to highly directive patterns [IEEE809c]. Obviously, this leads to significantly varying channel conditions for one and the same system. Hence, an antenna-independent channel description is required in order to evaluate such smart antenna systems. At this point, antenna independence refers to a double directional channel characterization, which includes information about amplitude, ToA, AoA and AoD of individual MPCs [Stein01].

In order to provide such a characterization, this section presents radio channel measurements and ray tracing simulations. In particular, angular dependent wideband measurements with highly directive antennas have been performed. As a result, the spatial as well as the temporal characteristics of the radio channel are analyzed. Additionally path loss measurements are presented. Isolated from the sole channel characterization, the measurement results serve to verify and calibrate the RT. A calibration algorithm is presented, which uses information about ToA, AoA and AoD. This way an unambiguous matching of measured and simulated MPCs is possible, which in turn increases the calibration accuracy.

For the channel investigations, three environments have been chosen, namely a conference room, a living room and a kiosk download scenario. According to the envisaged applications of 60 GHz indoor communications, these scenarios are among the most relevant ones (cf. chapter 1). Within all scenarios radio channel measurements have been conducted. The conference room as well as the living room additionally serve as reference scenarios for the use in further theoretical studies in Chapter 5.

Please note that parts of the work presented in this chapter have already been published by the author in [Piesi08, Malko08, Jacob09a, Jacob09d, Jacob09c, Kürne09, Jacob09f, Czink12,

Prieb12]. In particular, the measurements in the kiosk download scenario have been performed jointly with Dr.-Ing. Radosław Piesiewicz. However, a detailed analysis of these measurements are presented in this thesis for the first time. Furthermore, the fundamental structure and features of the calibration algorithm introduced in section 3.3 have been developed jointly with Dr.-Ing. Sebastian Priebe. The author of this thesis has especially contributed with the framework of the algorithm. Furthermore, the focus in this thesis lies on the impact of the number of different materials on the calibration performance. Additionally, the dependency of the calibration results on the initially assumed permittivity values is investigated. By contrast, Dr. Priebe has focussed on broadband calibration of dispersive materials in the THz band.

The chapter is in principal divided into three main sections. In section 3.2 the channel measurements are discussed. Based on this, the measurement results are used for the calibration of the RT in Section 3.3. Section 3.4 concludes the chapter. Since Section 3.2 already includes qualitative comparisons between measurements and RT, a basic understanding of the actual RT implementation is necessary. Hence, the chapter begins with a short overview about the RT tool.

## 3.1 Wideband Ray Tracing Simulations

A 3D ray-optical approach is used for the deterministic modeling of the 60 GHz indoor radio channel [Schac12, Nucke11]. This software has been developed at the Institut für Nachrichtentechnik and has been kindly provided by its developer Dr.-Ing. Moritz Schack. The input to the tool is a threedimensional representation of the environment as well as the relative permittivity $\varepsilon_r = \varepsilon_r' - j\varepsilon_r''$ of each scenario element. For the creation of the geometrical model the freely available 3D modeling software Google Sketchup has been used [Sket13]. A detailed description of the considered scenarios is given in combina-

**(a)** Photo. **(b)** 3D Geometrical model.

**Figure 3.1:** Living room scenario.

tion with the results of the analyses. Fig. 3.1 exemplarily depicts a photograph and the Sketchup model of the living room in order to give an impression of the resulting model. A brief description of the features of the RT tool is given in the following.

The RT tool is composed of a geometrical path search engine, which in a first step determines all possible geometrical ray paths and their geometrical representation. In a second processing step, the electromagnetic (EM) engine performs the relevant EM calculations in order to determine the complex field strengths of the MPCs. These calculations cover the free space loss, specular reflection losses as well as different diffuse scattering models such as the Lambertian emitter or the Kirchhoff scattering theory for rough surfaces [Prieb13b,Schac12]. Please note that in this thesis only the LOS path and reflections up to the third order have been considered. The first and second calculation step results in an antenna independent complex channel impulse response:

$$\mathbf{h}\left(\tau, \varphi_{RX}, \theta_{RX}, \varphi_{TX}, \theta_{TX}\right) = \sum_j \mathbf{P}^{(j)} \cdot \delta(\tau - \tau^{(j)}) \cdot \delta(\varphi_{RX} - \varphi_{RX}^{(j)}) \cdot \delta(\theta_{RX} - \theta_{RX}^{(j)}) \cdot \delta(\varphi_{TX} - \varphi_{TX}^{(j)}) \cdot \delta(\theta_{TX} - \theta_{TX}^{(j)}) \quad (3\text{-}1)$$

where:

- $\tau, \varphi_{RX}, \theta_{RX}, \varphi_{TX}, \theta_{TX}$ are delay as well as azimuth and elevation angles at the transmitter and receiver, respectively.
- $\delta(\bullet)$ is the Dirac delta function.
- $\tau^{(j)}, \varphi_{RX}^{(j)}, \theta_{RX}^{(j)}, \varphi_{TX}^{(j)}, \theta_{TX}^{(j)}$ are the geometry based parameters of the *i-th* MPC, calculated by the geometrical engine.
- $\mathbf{P}^{(j)}$ is the complex polarization matrix of the *j-th* MPC, computed by the electromagnetic engine.

In order to account for polarization changes during transmission, $\mathbf{P}^{(j)}$ and hence $\mathbf{h}$ are 2×2 polarization matrices [Malts10d]. Please note that $\mathbf{P}^{(j)}$ is not normalized and contains all propagation losses as well as the phase shift of the corresponding MPC. For a detailed description of the polarimetric calculations, the reader is referred to [Schac12]. At this point it should only be noted that the dielectric parameters of the scenario elements of course have to be chosen according to the frequency range of interest.

In order to determine antenna dependent channel impulse responses $h(\tau)$, the polarization matrix has to be weighed by the TX and RX antenna patterns respectively in a third and last step:

$$h(\tau) = \sum_j \vec{g}_{RX}(\varphi_{RX}^{(j)}, \theta_{RX}^{(j)})^H \cdot \mathbf{P}^{(j)} \cdot \vec{g}_{Tx}(\varphi_{Tx}^{(j)}, \theta_{Tx}^{(j)}) \cdot \delta(\tau - \tau^{(j)}), \quad (3\text{-}2)$$

where the superscript $H$ indicates the Hermitian transpose. The vectors $\vec{g}_{RX}$ and $\vec{g}_{TX}$ represent the antenna gain in terms of the Jones calculus. The Jones calculus fully describes the polarimetric antenna characteristics and is defined by the two orthogonal

field strength components $g_\theta$ and $g_\varphi$ [Jones41]. As will be discussed in Section 3.2.1, the antenna data used in this thesis originates from analytical expressions and HFSS simulations [HFSS13]. In the framework of this thesis, the implementation has been extended by the functionality of arbitrarily rotating the polarimetric antenna patterns by the means of Euler angle rotation matrices [Milli99].

The separation of the three different processing steps has the major benefit of significantly increasing the computational efficiency for some applications. In case of the calibration of the material parameters in Section 3.3 the time consuming geometric calculations have to be done only once for instance. In case of the comparison between different antennas as done in Section 5.1, additionally the calculation of $\mathbf{P}^{(i)}$ is only necessary once.

It is noteworthy that the electromagnetic calculations have been extended by the functionality of taking into account frequency dispersive materials and antennas by Dr.-Ing. Sebastian Priebe. Therefore, the electromagnetic calculations mentioned above are done in frequency domain followed by inverse Fourier transform in order to get the channel impulse response in time domain. For a detailed description of this functionality, the reader is referred to [Prieb13b].

## 3.2 Wideband 60 GHz Channel Measurements

This section reports on experimental investigations of the 60 GHz radio channel. The core subject here is the spatio-temporal channel characterization In the first part of the section, the measurement setup and the measurement antennas are introduced. The measurement results for a living room and a conference room are presented afterwards, divided into a subsection about path loss and shadowing and a subsection about the angular dispersive channel characteristics. Concludingly, measurements in a kiosk download environment are presented.

### 3.2.1 Measurement Setup and Antennas

All channel measurements are conducted in frequency domain followed by the calculation of channel impulse responses via inverse Fourier transform. For the measurements a system was available, which consists of an Agilent E8361A vector network analyzer and external transmitting and receiving test heads with WR-10 waveguide flanges covering the frequency band from 67 to 110 GHz. Due to the lower limit of 67 GHz, the presented measurements had to be conducted between 67 and 72 GHz, which is slightly higher than the actual spectrum allocated for WLAN/WPAN (57 - 66 GHz). Nevertheless, no significant differences of the propagation characteristics are expected in this frequency range. With this setup, extremely wideband measurements with a temporal delay resolution of 200 ps become possible. As a trade-off between measurement time, maximum resolvable excess delay and dynamic range, the channel is sampled at 401 frequency points with

an intermediate frequency (IF) filter bandwidth of 300 kHz. This allows for a maximum excess delay of 80 ns and a dynamic range of about 95 dB.

For the radio channel measurements, three different types of antennas are used, namely conical horn antennas, open-ended waveguides and half-wave dipole antennas. With these antennas it is for instance possible to implement a configuration, where a sector antenna (open-ended waveguide) serves as transmitter and a highly directive antenna (horn) as receiver (configuration 1). This setup emulates a typical antenna system for mm-wave WLAN applications. In addition, two other antenna configurations (horn-horn (2), open-open (3)) give the possibility to investigate the influence of the antenna on the propagation channel parameters. Furthermore, the spatial filtering properties of the horn antennas are utilized to determine the angular dispersive channel characteristics.

In order to interpret the measurement results correctly, a thorough knowledge of the antenna characteristics is essential. Hence, three-dimensional antenna patterns are required for the antennas, which will be incorporated into RT with the aim to compare RT and measurements directly. For these reasons, a detailed characterization of the mentioned antennas is given in the following. This is done in terms of antenna pattern measurements, closed-form expressions and full-wave electromagnetic field simulations. In the following, the conical horn antennas as well as the open-ended waveguides are described in detail. A description of the dipole is omitted as the characteristics are commonly known very well.

#### 3.2.1.1 Conical Horn Antenna

The horn antenna used for the measurements is a plain conical horn fed by a WR-10 rectangular waveguide. The antenna is linearly polarized. Its circular aperture has a radius $A$ of 8 mm and an angle of aperture $\alpha$ of 15°. Different approaches exist to calculate the three-dimensional radiated fields of aperture antennas. The aperture field method uses integration over the whole aperture to obtain the $\theta$- and $\varphi$-dependent far field pattern at distance $R$ [Ludwi66]:

$$g\left(R,\theta,\varphi\right)=\frac{jke^{jkR}}{4\pi R}\left(1+\cos\theta\right)A^2\int_0^1\int_0^{2\pi}f\left(\rho,\varphi'\right)e^{jkA\rho\sin\theta\cos(\varphi-\varphi')}\rho d\rho d\varphi', \tag{3-3}$$

where $k$ is the free-space propagation constant, $\rho$ and $\varphi'$ define a local polar coordinate system at the aperture and $f\left(\rho,\varphi'\right)$ is the aperture field. In case of circular structures, the dominant mode is the $\mathrm{TE}_{11}$ mode. Hence this mode is chosen as $f\left(\rho,\varphi'\right)$. The integration of Eq. (3-3) is tedious and will be omitted at this point. An analytic solution for $g\left(R,\theta,\varphi\right)$ as sums of members of special integral functions is given in [Green06]. The electrical field strength can be calculated by

$$E_\theta\left(R,\theta,\varphi\right)=\frac{jkAV_{11}e^{jkR}}{2R}\sin\varphi C_{11}k_{11}\left(W_0-W_2\right) \tag{3-4a}$$

$$E_\varphi\left(R,\theta,\varphi\right)=\frac{jkAV_{11}e^{jkR}}{2R}\cos\varphi\cos\theta C_{11}k_{11}\left(W_0+W_2\right) \tag{3-4b}$$

where $k_{11}$ equals 1.841, $V_{11}$ is the voltage at the aperture and $C_{11}$ and the integral functions $W_n$ can be easily calculated numerically according to

$$W_n\left(kA,\theta\right) = \int_0^1 wJ_n\left(k_{11}Aw\right)J_n\left(kAw\sin\theta\right)e^{-\frac{jkAw^2tan\alpha}{2}}dw \tag{3-5}$$

and

$$C_{11} = J_1\left(k\right)\sqrt{\frac{\pi}{2}(k_{11}^2-1)}. \tag{3-6}$$

Here, $J_n$ is the Bessel function of the first kind. This set of equations can be used to generate full 3D frequency dependent antenna patterns. As an example, Fig. 3.2a shows the normalized antenna patterns in the E and H plane for a frequency of 67 GHz. In addition to the theoretical curve, which is based on Eq. (3-4), measurement results are shown. The measurements have been conducted with the same Agilent E8361A vector network analyzer as for the channel measurements described in the beginning of this section. This setup has been adapted for the antenna measurements similar to the setup described in [Herre09, Herre10a].

As expected, the main lobe is symmetrical in both planes. The half power beamwidth amounts to 20° in the E plane and 17° in the H plane. The pattern is shown for angles between -20° and 20°. For angles exceeding this range the gain is always more than 15 dB lower than the maximum gain. In Fig. 3.2b the frequency dependent maximum gain is shown. The theoretical values range from 20.4 dBi at 67 GHz to 22.5 dBi at 110 GHz with an almost linear increase. The agreement between the analytically derived gain and the measured gain is very good for both the angle and frequency dependent curves. Hence, the simulated patterns can be employed in the RT simulations. In addition, the

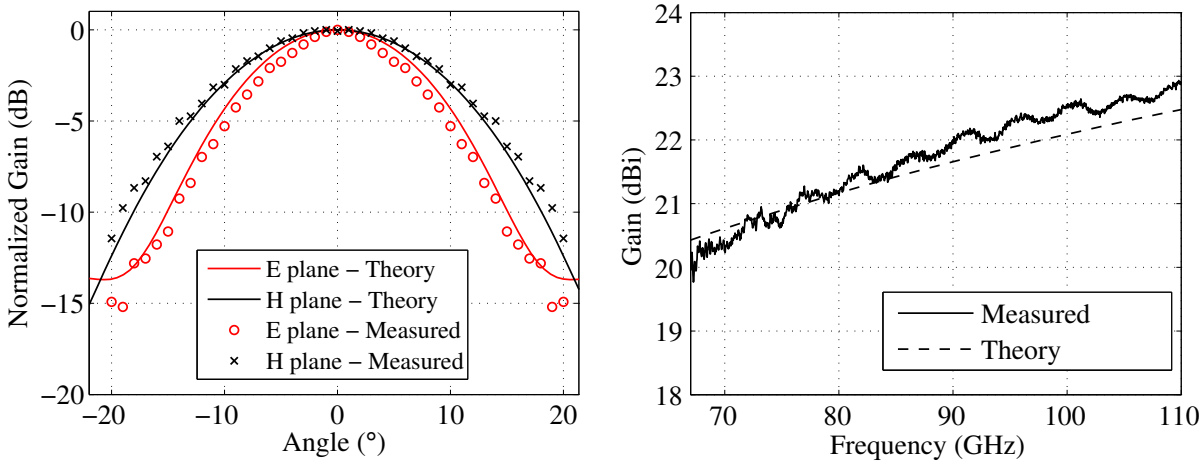


**(a)** Angular dependency.

**(b)** Frequency dependency.

**Figure 3.2:** Measured and theoretical angular and frequency dependent antenna gain of the conical horn antenna.

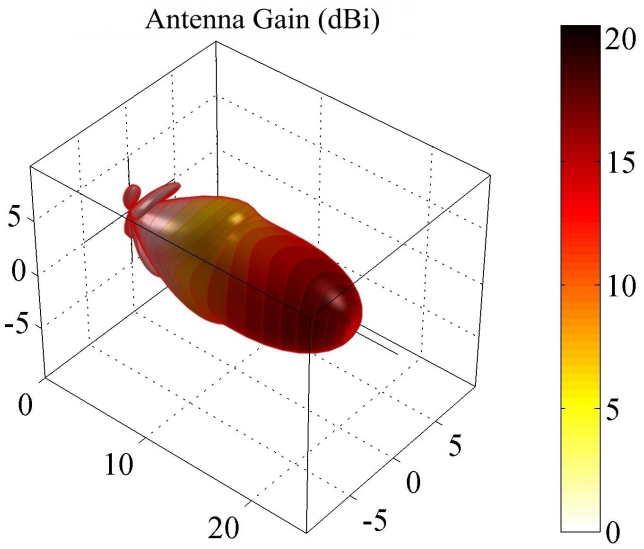


**Figure 3.3:** 3D pattern of the horn antenna.

cross polarization ratio has been determined experimentally to be higher than 30 dB. Fig. 3.3 shows the simulated three-dimensional pattern, which is used in the ray tracing simulations.

#### 3.2.1.2 Open-Ended Waveguides

Compared to the horn antenna, a different modeling approach has been followed. The radiation characteristics have been determined using the commercial 3D full wave solver HFSS, which is based on the finite element method [HFSS13]. Two types of open-ended waveguides have been used in this thesis, namely WR-15 waveguides *without* waveguide flanges and WR-10 waveguides *with* flanges.

The WR-15 antennas have been utilized in the radio channel measurements which will be presented in Section 4.1.2. These measurements have been performed by the HHI in Berlin. Since experimental data was not available for the WR-15 antennas, a comparison between modeling and measurements was not possible. Nevertheless, as the open-ended waveguide *without* flange possesses a very simple and well understood geometric structure, the HFSS simulation results can be assumed trustworthy. The simulated antenna patterns for the WR-15 waveguide are shown in Fig. 3.4 for a frequency of 60 GHz. At this frequency the total antenna gain amounts to 6.3 dBi and the HPBW to 96° in the vertical and 70° in the horizontal plane. In order to include the antenna patterns in the ray tracing simulations, the radiation characteristics have been exported from HFSS in terms of 3D data of the complex valued polarimetric Jones vectors.

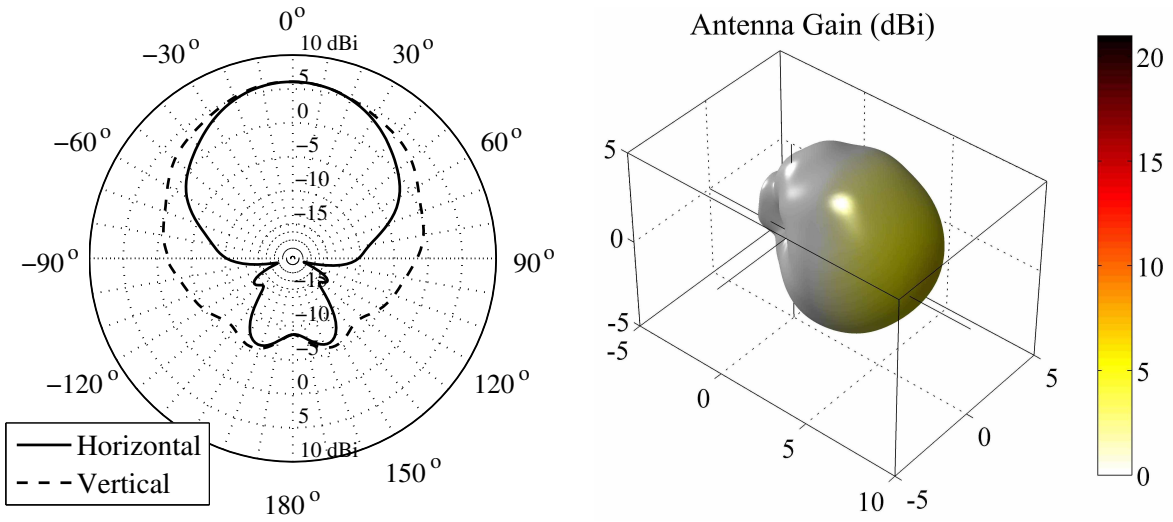


**(a)** 2D Pattern. **(b)** 3D Pattern.

**Figure 3.4:** Simulated angular dependent antenna gain of an open-ended WR-15 waveguide at 60 GHz.

A model for the WR-10 waveguide is not needed in the framework of this thesis, because the comparison between measurement and ray tracing is done for the horn antenna only (c.f. Section 3.2). The horn antennas has been chosen for this comparison due to its narrow HPBW, which is necessary to spatially filter single MPCs. Nevertheless, the knowledge of the basic radiation characteristics of the open-ended waveguide is helpful for the interpretation of the measurement results. The WR-10 waveguide possesses a typical connection flange (see Fig. 3.5a), which is not the case for the WR-15 waveguide. As will be shown in the following, this leads to different radiation characteristics. Like for the horn antenna, the radiation characteristics have been determined experimentally. Fig. 3.5b shows the maximum gain over frequency. The frequency range between 67 and 110 GHz have been chosen in order to demonstrate the differences between the case *with* and *without* flange. In the frequency range of interest (67 - 72 GHz), the measured gain increases from 5 to 7.5 dBi. It is noteworthy that the gain characteristic does not increase monotonically over the whole frequency range, as expected for an aperture antenna. In order to analyze this behavior further, an HFSS simulation with a detailed geometric model of the metallic waveguide flange, as depicted in Fig. 3.5a, has been conducted. In addition to the measurement results, Fig. 3.5b also includes the simulated gain with and without the waveguide flange. The gain without the waveguide flange has the expected increasing behavior similar to the horn antenna. By taking the flange into account, the measured characteristics cannot be reproduced exactly, as the radiation characteristics are very sensitive to even slight unavoidable geometric modeling errors. However, at this point the aim is only to demonstrate the general impact of the waveguide flange.

The simulated curves *with* and *without* flange highly deviate due to the fact that the whole waveguide flange serves as a radiator and the structure can no longer be seen as

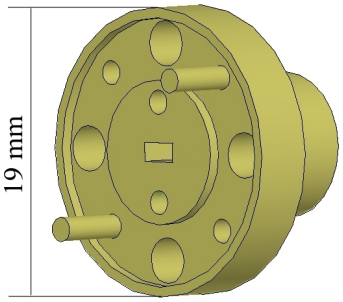


**(a)** HFSS model.

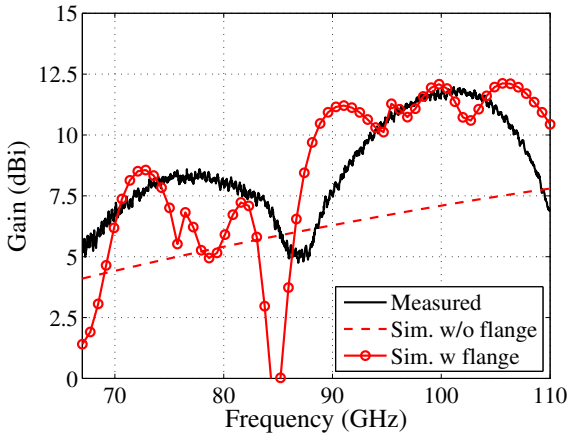


**(b)** Frequency dependency.

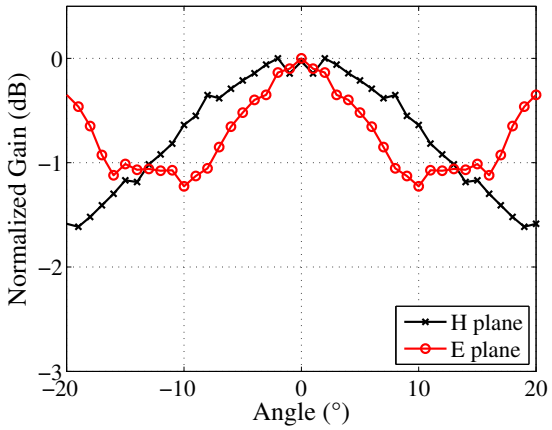


**(c)** Angular dependency (measured at 67 GHz).

**Figure 3.5:** HFSS model and antenna gain of the WR-10 waveguide.

a pure aperture antenna. The radiation pattern is in general supposed to be similar to the case without the waveguide flanges as shown in Fig. 3.4a. Only small fluctuations around the main beam direction are expected, which can be explained by the interference of the primary waveguide radiation source and secondary radiation sources on the flange [Owen46, Butso59]. These ripples can be clearly recognized in the angular dependent measurements with the flange shown in Fig. 3.5c. Please note that the measurement setup was intentionally built for highly directive antennas and hence is limited to an angular range of $-20°$ to $20°$. Nevertheless, the measurement results are in line with literature [Yoshi94, Baudr88, O'Kee10].

For the WR-10 waveguide antenna, the cross polarization ratio has been determined and amounts to more than 20 dB. As the increase of gain with frequency is low and approximately linear for the measured frequency band between 67 and 72 GHz, and because the ripples in the antenna pattern are quite low, the discussed issues will not influence the channel measurement results significantly.

### 3.2.2 Path Loss and Shadowing

In this section, path loss and shadowing are analyzed in the conference room and living room scenarios. Before the results are discussed, a brief overview about the choice of the TX and RX locations in the different scenarios is given. Fig. 3.6a shows a schematic of the conference room in top view with all relevant geometrical parameters. During the measurements, the transmitter position was kept fixed with the antenna pointing to the middle of the room. Complex transfer functions were measured at eleven positions distributed in the whole room with distances from 1.70 m to 5.70 m. The main beam of the receiving antenna was always orientated in the direction of the receiver.

A schematic of the living room scenario is depicted in Fig. 3.6b. The room is equipped with typical furniture like an armchair, a couch or bookshelves. The methodology for the derivation of the distance dependent path loss is basically identical to the one used in the conference room. The transmitter is placed at a fixed position close to the TV. Altogether thirteen receiver positions were distributed in the whole room, whereas LOS conditions were ensured. The distances between TX and RX varies between 1 and 5 m. In both rooms TX and RX are positioned at the same height of 1.10 m.

The determined parameters are based on an average of every measured transfer function. Afterwards, a least square fitting has been applied to approximate the distance dependent path loss in dB by

$$PL = 10 \cdot n \cdot \log_{10}(d) + PL_0 \tag{3-7}$$

for the different antenna configurations. Here, $PL_0$ is the reference path loss at 1 m and $n$ is the path loss exponent.

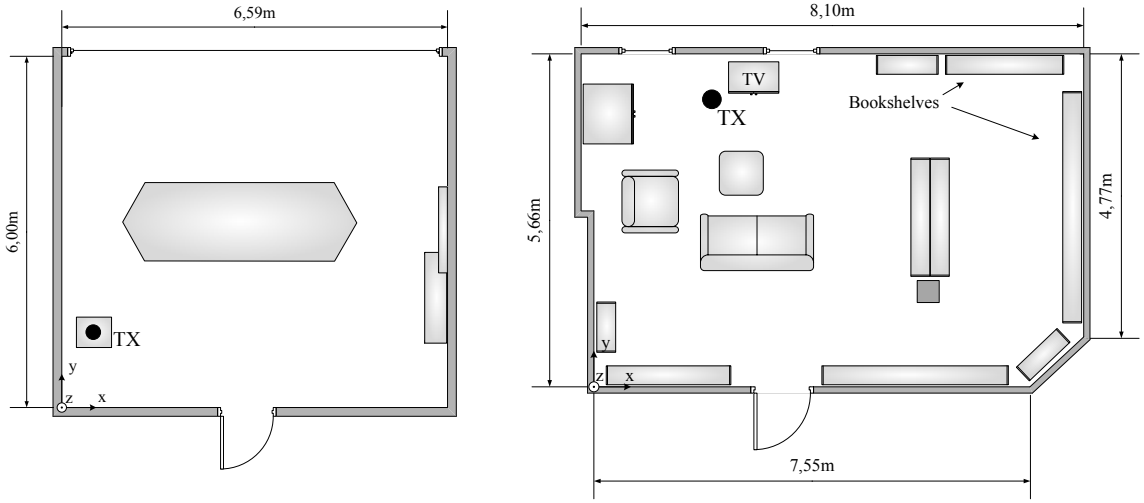


**(a)** Conference room. **(b)** Living room.

**Figure 3.6:** Schematics of conference and living room.

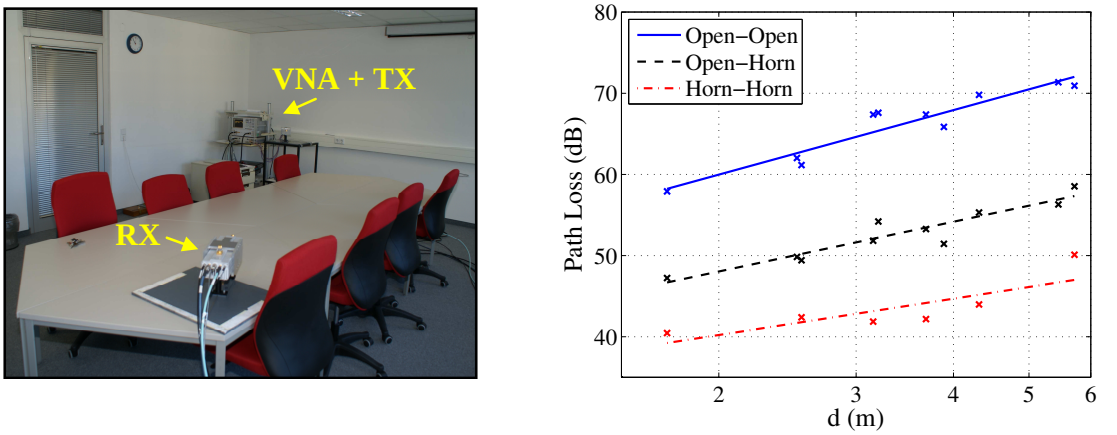


**(a)** Example positions of the TX and RX antennas.

**(b)** Distance dependent average path loss in the conference room. The markers correspond to the measured values.

**Figure 3.7:** Photograph of measurement setup and distant dependent path loss.

Table 3.1 summarizes the path loss and shadowing parameters. In order to account for large-scale fading, the standard deviation $\sigma_{PL}$ of the difference between the fitted curve and the measurement values is given also. For the conference room, the values of the path loss exponent lie between 1.5 and 1.7 and the reference values $PL_0$ lie between 34 and 60 dB depending on the antenna configuration. The factor $\sigma_{PL}$ amounts to 1.5 and 1.6 dB. In case of the living room measurements, regarding the path loss exponent free space conditions, i.e. $n = 2$ could be observed, whereas $PL_0$ is slightly lower than for the conference room.

Fig. 3.7b shows the path loss as a function of distance between transmitter and receiver in the conference room. Here, the measurement results are shown together with curves fitted according to Eq. (3-7) for the three different antenna configurations. The influence of the antenna gain can clearly be recognized. For the configuration with the open-ended waveguide TX and the high gain horn antenna at the RX, the path loss amounts to values between 47 dB and 57 dB. For the other configurations, the values are higher by 15 dB and lower by 10 dB, respectively.

**Table 3.1:** Path loss and shadowing parameters.

| | Conf. Room | | | Liv. Room | |
|---|---|---|---|---|---|
| **Ant. Config.:** | **1** | **2** | **3** | **1** | **3** |
| $n$ | 1.6 | 1.7 | 1.5 | 2.0 | 2.0 |
| $PL_0$ | 34 | 46 | 60 | 30 | 58 |
| $\sigma_{PL}$ | 1.6 | 1.5 | 1.5 | 1.4 | 1.5 |

**Table 3.2:** Maximum achievable range dependent on MCS and scenario.

| | Conference Room | | | Living Room | |
|---|---|---|---|---|---|
| **Ant. Config.:** | **1** | **2** | **3** | **1** | **3** |
| MCS 1 (0.39 Gbps) | 421.4 m | 58.1 m | 11.6 m | 222.0 m | 18.8 m |
| MCS 24 (6.80 Gbps) | 20.5 m | 3.3 m | 0.4 m | 7.8 m | 0.7 m |

**Table 3.3:** Time Dispersion Parameters

| | Conference Room | | | Living Room | |
|---|---|---|---|---|---|
| **Ant. Config.:** | **1** | **2** | **3** | **1** | **3** |
| **RDS (ns)** | 0 - 1.4 | 0 - 1.2 | 0 - 12 | 0 - 1.5 | 0.5 - 2 |
| **MED (ns)** | 0 - 50 | 0.5 - 45 | 5 - 55 | 0 - 60 | 10 - 60 |

With these path loss models it is possible to get a first impression of the range of 60 GHz communication systems in the considered scenarios. The *IEEE802.11ad* standard provides a list of the required receiver sensitivities for different Modulation and Coding Schemes (MCS). These sensitivities range from -68 dBm for MCS 1 (BPSK, SC, 0.39 Gbps) to -47 dBm for MCS 24 (64-QAM, OFDM, 6.80 Gbps) [IEEE812]. Based on these values and the path loss models, the maximum achievable data rates can be calculated. These are summarized in Table 3.2 under the assumption of a realistic PA output power of 10 dBm [Yong11]. Furthermore, a large-scale fading margin of 2 dB is taken into account, which corresponds to an outage of about 90 % under the assumption of a log-normal fading with standard deviation $\sigma_{PL}$. Regarding MCS 1, communication is feasible in both scenarios and with all antenna configurations as the maximum ranges exceeds the typical dimensions of conference and living rooms. This does not hold for MCS 24. The results show that the use of directive antennas will be mandatory or such high data rates will be limited to short-range applications. It is noteworthy that these results are valid for LOS conditions and perfectly aligned antennas, only. If these conditions are not satisfied, the maximum range can decrease significantly. More advanced feasibility studies, which take into account NLOS and human blockage will be presented in Chapter 5.

### 3.2.3 Time Dispersion Parameters

Time dispersion parameters including RMS delay spread (RDS) and maximum excess delay (MED) are used to quantify the time dispersive properties of the measured wideband multipath channel. Both of them are determined from the power delay profiles based on the measurements taken in the different scenarios. The RDS is defined as the normalized second order central moment of the PDP [Molis05]. The MED is defined as the time delay between the first arriving signal and the multipath component within a pre-determined threshold of the strongest arriving multipath signal.

Table 3.3 summarizes the resulting parameters. A noise threshold of 30 dB is applied. The RDS values are extremely small, especially for the antenna configurations with one or two horn antennas, because here the direct path is extremely dominant and is more than 30 dB stronger than the other paths. The maximum excess delay is similar for all antenna configurations and amounts to values up to 60 ns. However, it is smaller in most of the cases. The two different scenarios show no significant differences. A more detaild investigation of the time dispersive channel properties can be found in the author's separate publication [Jacob09a].

### 3.2.4 Spatio-Temporal Channel Measurements

In this section, the spatio-temporal characteristics of the 60 GHz multipath channel are investigated experimentally. Besides the delay domain, the azimuth domain is also considered in the measurements. For this purpose, both the TX and the RX antennas are rotated around a vertical axis (see Fig. 3.8). In case of the TX, the rotation is done with a motorized rotation stage. The RX is rotated manually. The VNA and the motorized rotation stage are controlled by one PC using the General Purpose Interface Bus (GPIB) and the USB interface. The control software has been programmed in Python.

The result for one TX/RX placement is a set of angular-dependent channel impulse responses $h(\tau, \varphi_{AoA}, \varphi_{AoD})$. In order to spatially resolve individual MPCs, the directive horn antennas are used. The antennas enhance the dynamic range of the VNA further by 41 dB. Hence, MPCs with a path loss of up to about 136 dB can be detected. According to the antenna HPBW a spatial measurement resolution of 5° is chosen. With the parameters above, a measurements cycle for the entire azimuth domain ($360° \times 360°$) takes about two hours. As the horn antennas are linearly polarized and the test heads can be orientated horizontally and vertically, all entries of the polarization matrix $\mathbf{P}$ can be determined.

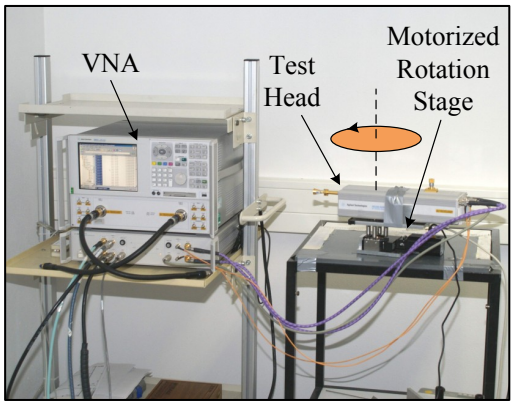


**Figure 3.8:** Measurement setup for the spatially resolved measurements.

### 3.2.4.1 Conference Room

**Path Loss of the MPCs** In the conference room, angular dependent measurements have been taken at two positions ($RX_1$, $RX_2$). The TX position is the same as for the path loss measurements. Fig. 3.9b shows the quasi-omnidirectional power delay profile $|h(\tau)|^2$ for position $RX_1$. This PDP has been composed from all angular dependent measurements $h(\tau, \varphi_{AoA}, \varphi_{AoD})$ by performing a maximum search across all angles for each value of $\tau$. Corresponding to the link distance of 5.58 m, the LOS component arrives at 18.6 ns. The ToAs of the reflected MPCs have been determined by ray tracing simulations and are marked according to the numbering in Fig. 3.9a. Please note that at this point the RT simulations are consulted in order to interprete the measurement results better. For instance, RT provides the opportunity to assign the measured MPCs unambiguously to one geometrical path. A detailed quantitative comparison between RT and the measurement results for position $RX_2$ will be presented in combination with the calibration in Section 3.3.

Altogether five first order MPCs exist (see Fig. 3.9a), resulting from reflections at the four walls and the ceiling. The first order reflection from the floor is blocked by the table. Moreover, six second order reflections and seven third order reflections could be detected. The total loss of the individual MPCs consists of two parts, namely the free space loss according to the travelling distance and the reflection losses. With the knowledge of the ToA, both can be calculated. Fig. 3.10 shows these losses for all MPCs. The total loss of the reflected MPCs is at least 6.8 dB higher than the LOS loss, which is far less than

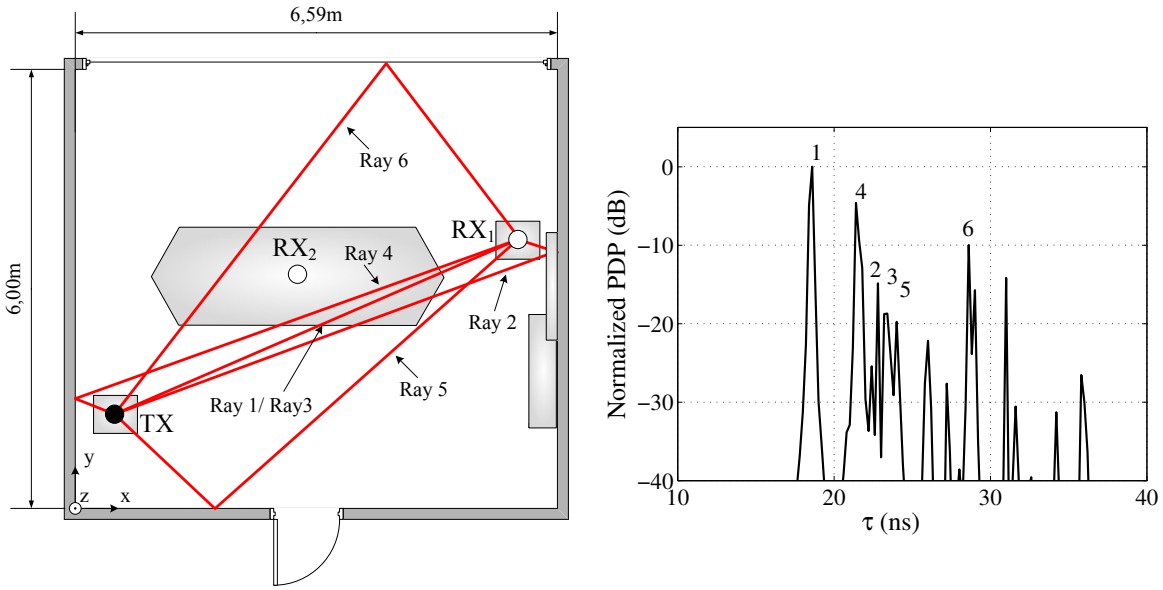


**(a)** Conference room. **(b)** Cut-out of the measured PDP.

**Figure 3.9:** Conference room scenario and measured power delay profile for position $RX_1$.

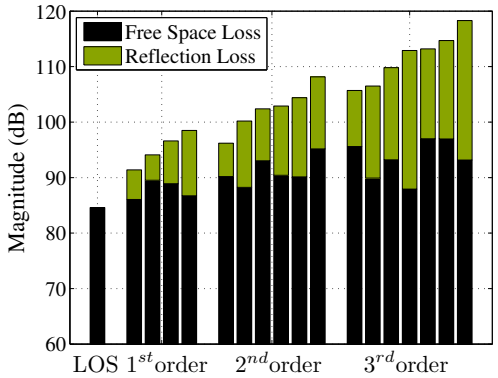


**Figure 3.10:** Path loss per MPC.

| | Free Space | Refl. | Total |
|---|---|---|---|
| **LOS** | 84.6 dB | - | 84.6 dB |
| **1** | 87.8 dB | 7.4 dB | 95.2 dB |
| **2** | 91.2 dB | 11.2 dB | 102.4 dB |
| **3** | 93.4 dB | 18.2 dB | 111.6 dB |

**Table 3.4:** Average path loss of the MPCs.

the influence of human blockage. The loss generally increases with the reflection order. This has two reasons. First, each reflection process attenuates the electromagnetic wave more. Second, the higher the reflection order is, the longer is the distance covered by the wave. The average loss values, summarized in Table 3.4, confirm both facts. In case of the single reflections, the reflection losses amount to values between 4.6 and 11.8 dB. The average reflection losses are higher by 3.8 dB in case of the $2^{nd}$ order reflections and by 10.8 dB in case of $3^{rd}$ order reflections. The total loss increases by about 7 dB to 11 dB per reflection, whereas here the contribution of the free space loss increase is only 2 dB to 3 dB.

**Angular Dispersion** The angular dispersion behavior of the 60 GHz radio channel is of special interest, as antenna systems will be employed, which adapt to varying conditions in the spatial domain. The goal of this section is twofold. On the one hand the angular dispersive channel characteristics are qualitatively and quantitatively evaluated. On the other hand, a comparison with RT should demonstrate the validity of the RT simulations.

In Fig. 3.11a a complete angular power profile (APP) is shown, measured at position $RX_1$. The APP represents the power of the strongest MPC for each $\varphi_{AoA}/\varphi_{AoD}$ combination. In the figure, the expected $\varphi_{AoA}/\varphi_{AoD}$ combinations computed by RT are marked additionally. As it can be seen, the single MPCs span a certain angular range. This can be traced back to the antenna patterns, which broaden the MPCs in the spatial domain. Fig. 3.11b shows the same APP derived from RT simulations. The rotation of the antennas is considered in the RT in the same way as in the measurements. A qualitative comparison reveals that the agreement between simulation and measurement is very good. With a few exceptions, the relevant paths are visible in both APPs. As mentioned above, a detailed analysis of this comparison will be presented in Section 3.3.

The representation of the APP in Fig. 3.11 is not very intuitive and lacks the information about the ToAs. In order to interprete the results better, other representations are more appropriate. For a better interpretation of the results, Fig.3.12 shows a panorama view seen from the RX and the TX. The yellow marks correspond to LOS and first order MPCs,

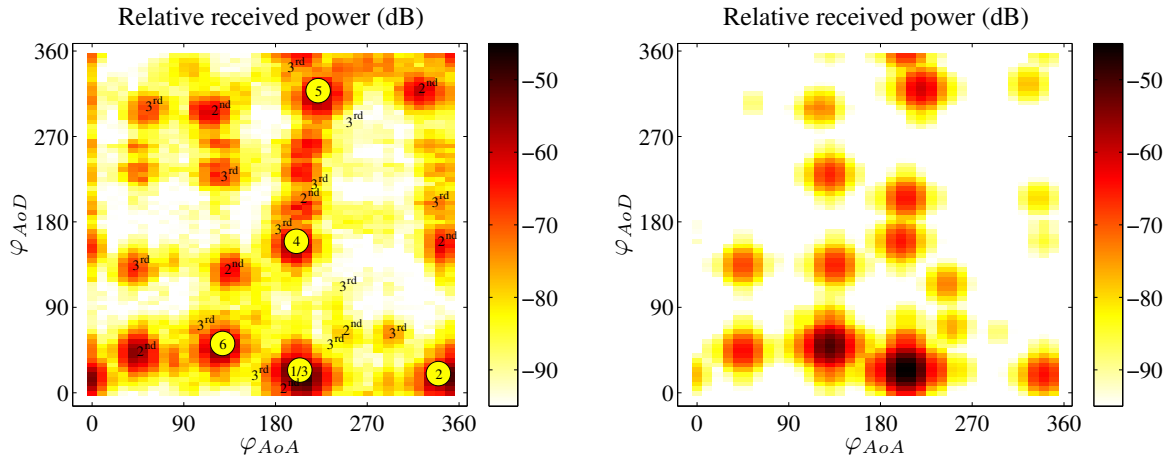


**(a)** Measurement. **(b)** Ray tracing.

**Figure 3.11:** Comparison of simulated and measured angular power profiles. The yellow circles mark the direction of the LOS and first order ray tracing MPCs.

the red circles correspond to higher order reflections. The radii of the circles qualitatively indicate the received power. Fig. 3.13 depicts angular dependent power delay profiles extracted from the measurement results. Again, measurement and RT are contrasted. In theory, a single MPC is expected to cause one sharp peak in the spatio-temporal domain. The phenomenon of the broadening in the angular domain has been already discussed above. The pulse broadening in the delay domain is caused by IFFT leakage [Prieb13b]. As a countermeasure to this effect, a Kaiser windowing ($\alpha = 2.5$) has been applied in frequency domain before the inverse Fourier transformation.

Regarding the AoA profile, it is notable that the MPCs are arranged in clusters with similar AoAs and ToAs. For instance, the MPCs 1, 3, 4 and 5 arrive at an angle of about 200°. Additionally, three further clusters exist at about 50°, 140° and 350°. All four clusters can be also observed in the RT result. It is also noteworthy that there are angular ranges, where no significant MPCs exist (e.g. around 25°, 180° or 290°). In the AoD domain, the MPCs are distributed more equally over the whole angular range. This is particularly evident when the panorama views are compared. In the AoD domain in principle a similar behavior can be observed, which will be discussed below.

The comparison between RT simulations and measurements reveals that the spatio-temporal characteristics agree in principle. Nevertheless, a few differences can be noticed. These should be analyzed more detailed in the following. Therefore the temporal as well as angular features of exemplary MPCs are shown in Fig. 3.14 in terms of PDPs and AoD profiles. Regarding the characteristics in the delay domain, the results experience a pulse broadening, which is partly caused by IFFT leakage effects, as it occurs in the RT simula-

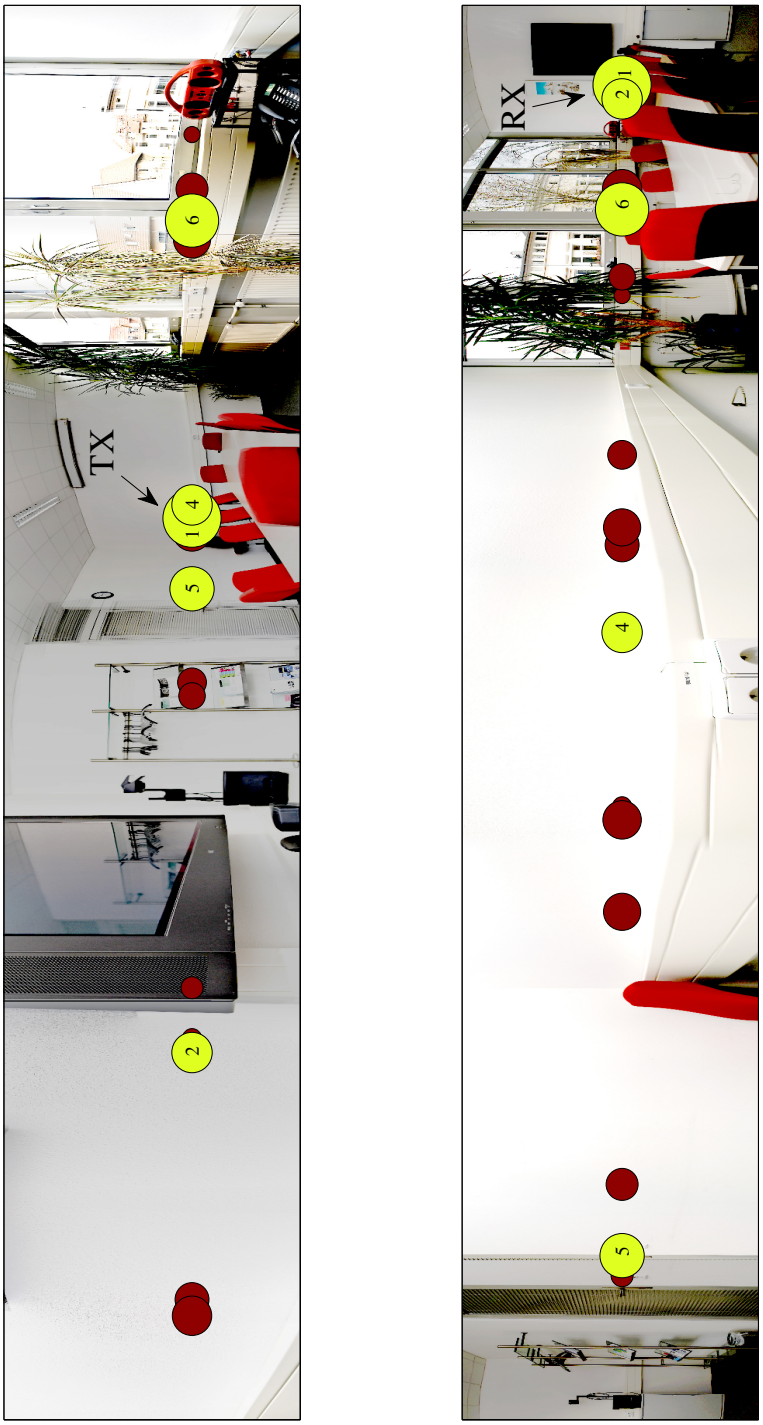


**(a)** RX perspective. **(b)** TX perspective.

**Figure 3.12:** Direction of arrival/departure of RT MPCs superimposed on panorama views seen from TX and RX positions, respectively.

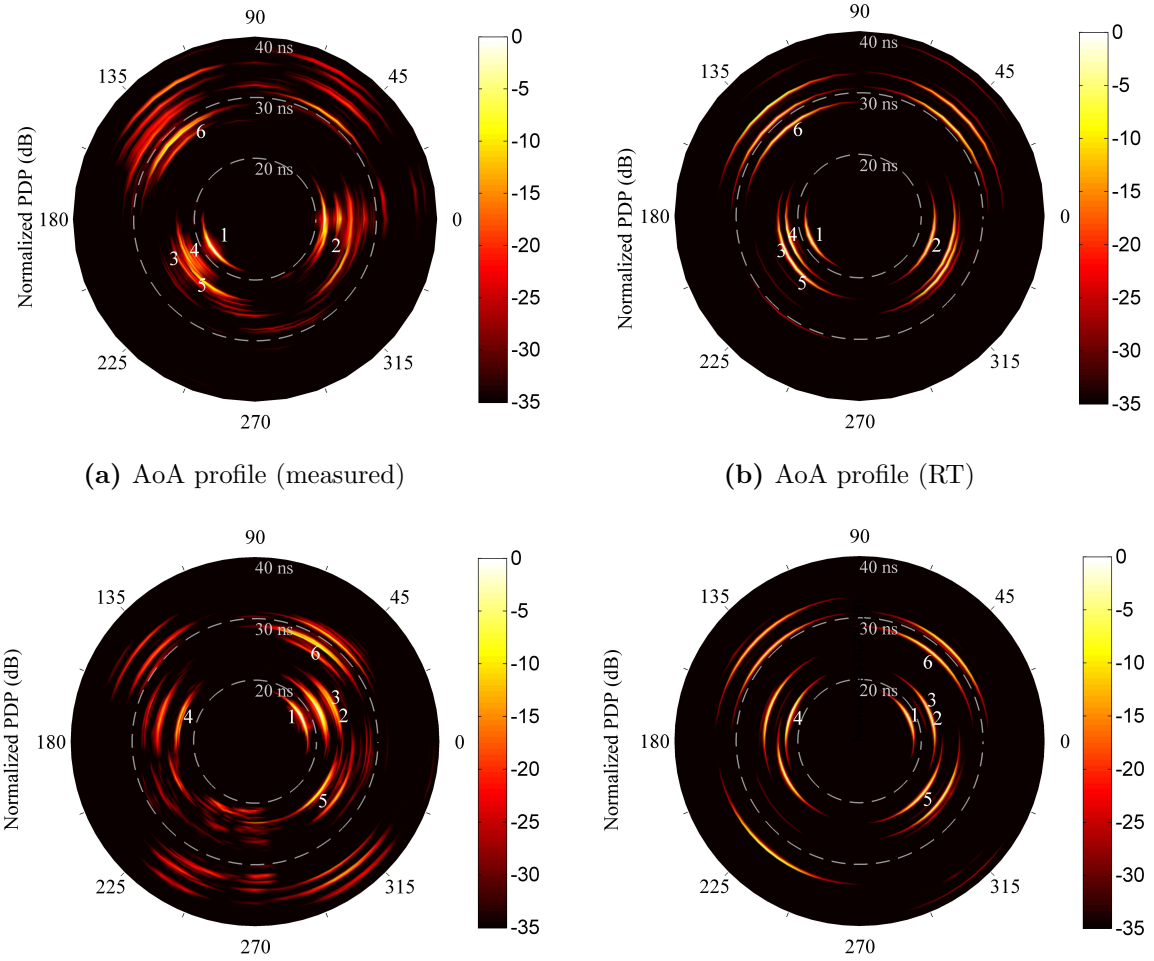


**(a)** AoA profile (measured)

**(b)** AoA profile (RT)

**(c)** AoD profile (measured)

**(d)** AoD profile (RT)

**Figure 3.13:** Comparison of simulated and measured angular-dependent power delay profiles. The LOS and first order ray tracing MPCs are marked.

tions also. However, contrary to the measurements, single peaks can be recognized in the RT results. Especially, in case of MPC 5 and 6, this is not the case for the measurements. For instance in Fig. 3.14c, the major peak is followed by a peak with approximately half the amplitude. This could be caused by propagation mechanisms, which are not taken into account by RT. These could be for example scattering at rough surfaces or multiple reflections within objects. In order to further evaluate this effect, the angular domain is analyzed in the following. For this purpose, Fig. 3.14 additionally includes AoD power profiles of three selected MPCs. These are basically vertical cut-outs from the APPs in Fig. 3.11. In case of the LOS path, the measured and simulated angular profile agree perfectly. The same holds true for MPC 6, although another peak could be observed in time domain. In both cases the characteristics are dominated by the spatial filtering of one MPC by the antenna pattern. Regarding MPC 5, the measured AoD profile is slightly distorted compared to the simulated one. The level at lower angles are for instance higher

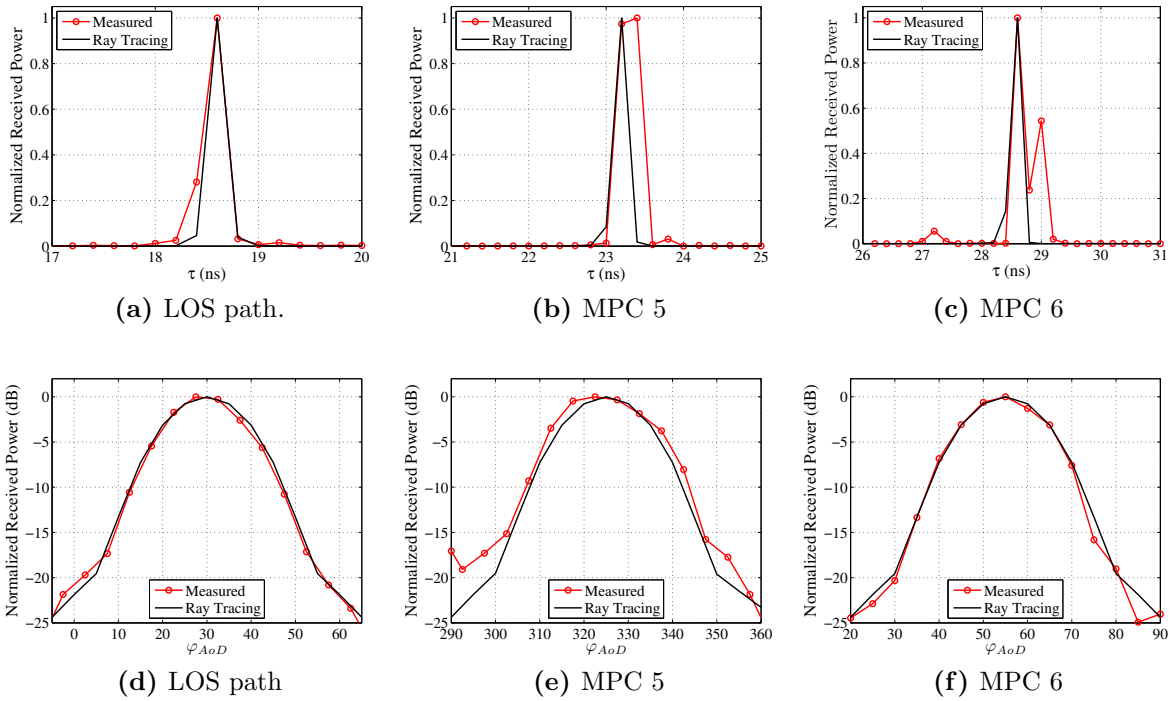


**(a)** LOS path. **(b)** MPC 5 **(c)** MPC 6

**(d)** LOS path **(e)** MPC 5 **(f)** MPC 6

**Figure 3.14:** Exemplary MPCs separated in the temporal domain and the AoD domain.

in the measurements, which can be explained by the absence of the MPC with the center at approximately $[\varphi_{AoA}, \varphi_{AoD}] = [260^\circ, 200^\circ]$ in the RT results. However, together with the findings in the temporal domain, it seems likely that the RT lacks another MPC adjacent to MPC 5. Concluding this qualitative comparison, a good agreement between RT and measurements could be observed, except some minor deviations.

**Condensed Angular Dispersion Parameters** An appropriate measure for the angular dispersion is the RMS angular spread. Similar to the delay spread of the PDP, it is defined as the standard deviation of the APP. However, the conventional calculation of the standard deviation would lead to an overestimation of the angular dispersion due to the ambiguity of the angle definition on a circle ($\varphi \mathrel{\widehat{=}} \varphi \pm n \cdot 2\pi$). Therefore [Fleur00] proposes to use a complex representation of AoA and AoD. Then the RMS angular spread is defined as:

$$\sigma_\varphi = \sqrt{\int_0^{2\pi} |e^{j\varphi} - \mu_\varphi| P(\varphi) d\varphi}, \text{with} \tag{3-8a}$$

$$\mu_\varphi = \int_0^{2\pi} e^{j\varphi} P(\varphi) d\varphi. \tag{3-8b}$$

Please note that the azimuth profile $P(\varphi)$ has to be normalized so that its integral is unity. Under this assumption, it can be shown that $0 \leq \sigma_\varphi \leq 1$ [Fleur00], whereby $\sigma_\varphi = 1$

indicates a high dispersion with approximately equally strong MPCs evenly spaced across the entire angular range. $\sigma_\varphi = 0$ describes a channel with one relevant MPC only. This makes it a very convenient parameter, which is intuitively understandable.

Table 3.5 summarizes the angular spread for all measured APPs. In order to characterize the sole channel, the local maxima of the APPs are considered only. Otherwise the broadening in the angular domain, which is caused by the measurement antennas would distort the results. The results are given for the original APPs as well as for APPs, where the LOS component has been removed. This is done in order to analyze the angular distribution of the reflected MPCs only. In addition to the conference room, Table 3.5 also includes data for the living room, in which polarization dependent measurements have been performed. The results of these will be discussed in detail in the next section. The measured angular spreads lie between 0.25 and 0.97. The APPs, which corresponds to the maximum and minimum spread, are depicted in Fig. 3.15. In Fig. 3.15a, the LOS component clearly dominates the APP. In this specific case, all other MPCs are at least 18 dB below the LOS component and have only marginal influence on the angular spread (cf. Fig. 3.18a). This is different for the APP corresponding to the maximum spread (see Fig. 3.15b). Here, several strong path exist, distributed across the whole 360°. Remarkably, the minimum as well as maximum angular spread has been observed under LOS conditions. However, as expected the angular spread is typically higher in NLOS situations.

The discussion of the APPs in Fig. 3.13 and Fig. 3.12 has lead to the observation that the MPCs are more equally distributed in the AoD domain than in the AoA domain. However, against intuitive expectation, the angular spread value is higher for the AoA measurements. The reason for this is that MPCs are in fact distributed over the whole angular range, but the main fraction of the power is transferred via the MPCs 1, 2, 5 and 6, which are closely spaced in the AoD domain. In the AoD domain 62% of the power is distributed over a 90° wide range, whereas it takes at least 160° in the AoA domain to receive this amount of power.

The findings stated above are based on a few measurements only. Nevertheless, it may be assumed that depending on the placement of TX and RX, significantly different situations

**Table 3.5:** Measured RMS angular spread.

| | | **Conference Room** | | **Living Room** | |
|---|---|---|---|---|---|
| | **Position[1]:** | **$RX_1$(V)** | **$RX_2$(V)** | **$RX_1$(V)** | **$RX_1$(H)** |
| **w/ LOS** | **AoA** | 0.97 | 0.62 | 0.48 | 0.28 |
| | **AoD** | 0.67 | 0.43 | 0.30 | 0.25 |
| **w/o LOS** | **AoA** | 0.97 | 0.73 | 0.76 | 0.95 |
| | **AoD** | 0.80 | 0.67 | 0.67 | 0.90 |

[1] vertical polarization (V), horizontal polarization (H)

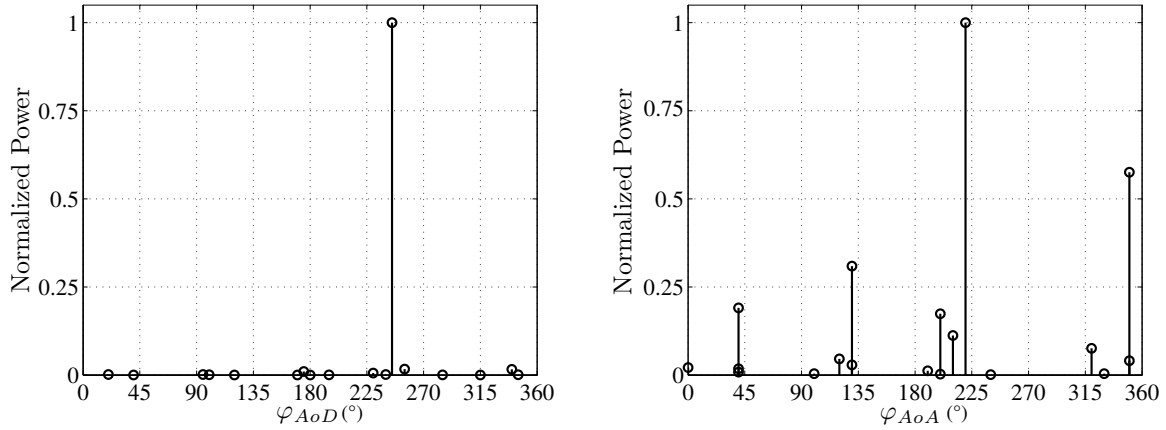


**(a)** AoD profile, $RX_1$(H) living room, $\sigma_\varphi = 0.28$.

**(b)** AoA profile, $RX_1$(V) conference room, $\sigma_\varphi = 0.97$.

**Figure 3.15:** Exemplary APPs which are used as base for the angular spread calculations.

may occur in one and the same environment. The results from extensive ray tracing simulations in the conference room scenario confirm this statement [Kürne09].

#### 3.2.4.2 Living Room

In this section, the angular-dependent measurements in the living room are presented. The focus here lies on the polarimetric features of the radio channel. The influence of the type of antenna polarization on the 60 GHz radio propagation channel as well as on the whole system performance has already been investigated by different research groups [Manab95, Manab96, Zhao03, Yong06, Yang08b, Yıldı08, Malts10c]. To summarize the results, linear polarization would be the best choice if multipath components should be utilized. In LOS situations, circular polarization would be better than linear polarization because unwanted multipath components are suppressed. But, in case of directive antennas multipath components are suppressed anyway. In addition, when the communication link has to rely on NLOS paths, this would be a drawback and the path loss for circular polarization would be higher than for linear polarization. Comparing vertical and horizontal polarization there is no significant difference, although vertical polarization leads to a slightly lower path loss because reflections from the side walls are more effective than for horizontal polarization.

The polarization impact is analyzed based on measurements in the living room. In order to determine angular power spectra, the same measurement procedure as in the conference room has been carried out. With the measurement setup, horizontally as well as vertically polarized radiation is possible by simply rotating the antennas by 90°. Due to

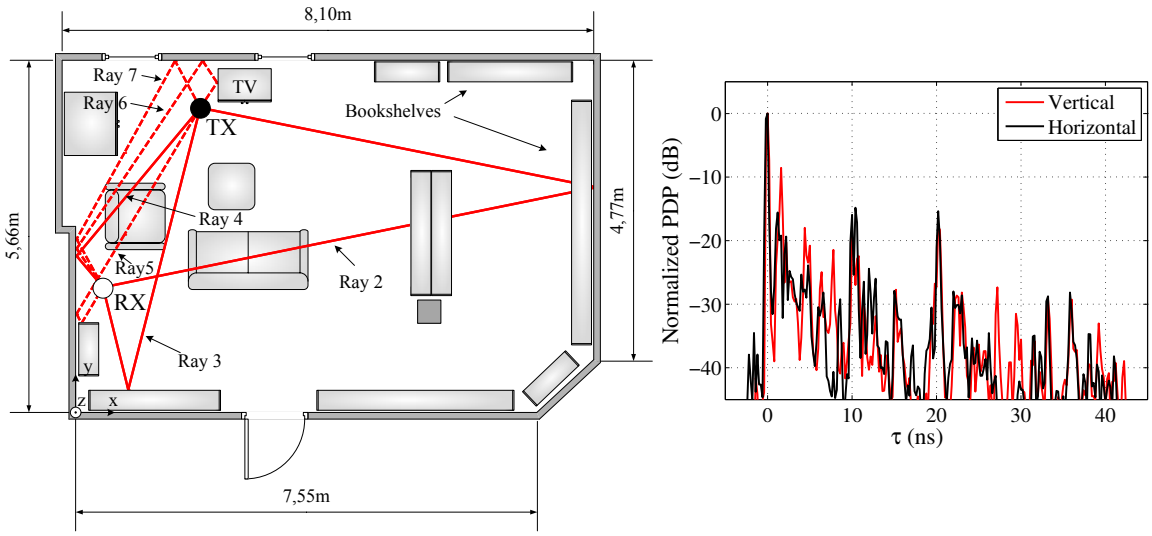


**(a)** Living room scenario. **(b)** PDPs for different polarizations.

**Figure 3.16:** Living room geometry and power delay profiles.

the good spatial filtering capability of the horn antennas, the polarization properties of single transmission paths can be determined

The living room scenario has been described already above. In this investigation, the transmitter has been placed near the television setup (see Fig. 3.16a). The receiver position is located near the left wall of the room at a distance of 2.94 m to the transmitter. In addition to the room geometry, chosen rays obtained from RT are shown in the figure also. These rays serve for explanations in the text below.

Fig. 3.16b shows power delay profiles extracted from the angular dependent measurements. Here, the maximum value of the angular dependent channel impulse response $h(\tau, \varphi_{RX}, \varphi_{Tx})$ has been determined for each delay value $\tau$. In this way, an antenna with omnidirectional characteristic in the horizontal plane can be emulated. Under the assumption of a threshold of -30 dB, the maximum excess delay amounts to 36 ns for both polarizations. Regarding a comparison between both polarizations, the qualitative behaviour is in accordance with the literature mentioned above. As the reflection processes are in general more effective for vertically polarized waves, the multipath components are stronger in most of the cases. A slightly higher delay spread (5 ns compared to 4 ns) substantiates this conclusion. A more detailed analysis based on the angular dependent measurement data will be given in the following.

In Figs. 3.17a and 3.17b, the angular power spectra are shown for both polarizations. The general characteristics are similar to those already described in conjunction with the conference room measurements. The yellow circles as well as the green squares mark the positions of the rays in Fig. 3.16a. The circles indicate the LOS and first order reflections, the squares indicate second and third order reflections. These seven rays have been chosen

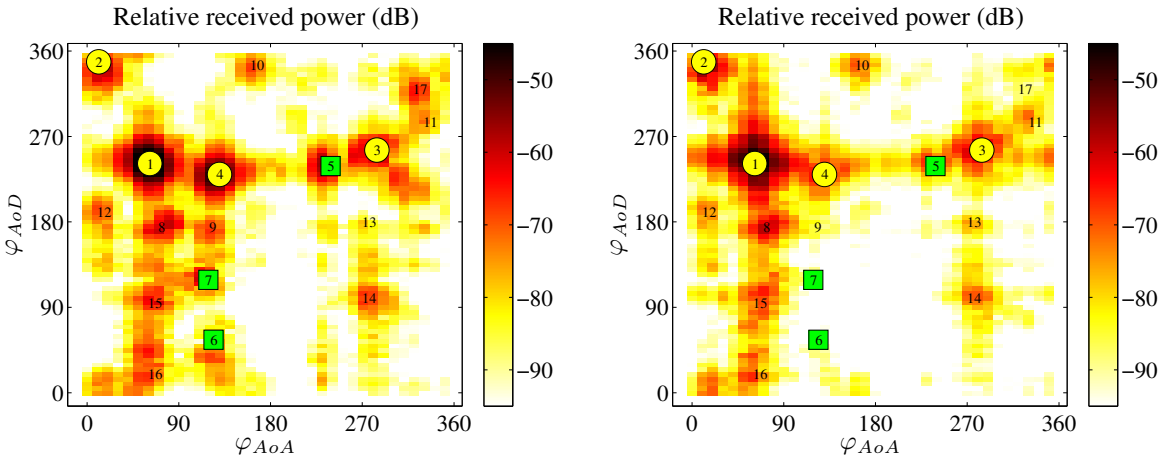


**(a)** Vertical polarization. **(b)** Horizontal polarization.

**Figure 3.17:** Angular power profiles measured in the living room. The markers correspond to the rays in Fig. 3.16a. The circles represent the first order reflections, the squares represent second order reflections. In addition, MPCs which are not depicted in Fig. 3.16a are marked by numbers.

exemplarily, as otherwise in Fig. 3.16a a clear illustration would not be possible. The other MPCs are also consecutively numbered. Their power is analyzed below. From the angular power spectra it can be observed again that the MPCs are in general stronger in case of the vertical polarization.

Fig. 3.18a depicts the normalized received powers, where the dependency on $\varphi_{AoD}$ has been eliminated by taking the maximum power value for each angle $\varphi_{AoA}$. It is noteworthy that even the LOS power differs by about 3 dB. Explanations for this are inaccuracies of the mechanical measurement setup and the measurement uncertainties of the VNA [Schra11]. In case of MPC 2 and 3, the power for the horizontal polarization is slightly higher, whereas in case of MPC 4 and 5 the power is significantly higher for vertical polarization. The difference between the received power $\Delta P$ for the vertical polarization and the horizontal polarization for all MPCs is illustrated in Fig 3.18b. In 6 out of 16 MPCs the power level is higher for the horizontal polarization, but the difference amounts to only 2.5 dB at maximum. This behavior is physically implausible as no polarization change is expected, and can only be explained by the errors already mentioned above. In general, the received power for vertical polarization is considerably higher. The MPCs 4 to 7 for instance exhibit values of $\Delta P$ between 11 and 29 dB. They all have in common that they are reflected at the left wall under similar angles. The relatively high deviations occur, because the reflection angles all lie in the angular range around the Brewster angle.

In addition to the measurements with co-polarized antennas, the depolarization of the MPCs is measured. It has been found that the cross polarization discrimination of all MPCs is higher than at least 17 dB, which makes depolarization effects negligible. These high values are plausible as the TX and the RX lie in one horizontal plane. However,

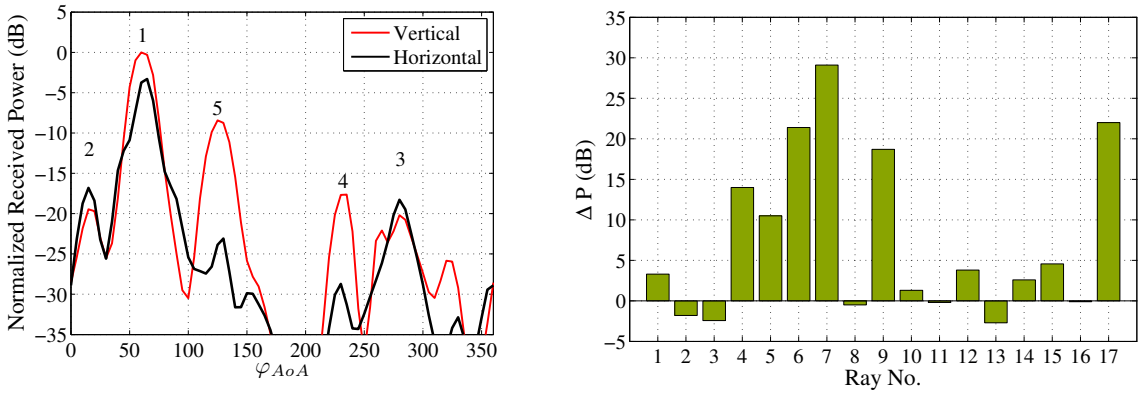


**(a)** AoA power profile. **(b)** Power difference.

**Figure 3.18:** Results of the angular dependent measurements in the living room regarding the polarization impact. The numbering correspond to the labels in Fig. 3.17.

geometrical depolarization can be expected if the TX and the RX do not lie in a horizontal plane.

In the following, radio channel measurements will be presented for a kiosk download scenarios. In contrast to the applications, which are adressed so far, here the transmission distances are significantly shorter.

### 3.2.5 Kiosk Download Scenario

Wireless data kiosks are among the most important use cases for multi-gigabit systems. Such kiosks enable up- and downloads of e.g. video or music files. As the operational distance is limited to ranges of about 1 m it is likely that low-complexity devices with conventional antennas will be employed [Bayka11]. Only few propagation studies for this scenario exist. In [Sato07] for example, a channel impulse response model based on measurements is proposed. Another study reveals that the kiosk scenario provides nearly AWGN conditions, but, the coherence bandwidth may be in the order of the envisaged transmission bandwidth [Garci11].

Two exemplary issues will be discussed at this point. The first study analyzes a possible misalignment between the antennas of the mobile device and the kiosk. The second analysis treats multipath components caused by multiple reflections between transmitter and receiver. Both studies are based on an extensive measurement campaign using the equipment already described above. The setup is shown in Fig. 3.19a. It consits of a transmitter with a fixed position at the origin of a local coordinate system. The receiver is located on a translation stage that can be moved in x- and y-direction with a spatial resolution of 1 mm. In the measurements its x-position has been varied between -10 and 10 cm and the y-position between 5 and 30 cm. As for the conference room scenario,

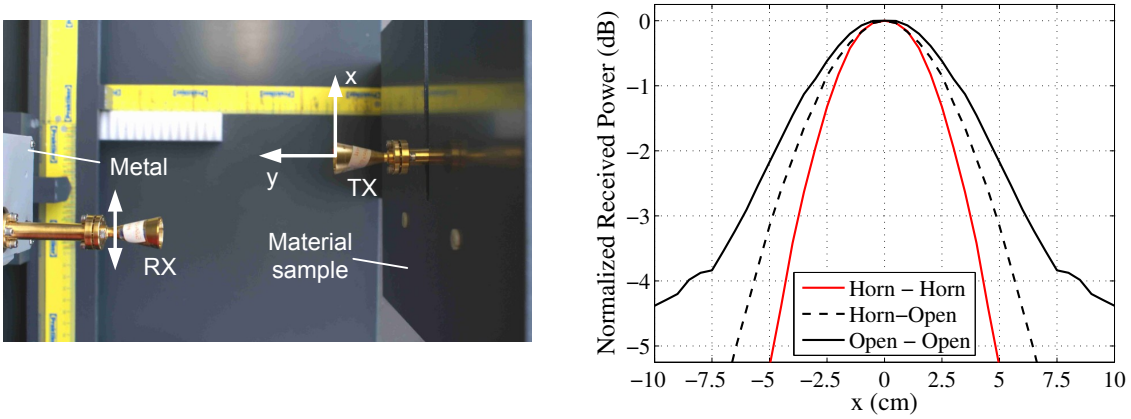


**(a)** Measurement setup. **(b)** Antenna misalignment measurements.

**Figure 3.19:** Measurement setup and results of the kiosk download scenario analysis.

three antenna configurations have been considered (horn-horn, open-horn, open-open). Behind the transmitter, different housing materials are emulated by metal, PVC and ply wood samples (see Fig. 3.19a). On the receiver side, the electromagnetic waves may be reflected at the metal housing of the mm-wave test head.

For the misalignment analysis, the receiver has been moved in x-direction for a fixed longitudinal displacement of y = 30 cm. The measured received power is depicted in Fig. 3.19b. It is normalized to the maximum value for each antenna seperately. In any case, the measurement follow the antenna characteristics of the considered antennas. Hence, multipath propagation seems to have no significant influence on the received power, which agrees with the results in [Garci11]. A likely antenna configuration in such a short range scenario will employ omnidirectional or at least only slightly directive antennas. Hence, the open-open configuration seems to be the most representative configuration for this scenario. In this case, the maximum loss due to misalignment amounts to 4.4 dB at an x-shift of 10 cm. It is noteworthy that the actual maximum received power of course strongly depends on the maximum antenna gain. The horn-horn configuration for instance provides a power level 26 dB higher than the open-open configuration.

Fig. 3.20a shows two measured power delay profiles for TX and RX separated by 30 cm. Here the case of a perfect antenna alignment is depicted for a metal as well as a PVC housing material. The strong LOS component is identical for both materials. In case of metal, five distinct MPCs can be recognized. The first MPC is caused by a wave being reflected at the metal housing of the receiver and at the material sample at the transmitter before reaching the receiver. The next MPCs each travel between TX and RX once more. The delay between consecutive MPCs amounts to 2.8 ns, corresponding to a path length difference of 84 cm, which is approximately twice the distance between material sample and metal housing. Four of the MPCs are less than 35 dB below the LOS component and

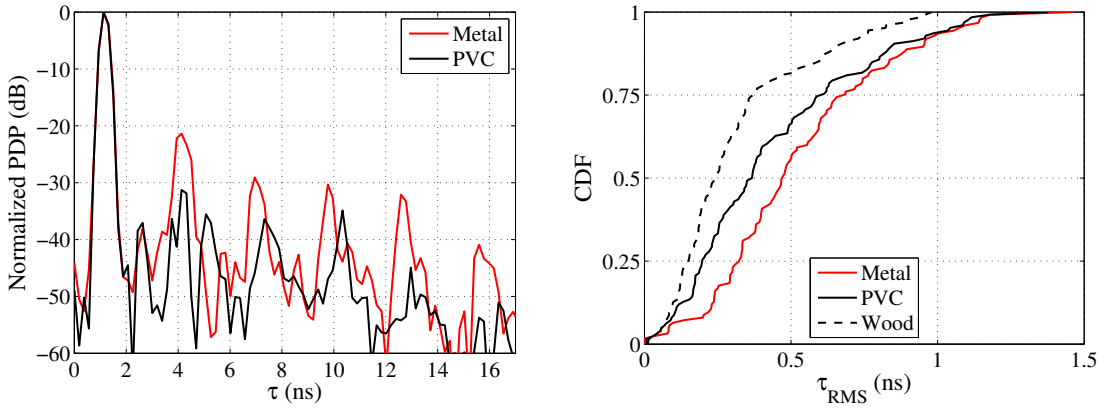


**(a)** Power selay profiles. **(b)** RMS delay spread statistics.

**Figure 3.20:** Results of the kiosk download scenario analysis.

may have an impact on data transmission. In case of the PVC sample, these components are 5 to 12 dB lower.

In order to quantitatively compare the influence of the different materials, statistics of the RMS delay spread have been derived. These are based on all translational displacement configurations with the open-open configuration. Fig. 3.20b illustrates these statistics in terms of cumulative distribution functions for the different materials. Here, MPCs up to 30 dB below the LOS component have been taken into account. As expected, the delay spread is the highest for the metal sample because the MPCs are stronger than for the other materials. The average delay spread amounts to 0.52 ns in the case of metal. According to the reflectivity of the materials, the values for the PVC measurements are on average lower by 0.09 ns and lower by 0.21 ns for the wood respectively. All delay spread values lie between almost 0 and 1.5 ns. These low values even for highly reflective housings are in line with [Garci11] and support the findings that nearly AWGN conditions can be assumed in the kiosk scenario. However, in face of the high envisaged data rates, even a slight temporal dispersion may lead to a performance degradation.

## 3.3 Ray Tracing Calibration

The discussion of the measurement results above has shown that the qualitative agreement between measurement results and RT results is very good. However, the RT accuracy in terms of the MPCs' amplitudes has not been considered so far. As mentioned above, reflections up to the third order have been considered in the RT. The amplitudes of the reflected MPCs are calculated based on the free space loss according to the MPCs' path length and the reflection losses calculated by the well known Fresnel equations [Schac12, Prieb13b]. The component which is critical for the accuracy is the reflection loss, as it relies on an accurate knowledge of the dielectrical parameters of the objects in the simulated

environment. This knowledge rarely exists, especially in complex environments with a multitude of different materials. Besides the possibilty to determine the parameters by time-consuming direct measurements of building materials [Seide94], a site-specific calibration of the RT by only a few radio channel measurements can be used [Jemai09]. In this thesis the calibration methodology presented in [Jemai09] is seized and extended. The concept of RT calibration is to minimize the deviation between measured and simulated CIRs by adjusting the dielectric material parameters. Usually this is done in the delay domain only, i.e. for $h(\tau)$. In [Jemai05] it is proposed to include the AoA domain. However, [Jemai05] does not reach beyond the presentation of early results. In this thesis, this approach is further extended by taking into account the directional information at RX as well as TX, which improves the assignment between measured and simulated MPCs significantly. Thus, the base for the calibration are angular-dependent CIRs $h\left(\tau, \varphi_{RX}, \varphi_{Tx}\right)$. In the following, the calibration algorithm is explained and the calibration performance will be presented exemplarily for the conference room scenario.

### 3.3.1 The Calibration Algorithm

As the basis for the calibration algorithm, a simulated annealing approach is employed. Simulated annealing is derived from the simulation of thermal annealing of critically heated solids, which is done by slowly decreasing their temperature [Rao09]. This algorithm is an iterative optimization technique, being able to provide a global optimal solution for arbitrary degrees of nonlinearity.

A cost function describes the deviations between the intended solution and the current solution for a certain parameter set. Here, the cost function is defined as the difference between the powers $P_{j,meas}$ and $P_{j,RT}$ of the measured and the simulated MPCs of a ray tracing solution $\mathbf{X}$:

$$f\left(\mathbf{X}\right) = \sqrt{\frac{\sum_{j=1}^{N_{Rays}} \left(P_{j,meas} - P_{j,RT}\right)^2}{N_{Rays}}}, \tag{3-9}$$

which must be minimized in order to determine the best-fitting, i.e. the most realistic, material parameters from the measurements for the ray tracing simulations. The core of the algorithm is the so called *Metropolis criterion*, which defines the probability $p_{acc}$ for the acceptance of a new cost function $f\left(\mathbf{X}\right)$ at a given temperature $T$ [Rao09]:

$$p_{acc} = \begin{cases} e^{-\Delta f/T} & \text{for } \Delta f > 0 \\ 1 & \text{for } \Delta f < 0, \end{cases} \tag{3-10}$$

with $\Delta f = f_{i+1} - f_i$. Thus, with a probality of $e^{-\Delta f/T}$ a new ray tracing solution $\mathbf{X_{i+1}}$ is allowed to be worse compared to $X_i$. The lower the temperature gets the lower this probability gets. In contrast to simple hillclimbing methods, it is made sure that the algorithm is able to leave a local minimum of the cost function in order to reach the global minimum.

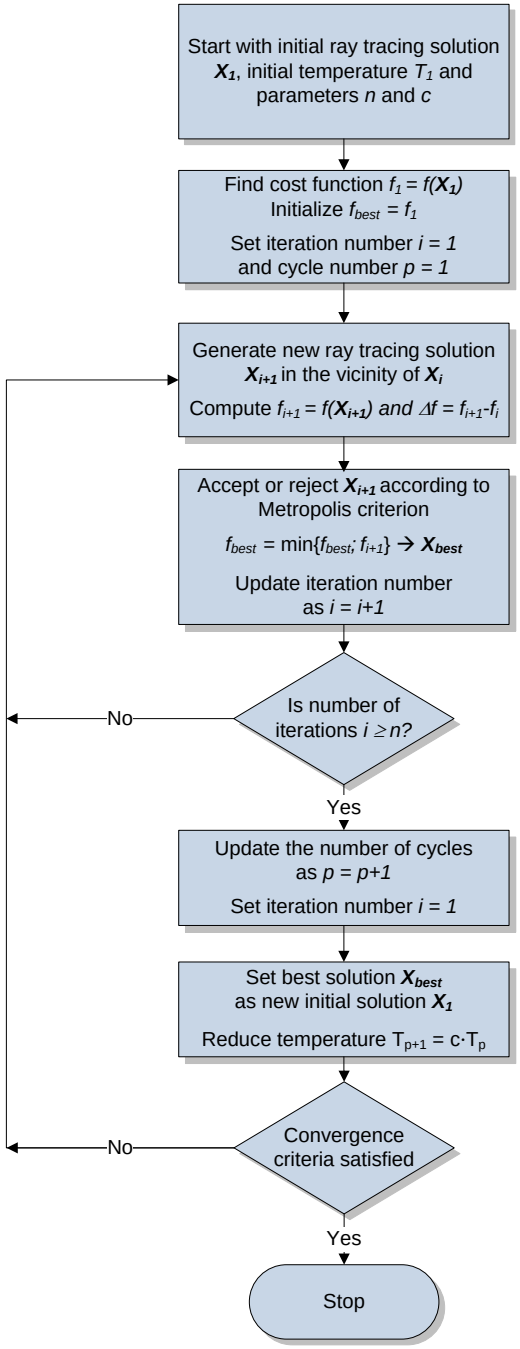


**Figure 3.21:** Flow chart of the simulated annealing algorithm. Adapted from [Rao09].

Subsequently, the algorithm is applied to our specific problem. For a general more detailed description, a variety of literature exists, e.g. [Ingbe93]. Fig. 3.21 depicts a flow chart of the algorithm. The algorithm begins with an initial ray tracing solution $\mathbf{X_1}$ and the initial temperature $T_1$. The initial set of material parameters can be based upon typical known values, e.g. from literature. In addition the control parameters $c$ and $n$ have to be

set. They define the temperature reduction and the number of iterations per temperature step.

In a first step, the initial cost function $f_1{=}f\left(\mathbf{X_1}\right)$ is determined according to Eq. (3-9). The parameters $i$ and $p$ specify the indices for temperature reduction and number of iterations per temperature step. In the next step a new ray tracing solution $\mathbf{X_{i+1}}$ is generated. This is done by performing the electromagnetic computations for a new random set of material parameters and the subsequent calculation of the ray power $P_{j,RT}$. The new solution is then accepted with the probability defined by Eq. (3-10). This process is repeated $n$ times, before the temperature is reduced by the factor $c$. If the convergence criteria are satisfied, the algorithm stops, otherwise the algorithm starts again with the generation of a new ray tracing solution. The convergence criteria is given by a maximum number of $p$ cycles.

In this specific application the choice of the algorithm's input parameters $[c, n, T_1, p]$ and the way of generating random material parameters is crucial and has high impact of the convergence of the solution. An analysis revealed shown that $[c, n, T_1, p] = [0.95, 10, 4, 100]$ provide good results in terms of convergence to a global optimum. For the generation of new random material parameters the current values are taken and a random number is added to its value. The random numbers follow a uniform distribution between -0.5 and 0.5 in order to get new parameters in the vicinity of the current ones. The random numbers are additionally weighted by the factor $T/T_1$ in order to limit the variation of possible new parameters with increasing temperature. The randomization is done separately for the real and imaginary part of the relative permittivity. As boundary conditions for valid permittivities $\varepsilon_r > 1$ and $0 < \tan\delta < 0.5$ have been chosen[1], as a smaller $\varepsilon_r$ is implausible and the loss tangent typically lies in the mentioned range [BROAD02]. Please note that the parameters are assumed to be constant over the whole frequency range of interest.

### 3.3.2 Mapping of Channel Measurement and Ray Tracing Data in the Spatio-Temporal Domain

Conventional RT calibration algorithms like in [Jemai09] only contrast measured and simulated PDPs without assigning corresponding rays to each other in the cost function. Without further information, this would require a perfect match of measured and simulated ToAs, which is virtually impossible. Hence the cost function definition is erroneous from the outset. In this thesis, a mapping of measured and simulated rays improves the calibration accuracy. The mapping is done in the spatio-temporal domain by using the angular dependent measurements introduced in Section 3.2.4. The advantage of this methodology is that MPCs, which overlap in the temporal domain, are very likely to be resolved unambiguously in the joint AoA/AoD/ToA domain. In order to set up the

[1] $\tan\delta = \frac{\varepsilon_r''}{\varepsilon_r'}$

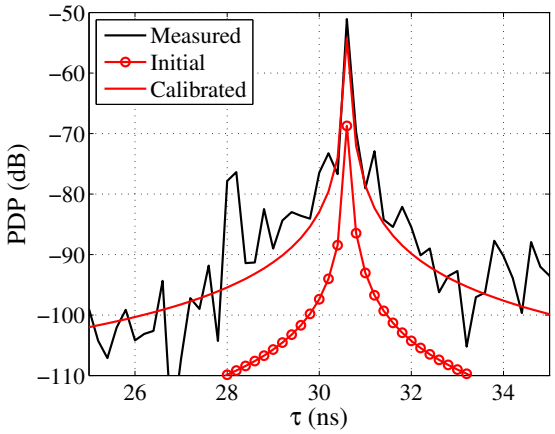


**Figure 3.22:** Comparison between measured and simulated PDP for MPC 2 at position $RX_1$ before and after the calibration.

cost function, the powers $P_{j,meas}$ and $P_{j,RT}$ of each MPC have to be extracted from the measured and simulated APPs $h(\tau, \varphi_{RX}, \varphi_{Tx})$.

The extraction proceeds as follows. In a first step, the initial expected power from RT is determined for each MPC. Then, the MPCs, which definitely lie under the noise threshold of the measurement system are suspended. Now, the expected values $\tau_{exp}, \varphi_{RX,exp}$ and $\varphi_{Tx,exp}$ are known for each potentially measured MPC from RT. Based upon this, the measured and simulated PDPs $h(\tau, \varphi_{RX}, \varphi_{Tx})\,|_{\varphi_{RX,exp},\varphi_{Tx,exp}}$ are contrasted at the corresponding angle coordinates. Fig. 3.22 shows this comparison exemplarily for MPC 2 for position $RX_1$ in the conference room. In the measurements a clear peak is observed, whereas other MPCs are suppressed by more than 20 dB due to the high directivity of the horn antennas. Although the measured characteristic is not as smooth as the RT results, the figure demonstrates very well that it is possible to unambiguously match the MPCs. Fig. 3.22 also demonstrates the impact of the calibration as it shows the RT result before and after the calibration. Due to the change of the material parameters, the deviations between RT and measurement are reduced significantly. For the actual comparison in the cost function, the peak values of the MPCs are chosen. Due to the limited measurement resolution as well as inaccuracies of the geometrical scenario, the expected values may deviate from the measured ones. For this reason, an additional peak search in the vicinity of the expected position of the MPC is performed in the spatio-temporal domain. The MPCs from the RT, which are used for the calibration in the conference room, are marked in Fig. 3.11 on page 54. All of them could be assigned to measured MPCs. Vice versa, all measured MPCs except three could be assigned to simulated ones.

### 3.3.3 Calibration Performance and Validation

As stated above, the performance of the developed calibration methodology will be demonstrated in the conference room scenario. The measurements at position $RX_1$ are used for the actual calibration. Subsequently $RX_2$ is used to validate the calibration results. The cost function is based on the marked MPCs in Fig. 3.11a. In detail, these are four first order, six second order and seven third order reflections. For the RT simulations, six different materials have been assigned to each surface element, namely carpet, wood, plastic, plaster, glass and metal. The initial dielectric parameters are taken from literature [BROAD02]. They are summarized in Table 3.6. Please note that in case of metal, a PEC has been assumed initially. However, the boundary conditions mentioned above proved sufficient to represent the high reflectivity of metal. Hence, during the calibration the same boundary as for the other materials have been used.

The randomization of the material parameters has been done following two different approaches. On the one hand, the material database has been calibrated, i.e. for each calibration cycle six new complex permittivities have been assigned to the six materials. On the other hand, the surface elements of the scenario have been calibrated individually, i.e. one permittivity value has been assigned to each surface element. Both approaches have advantages as well as disadvantages. The assumption of one dielectric parameter per material may be unrealistic in case of the database calibration. In addition, different types of a material class may have significantly different dielectric properties. On the other hand, the element-wise approach can only calibrate elements where reflections actually take place. Other elements remain unaffected by the calibration procedure. In this regard, it is definitely more advantageous to calibrate the material database. Furthermore, the number of cycles, which are needed for convergence of the surface calibration depends on the number of scenario elements. This may be a significant drawback for large scenarios.

The calibration performance is demonstrated in Fig. 3.23. Here, the cost function progress is shown over the number of cycles $m$. Please note that the cost function is averaged over 100 calibration runs, which explains the very smooth characteristics. The results are shown for three different cost function definitions. The different definitions comprise MPCs up to the third order, up to the second order or the first order reflections only. All cost functions decrease exponentially with the number of cycles until they converge to the

**Table 3.6:** Initial and calibrated material parameters.

| | | **Carpet** | **Wood** | **Plastic** | **Plaster** | **Glass** | **Metal** |
|---|---|---|---|---|---|---|---|
| Initial | $\varepsilon_r'$ | 1.50 | 2.07 | 3.91 | 6.46 | 7.78 | PEC |
| | $\tan\delta$ | 0.007 | 0.200 | 0.084 | 0.070 | 0.110 | |
| Calibrated | $\varepsilon_r'$ | 5.16 | 6.60 | 4.86 | 11.33 | 9.13 | 4.78 |
| | $\tan\delta$ | 0.029 | 0.068 | 0.133 | 0.100 | 0.112 | 0.462 |

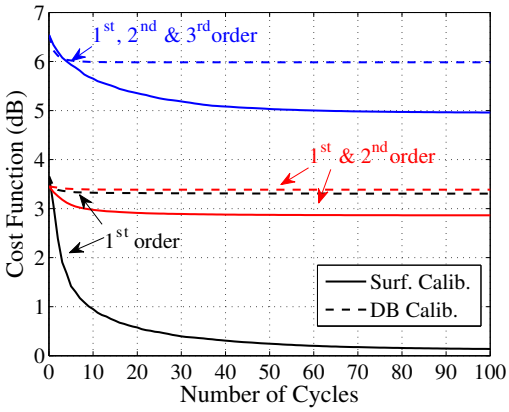


**Figure 3.23:** Convergence of the cost function.

| Cost Def. | Initial | DB | Surf. |
|---|---|---|---|
| $1^{st}$ order | 3.7 dB | 3.3 dB | 0.0 dB |
| $1^{st}$ - $2^{nd}$ order | 3.5 dB | 3.4 dB | 2.8 dB |
| $1^{st}$ - $3^{rd}$ order | 6.6 dB | 6.0 dB | 4.7 dB |

**Table 3.7:** Minimum cost function after calibration.

optimum solution. The initial value and the minimum cost function after calibration are additionally summarized in Table 3.7. In general, the element-wise calibration outperforms the database calibration, which is immediately obvious. For instance, the database calibration provides only marginal improvement in case of a calibration based on the first order reflections only. On the contrary, the cost function becomes zero by applying the element-wise calibration. The reason for this is that the calibration involves four surface elements, one for each reflection, but only three different materials. Hence, two MPCs are reflected allegedly at the same material. On closer inspection, it could be observed that the calibration algorithm was not able to minimize the deviations between RT and measurements for these two MPCs at the same time. This raises the conclusion that the assumption of one and the same material is not realistic here.

By contrast, four different material parameters are assigned to each of the four elements after the element-wise calibration, which seems to be more realistic under the mentioned circumstances. The better performance of the surface calibration for the cost functions employing higher order MPCs can be explained analogously. Regarding the absolute calibration performance, it is noteworthy that the minimum cost function lies in the same order as the initial solution. For instance, a database calibration based on all MPCs leads to an improvement of the cost function by only 0.6 dB. This suggests that the initial material database, which has been taken from literature, may be already nearly optimal. On the other hand it could mean that the assumption of a limited number of materials may not be sufficient to describe the scenario. In the following, this will be further analyzed.

Fig. 3.24a shows the distribution of the minimum cost function based on 100 calibration runs. All characteristics are very steep, i.e. the optimal solution is quasi-identical for all

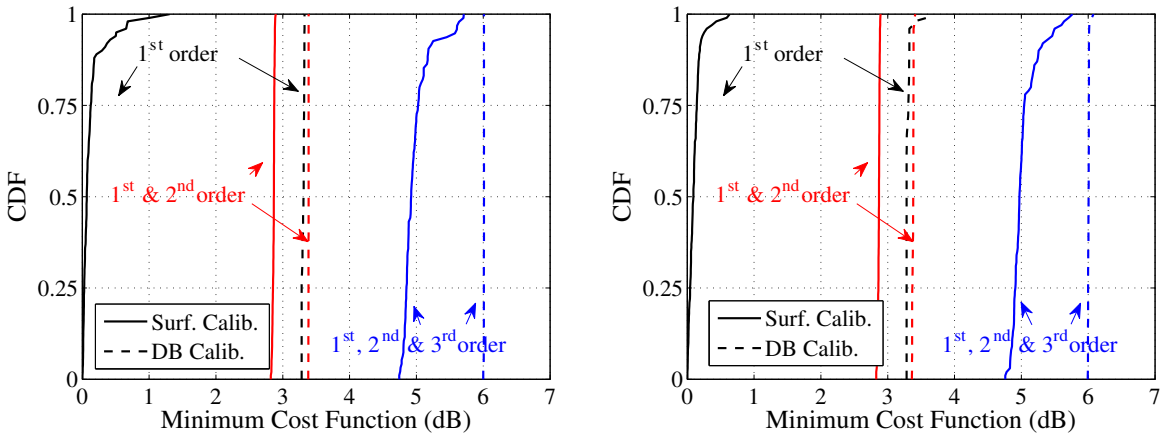


**(a)** Initial parameters from literature. **(b)** Initial parameters randomized.

**Figure 3.24:** Distribution of the minimum cost functions based on 100 calibration runs.

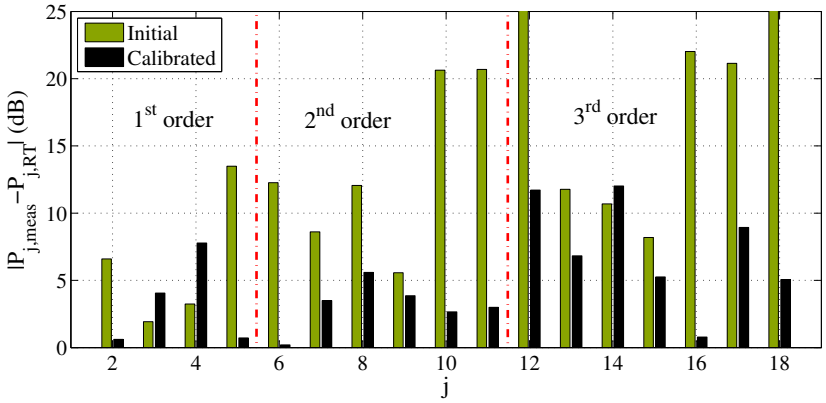


**Figure 3.25:** Deviations between RT and measurements before and after calibration.

calibration runs. This is especially the case for the database calibration, where standard deviations of the minimum cost function of 0.01 and below occur.

In order to further analyze the robustness of the algorithm, randomly generated material databases have been used as initial values for the calibration. The values of $\varepsilon_r$ have been varied independently between 1 and 10 and the loss tangent between 0 and 0.5 according to uniform distributions. This has been done for 100 calibration runs and lead to initial cost functions of 20 dB and more, which is far higher than using the data from literature. Fig. 3.25 shows the deviations between simulated and measured multipath power before and after the calibration for one examplary run. Here, a database calibration has been performed. The initial differences amount to 2 to 35 dB. In most of the cases, the power differences decrease by 5 dB and more after the calibration. In this example, the cost function converges from the initial value of 16.5 dB to 6.0 dB. Hence, the same performance is achieved as for initial parameters taken from literature (cf. Fig. 3.23).

The CDFs of the minimum cost functions with randomized initial materials are shown in Fig. 3.24b. When comparing these distributions with the ones in Fig 3.24a, virtually no difference can be observed. The averages are in fact identical. Hence, it has been proven that the optimum solution does not depend on the initial conditions, which demonstrates the high robustness of the algorithm. At the same time it can be concluded that the initial set from literature already provides realistic parameters.

#### 3.3.3.1 Verification with Different Measurements

So far, the cost function $f(\mathbf{X})$ used for the calibration has relied on measurements and RT results at position $RX_1$ only. Hence, no statements about the general validity of the optimum calibration solution have been possible. In the following, the validity of the determined solution will be proven for another position in the room. In particular, it is tested whether the parameter sets calibrated with measurement data from position $RX_1$ improve the RT accuracy at position $RX_2$. During the actual calibration, reflections are taken into account up to the third order at position $RX_1$ only. Afterwards the deviation between measurement and RT is calculated for position $RX_2$ according to Eq. (3-9). Fig. 3.26 shows CDFs of this deviation. These are based on the results from 100 calibration runs. The initial cost at $RX_2$ is calculated based on the literature values from Table 3.6. On Contrary to the RT simulations for $RX_1$, here the initial cost function is relatively high and amounts to 17.6 dB corresponding to a high deviation between RT and measurements. Regardless of the approach, i.e surface or database calibration, the cost function significantly decreases after the calibration. The cost functions after calibration mostly lie between 8 and 9.4 dB. Interestingly, the database calibration outperforms the surface calibration on average by about 0.7 dB. This can be explained by the drawbacks of the latter approach mentioned above. Although the cost function is 4 to 5 dB higher

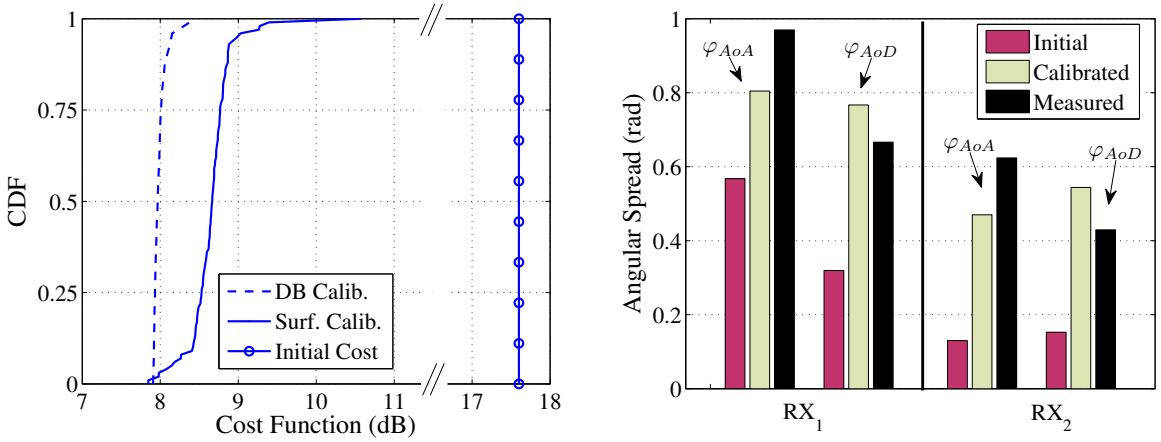


**(a)** CDF of cost function at $RX_2$. **(b)** Angular Spread.

**Figure 3.26:** Cost function and angular spread before and after calibration.

than for $RX_1$, the analysis reveals that the RT accuracy is significantly increased even at a position which had not been involved in the actual calibration process. Please note that this has been shown for one RX position only here. Nevertheless, in [Prieb13a] the presented procedure has been used for RT calibration in the THz regime. There, it could be shown that it is possible to increase the accuracy even at more than one position which has not been respected during the calibration.

Additionally, the angular spread is evaluated in order to further verify the calibration accuracy. For the measurements, the angular spread has been presented already in Table 3.5 in Section 3.2.4. Fig. 3.26b compares the measured values with the results from RT before and after calibration. These data again rely on the average over 100 calibration runs. However, the results virtually do not vary between the individual runs. Interestingly, the angular spread is always underestimated by the RT for the initial material parameters. This agrees with Table 3.6, which shows that the material reflectivity generally increases after calibration. Hence the amplitudes of the reflected MPCs increase also, which in turn causes a higher angular spread. As a result the deviations between RT and measurements are reduced from an average of 0.38 to 0.13. The fact that the improvement is possible for both $RX_1$ and $RX_2$ confirms the general validity of the calibration approach.

## 3.4 Concluding Remarks

In this chapter, the spatial and temporal characteristics of the 60 GHz indoor radio channel have been investigated experimentally. Additionally, the experimental data has been utilized to calibrate wideband ray tracing simulations.

- Path loss measurements have been conducted in a living room and a conference room scenario using circular horn antennas and open-ended waveguide antennas. A full set of parameters has been given to model the distance dependent path loss for LOS situations. Path loss exponents $n$ are found in between 1.5 and 2.0 dependent on the antenna configuration. Based on these models, the potential range of 60 GHz systems has been estimated. Concludingly, sub-gigabit data rates are feasible in both scenarios regardless of the type of antenna, whereas for multi-gigabit communication highly directive antennas are necessary.

  Regarding the small-scale channel features, RMS delay spread and maximum excess delay values have been determined. The involved highly directive antennas cause a very low-dispersive channel with small delay spreads of 2 ns and less in most of the cases. Nevertheless, as the envisaged data rates necessitate symbol durations in the order of nanoseconds, precautions must be taken against inter-symbol interference.

- The core contribution of this chapter is the experimental characterisation of the spatio-temporal 60 GHz radio channel within the conference room and a living room. With AoD- and AoA-dependent measurements in both scenarios it has been possible to separate single transmission paths in the spatio-temporal domain. Hence, the

results provide information about the path loss of these MPCs. This is of special interest as 60 GHz systems have to rely on reflected transmission paths when the LOS path is blocked, e.g. by a person. It is found that a sufficient number of MPCs are likely to exist, which can be used to maintain the communication link, if the LOS path is not available.

Based on the measurements, the angular dispersive channel characteristics have been evaluated. These are important when beamsteering is applied at both transmitter and receiver, which is planned for 60 GHz communications. Regarding the distribution of MPCs in the AoA/AoD-domain, diversified situations in one and the same environment occur. The observed angular spread values lie between 0.25 and almost 1. This indicates, that there are positions in the room where the received power is spread over a large angular range as well as positions where the power is mainly received from a confined direction. The implications of these findings will be analyzed further in Chapter 5.

The high axial ratio of the horn antennas allowed for a complete characterization of the polarimetric channel properties. Horizontal and vertical polarization have been compared by means of measurements, where the TX and RX antennas were co-polarized. The amplitude of MPCs has been found to be significantly higher in case of vertically polarized antennas, which is plausible. Moreover, no significant depolarization is expected for the TX and RX positioned at the same height, which has been confirmed by measurements with cross-polarized antennas.

- In addition to the conference and living room, measurements have been conducted in a scenario emulating a data kiosk. It has been shown that multiple reflections between the data kiosk and the user device may distort the channel. Moreover the housing material of the data kiosk has a significant influence on the MPCs in the CIR. E.g. the MPC amplitudes are 5 to 12 dB higher in case of metal compared to PVC. This in turn causes an increase of the delay spread. In general, the delay spread is very low and lies between 0 and 1.5 ns. However, in face of the high envisaged data rates, even a slight temporal dispersion may lead to a performance degradation.

- Concluding the chapter, the channel measurements have been used to calibrate the RT scenario data. In contrast to calibration techniques which utilize CIRs only, here a mapping of experimental and RT data has been done in the spatio-temporal domain. Consequently, an unambiguous assignment of MPCs is possible. The calibration is based on simulated annealing. Its performance has been demonstrated in the conference room. In a statistic study based on hundreds of calibration runs, it has been shown that the deviations between RT and measurements can be significantly reduced. Additionally, the fact that the optimum solution does not depend on the initial material database underlines the robustness of the method.

  In order to verify the calibration results, RT has been compared with measurements, which had not been used for the calibration. It could be shown that in this case

the RT accuracy increases significantly, which validates that the calibrated scenario data is considerably more realistic than the initially assumed data.

Concludingly, this chapter presents a comprehensive view of the 60 GHz radio channel in different indoor environments. The measurements quantitatively describe the propagation conditions and its results give a first estimation of the performance of multi-gigabit-systems. In addition, the calibrated RT provides an accurate deterministic channel model. Together with the human blockage model derived in Chapter 2 it lays the foundation for the investigations in the following chapters.

# 4

# Modeling the Human-Induced 60 GHz Channel Dynamics

In this chapter, one deterministic and two stochastic radio channel models accounting for human shadowing are proposed. The deterministic model is based on the validated RT and the MKE model, which has been presented in Chapter 2. The stochastic models complement the IEEE 802.11ad 60 GHz radio channel model as they introduce the influence of human shadowing. The first one is a semi-static stochastic snap shot model derived from extensive deterministic wideband simulations. Statistics are generated for the probability of cluster blockage and the attenuation due to human-induced shadowing. The result is a channel impulse response model with the ability to account for multiple persons. In this approach, each channel realization is generated independently. Hence, it does not take into account the time-variance of the channel. This is indeed enough for some applications, but as 60 GHz systems will definitely incorporate non-convential smart antenna concepts like beamforming, the temporal change of the channel is of great interest. For this reason, another model has been developed. It also uses blockage probabilities, but additionally emulates the temporal characteristics of human shadowing based on an empirically derived model. Both models are able to support the design process of 60 GHz indoor communication systems.

The chapter is structured as follows. In Section 4.1, the deterministic wideband human blockage model is presented and validated. In Section 4.2, extensive simulation data is produced by means of this model, which are used to derive the semi-static channel model. The time-variant model together with the underlying measurements is described in Section 4.3. Additionally, a study about the human induced Doppler shift is presented in Section 4.4. Section 4.5 concludes the chapter.

Please note that parts of the work presented in this chapter have been already published by the author in [Czink12, Jacob10d, Jacob11a, Jacob13c, Jacob13b, Jacob09b, Jacob09e, Jacob09g, Jacob10e, Malts10d]. The measurement data used for the validation in Section 4.1 were kindly provided by the Heinrich-Hertz-Institut in Berlin.

## 4.1 Deterministic Wideband Modeling of Human Shadowing

In Chapter 2, different theories for the modeling of human blockage have already been presented and compared. There, the motivation was to choose one model which should be incorporated in ray tracing simulations. This hybrid deterministic approach of ray tracing combined with a diffraction model will be used in Section 4.2 to develop stochastic channel impulse response models and is the base for the investigations in Chapter 5. In the following, it will be described how the chosen MKE model is linked to the ray tracing simulations and then the model is validated with measurements.

### 4.1.1 Model Description

In Chapter 2, the MKE model has already been described for a single LOS link in presence of a moving human body. At this point, the enhancement of this functionality to the shadowing of reflected MPCs will be given. In principle the implementation is straightforward. Instead of the interaction between the human body with the LOS link, the interaction with the reflected rays has to be modeled. For a better understanding, an introductory example is analyzed, where a person crosses a once reflected ray. Fig. 4.1a illustrates this scenario. The crossing of the ray leads to two consecutive shadowing events. The first one can be described by the crossing of the partial ray between TX and the wall. The second event arises from the affection of the partial ray between the wall and the RX.

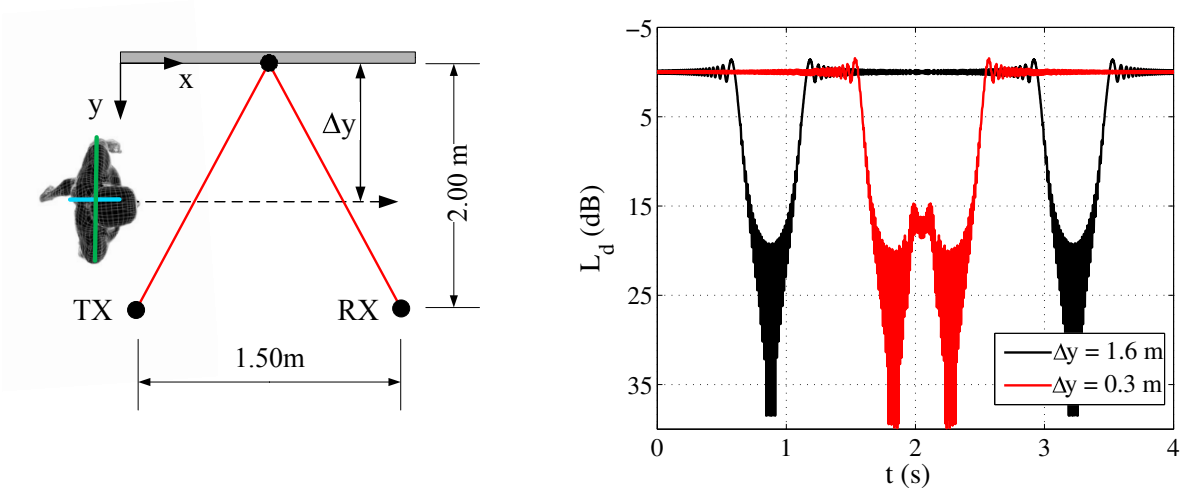


**(a)** Scenario. **(b)** Loss characteristics.

**Figure 4.1:** Example for the shadowing of a reflected ray, simulated by ray tracing and the MKE model.

The corresponding loss characteristic is shown in Fig. 4.1b. The black curve represents the case when the person walks in parallel to the wall at a distance of $\Delta y = 1.6\,m$. In this case, two distinct consecutive shadowing events occur. When the person steps closer to the wall and simultaneously affects both parts of the ray path, it may happen that the two shadowing events temporarily overlap. The losses are then determined by a coherent superposition of both events. This case with $\Delta y = 0.3\,m$ is also shown in the figure. Analogous to the once reflected rays, this methodology is generalized to reflections of arbitrary order $n$ derived by RT. The number of potential intersections between the person and the ray is always *n+1*. After treating each ray this way, the result is a time-variant channel impulse response. Please note that for the constellation, the person may also have an impact on the LOS connection, which is not discussed here for the sake of briefness.

Additional information about implementational aspects are given in Appendix B. In order to verify the model, its results are compared to channel measurements in the following.

### 4.1.2 Validation with Measurements

The MKE model has been already validated for blocked LOS connections by narrowband measurements carried out with a simple VNA based setup in Chapter 2. In this context, a holistic validation is carried out not only for the LOS link, but also for the blocked MPCs. For this reason, wideband channel measurements have been performed with a real-time 60 GHz channel sounder by the Heinrich-Hertz-Institut, Berlin [Peter12]. A schematic view of the conference room in which the measurements have been performed is depicted in Fig. 4.2a. The measurement setup achieves a bandwidth of about 3 GHz at a center frequency of 60 GHz. The receive signal is recorded by a digital sampling oscilloscope with an oversampling factor of 6.5. In addition, a Kaiser windowing has been applied in frequency domain in order to minimize sidelobe effects in time domain. A more detailed description of the measurements can be found in [Peter12].

These measurements are then compared to the broadband human blockage simulations developed in this thesis. The simulations are based on frequency domain ray tracing simulations for the same frequency band and with the same post processing as for the measurements. In the ray tracing simulations, only a very simple geometrical model of the conference room scenario has been used. It basically contains the four walls, the floor and the ceiling. As the aim of this section is not the validation the ray tracing accuracy itself but the methodology described above, this approach is sufficient. The dielectric properties are taken from [Peter07]. Fig. 4.2a additionally contains the six most relevant rays determined by the ray tracer. The first arriving multipath component (MPC 1) represents the LOS ray. MPC 2 and 3 are the first order reflections at the floor and the ceiling. The remaining rays are reflections at walls.

Fig. 4.2b shows the comparison between ray tracing and measurement results for the static case without human activity. This comparison is done in terms of normalized power delay profiles. Additionally, the rays corresponding to the illustration in Fig. 4.2a

are indicated by their number. The agreement of the simulated and measured ToAs is very good for MPC 1 to 4. In case of MPC 5 and 6, the ToAs of both MPCs are similar. Due to the low complexity of the geometric model no clear assignment of measured to simulated MPCs is possible as the ToA difference could not be definitely resolved. The amplitudes of the individual MPCs can differ by up to 8 dB. In addition the ray tracer was not able to determine all MPCs observed in the measurements. These deviations are caused by the low complexity of the geometric model, as well as the fact, that the ray tracer has not been calibrated in this case.

In the time-variant measurements a person crossed the LOS between transmitter (TX) and receiver (RX) perpendicularly. Measurement snapshots were taken with a period of approximately 9 ms. The resulting time-variant power delay profiles derived from measurements and simulations are shown in Fig. 4.3. Again, the rays corresponding to the illustration in Fig. 4.2a are indicated by their number. The constraints resulting from the simple geometrical model of the room are again visible. A qualitative comparison, e.g. for the LOS path, reveals that the general agreement is quite good. Shortly after the LOS ray, it is noticeable that another MPC occurs before and after the shadowing event. This MPC is caused by reflections at the human body and is not visible in the simulated PDP as the simulations do not account for the reflections. A detailed analysis of this phenomenon will be given in the context of the Doppler spread investigations in Section 4.4.

The other MPCs are analyzed separately in the following. Therefore, the attenuation of each of the rays is exemplarily contrasted in Fig. 4.4. As a reference level, the case without shadowing is assumed here. As stated above, a detailed analysis for the LOS link is already given in Section 2.2 and hence is omitted here. Nevertheless, the corresponding

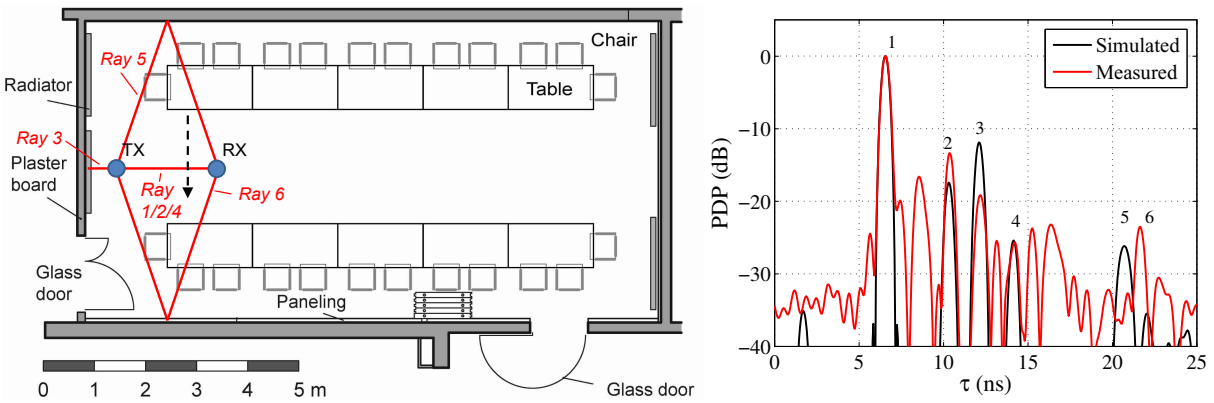


**(a)** Conference Room Scenario. **(b)** Measured and simulated PDP.

**Figure 4.2:** Scenario and modeled and simulated power delay profiles for a static channel without human activity.

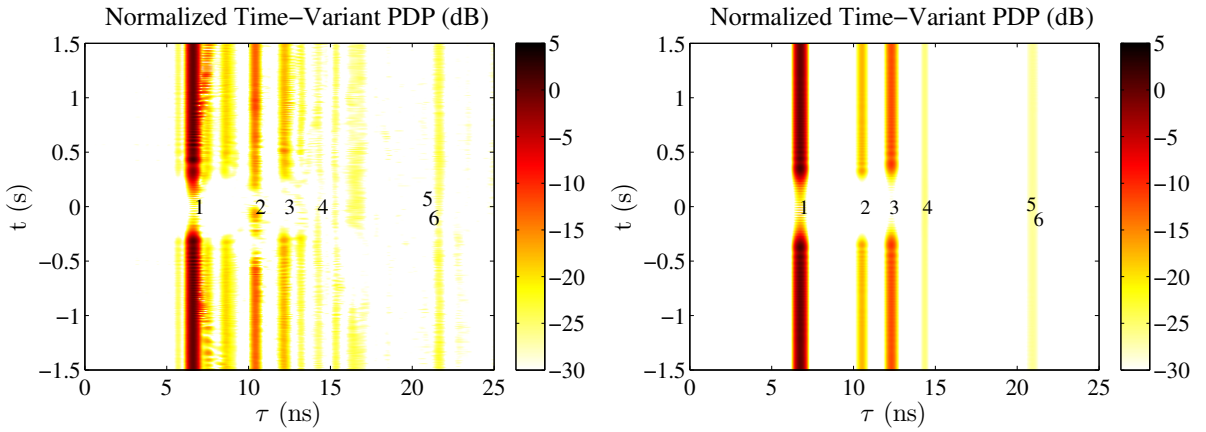


**(a)** Measurement. **(b)** Simulation.

**Figure 4.3:** Modeled and simulated time-variant power delay profiles.

temporal characteristics are also depicted here for the sake of completeness. In case of reflected rays, the general agreement between model and measurement is good.

Regarding MPC 3, especially the duration and the increase and decrease of the shadowing event is very well reproduced by the model. In the deep shadow region the attenuation is overestimated and the oscillations before the shadowing event are underestimated. Reasons for this have already been given in Chapter 2. In case of MPC 4 and MPC 5/6, the received power is on the one hand already affected by the noise of the receiver. On the other hand, a slight drop can be observed when the person crosses the LOS path, which is not visible in the simulated curves. Nevertheless, in both cases the deviations are tolerable. MPC 2 illustrates another significant constraint of the model. In this case, the agreement is quite poor. In contrast to the simulations, not a single but two shadowing events can be recognized in the measured curve. The reason of this deviation becomes clear, if we pay attention to the cluster itself. MPC 2 represents the reflection at the floor. Hence, during the measurements the reflected ray is shadowed by one leg first and then by the other one. It is needless to say, that this behavior cannot be reproduced by the simple geometry used in the MKE modeling.

To conclude this section, now a tool is available to realistically model time-variant 60 GHz radio channels. This tool will now be used to derive stochastic channel models in the following Sections.

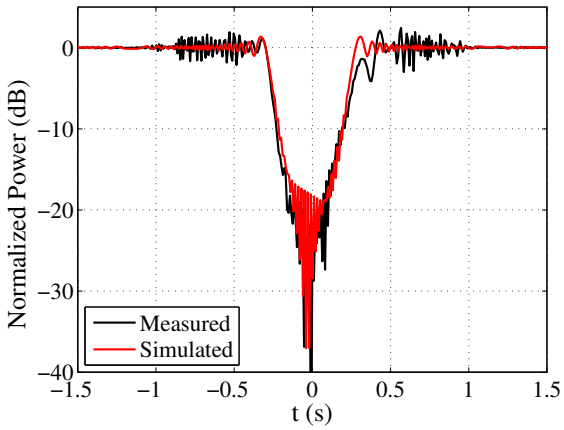


**(a)** MPC 1.

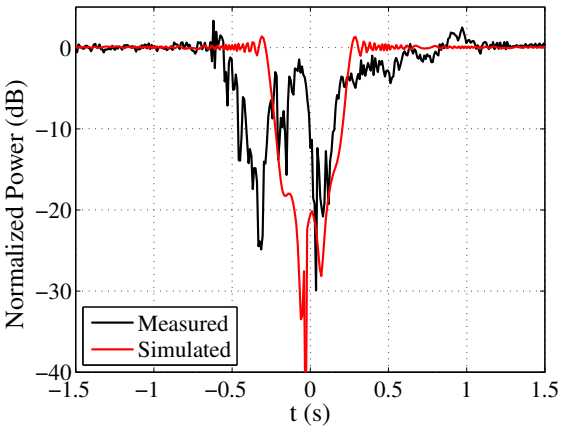


**(b)** MPC 2.

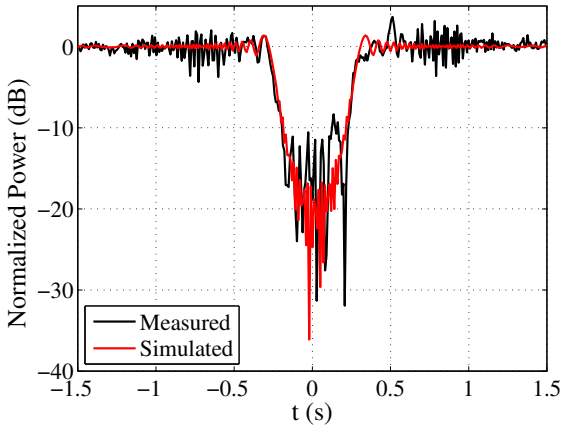


**(c)** MPC 3.

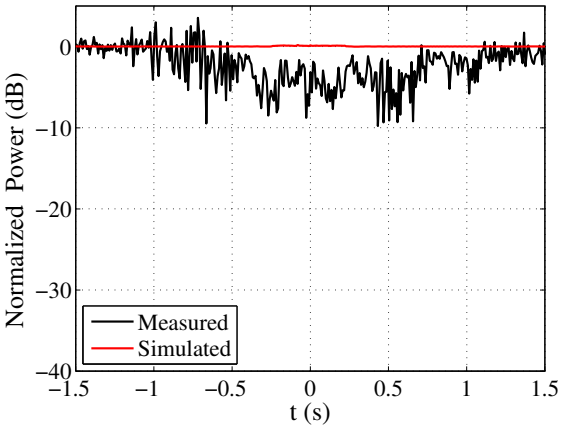


**(d)** MPC 4.

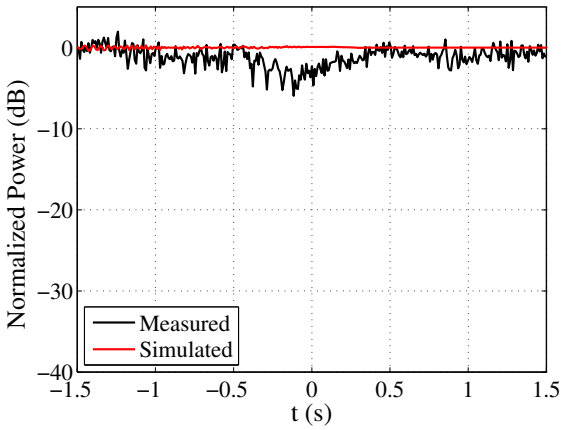


**(e)** MPC 5/6.

**Figure 4.4:** Modeled and simulated MPC power.

## 4.2 Stochastic Semi-Static Wideband Radio Channel Model

Within the IEEE 802.11 Task Group ad, a channel model for 60 GHz WLANs systems has been developed. Its purpose is to support the evaluation of proposals during the 60 GHz WLAN standardization process [Perah10]. The main assumption of the model is that MPCs arrive at the receiver in clusters, wherein the rays are spaced closely in both the time and angular domain. Besides other features like the information about AoA/AoD or polarization characteristics, the model also supports non-stationarity arising from the motion of people. The modeling part for the human shadowing has been done by the author of this thesis. A short overview of the TGad model is given in Appendix A.

This Section focusses on the human blockage model based on the author's work for the IEEE 802.11ad channel model (see Appendix C). The presented approach is based on ray tracing simulations in combination with the multiple knife edge diffraction model (see Section 2.2.1.4, p. 26). Human movement is simulated by a random walk algorithm. Section 4.2.1 introduces the general modeling methodology and Section 4.2.2 presents the stochastic model as it is included in the TGad channel model. This model is extended by taking into account multiple persons in Section 4.2.3. Additionally, a first investigation of the influence of human blockage on the large- and small-scale channel characteristics is presented.

### 4.2.1 Modeling Methodology

#### 4.2.1.1 Scenarios and Ray Tracing

According to the main applications of 60 GHz WLAN systems, TGad has defined two different conference room sub-scenarios [Perah10]. Schematics with all dimensions are depicted in Fig. 4.5. A large table is placed in the middle of the room, on which possible stationary devices (STAs) are randomly placed. In the STA-AP sub-scenario, an access point (AP) is mounted under the ceiling to cover the whole room, whereas in the STA-STA sub-scenario, the ad-hoc connection between two STAs on the table is considered.

The propagation between TX and RX device is modeled via ray tracing including the direct path and reflected paths with a maximum of two reflections. Reflections from the floor are neglected. In the STA-AP sub-scenario the ceiling reflections are also neglected. The number of clusters is constant for each RX/TX pair and is summarized in Table 4.1. Exemplary rays are depicted in Fig. 4.5. Altogether, there are 18 clusters in the STA-STA and 13 clusters in the STA-AP sub-scenario. In both setups, ray tracing simulations have been performed for a few hundred TX/RX combinations. The goal here has been

**Table 4.1:** Number of clusters $N$ for the STA-STA and STA-AP sub-scenarios according to [Malts10d].

| Cluster type | STA-STA | STA-AP |
|---|---|---|
| LOS | 1 | 1 |
| First order reflections (walls) | 4 | 4 |
| Second order reflections (walls) | 8 | 8 |
| First order reflections (ceiling) | 1 | - |
| Second order reflections (wall and ceiling) | 4 | - |

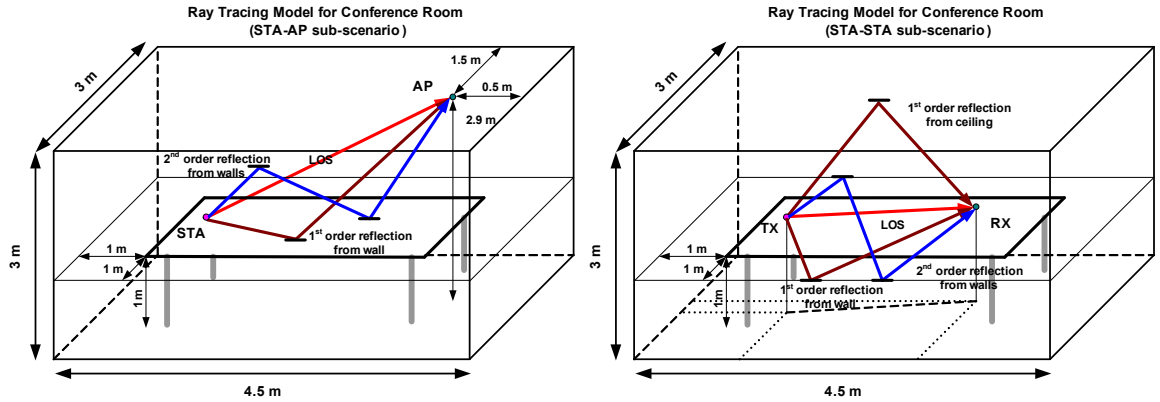


**(a)** STA-AP sub-scenario. **(b)** STA-STA sub-scenario.

**Figure 4.5:** 3D model of the conference room used for ray tracing. Taken from [Malts10d].

to determine the geometrical characteristics of the different rays in order to respect the human blockage during post processing based on the ray tracing results.

#### 4.2.1.2 Random Walk Model

The movement of the person is modeled with a random walk algorithm with the aim to reproduce the non-deterministic motion of people as realistic as possible. For this, MKE geometry with the dimensions $170 \times 45 \times 40$ cm$^3$ as well as a walking speed of $1 \frac{\text{m}}{\text{s}}$ and a step length of 60 cm has been assumed as a representation of the walking person. In the beginning of each simulation run, a random starting point and an initial random walking direction $\phi$ is determined. After this, the person makes one step forward with the specified walking speed and temporal resolution. Then, a new walking direction is determined by adding a uniformly distributed angle between +15° and -15° to the previous angle $\phi$. In principle, this procedure leads to a random movement with preferential straightforward direction. When the person reaches a wall or any other obstacle, it is forced to turn in a preferred direction by incrementing the newly determined angle $\phi$ by a uniformly distributed random variable between 0° and 10°. Effectively, the person walks around the table in counter clockwise direction. As an example, Fig 4.6 shows a random walk with

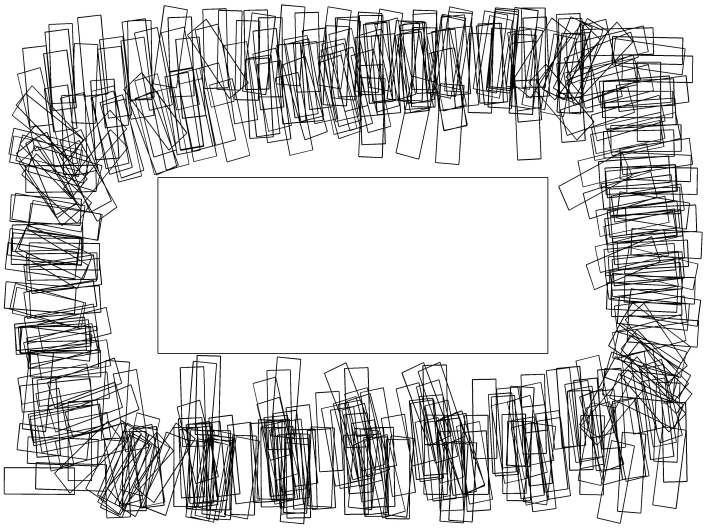

**Figure 4.6:** Exemplary random walk in top view.

500 positions of the person at intervals of the step length. For the sake of clearness, the person is represented by a rectangle. Please note, that for the derivation of a semi-static model as presented in this section, no random walk algorithm would be necessary. A simple distribution of position and viewing direction would be sufficient. Nevertheless, this concept is already introduced here, and will be followed up in Chapter 5, where the temporal behavior of human-induced shadowing is analyzed.

The random walk algorithm in principle works for arbitrary scenarios, as it is implemented in a way that prohibited areas like furniture or walls can be specified, which the person must not intersect or move into. In the case of the scenarios considered here, only the conference table represents a forbidden area.

### 4.2.2 Stochastic Model for a Single Person

The model presented in this Section has been included in the TGad channel model document [Malts10d]. Moreover, the model will be extended from a single person as in the TGad model to up to 10 persons in the next section. Applying the methodology presented in the previous section, this section describes the statistical modeling of dynamic human blockage for the 60 GHz channel model. The data for the stochastic analysis is based on ray tracing results for 1071 TX/RX combinations equally distributed on the table and a simulation time of 30 seconds. Together with the temporal resolution of 10 ms this leads to a database of 3 million snap shots per TX/RX combination.

The influence of a person manifests itself in drops of the received signal power by up to 40 dB (see Fig. 4.4). Such events are used to introduce dynamics to the TGad channel model. The complexity of the model can be reduced using the simplifying assumption that the channel realizations are generated independently for random time instances and

that the blockage events are independent for different clusters. A complete model is then sufficiently described by

1. Defining the **probability of a cluster blockage event** and
2. Finding the **attenuation distribution** of cluster blockage events.

In the following, the derivation of both is discussed.

#### 4.2.2.1 Probability of Cluster Blockage

Besides the LOS path, two types of relevant clusters have been defined in the STA-AP conference room scenario: four first order reflections and eight second order reflections from the walls. In case of the first order reflections, the simulation results show that not more than one single cluster is blocked at a time. The RT and random walk simulations has lead to the conclusion that the probability for the blockage of one cluster is 0.126. In order to model this behavior, one of the four clusters is chosen randomly with equal probability. Then, this cluster is blocked with a probability of 0.126. This procedure is repeated for the generation of every channel realization. In case of the second order reflections, the simulations have revealed that multiple clusters can be blocked simultaneously. The occurence rate of simultaneously blocked clusters is shown in Fig. 4.7a. This PDF can be approximated with a binomial distribution:

$$f(k) = \binom{N}{k} p_{Bino}^{k} \left(1 - p_{Bino}\right)^{N-k} \tag{4-1}$$

where $N$ is the total number of clusters, $k$ is the number of blocked clusters and $p_{Bino}$ is the probability that one randomly chosen cluster is blocked by a person. Here, the

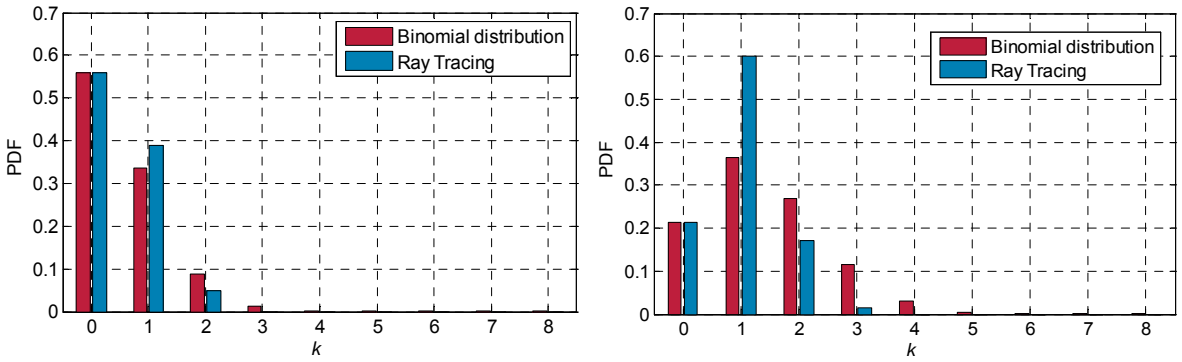


**(a)** STA-AP scenario. **(b)** STA-STA scenario.

**Figure 4.7:** PDFs of the number of simultaneously blocked clusters for second-order reflections.

**Table 4.2:** Probabilities of clusters blockage for the STA-STA sub-scenario.

| Cluster type | Probability of single cluster blockage |
|---|---|
| LOS | 0 or 1 (set as model parameter) |
| First order reflections (walls) | 0.24 |
| Second order reflections (wall and ceiling) | 0.037 |
| Second order reflections (walls) | $p_{Bino} = 0.175$ (binomial distr. parameter) |

parameter $p_{Bino}$ has been chosen to 0.07 as this leads to a probability of 0.56 that no cluster is blocked, which agrees with the ray tracing results. The differences between the ray tracing simulations and the binomial distribution only amount to up to 0.05.

For the STA-STA scenario, statistics have been derived as well. Due to the fact that both devices are positioned on the table, the first order reflection from the ceiling is not influenced by human movement and hence has a blockage probability of 0. In case of first order reflections from walls and second order reflections from walls and ceiling, the simulation results show that the probability for the simultaneous blockage of multiple clusters is also 0. The probabilities that a single cluster is blocked are given in Table 4.2. All clusters are chosen with equal probabilities. In case of second order reflections from walls, the simulations have shown that multiple clusters can be blocked at the same time. The number of simultaneously blocked clusters is again modeled with a binomial distribution. The probability for a cluster blockage event amounts to $p_{Bino} = 0.175$, leading to a probability of 0.215 that no cluster is blocked, which agrees with the ray tracing simulations (see Fig. 4.7b).

Due to the possible TX and RX locations, the LOS cluster is not influenced by human movement in either of the scenarios. In order to still account for NLOS situations, as they may occur in the event that objects are placed on the table, it is proposed to simply suppress the LOS cluster in the generated channel realization.

#### 4.2.2.2 Attenuation Distributions

A statistical model for the attenuation characteristics due to ray obstruction by a single moving human body is provided next. Regarding the attenuation characteristics of a blockage event, the ray tracing/random walk simulations have shown that clusters with and without a reflection at the ceiling need to be distinguished. The simulation results have also shown that the attenuation distributions are equal for both sub-scenarios (STA-STA and STA-AP).

Fig. 4.8 shows histograms of simulated cluster blockage attenuations for the second order clusters reflected from walls and ceiling as well as for the first/second order clusters reflected from walls. In addition, analytical approximations are given for the stochastic modeling. A truncated Gaussian function in log-scale well approximates the attenuation

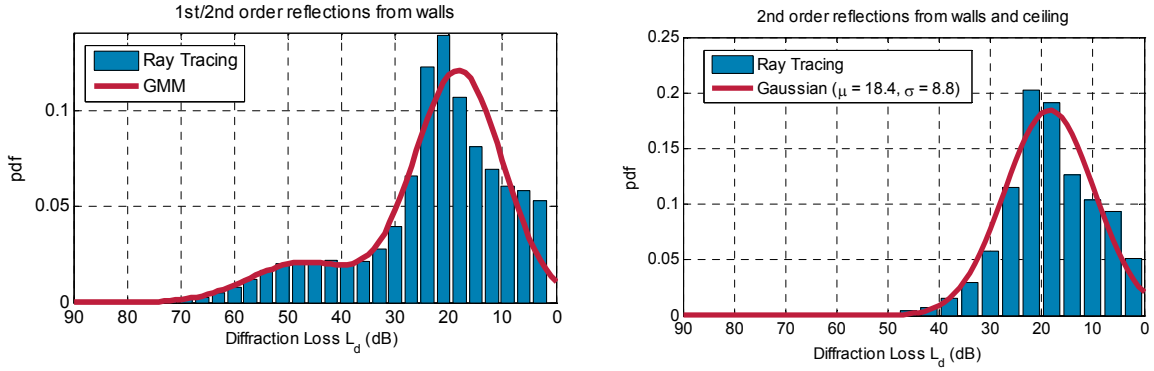


**(a)** First/second order clusters reflected from walls.

**(b)** Second order clusters reflected from walls and ceiling.

**Figure 4.8:** Histograms of simulated power attenuation due to human blockage and approximation for the STA-STA scenario.

distribution in the case of clusters including ceiling reflection. The parameters of the Gaussian distribution are $\mu = 18.4$ dB and $\sigma = 8.8$ dB. In the case of clusters without a ceiling reflection the model is given by a truncated Gaussian mixture model (GMM) in log-scale with the probability density function:

$$f(L) = \begin{cases} \sum_{i=1}^{n} a_i \frac{1}{\sigma_i \sqrt{2\pi}} e^{\frac{-(L-\mu_i)^2}{2\sigma_i^2}}, & \text{for } L \geq L_{trunc} \\ 0, & \text{else.} \end{cases} \tag{4-2}$$

Both distributions are proposed to be of second order and truncated at $L_{trunc} = 0$ dB. The distribution parameters are $\mu_1 = 18.2$ dB, $\sigma_1 = 8.3$ dB, $a_1 = 0.83$, $\mu_2 = 47.2$ dB, $\sigma_2 = 10.0$ dB, $a_2 = 0.17$.

### 4.2.3 Stochastic Model for Multiple Persons

In addition to the model for a single person which has been included in the TGad model, another model is developed in this thesis taking into account up to ten persons. In principle, the same methodology as for the single person model is used here. The model is again completely described by the probability of the number of simultaneously blocked clusters and the attenuation distribution of the shadowing events.

The only difference is that the movement of up to ten persons is simulated, which is more realistic than a single person for the conference room scenario. At the beginning of the simulations, a random starting position is assigned to each person. Then, every person performs an individual random walk according to the constraints given above.

Please note that for each person individual constant walking speeds have been assumed, which are uniformly distributed between 0.5 and 1.5$\frac{m}{s}$. The person dimensions are the

same for each person (175 × 50 x 25 cm). In the stochastic model, the number of persons $N_{persons}$ is introduced as further degree of freedom.

#### 4.2.3.1 Probability of Cluster Blockage

The simulated probability density functions (PDFs) as well as their approximations for the STA-AP scenario are shown in Fig. 4.9. For each value of $N_{persons}$ the probability distribution density is approximated via least square fitting by a binomial distribution. Regarding the first order reflections (Figs. 4.9a and 4.9b), one of the four clusters is blocked with a probability of 5 % assuming a single person. With an increasing number of persons

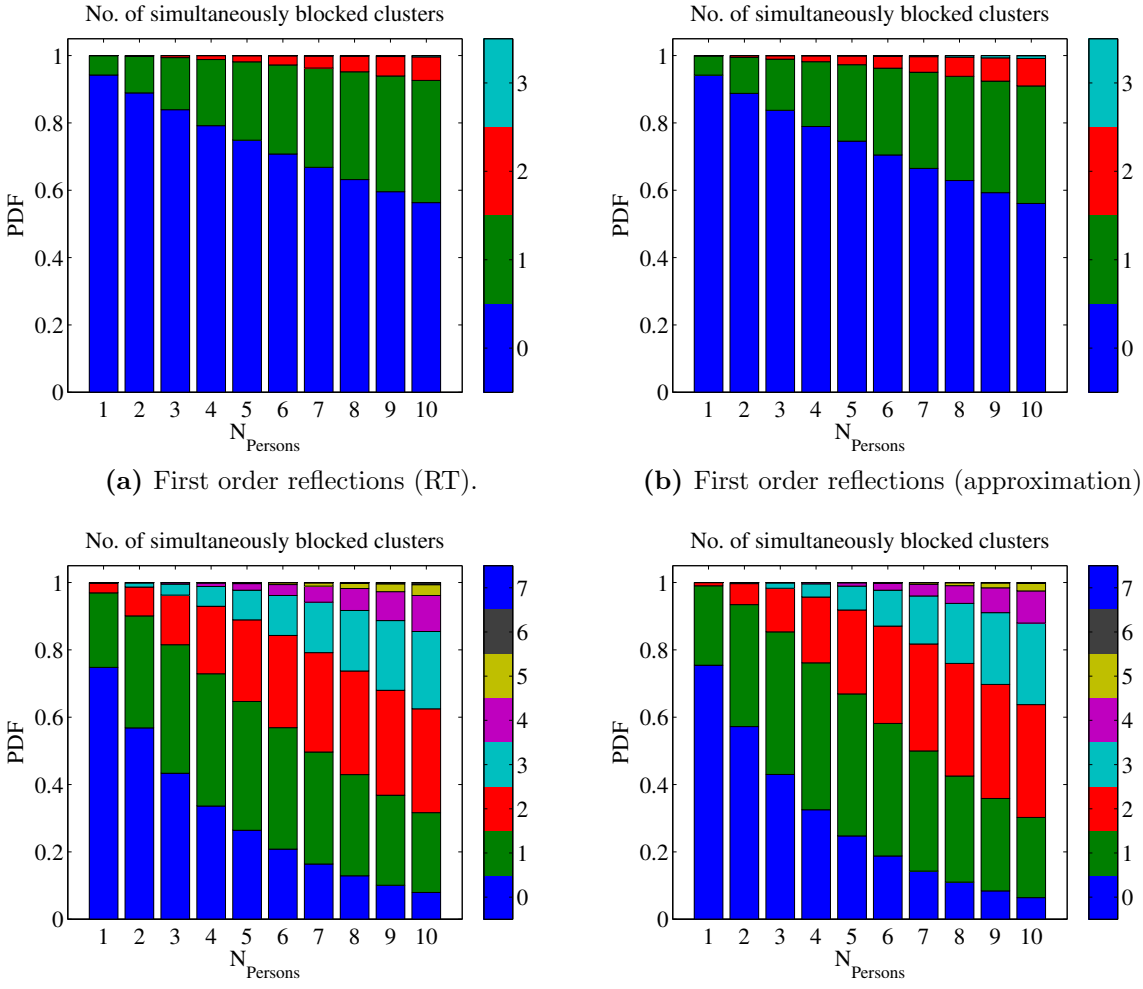


**(a)** First order reflections (RT).

**(b)** First order reflections (approximation).

**(c)** Second order reflections (RT).

**(d)** Second order reflections (approximation).

**Figure 4.9:** Probability density functions of the number of simultaneously blocked clusters in the STA-AP scenario.

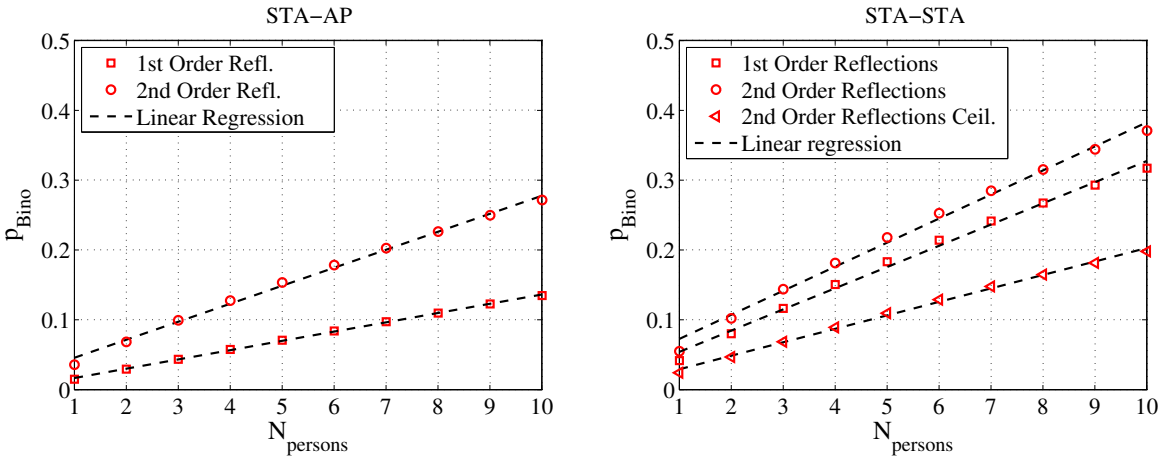


**(a)** STA-AP **(b)** STA-STA

**Figure 4.10:** Cluster blockage probability $p_{Bino}$ depending on the number of persons.

the probability of cluster blockage increases as expected. A non-zero probability that two clusters are blocked occurs for three and more persons.

The statistics of the second order reflections are depicted in Figs. 4.9c and 4.9d. Here, the probability that no cluster is blocked (blue) decreases exponentially with an increasing number of persons. The probability for the blockage of one cluster is almost constant, whereas the probability of more than one blocked clusters increases. For ten persons, for example, the probability that no cluster is blocked amounts to only 7.6 % compared to 75 % for one person. Regardless of the reflection order, at least one cluster remains unaffected by the persons.

For each value of $N_{persons}$ the probability distribution densities is approximated by a binomial distribution defined by the parameter $p_{Bino}$. The model parameters have been determined by a least square fitting. Fig. 4.10a shows the dependency of $p_{Bino}$ on the number of persons $N_{Persons}$ for the STA-AP scenario. As expected, the probability $p_{Bino}$ that a randomly chosen cluster is blocked increases with $N_{persons}$. For instance, it amounts to 5% for a single person and 27% for ten persons in case of the second order reflections. The probability for the first order reflections is approximately half as that for the second order reflections. The dependency on the number of persons can be approximated very well by a linear regression:

$$p_{Bino}\left(N_{Persons}\right) = m \cdot N_{Persons} + c \tag{4-3}$$

Thus, the PDFs as depicted in Figs. 4.11 are described by only two model parameters. These parameters are again estimated by least square fitting and can be found in Table 4.3. The table also contains the data for the STA-STA scenario.

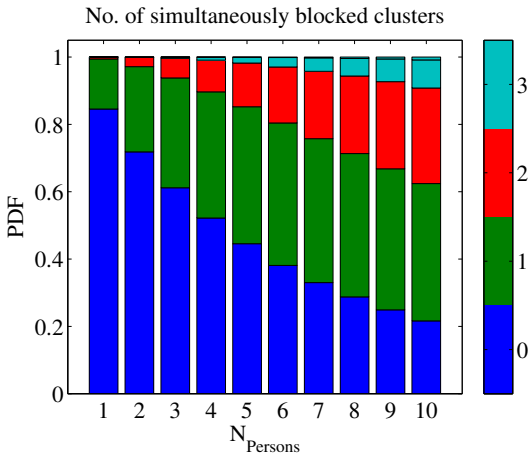


**(a)** First order reflections from walls (RT).

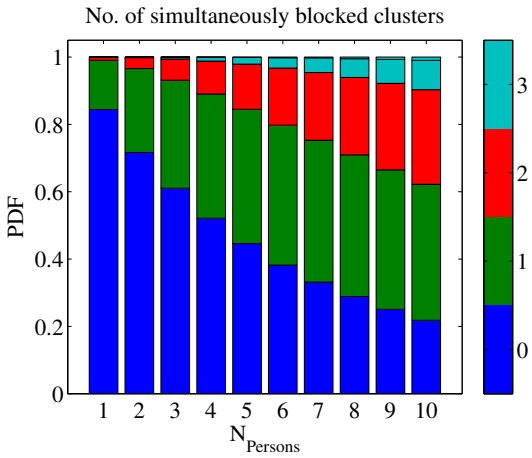


**(b)** First order reflections from walls (approximation).

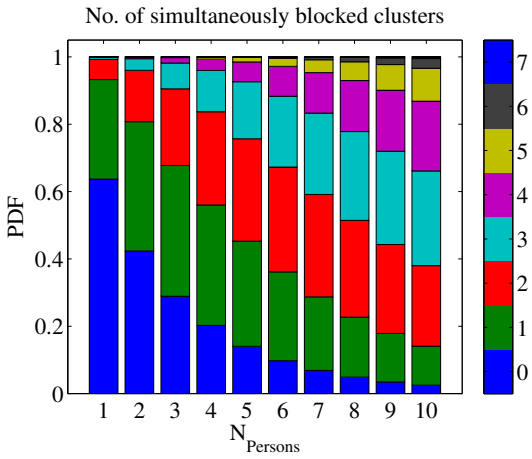


**(c)** Second order reflections from walls (RT).

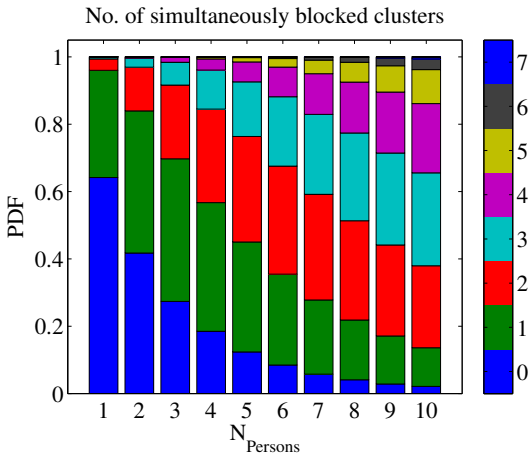


**(d)** Second order reflections from walls (approximation).

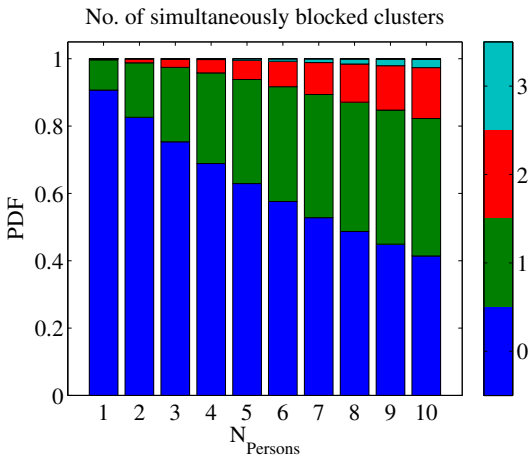


**(e)** Second order reflections from walls and ceiling (RT).

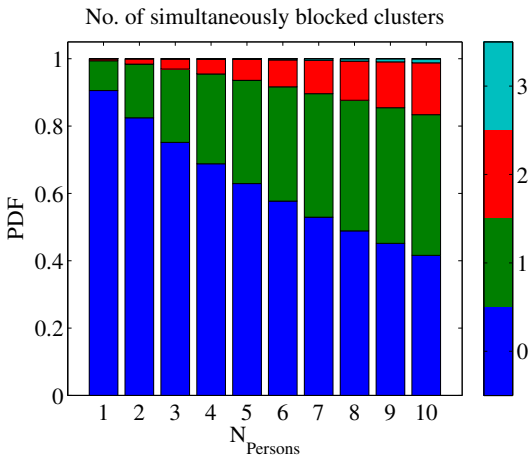


**(f)** Second order reflections from walls and ceiling (approximation).

**Figure 4.11:** Probability density functions of the number of simultaneously blocked clusters in the STA-STA scenario.

**Table 4.3:** Parameters for the modeling of simultaneously blocked clusters depending on the number of persons.

| **Cluster type** | | **STA-STA** | | **STA-AP** | |
|---|---|---|---|---|---|
| | ***N*** | ***m*** | ***c*** | ***m*** | ***c*** |
| First order reflections walls | 4 | 0.0304 | 0.0237 | 0.0133 | 0.0033 |
| Second order reflections walls | 8 | 0.0344 | 0.0381 | 0.0258 | 0.0198 |
| Second order reflections wall and ceiling | 4 | 0.0193 | 0.0099 | - | |

The data basis for the STA-STA scenario is depicted in Fig. 4.11 in terms of probability densities. The statistics of the first order as well as the second order reflections at the wall are similar compared to the statistics for the STA-AP scenario. Only the probability $p_{Bino}$ that a cluster is shadowed is slightly higher in this scenario. This can also be observed comparing Figs. 4.10a and 4.10b. For example, the blockage probability of a first order reflected cluster is 32% for the STA-STA scenario and 13% in case of the STA-AP scenario. The reason is that in case of the STA-STA scenario all rays lie in a horizontal plane at table height, which is intersected by the human bodies in any case. In this scenario another type of clusters exist: second order reflections from walls and ceilings. The statistics of these clusters are shown in Fig. 4.11e. They are qualitatively similar to the first order clusters from the wall, but here the corresponding probability $p_{Bino}$ is generally lower. Again, the agreement between RT/random walk data and the approximation is very good for all kinds of clusters. The first order reflections from the ceiling are not affected in any case independent of the number of persons in the STA-STA scenario. The same holds true for the LOS cluster in both scenarios due to the placement of the transmitters and receivers. The RMS modeling error between stochastic model and RT/MKE simulations in both scenarios lies between $2 \cdot 10^{-3}$ and $2 \cdot 10^{-3}$.

#### 4.2.3.2 Attenuation Distributions

The analysis above has revealed that the probability of the cluster blockage is higher in the STA-STA scenario due to the fact that TX and RX always lie in a horizontal plane. The analysis of the attenuation $L_D$ shows that the average loss due to human blockage is also higher in the STA-STA scenario. The reason is that one ray is more likely affected twice by a single person. This can happen when a person is close to a wall and shadows

**Table 4.4:** GMM parameters for the attenuation distribution model.

| | $a_1$ | $\mu_1$ | $\sigma_1$ | $a_2$ | $\mu_2$ | $\sigma_2$ | $a_3$ | $\mu_3$ | $\sigma_3$ |
|---|---|---|---|---|---|---|---|---|---|
| STA-STA | 0.39 | 35.7 | 15.1 | 0.18 | 20.1 | 3.0 | 0.43 | 11.8 | 11.1 |
| STA-AP | 0.14 | 39.5 | 12.8 | 0.16 | 19.9 | 9.1 | 0.70 | 12.8 | 11.5 |

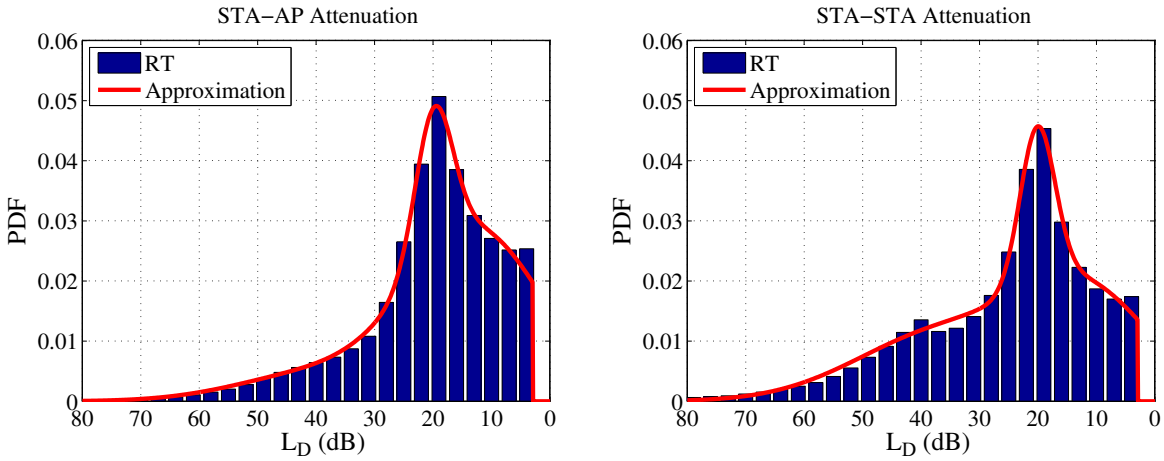


**(a)** STA-AP **(b)** STA-STA

**Figure 4.12:** Histograms of simulated attenuation due to human blockage and approximation by GMM.

the ray before and after the reflection takes place. In addition, the influence of the number of persons is also higher as the characteristics are steeper for the STA-STA scenario.

It is proposed to use a single attenuation distribution for each scenario based on a statistic over all simulations for $N_{persons} = 1...10$ and all types of clusters. Of course this leads to errors, which are mainly caused by the fact, that the attenuation generally increases with the number of persons. However, these errors are on average mostly lower than 3 dB. The histograms of the attenuation are shown in Fig. 4.12. For the use in the stochastic model, the histograms have been approximated via least square fitting by truncated third order GMMs. The model parameters are given in Table 4.4. The RMS modeling error lies in the order of $1 \cdot 10^{-3}$. Both characteristics can be plausibly interpreted. The maximum at about 20 dB and the tail up to 80 dB represents the deep shadowing area. The maximum results from the strong fading caused by the interference of the diffracted field components (i.e. shadowing event in Fig. 4.4a). The main difference between both scenarios is a further maximum at about 40 dB in case of the STA-STA scenario. The reason for this is that the it is more likely here that electromagnetic wave interacts twice with the person.

In the following section, the influence of persons on the radio channel is discussed.

### 4.2.4 Impact of the Number of Persons on the Radio Channel

An implementation of the TGad channel model has been developed by Maslennikov and Lomayev [Masle10]. It is freely available in terms of MATLAB and C routines [Masle10]. These routines have been extended by the author of this thesis. The functionality of taking into account multiple persons in the conference room scenario has been added, as the available implementation only accounts for a single person. This extended model will

be used to investigate the influence of the number of persons on the channel characteristics. As figures of merit, the RMS delay spread as well as the receive power have been chosen.

Statistics have been derived for these parameters. In a first step, a total number of 40 different angular-dependent channel realizations is generated for the conference room scenario without persons. Then, the influence of human blockage is added to the channel impulse responses according to the procedure described in Section 4.2.3. Altogether, this is done 200 times for each value of $N_{Persons} = [1, 5, 10]$. As the last step, the antenna models included in [Masle10] are applied to the impulse responses. On the one hand, ideal omnidirectional antennas, on the other hand beamforming antennas with half power beamwidths of 10° and 50° have been chosen. In the static scenario without persons, the beamforming antennas are modeled by Gaussian beam patterns steered to the strongest cluster [Malts10d]. In case of the dynamic scenario, two cases are considered. Once the strongest cluster is shadowed by a person, the antenna is directed to the strongest of the remaining clusters. In order to highlight the necessity of beamtracking or beamswitching, the case where the antenna remains fixed on the blocked cluster and is not switched to another cluster is also investigated. Summing up all possible parameter combinations, the results of this study are based on a total number of 128,000 channel impulse responses. Please note that according to a channel bandwidth of 1.76 GHz, a temporal resolution of 0.463 ns has been chosen.

In order to evaluate the impact on the receive power, $\Delta P$ is defined as the difference between the receive power with and without human blockage averaged over the whole channel bandwidth. As an example, Fig. 4.13a shows the CDF of $\Delta P$ for the STA-AP sub-scenario and NLOS channels. Here, omnidirectional antennas have been assumed at the receiver and transmitter side. As expected, human presence causes a decrease of the received power in most of the cases. This decrease gets stronger as well as more likely with an increasing number of persons. For a single person, the power remains unaffected in about 80% of the cases. Regardless of the number of persons, the power is increased by up to 1 dB in very few cases. This happens, when a cluster is blocked which would otherwise destructively interfere with another one. Fig. 4.13b illustrates the mean value as well as the 5%-quantile $Q_5$ of $\Delta P$ assuming different antennas. Besides the facts, that the power decreases with the number of people and that a single person does not affect the channel, other dependencies can be observed here. $\Delta P$ behaves very similarly comparing the omnidirectional antenna and the 10° beamtracking system. The influence of persons is relatively low. In 95% of the cases $\Delta P$ is smaller than 3 dB. When no beamtracking or beamswitching is applied, the average power decrease lies in the same order of magnitude and hence is also low. However, it is noteworthy that in 5% of the cases the received power drops by more than 25 dB. The explanation for this is as follows. When a highly directive antenna is pointed to a single cluster, the situation is that one cluster dominates the channel as the others are mainly suppressed. When the dominating cluster is blocked and the antenna remains directed at this cluster the signal is highly attenuated. However, this happens very rarely. A more probable situation is that clusters already attenuated by the antennas are blocked. These of course do not have a significant influence on the

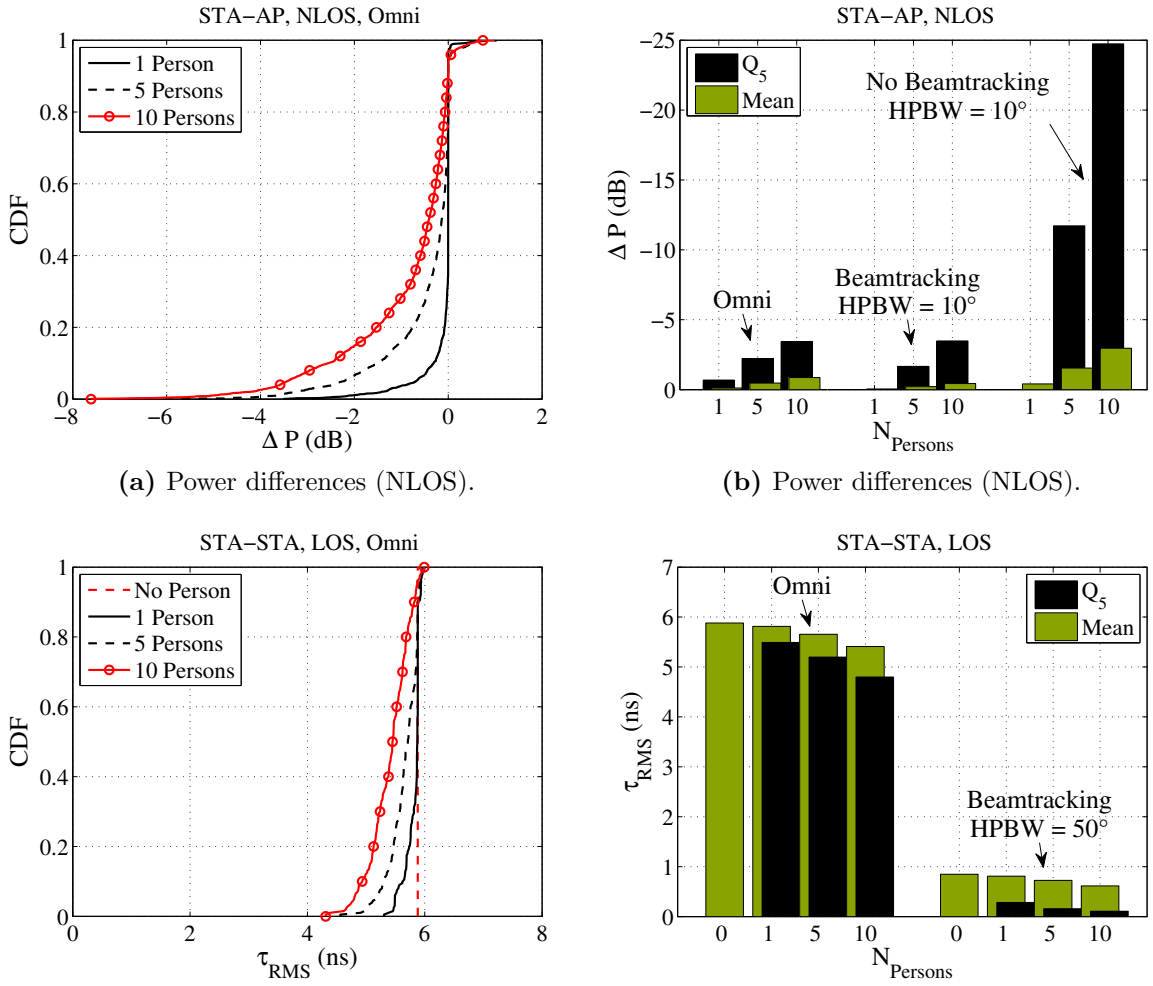


**(a)** Power differences (NLOS).

**(b)** Power differences (NLOS).

**(c)** RMS delay spread (LOS)

**(d)** RMS delay spread (LOS)

**Figure 4.13:** Statistics about the impact of persons on the radio channel.

overall received power. In face of the significantly lower attenuation in the beamtracking case, it becomes obviously that switching to a stronger cluster, which is unaffected by the person is essential to maintain the signal quality.

Fig. 4.13c depicts the RMS delay spread CDF for one exemplary CIR and 200 shadowing realizations. In this case, omnidirectional antennas in the STA-STA scenario under LOS conditions are assumed. The delay spread amounts to 5.9 ns for the case without shadowing. The qualitative characteristics of the CDFs are similar to the behavior of $\Delta P$. The presence of persons in the room leads to lower delay spreads as less significant clusters occur in the impulse response. An increase of the delay spread virtually never occurs. In Fig. 4.13d the omnidirectional case is compared to the 50° beamtracking system. As expected, the absolute delay spread is lower for the antenna with the narrower beam. On average, the delay decreases from 5.9 ns to 5.4 ns and from 0.8 ns to 0.6 ns, respectively. In case of the omnidirectional antennas, the $Q_5$ values are only slightly lower than the

average. In case of the beamtracking antenna, the delay spread is far below the average for 5% of the considered channel realizations. It is noteworthy that a further reduction of the half power beamwidth leads to delay spreads of practically *0*, because then only one single significant multipath component is received. In general, no relevant differences could be observed between the two sub-scenarios.

Other findings that are not illustrated in Fig. 4.13 include the fact that persons do not have a significant influence on the received power in LOS situations. This can be traced back to the fact that in both sub-scenarios the LOS path is not affected by the persons due to geometric reasons as already described in section 4.2.2. In addition, no general differences could be observed between the two sub-scenarios.

To conclude the analysis, path loss and delay spread tend to decrease with the number of persons. This induces that it is definitely important to consider more than one person, as this is a more realistic assumption for a conference scenario.

The disadvantage of the semi-static human blockage model is that it does not account for the time-variance of the radio channel. In order to evaluate adaptive antennas a fully time-variant model is proposed in the next section.

## 4.3 Stochastic Time-Variant Radio Channel Model Based on Human Blockage Measurements

In this section, a time-variant radio channel model is proposed based on a hybrid approach consisting of measurements and the model presented in the last section. The resulting model can e.g. be used as a dynamic 60 GHz radio channel model for system level simulations with MAC protocols. Besides the general functionality of providing the channel access, the MAC layer has a further task in case of 60 GHz systems, namely controlling the beamforming procedure [IEEE809b]. Measurements and simulations have shown that the PHY layer performance will be nearly optimal when using a single MPC cluster due to the resulting flat channel characteristics indicated by low RMS delay spread values (cf. Chapter 3, and [Malts10a, Nicol10]).

Hence, the MAC layer performance is of special interest as the antenna characteristics potentially have to be adapted to the new situation resulting from human blockage. In order to evaluate beamforming strategies of the MAC layer in this case, information about the time-variance is needed. This information is not included in the semi-static model presented in Section 4.2 and hence has to be introduced to the channel model, which will be described in the following. Apart from MAC layer simulations, the model can of course also be used for simulations of the PHY layer.

The section is organized in two subsections. At first, the measurements are discussed and the measurement results are presented. Then, the model for human-induced shadow

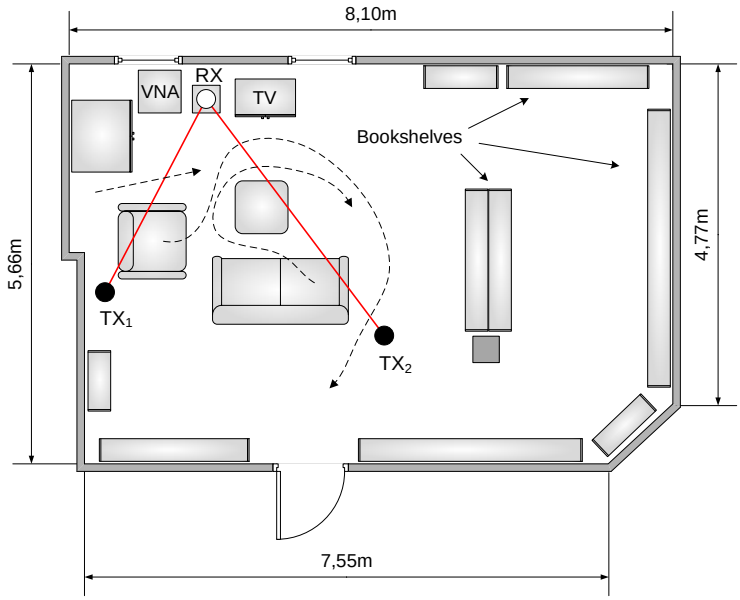


**Figure 4.14:** Schematic of living room scenario with TX/RX positions and walking paths.

fading events in the 60 GHz range as well as its application to MAC layer simulations is proposed.

## 4.3.1 Measurements

### 4.3.1.1 Measurement Setup

The propagation measurements were conducted using an Agilent E8361A vector network analyzer and external transmitting and receiving test heads with WR-10 waveguide flanges. The system has been set up to perform time sweeping with a temporal resolution of 1.3 milliseconds at a single frequency of 67 GHz. For the measurements, vertically polarized circular horn antennas (21 dBi gain) with a half-power beamwidth of 10 degrees have been used at both transmitter and receiver (see Section 3.2.1). The small beamwidth has been chosen in order to measure the influence of the person on one single transmission path only. All measurements have been additionally recorded on video. This has been done in order to analyze the impact of specific movements or the position of the person on the measurements results.

Two different scenarios have been investigated. The first scenario is a living room equipped with typical furniture, where a single person has moved on three different specified walking paths (see Fig. 4.14). The receiver position (RX) was kept fixed close to a television during the measurements, whereas two different transmitter positions ($TX_1$, $TX_2$) were chosen, both assuring LOS conditions. They were placed at a height of 1.10 meters and at a distance of 4.38 m and 2.58 m between TX and RX, respectively. These configura-

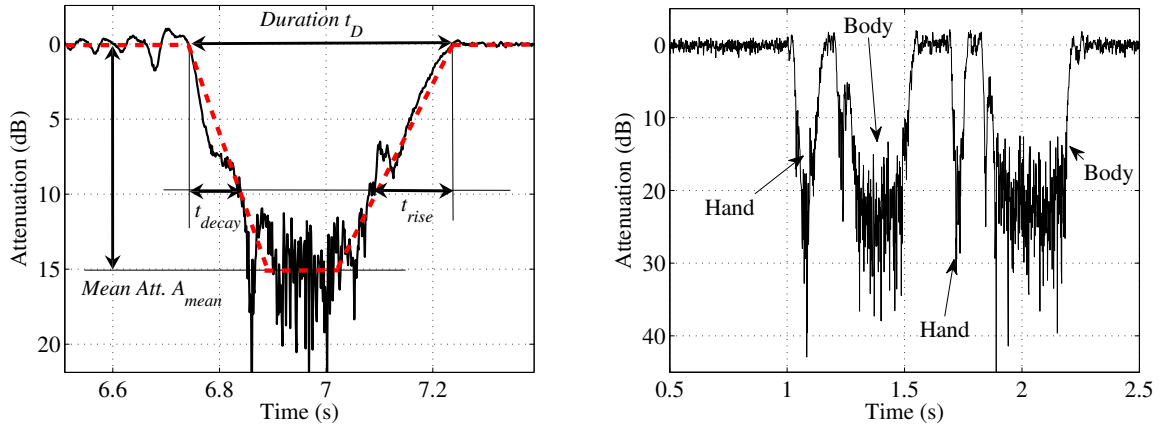


**(a)** Single human-induced shadowing event with definitions and corresponding model.

**(b)** Shadowing events due to the body and the swinging motion of the hand.

**Figure 4.15:** Example for temporal characteristics of human-induced shadowing events in both scenarios.

tions have been chosen in order to emulate a realistic application scenario where a video streaming device (TX) is connected to a television (RX) and a moving person disturbs the transmission link.

In case of a blocked LOS path, a reflection at a wall could be used to maintain transmission. This reflected wave in turn can also be disturbed by people. The behavior in this case was to be examined in the second scenario. The corresponding setup has been already shown in Fig. 4.1a. The measurements were carried out in a conference room. Transmitter and receiver were placed at a height of 0.75 meters on a parallel line at a distance of 2.00 meters to a wall with approximately 10 dB reflection losses. They were separated by 1.50 meters and directed to the specular reflection point at the wall. The person was moving parallel to the wall with different walking speeds and at different distances to the wall.

#### 4.3.1.2 Measurement Results

Fig. 4.15a shows an exemplary shadowing event obtained from measurements (solid line) in the living room as well as the corresponding shape of the model proposed to describe this event (dashed line) (cf. Section 4.3.2.1). In Fig. 4.15b, an example for the temporal characteristics of human-induced shadowing in the reflection scenario is shown. Here, a significant difference between the two scenarios can be recognized. The natural swinging motion of the human hand at higher walking speeds causes shorter fading events before the whole body crosses the propagation path. The reason for the distinct visibility of this phenomenon is the fact that TX and RX are positioned at a lower height than in the

living room and the radio wave interacts with the person at the height of the swinging hands.

Similar to [Collo03a, Collo04, Collo03b], four parameters have been chosen to describe a shadow fading event (see Fig. 4.15a). The duration $t_D$ characterizes the time between the last zero crossing before and the first zero crossing after the shadowing event. The decay time $t_{decay}$ and the rising time $t_{rise}$ specify the time span between the zero crossings of the signal level and a given threshold (10 dB in the figure) in each case. The mean attenuation $A_{mean}$ is calculated in the interval $[\frac{1}{3}t_D < t < \frac{2}{3}t_D]$ and is based on the received power without the influence of the person. The parameters above mentioned have been analyzed statistically based on several hundred measurements.

The results for the living room scenario are shown in Fig. 4.16 in the form of CDFs. The investigations have shown that the drop of signal level happens in the order of tens of milliseconds. In average the signal decreases by 20 dB in 230 ms, whereas it takes 16 ms (61 ms) for a drop of 1 dB (5 dB). In 90% of the cases the signal decrease took at least 4 ms for a 1 dB, 27 ms for a 5 dB and 101 ms for a 20 dB threshold. The duration of a single fading event amounts to 550 ms in average and the mean attenuation $A_{mean}$ lies

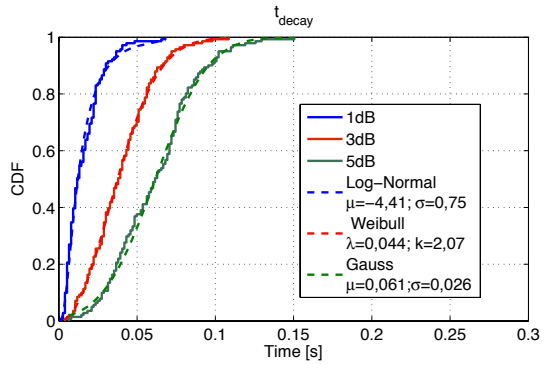


**(a)** CDF of decay time $t_{decay}$.

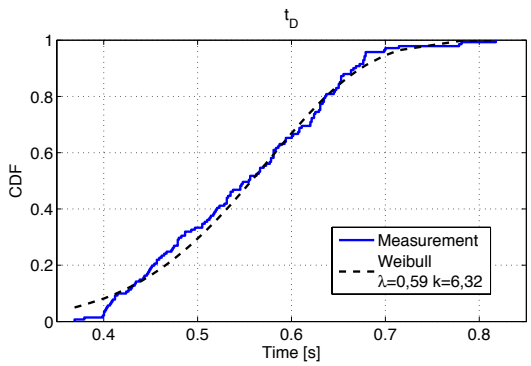


**(b)** CDF of duration $t_D$.

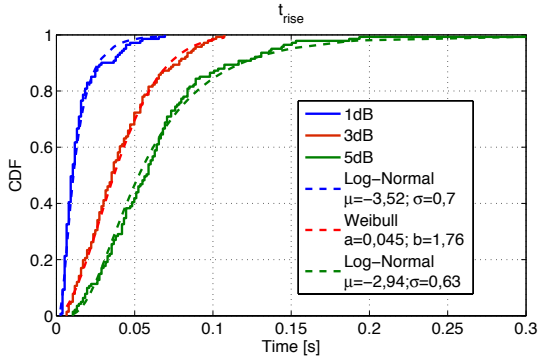


**(c)** CDF of rise time $t_{rise}$.

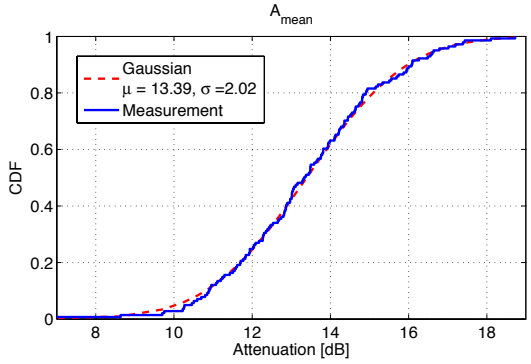


**(d)** CDF of mean attenuation $A_{mean}$.

**Figure 4.16:** CDFs (measurement and model) for the analyzed parameters $t_{decay}$, $t_{rise}$, $t_D$ and $A_{mean}$ in the living room.

| Parameter | Direct path | Reflection |
|---|---|---|
| $t_D$ | 550 ms | 460/150 ms |
| $A_{mean}$ | 13.4 dB | - |
| $A_{max}$ | 26.0 dB | - |
| $r_{decay}$ | 82.0 dB/s | 167 dB/s |
| $r_{rise}$ | 76.9 dB/s | 217 dB/s |

**Table 4.5:** Mean value of the analyzed parameters.

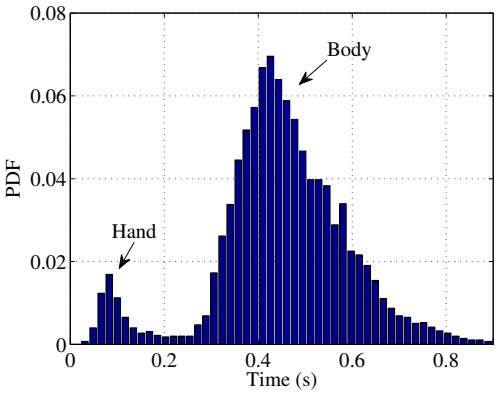


**Figure 4.17:** PDF of the parameter $t_D$ in the conference room.

between 6 and 18 dB, whereas the maximum attenuation $A_{max}$ (not shown) can amount to up to 36 dB. An overview with the mean values of the analyzed parameters can be found in Table 4.5. Please note that here not the rise time and the decay time are listed, but the slew rates based on a 5 dB threshold:

$$r_{rise} = \frac{5dB}{t_{rise}} \tag{4-4}$$

$$r_{decay} = \frac{5dB}{t_{decay}}. \tag{4-5}$$

The results for the conference room scenario are shown in Fig. 4.17 and Fig. 4.18 in the form of CDFs for $t_{decay}$ and $t_{rise}$ and a PDF for $t_D$. The CDFs of $t_{decay}$ and $t_{rise}$ are shown for thresholds of 5, 10 and 15 dB. They have similar shapes as the CDFs for the living room, but the slew rates based on a 5 dB threshold are significantly higher here and amount to 167 and 217 dB/s, respectively. This is caused by the shorter distance between TX and RX and a higher walking speed. In the PDF of $t_D$, the influence of the human hand can clearly be recognized in terms of two maxima. The duration of the events caused by the swinging motion of the hands amounts to 150 ms on average, however, these events occur much less frequently than those caused by the whole body. With a mean value of 460 ms, these events are shorter than in the living room, which is again mainly caused by a higher walking speed, but also by the shorter distance between TX and RX and hence a smaller Fresnel zone.

In order to prove whether the measurement results are reasonable, the temporal parameters can be estimated with the knife edge diffraction theory (see Section 2.1.1.1). When a person steps into the zone given by 0.6 times the radius of the first Fresnel zone, the actual shadowing begins. In case of a distance of 4.38 m between TX and RX, the radius of the first Fresnel zone amounts to 7 cm. Under the assumption of a constant walking

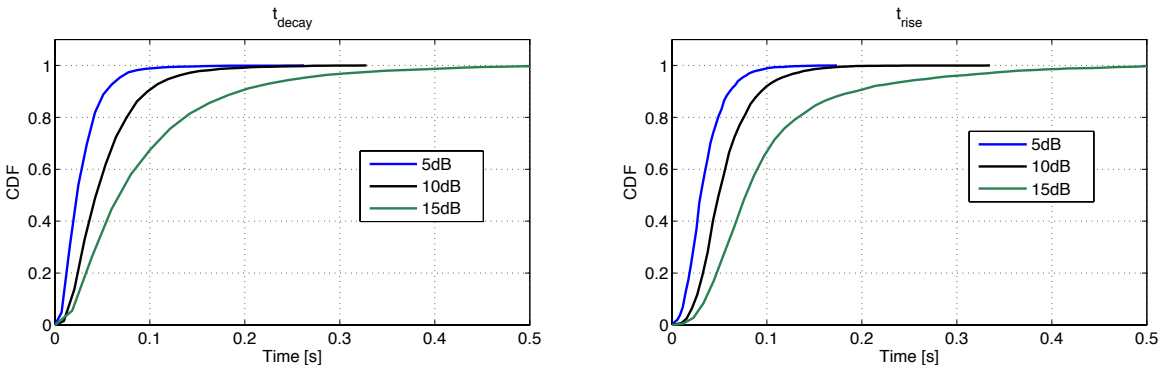


**(a)** CDF of decay time $t_{decay}$ **(b)** CDF of rise time $t_{rise}$

**Figure 4.18:** CDFs of the analyzed parameters $t_{decay}$ and $t_{rise}$ in the conference room.

speed of 0.6 $\frac{\text{m}}{\text{s}}$ it takes 70 ms until half of the first Fresnel zone is occupied by the person. This corresponds to a signal drop of 6 dB and hence a slew rate of 85.6 dB/s, which is very close to the observed value in the living room scenario.

## 4.3.2 Modeling

In order to cover the influence of human-induced channel dynamics in system level simulations that include MAC protocols, both wideband characteristics as well as signal level/SNR degradation may be considered. Therefore, a stochastic model has been developed that is based on the measurement results presented in Section 4.3.1. This model emulates the temporal behavior of human-induced shadowing events.

### 4.3.2.1 Single Shadowing Events

The dashed curve in Fig. 4.15a illustrates the modeling approach for a human blockage event. The shadowing event $A(t)$ in dB scale is in principle modeled by a series consisting of a linearly decaying period, a period with a constant attenuated signal level $A_{mean}$ and a period with a linearly increasing signal level. In case of the increasing and decreasing

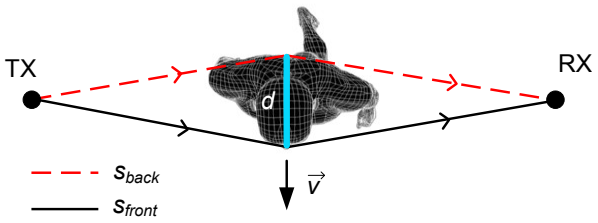


**Figure 4.19:** Geometry for the calculation of the correlated fading..

periods, the agreement between model and experiment is good, whereas the constant period disregards fading around the average. These fluctuations possess a specific profile according to the interference of the two field components diffracted at the front and the back of the human body (cf. Figs. 4.4 or 4.15). From literature various stochastic methods are known to generate correlated fading (see e.g. [Rappa96, Clark68, Young00]). In [Rappa96] for example, a two ray Rayleigh fading model is presented assuming MPCs with statistically independent amplitude and phase. However, this assumption is not valid in the present case since both, amplitude and phase of the field components, are strongly correlated. In order to account for this fact, a deterministic approach is proposed here, which superimposes the two field components under the assumption of a double knife edge crossing a LOS link perpendicularly in the middle (cf. Fig. 4.19). The temporal characteristics then calculates as:

$$\chi\left(t, A_{mean}\right) = \sqrt{10^{\frac{A_{mean}}{20}}}\left(e^{-jks_{front}(t)} + e^{-jks_{back}(t)}\right). \tag{4-6}$$

As a simplification, the amplitudes of the diffracted components are assumed to be equal. Otherwise, more complex electromagnetic calculations would be necessary. This is done in order to apply as few electromagnetic calculations as possible, so that even users without a deep knowledge of radio wave propagation are able to implement the model. Due to this assumption, the constructive interference of both components leads to a minimum attenuation of

$$A_{min} = A_{mean} - 6\text{dB}. \tag{4-7}$$

$s_{front}$ and $s_{back}$ are the lengths of the diffracted rays. The derivation of both is identical with the derivation of the reflected rays given below in Eq. (4-12) and Eq. (4-13):

$$s_{front}\left(t\right) = 2\sqrt{\left(v \cdot t - \frac{1}{2}d\right)^2 + \left(\frac{s}{2}\right)^2} \tag{4-8}$$

$$s_{back}\left(t\right) = 2\sqrt{\left(v \cdot t + \frac{1}{2}d\right)^2 + \left(\frac{s}{2}\right)^2} \tag{4-9}$$

In this case, $t = 0$ corresponds to the middle of the shadowing event where $s_{back} = s_{front}$. In order to achieve realistic values of e.g. fading duration or level crossing rates, the parameters $v, d$ and $s$ have to be carefully chosen. In this context, it is proposed to assume a constant body depth of $d = 0.38\,\text{m}$, which corresponds approximately to the person crossing the propagation paths during the measurements. The walking speed can then be determined from the duration of the shadowing event and the position of the 6 dB level crossings as already described in Section 2.2.2 on page 32:

$$v = \frac{d}{t_D - \frac{6dB}{r_{decay}} - \frac{6dB}{r_{rise}}}. \tag{4-10}$$

**Table 4.6:** Model parameters

| Parameter | Distribution | Distribution parameters |
|---|---|---|
| $t_D(s)$ | Weibull | $\alpha = 0.591, \beta = 6.321$ |
| $A_{mean}(dB)$ | Gaussian | $\mu = 13.4, \sigma = 2.0$ |
| $t_{decay,5\,dB}(s)$ | Gaussian | $\mu = 0.061, \sigma = 0.026$ |
| $t_{rise,5\,dB}(s)$ | Log-Normal | $\eta = -2.94, \sigma = 0.63)$ |

In addition, the parameter $s$ is assumed as the path length of the corresponding MPC. With this knowledge, a complete shadowing event can be described by:

$$A(t) = \begin{cases} r_{decay} \cdot t, & \text{for } 0 \leq t \leq \frac{A_{min}}{r_{decay}} \\ 20 \log_{10} \left( |\chi \left( t, A_{mean} \right)| \right), & \text{for } \frac{A_{min}}{r_{decay}} \leq t \leq t_D - \frac{A_{min}}{r_{rise}} \\ r_{rise} \cdot \left( t_D t \right), & \text{for } t_D - \frac{A_{min}}{r_{rise}} \leq t \leq t_D \\ 0, & \text{else} \end{cases} \tag{4-11}$$

The decay rate $r_{decay}$ as well as the rate of increase $r_{rise}$ can be calculated from the parameters $t_{rise}$ and $t_{decay}$ with Eq. (4-4) and Eq. (4-5). Approximate probability distributions have been derived for all parameters. Therefore, analytical distributions are compared to the experimental results and validated by the Kolmogorov-Smirnov test with a significance level of 1 % [Papou02]. The tested distribution functions are Gaussian, Weibull and log-normal distribution, whereas the one distribution has been chosen which yielded the best Kolmogorov-Smirnov test results. Detailed results of the test are omitted here for the sake of briefness and can be found in [Mbian10]. The type of distribution functions and the corresponding model parameters according to [Papou02] are given in Figs. 4.16a - 4.16d as well as in Table 4.6. In case of the parameters $t_{rise}$ and $t_{decay}$ the values for a 5 dB threshold have been chosen. The actual generation of the channel realizations is discussed next.

#### 4.3.2.2 Coupling with TGad Channel Model

In the previous subsection the generation of single shadowing events has been described. The result is a temporal narrowband characteristic of human blockage. Such a single shadowing event can be further used in system simulations to describe the SNR degradation for example. In order to extend this model to the usability for wideband applications, the coupling with the TGad channel impulse response model is described in the following.

The basic procedure is illustrated in Fig. 4.20. A cluster-based TGad channel realization including the dependency on azimuth and elevation angles $(\theta_{RX}, \phi_{RX}, \theta_{Tx}, \phi_{Tx})$ serves

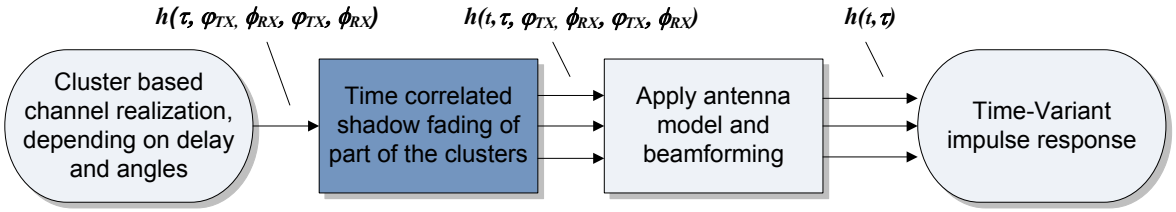


**Figure 4.20:** Flow chart of the procedure for the coupling of the temporal channel characteristics and the TGad channel impulse response model.

as a starting point. The methods presented in section 4.2.3 are used to determine the clusters that are affected by human blockage. In contrast to the semi-static snap shot model in Section 4.2, these clusters are not attenuated independently here, but actually a temporal coupling between the ray-specific shadowing events is taken into account. That way, a realistic time-variant channel impulse response $h\,(t,\tau)$ is generated. An exemplary realization of $h\,(t,\tau)$ for the STA-AP conference room sub-scenario is shown in Fig. 4.21. For the sake of clarity, only the central rays of each cluster are shown. In the following, the generation process is described by means of this example. As defined in [Malts10d], the realization consists of the LOS component and eight MPCs. In this case, the LOS link as well as three MPCs are affected by human blockage.

The generation of $h\,(t,\tau)$ starts with the randomization of $r_{decay}, r_{rise}, t_D$ and $A_{mean}$ according to the PDFs defined beforehand. The geometry and the spatial position of the propagation paths of different clusters are in general dissimilar from each other. Hence, a person induces shadowing events of different shapes, different offsets and end times for each cluster. As a simplification, here the same values of $r_{decay}, r_{rise}, t_D$ and $A_{mean}$ are proposed to be used for all clusters. Nevertheless, a certain correlation between the

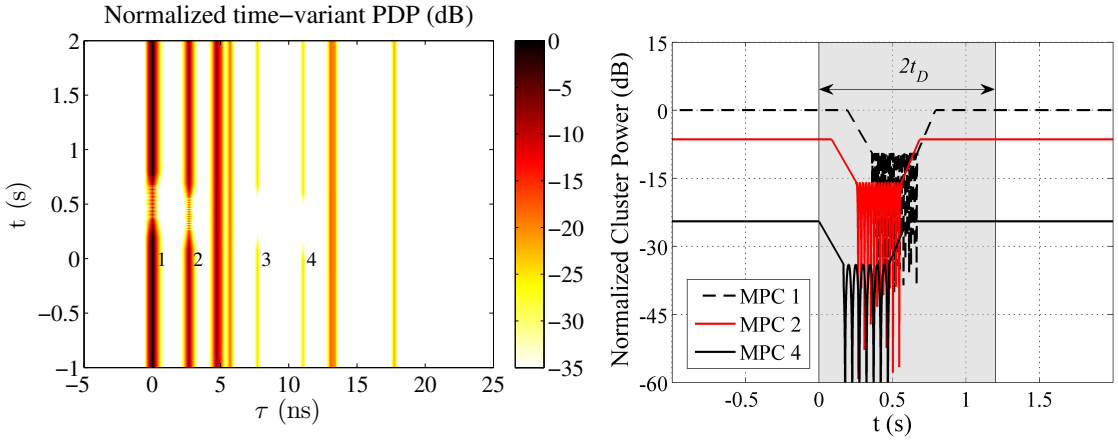


**(a)** Time-variant power delay profile. **(b)** Cluster power.

**Figure 4.21:** Exemplary realization of $h\,(t,\tau)$.

shadowing events of different clusters is expected. This could be taken into account by analyzing and modeling the relation between the temporal and amplitude characteristics for different clusters based on simulations in the future. Of course the model complexity will increase significantly as in general all four parameters are correlated in dependence of the geometry. However, the simplified case has the advantage, that all shadowing events have to lie in the interval $[0; 2t_D[$. Otherwise they would not overlap. In order to achieve a temporal shift of the clusters relative to each other, the offset time is randomized according to a uniform distribution between 0 and $2t_D$. The temporal shift can be very well recognized in Fig. 4.21b, where the shadowing events of three of the four blocked clusters are shown. In this figure, the cluster power is normalized to the unobstructed case of the LOS power.

As stated before, the length of each multipath component is used to determine the fading characteristics according to Eq. (4-11). This leads to fading with different periods between minima and maxima (see Fig. 4.21b). In Chapter 2 it has been shown, that the phase of a shadowing event changes rapidly over time in the shadow region (cf. Fig. 2.16, page 34). In order to account for this behavior, it is proposed to not only use the amplitude, but also the phase characteristics of Eq. (4-11) for $\frac{A_{min}}{r_{decay}} \leq t \leq t_D - \frac{A_{min}}{r_{rise}}$.

The attenuation of clusters yields a set of impulse responses $h\left(t, \tau, \theta_{RX}, \phi_{RX}, \theta_{Tx}, \phi_{Tx}\right)$. After this, antenna models and beamforming algorithms can be applied to the correlated channel realizations, so that angle-independent impulse responses $h(t, \tau)$ are obtained. Please note that an ideal omnidirectional antenna has been assumed for the example in Fig. 4.21 .

Usually, MAC layer simulations are based on a power/SNR basis, not involving wideband channel simulations as they are too time-consuming [Lan11, Perge11]. Hence, the receive power/SNR can be easily calculated from the time-variant impulse responses, if needed. Another rather simplified alternative to the mentioned process would be using Eq. (4-11) for the direct calculation of the SNR characteristics. Of course, $h(t, \tau)$ can also be used in PHY layer simulations to test the robustness of baseband algorithms in the presence of a varying channel.

## 4.4 Doppler Effect

In this thesis, the application scenarios consider transmitters and receivers without the movement of the devices themselves. Nevertheless, human activity may lead to a Doppler shift due to time-variant multipath components diffracted or reflected at moving persons. In the mm-wave range, this behavior has already been treated in literature theoretically [Smuld09,Smuld95,Yang08b,Yang07] as well as experimentally [Bulti98,Morai04,Ander02]. Nevertheless, a direct comparison between measurement results and simulations cannot be found and is presented here for the first time.

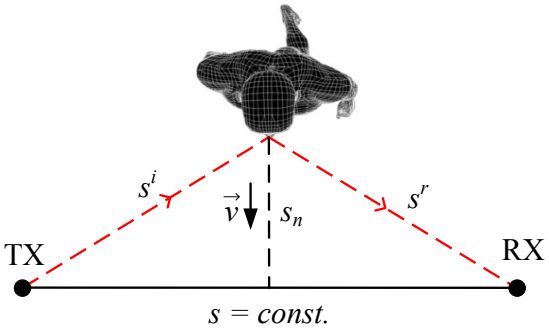


**Figure 4.22:** Geometry for the calculation of the Doppler shift.

In order to estimate the maximum expected Doppler shift, a worst case scenario is examined here, namely a person perpendicularly crossing the LOS link in the middle with walking speed $v$. A schematic with all required geometrical parameters is shown in Fig. 4.22. Due to the movement of the person, the value of $s_n$ varies with time:

$$s_n(t) = -v \cdot t \tag{4-12}$$

In this symmetrical example, the the ToA of the multipath component reflected at the front of the person can be derived with its length $s_{r+i}$ taking into account the geometry:

$$s_{r+i}(t) = 2s^i(t) \tag{4-13a}$$

$$= 2\sqrt{s_n^2(t) + \left(\frac{s}{2}\right)^2} \tag{4-13b}$$

$$= 2\sqrt{(v \cdot t)^2 + \left(\frac{s}{2}\right)^2}. \tag{4-13c}$$

The ToA of the reflection at the back, after the person has walked through the ray is determined analogously. Please note that Eq. (4-13) is only valid before and after the actual shadowing event. Additionally, the term $v \cdot t$ has to be corrected by the body width, which is omitted in the equation to support ease of reading. In the analysis, $t = 0$ is defined in the middle of the shadowing event. Fig. 4.23a and Fig.4.23b depict enlargements of the LOS MPC from the time-variant measurements presented on page 81 together with a simulation according to the UTD (see section 2.1.1.3). Additionally, the ToA characteristics expected according to Eq. (4-13) are shown as a dashed line. For the simulations, the cylinder radius as well as the walking speed have been determined from the length of the shadowing event as described in section 2.2.2. The UTD simulations are carried out in frequency domain for the same frequency range that has been used in the measurements. Afterwards, the results are transformed to the time domain via IFFT. Here, the same postprocessing procedure (oversampling, Kaiser windowing) as for the measurements has been applied. In the measurements quasi omnidirectional antennas have been used.

The simulated PDP agrees quite well with the measured one. In both PDPs, the LOS component as well as the hyperbolic characteristic of the MPC reflected at the body is

visible. Close to the actual shadowing event both components interfere, leading to fluctuations of the amplitude. It is noteworthy that the MPCs diffracted around the body are expected close to $t = 0$, but could not be resolved in the measurements due to the limited temporal measurement resolution. Reasons for occurring deviations between measurement are twofold. On the one hand, the perfect reflectivity of the assumed metallic body does not account for reflection losses due to clothing, for example. In addition, the walking speed in the simulation is assumed to be constant. This was also only approximately the case during the measurements and also causes deviations.

Additionally, Fig. 4.23c illustrates the suppression of the reflected MPC by directive antennas. There, Gaussian beam patterns [Malts10d] with half power beamwidths of 20°

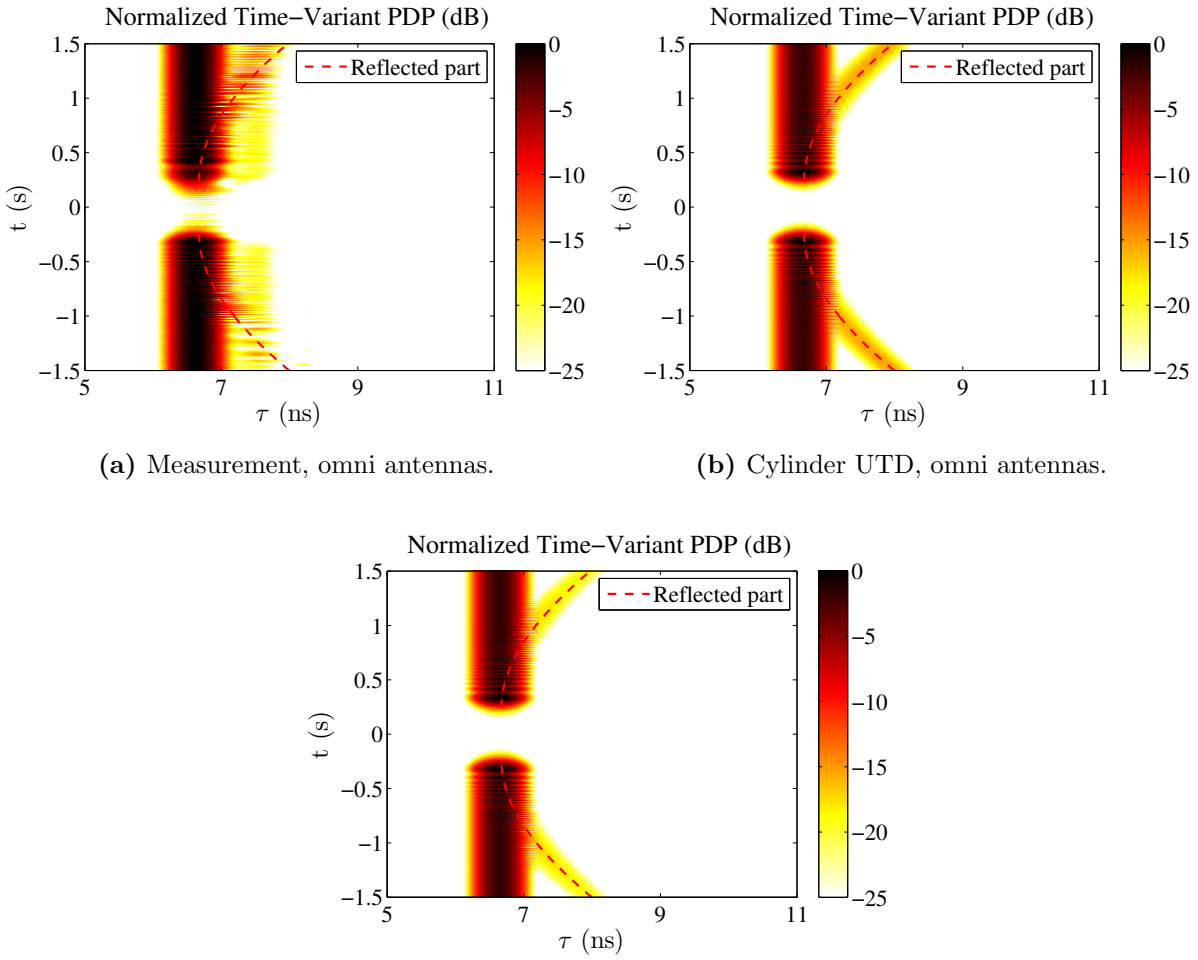


**(a)** Measurement, omni antennas.

**(b)** Cylinder UTD, omni antennas.

**(c)** Cylinder UTD, horn antennas.

**Figure 4.23:** Time-variant PDPs based on broadband measurements and simulations taking into account only the LOS component (MPC 1).

have been used in the UTD simulations. This will be additionally analyzed below together with the discussion of the Doppler shift.

The Doppler shift of the reflected MPC depends on the change of length of $s_{r+i}$. This change is the derivative with respect to time:

$$v_{r+i}(t) = \frac{ds_{r+i}(t)}{dt} \tag{4-14a}$$

$$= \frac{2v^2t}{\sqrt{(v\cdot t)^2 + \left(\frac{s}{2}\right)^2}}. \tag{4-14b}$$

With this knowledge, the time-variant Doppler shift can be determined according to [Molis05]:

$$\nu_{Doppler}(t) = -\frac{f_c \cdot v_{r+i}(t)}{c} \tag{4-15a}$$

$$= -\frac{2v^2tf_c}{c\sqrt{(v\cdot t)^2 + \left(\frac{s}{2}\right)^2}} \tag{4-15b}$$

The maximum absolute Doppler shift in this case occurs for $t \to \infty$, because then the change in length of $s_{r+i}$ is maximal. It hence calculates as:

$$max\{|\nu_{Doppler}(t)|\} = \lim_{t\to\infty} \frac{2v^2tf_c}{c\sqrt{(v\cdot t)^2 + \left(\frac{s}{2}\right)^2}} \tag{4-16a}$$

$$= 2\frac{f_c \cdot v}{c} \tag{4-16b}$$

Under assumption of a carrier frequency $f_c = 60\,\text{GHz}$ and a walking speed of $3\frac{m}{s}$, a maximum Doppler shift of 1.2 kHz would arise (c.f. [Smuld09]). It is noteworthy that in indoor environments, more complex scenarios appear. On the one hand, different MPCs will have different Doppler shifts. On the other hand, higher Doppler shifts can occur in case of multiple reflections at the human body and additional objects like walls or furniture. In addition, the movement of different persons relative to each other will also lead to higher Doppler shifts. As higher order MPCs simultaneously exhibit higher losses, nevertheless, the given case of a person crossing the direct path between TX and RX will definitely have the highest impact.

The evaluation above is only valid in LOS situations. During shadowing, the Doppler shift is induced by the change in length of the diffracted rays around the body. In case of the UTD, these changes correspond to the lengths $s' + w_1 + s^d$ and $s' + w_2 + s^d$ in Fig.2.2b on p. 12. Here, the analytical derivation of the Doppler shift is not possible as the geometrical parameters for the UTD are determined numerically (see Section 2.1.1).

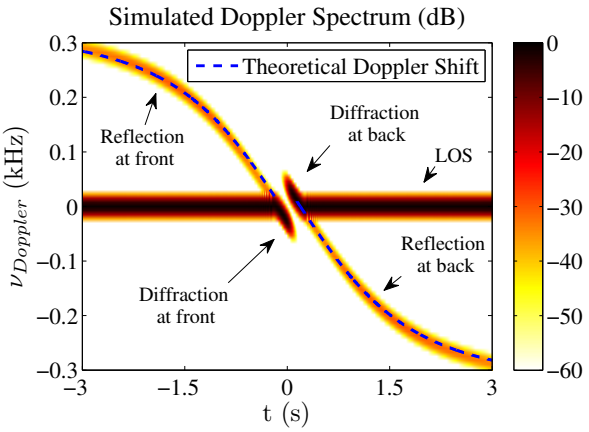


**(a)** Cylinder UTD, omni antennas.

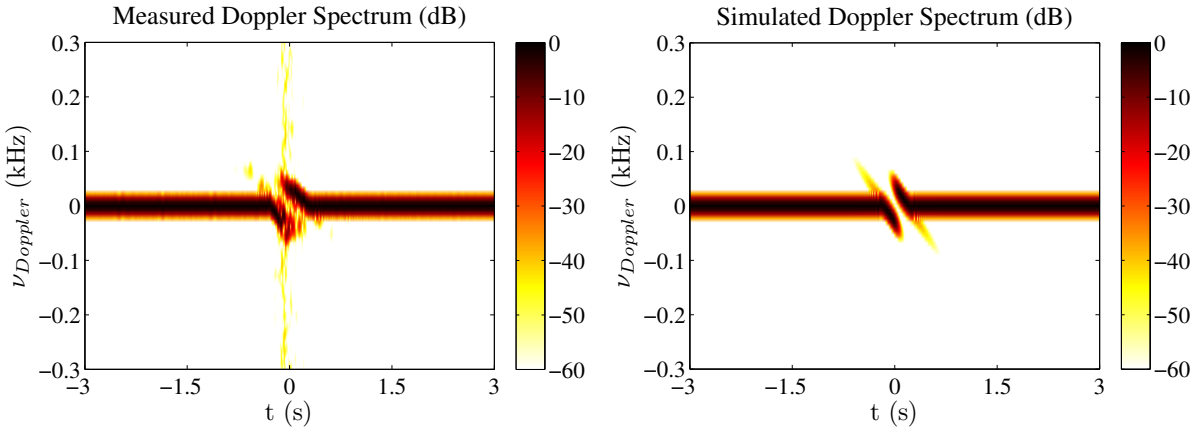


**(b)** Measurement, horn antennas.

**(c)** Cylinder UTD, horn antennas.

**Figure 4.24:** Time-variant PDPs based on narrowband measurements and simulations.

Fig. 4.24a depicts the time-variant Doppler spectrum derived from simulations assuming omnidirectional antennas. The Doppler spectrum $P_B(\nu_{Doppler})$ is calculated as the Fourier transform of the time correlation function $R_H(\Delta t)$ of the time variant transfer function $H(t)$ [Molis05]. For the calculation of $R_H(\Delta t)$, a time window of 66 ms has been used corresponding to a distance of about $10\,\lambda$ in order to fulfill the assumption of wide-sense stationarity. In addition, a Hamming window has been applied before the Fourier transform. A cylinder radius of 19 cm and a walking speed of $v = 0.75\,\frac{\mathrm{m}}{\mathrm{s}}$ have been assumed for the UTD simulations. TX and RX have been separated by 2.63 m. Here, the narrowband measurements as described in Section 4.3 form the basis for the investigations. According to Eq. (4-15), a maximum Doppler shift of 335 Hz is expected. It is noteworthy that due to the limited temporal resolution components of the Doppler spectrum will be slightly broadened. In the figure, a strong Doppler component is observed for $\nu_{Doppler} = 0$, coming from the time-invariant LOS component. Only in the shadowing area around $t = 0$, this component slightly shifts to values of a few ten Hz. This behavior is caused

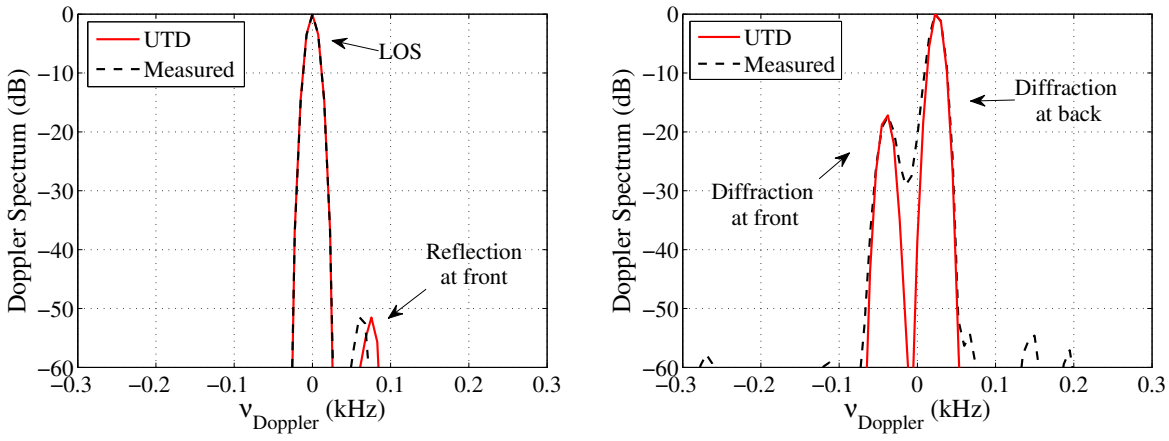


**(a)** Reflection region (t = -0.64 s). **(b)** Shadowing region (t = 0.03 s).

**Figure 4.25:** Modeled and simulated Doppler spectra for exemplary snap shots.

by the change in length of the diffracted rays around the body mentioned above. The reflected MPC causes a Doppler shift that decreases with time according to Eq. (4-15). As expected, the function tends to converge to the value of 335 Hz. In the corresponding measurements (Fig. 4.24b), this component disappears very fast, when the person moves away from the LOS link. The explanation for this is that here directive horn antennas have been used suppressing the reflected MPC (c.f. Fig. 4.23c). Accordingly, the antennas also suppress components in the Doppler spectrum. For the sake of completeness, Fig. 4.24c shows the UTD simulation results employing the Gaussian beam patterns. As expected, in this case, the simulations agree very well with the measurements.

In order to emphasize the difference between the shadowing region and the reflection region, Doppler spectra are shown for two exemplary snapshots in Figs. 4.25a and 4.25b. In the reflection region, the constant LOS link leads to a narrow component around $\nu_{Doppler} = 0$ dominating the Doppler spectrum. The reflection at the front of the moving body causes another bell-shaped peak at 75 Hz in the measurements, according to an instantaneous change of the MPC length of $v_{r+i} = 0.34\frac{m}{s}$. In the simulations this peak is slightly shifted to higher values of $\nu_{Doppler}$. For both simulation and measurement, this peak lies more than 50 dB below the LOS peak. This again can be explained by the assumption of a human body with circular cross section and a constant walking speed of the person. Please be aware that the bell shape of the Doppler spectra is induced by the postprocessing of the measurement and simulation data, i.e. the Fourier transform and the calculation of the time correlation function. Theoretically, infinitesimal peaks should be expected. In the shadow region, diffraction at the front as well as diffraction at the back of the person contribute to the Doppler spectrum. Here, measurement and simulation agree very well. Due to the fact that the LOS is blocked in the shadow region, here the component at $\nu_{Doppler} = 0$ does not exist. As expected, both Doppler components are slightly shifted away from $\nu_{Doppler} = 0$ to negative and positive values of a few ten Hz.

## 4.5 Concluding Remarks

In this chapter, three different channel models have been presented for the modeling of human blockage, namely a deterministic time-variant model, a stochastic semi-static model and a stochastic time-variant model. In addition, the Doppler effect has been investigated by simulations and measurements.

- At the beginning of the chapter, the coupling of the multiple knife edge model with ray tracing simulations has been presented. The MKE has already been described in Chapter 2 and has been extended in this section with the blockage of reflected multipath components. The methodology has been validated with wideband real-time channel sounder measurements. With this tool, it is possible to realistically model the time-variance of the broadband 60 GHz indoor radio channel.
- Based on this validated human blockage model, a semi-static human blockage model for the *IEEE 802.11ad* 60 GHz channel model has been developed. The model is intended to describe the influence of human movement on the 60 GHz channel. It is based on ray tracing simulations, the multiple knife edge model and a random walk model. A statistical analysis within a conference room scenario has demonstrated that different clusters can be blocked simultaneously. Due to geometrical reasons the LOS cluster is never blocked in this specific scenario. The maximum power attenuation can be up to 50 dB under usual conditions but as high as 60-70 dB in the worst case. However, the average values in the shadowing zone lie between 10 and 18 dB. To conclude, the presented model can be used to introduce the human blockage influence to cluster-based 60 GHz channel models in a realistic way.
- The model has also been extended with the functionality of taking into account up to ten persons. Remarkably, this extension, which introduces more realistic conditions, could be achieved without an increase of the model complexity. Additionally, the influence of the number of persons has been investigated. To conclude the analysis, both the path loss and delay spread tend to decrease with the number of persons. Therefore, it is definitely important to consider more than one person.
- Results from a dynamic 60 GHz channel measurement campaign have been presented. The investigations have shown that the drop of signal level happens in the order of tens of milliseconds. The measurements in a LOS scenario using directive antennas have revealed the following results. The 60 GHz signal decreases on average by 20 dB in 230 ms, whereas it takes 61 ms for a drop of 5 dB. The duration of a single fading event amounts to 550 ms on average and the mean attenuation $A_{mean}$ lies between 6 and 18 dB. The investigations have also shown that the shadowing event is not symmetrical as well as dependent on the walking speed and that even the swinging motion of the human hand can have a significant influence on the radio propagation channel. Similar findings are known from literature. Nevertheless, the targeted analysis of a single multipath cluster and the coupling with a channel impulse response model are shown for the first time in this thesis. Based on the measurement results, a full parameter set for the modeling of human-induced

shadow fading events and their application in system simulations with MAC protocols are provided. With this model time-variant 60 GHz channel realizations can be generated, which are valuable for the system design of beamforming/-steering systems for example.

- In addition, the Doppler shift due to human activity has been investigated. Time-variant Doppler spectra have been derived from simulations as well as from channel measurements. A comparison reveals that the Doppler behavior at 60 GHz can be reproduced with the cylinder UTD. Relevant Doppler components are estimated to lie in the order of 1 kHz at maximum. The measurement results have approved that directive antennas suppress the influence of multipath power as well as the Doppler spread on the signal quality. As such antennas are most likely to be deployed, the influence of the Doppler spread on 60 GHz wireless systems can be expected to be negligible for nomadic devices.

The models presented here will now be used to show how diversity techniques could help to overcome the challenges of human blockage.

# 5

# Antenna Diversity - Overcoming the Challenges of Human Blockage

In the previous parts of this thesis it has been shown that human activity has a significant influence on the spatio-temporal radio channel characteristics at 60 GHz. Furthermore, the impact on the performance of wireless 60 GHz systems has been already indicated. In this chapter, methods to counter the problem arising from human activity are analyzed. Therefore, two studies are presented which evaluate the capability of antenna diversity techniques to combat the human induced shadowing. These techniques are:

1. Beamforming based on antenna arrays,
2. Macro diversity with multiple TX/RX antennas.

As shown in Chapter 3, the 60 GHz indoor radio channel is rich of MPCs. From the measurement results presented there, it is known that once and even twice reflected MPCs, if not blocked, may experience lower losses than the LOS component blocked by a person. Beamforming based on antenna arrays can be used to enhance the receive power by utilizing these MPCs when the LOS connection is blocked. Concurrently, the antenna arrays provide the high gain that is necessary to overcome the high free space loss at 60 GHz. Macro diversity provides methods to mitigate shadow fading by using multiple antennas at TX and/or RX, which are separated by a sufficient distance. For example, two receive antennas could be used to establish two potential LOS links. When one link is blocked, the other one may still be available. In both cases, the validated deterministic wideband modeling approach as described in Section 4.1 has been used, which combines the calibrated RT with the MKE human blockage model. This way, the evaluation of the diversity techniques under realistic conditions is possible.

Please note that parts of the work presented in this chapter have been published already by the author in [Jacob11b, Jacob13a]. The antenna data used for the study in Section 5.1 was kindly provided by the Institut für Hochfrequenztechnik (IHF) in Braunschweig and NXP Semiconductors in Eindhoven. The chapter is divided into three parts. The studies

on beamforming and macro diversity are presented in Section 5.1 and 5.2. Section 5.3 concludes the chapter.

## 5.1 Beamforming to Overcome Human Blockage

It is commonly agreed that beamforming/-steering is an appropriate instrument to overcome the high free space attenuation in the mm-wave region (see e.g. [IEEE809b]). With beamforming antennas it is possible to achieve a high gain and a large virtual beamwidth at the same time. The cost for this is an antenna system with a much more complex signal processing compared to conventional systems employing only passive mostly omnidirectional antennas (e.g. IEEE802.11a/b). In contrast to the conventional systems with single antennas at TX and RX special importance must be paid to the antenna design process. Besides the radiation characteristics, additionally the beamforming has to be optimized on the hardware side and on the software side respectively. The beamforming has the goal of adapting the radiation characteristics to changing radio channel conditions which can occur due to human blockage or a movement of TX or RX for example. In turn, the modified radiation characteristic leads to a different overall channel response. Hence, time-variant double directional channel models in realistic environments are necessary to evaluate the beamforming performance. In this section, the deterministic channel model from Section 4.1, which takes into account human blockage, is combined with link budget calculations for modulation and coding schemes (MCS) of the IEEE802.15.3c standard [IEEE809b]. Based on this the performance of different antennas is evaluated in the living room environment.

The section is organized in three parts. At first, the antennas and their characteristics are introduced. Then, the RT simulations and the coverage calculations are described. In the third subsection the results are presented.

### 5.1.1 Antennas Under Consideration

In the following, three different planar antennas as well as an ideal half-wave dipole, providing an omnidirectional reference, will be analyzed. The planar antennas have been realized by the IHF and NXP for hardware demonstrators in the framework of the Qstream project (see Fig. 5.1). A fully polarimetric three-dimensional characterization of the antennas has been carried out using HFSS. The antenna gain patterns are depicted in Fig. 5.1c and 5.1d. Here, only the azimuth characteristics are shown, because the elevation characteristics have no major impact on the evaluation results. The first antenna is a planar dipole with a ground plane reflector [Spell12]. The second antenna is a planar dipole array consisting of two single elements also with a ground plane reflector. These antennas have a gain of 8.2 and 9.6 dBi. A HPBW of 70° and 77° in the azimuth plane and 55° and 51° in the elevation plane have been determined. The third antenna is a planar 8×4 patch array

with the capability of beamswitching in the azimuth plane. Here, four different beams can be selected by choosing a different feed port of a Rotman lens [Herre10b]. The single beams have a gain of 15 dBi and a HPBW of 19° in the horizontal and 17° in the vertical plane. Altogether, the four beams lead to a virtual HPBW of 104° (see Fig. 5.1d). Please note that the gain within the virtual HPBW decreases by more than 3 dB at some angles. A detailed description of the antenna geometries and designs is omitted here, because the

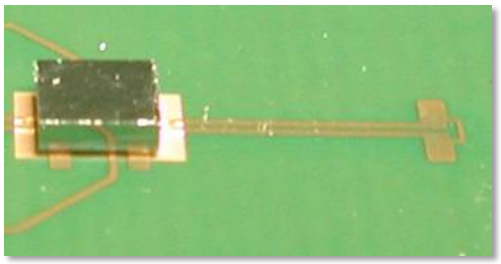

**(a)** Planar dipole antenna [Spell12].

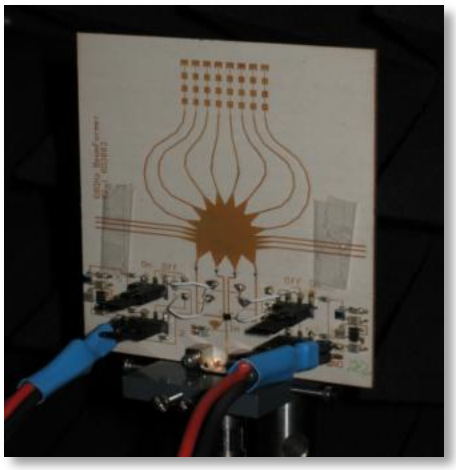

**(b)** Rotman lens antenna. Taken from [Herre10a].

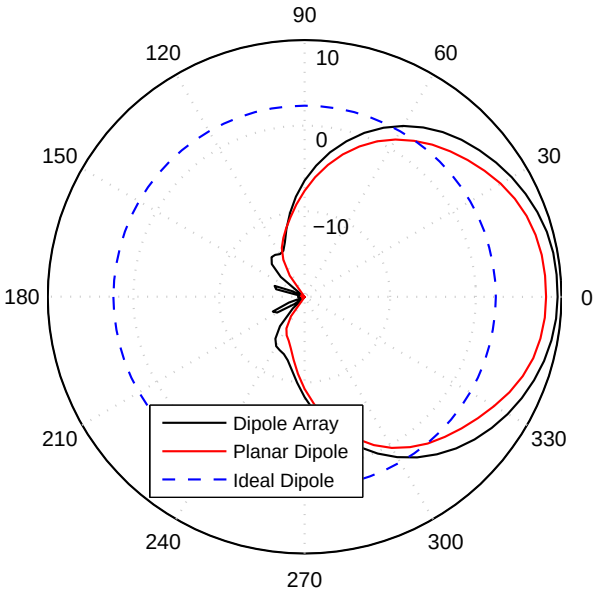


**(c)** Gain of the dipole antennas (dBi).

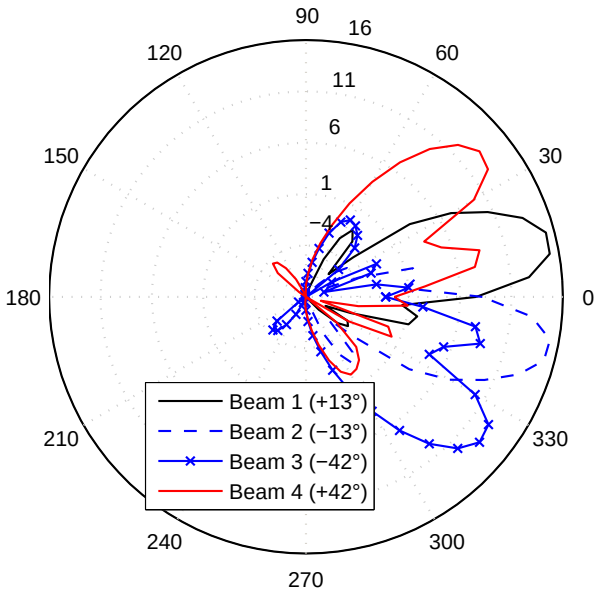


**(d)** Gain of the Rotman lens antenna (dBi).

**Figure 5.1:** Patterns of the analyzed antennas in azimuth domain.

focus of the section lies on the evaluation methodology and the performance assessment under realistic conditions.

### 5.1.2 Ray Tracing Simulations and Coverage Calculations

In order to analyze the coverage in the living room scenario, ray tracing simulations have been performed. The receiver (for instance a TV set) has been kept fixed in space. Channel impulse responses (CIR) have been determined for 2183 different transmitter positions equally spaced within the whole room. All further calculations are performed considering the entire scenario. Both the furnishing as well as all dimensions of the room can be found in Fig. 3.16a on page 60. The polarization of the antennas as well as polarization changes along the propagation paths are taken into account. The same antennas are used at both transmitter and receiver. The TX antennas are located 0.9 m above the floor emulating devices connected to the TV, whereas the RX antenna is located at a height of 1.4 m. The RX antenna has a fixed orientation in -$y$-direction. The TX antennas always point to the direction of the RX. To both antennas, no elevation tilt is applied. For the Rotman lens antenna all 16 possible combinations of the four beams have been used in the ray tracing simulations.

In addition to the scenario without human presence, the human blockage model is applied to the ray tracing results. Here, a scenario is assumed where one person stands directly between TX an RX and hence blocks the LOS connection in any case, but also attenuates other clusters. The influence of the person on the CIR is modeled according to the multiple knife edge model as described in Section 2.2.1.4. It is noteworthy that the term NLOS in the following explicitly corresponds to positions that are shadowed by furniture and not by a person. Following this definition approximately 25 % of the links correspond to NLOS links.

From the ray tracing the propagation loss ($L_p$) is calculated by a non coherent summation of the MPC power. In addition, the Rician *k-factor* has been extracted [Simon05]. This parameter is a measure for the multipath richness of the CIR. Propagation loss maps for all analyzed antennas can be found in Fig. 5.2. In case of the Rotman lens antenna, the TX/RX beam combination with the lowest loss has been chosen. Here, the apparent unsteadiness in the propagation loss map can be traced back to the Rotman lens antenna patterns in the elevation plane. The relatively high losses of all antennas close to the TV can be attributed to the different heights of the TX and RX antennas and the fact that no down tilt has been used. From $L_p$ the signal-to-noise-ratio (SNR) is calculated according to:

$$SNR = P_{PA} - L_p - L_{RF} - NF - N, \tag{5-1}$$

where $P_{PA}$ is the output of the power amplifier at the transmitter in dBm, $L_{RF}$ are losses in the RF front ends, $NF$ is the receiver noise figure and $N$ is the thermal noise power in dBm according to the channel bandwidth of 2.16 GHz. The parameters $L_{RF}$ and $NF$ are kept fixed to values of 3 dB and 7 dB which is in line with a 45 nm CMOS process. The

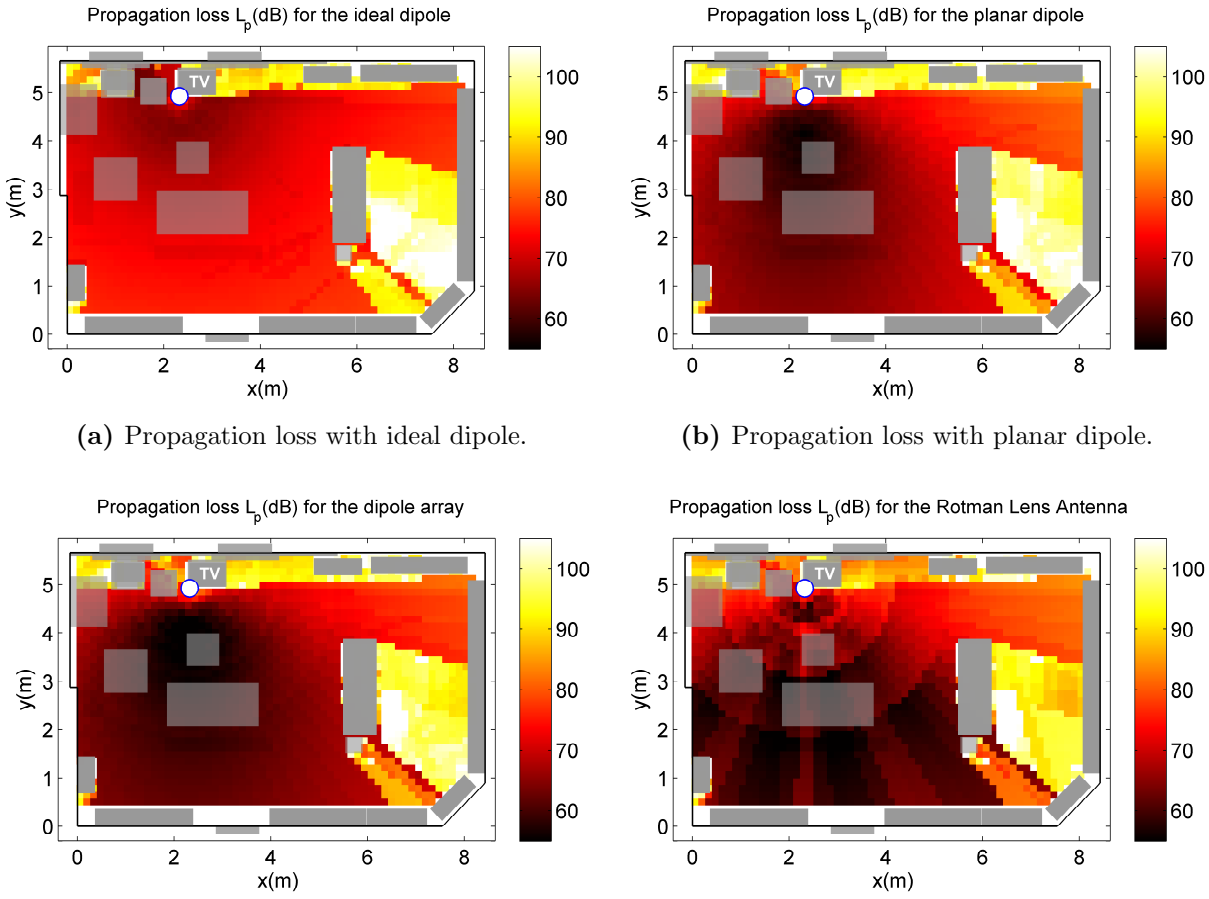


**(a)** Propagation loss with ideal dipole.

**(b)** Propagation loss with planar dipole.

**(c)** Propagation loss with planar dipole array.

**(d)** Propagation loss with Rotman lens antenna.

**Figure 5.2:** Propagation loss maps for the different antennas.

SNR and the *k-factor* are used to determine the BER for each TX position and the MCS *6, 8, 12* and *13* of the IEEE802.15.3c standard. These MCS employ BPSK, QPSK, 8-PSK and 16-QAM with LDPC forward error correction (FEC) (code rates 1/2 or 3/4). In order to account for small-scale effects, analytical expressions for the BER performance in Rician fading channels have been used ( [Simon05], p.252ff.). It is noteworthy that these expressions do not account for any FEC. In order to nevertheless consider this it is assumed that a certain BER is necessary before the error correction to guarantee quasi error free communication. Unless otherwise indicated this threshold is set to a value of $10^{-2}$. TG3c has also defined an error rate criterion for the different MCSs [IEEE809b]. While their requirements assume AWGN conditions, they are nevertheless slightly more restrictive as they assume higher noise figures and implementation losses.

For the Rotman lens antenna an ideal beamswitching procedure is assumed, i.e. the TX/RX beam combination with the lowest BER is always chosen. Depending on the *k-factor* and the MCS, the required SNR typically lies between 4 and 23 dB for a BER of $10^{-2}$ before any error correction [Simon05]. The coverage probability $p$ is defined as the

ratio between the number of TX positions with a BER lower than the defined threshold and the number of all TX positions.

### 5.1.3 Evaluation Results

The coverage within the scenarios is analyzed by varying the transmit power $P_{PA}$ as well as the BER threshold and by comparing the different MCS. In Fig. 5.3a the coverage without human blockage is depicted as a function of output power. In this case the output power is varied between 0 and 25 dBm for a BPSK modulation (*MCS 6*). The upper limit of 25 dBm has been chosen because this leads to the maximum allowed average EIRP (40 dBm) for wireless 60 GHz systems based on the gain of the Rotman lens antenna. In general, the coverage increases with increasing power. In the case without human blockage the coverage for the three planar antennas is similar. Nevertheless, at certain coverage values the dipole array and the Rotman lens antenna outperform the other antennas by up to 5 dB. At power values above 12 dBm the ideal dipole behaves like the planar dipole array, whereas below this value the ideal dipole coverage decreases rapidly. This is due to the fact that lower transmit powers lead to a smaller range because of the low antenna gain in case of the ideal dipole. In addition, the CIRs in this case exhibit significantly more MPCs, which leads to lower *k-factors* and hence a further performance degradation. For higher transmit powers there is no significant difference between the three dipole, since NLOS areas cannot be covered regardless of the antenna type for the reason of too high propagation losses. This is also clearly visible in the figure, as the curves tends to converge to a value of 75 % which corresponds to the fraction of LOS positions in the room. Only the Rotman lens antenna is able to cover part of the NLOS areas. Fig. 5.3b

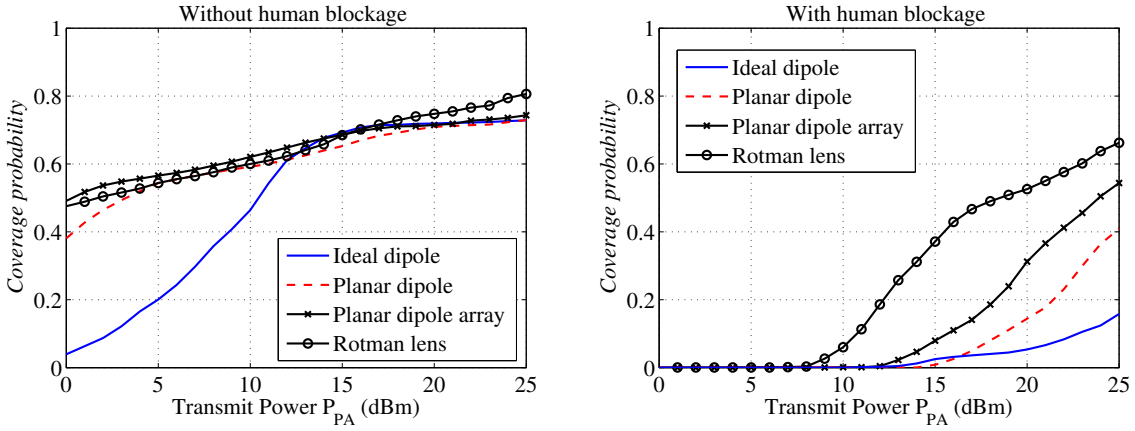


**(a)** Without human blockage.

**(b)** With human blockage.

**Figure 5.3:** Output power dependency with and without human blockage for BPSK.

shows the influence of the human blockage. The coverage is generally lower than without human blockage, because the presence of a person can diminish the SNR by up to 30 dB and in addition leads to lower *k-factors*. Both aspects contribute to a higher bit error rate. The figure clearly shows that up to a power of 8 dBm no coverage is achieved at all. At higher powers, a clear ranking according to the gain of the antennas is observed. Here, the Rotman lens antenna shows its strength of having a large virtual beamwidth paired with a high gain.

The trends described above are also observed when the coverage in LOS and NLOS situations without human blockage is compared. Here, an output power of 14 dBm is assumed, which is feasible with 60 GHz CMOS technology [Zhao11]. Fig. 5.4 shows this comparison

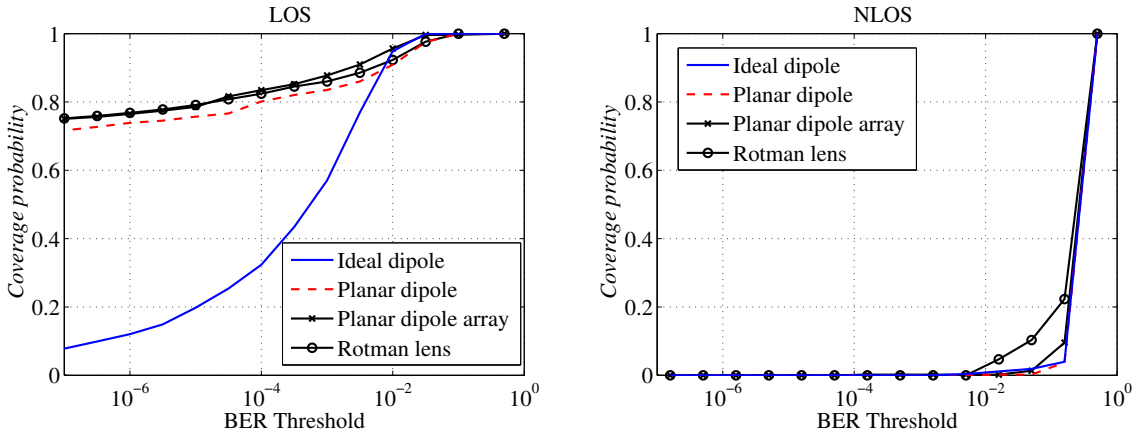


**(a)** LOS. **(b)** NLOS.

**Figure 5.4:** Influence of BER threshold on coverage (BPSK) for LOS and NLOS situations and a transmit power $P_{PA}$ of 14 dBm without human blockage.

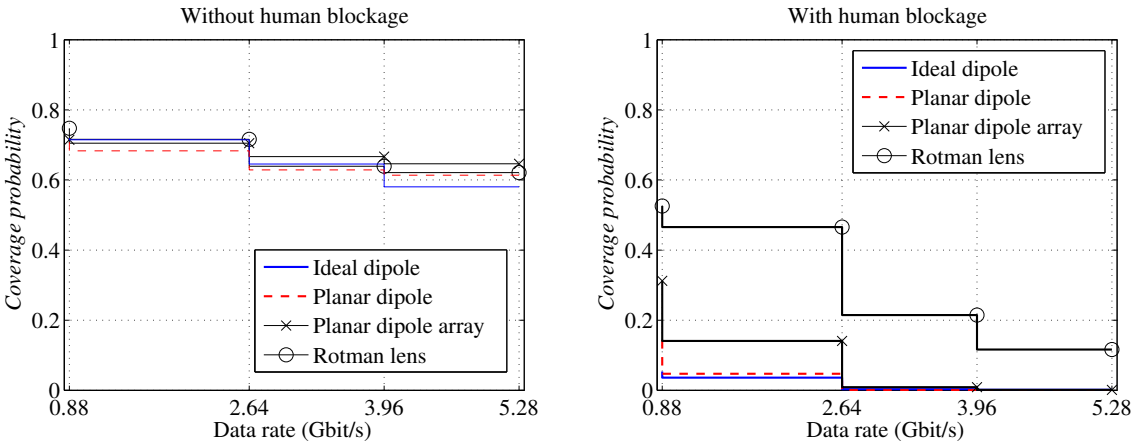


**(a)** Without human blockage. **(b)** With human blockage.

**Figure 5.5:** Coverage for different MCS ($P_{PA}$ = 20 dBm, BER threshold: $10^{-2}$).

as a function of the BER threshold. In LOS situations, again a similar behavior of all planar antennas can be observed, whereas the ideal dipole shows a significantly worse performance for stricter BER requirements. The reasons for this have been given already above. At the reasonable threshold of $10^{-2}$ before error correction all antennas achieve a good performance covering between 90 and 95% of the room. In NLOS situations, all antennas have a very low coverage probability, which shows that either higher transmission powers or higher antenna gains are necessary.

In Fig. 5.5a the coverage is compared for the different MCS assuming an output power of 20 dBm. In the case without human blockage a data rate of 880 Mbit/s is achieved at approximately 70% of the positions in the room. The coverage drops to 60% at a data rate of 5.28 Gbit/s. The difference between the antennas is 3% at maximum. In the case with human blockage, the Rotman lens antenna again outperforms the other antennas, but the coverage is very low for all types of antennas, especially for the multi-gigabit rates. Even the Rotman lens is not capable of covering more than 11 % of the whole room , with persons affecting the transmission links. This supports the conclusion already drawn above that an antenna gain even as high as 15 dBi is not sufficient. This holds true especially in situations where no LOS connection exists or the LOS path is shadowed by a person.

## 5.2 Macro Diversity to Overcome Human Blockage

Macro diversity provides techniques to mitigate large-scale fading, which is created by shadowing effects [Molis05]. Hence, these techniques are suitable to combat the severe human-induced shadowing at 60 GHz. The term macro diversity implies a relatively large distance between the redundant antennas. For example in [Garci10c, Schul11, Flame02] it is proposed to install multiple access points or repeaters at different locations to cover even small indoor and in-cabin environments. The results, which are derived from measurements as well as simulations, demonstrate the performance increase. However, further analyses are required as the considered scenarios focus on typical WLAN scenarios only and the simulation approach in [Schul11] e.g. lacks models for human movement. In contrast to the mentioned literature, macro diversity is investigated here for constellations, where the diversity antennas are placed in one and the same device, e.g. in a flat panel display. Especially for video streaming applications, this seems to be a realistic approach. It is noteworthy that the intention of this section is to solely study possibilities for the maximization of the SNR at the RX by means of macro diversity. Micro diversity techniques and space-time codes may also be employed at 60 GHz in order to mitigate small-scale fading effects [Luo12]. However, they do not lie within the scope of the thesis as they have no potential to overcome human induced shadowing.

For the evaluation, the concept of *selection diversity* is chosen [Molis05]. Here, two or more antennas are applied at the RX device and the antenna with the *best* signal is selected for reception. The term *best* here corresponds to the selection criterion, which

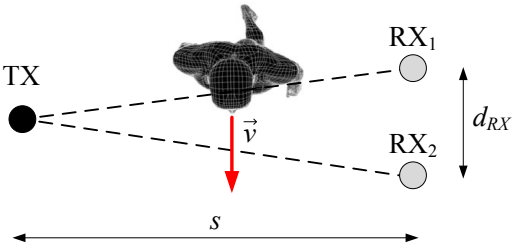


**(a)** Person crossing a link with a single TX antenna and two RX antennas.

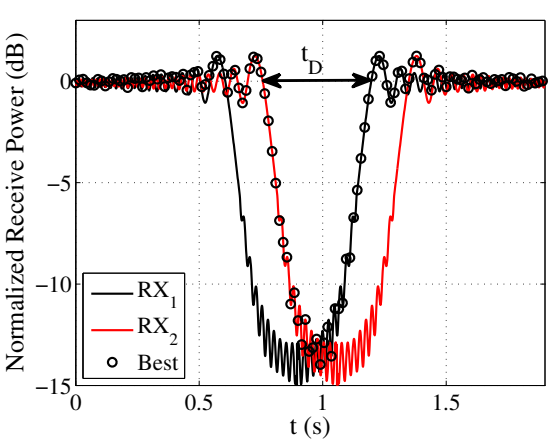


**(b)** Normalized receive power.

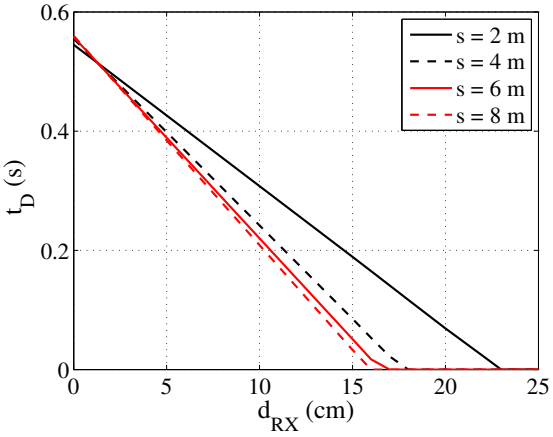


**(c)** Duration of shadowing events.

**Figure 5.6:** Example of a person crossing a LOS link with one TX antenna and two RX antennas.

can be based for example on the highest receive power or the lowest BER. In principle, this technique requires only one RF chain if the receive power is used as selection criterion. Then, the power is monitored before downconversion and demodulation[1]. Furthermore, the analysis of this scheme allows statements about the sole diversity gain isolated from the array gain. The general idea behind the concept is illustrated in Fig. 5.6. Allowing for a quantitative evaluation of macro diversity the scenario depicted in Fig. 5.6a is studied. Here a person crosses the direct path between a TX and a RX with two antennas. For geometric reasons, two temporarily shifted shadowing events can be observed at the RX antennas (cf. Fig. 5.6b). Applying selection diversity leads to a foreshortening of the human-induced shadowing event, as can be recognized well in the figure.

The influence of the antenna spacing $d_{RX}$ and of the distance $s$ on the duration $t_{D,0dB}$ is additionally depicted in Fig. 5.6c. The parameter $t_{D,0dB}$ is defined as the duration of the shortened shadowing event. As expected, larger antenna spacings lead to a decrease of $t_{D,0dB}$, whereas larger values of $s$ lead to an increase of $t_{D,0dB}$. The shadowing can be

[1]Please note that it may be easier to implement the monitoring and multiplexing of the signals at an intermediate frequency, which would make it necessary to realize parts of the RF chain more than once.

suppressed totally for antenna spacings of 15 to 23 cm depending on the distance between TX and RX.

In the following sections, a more comprehensive analysis will be presented based on RT and the MKE model.

### 5.2.1 Evaluation Methodology and Scenario Description

In this section, the performance benefit of macro diversity is evaluated in a realistic time-variant scenario. The evaluation methodology is the same as the one used to derive the stochastic channel model in Section 4.2, i.e. RT simulations in combination with the MKE model. Human activity is taken into account with independent random walks of up to ten persons. All simulations have been conducted within the conference room scenario, which has been introduced in Chapter 3. A schematic of the room can be found on page 48. As dielectric material parameters, the calibrated values from Tab. 3.6 have been used.

A time span of 60 seconds with a resolution of 50 ms is simulated. This ensures that the random walk of each person covers the entire room and that all relevant large scale effects can be resolved. As small-scale effects would impair the evaluation results, the receive power of a snapshot CIR is determined by a non-coherent power summation of the MPCs. In addition, a moving temporal averaging over 3 sampling points has been applied to the time-variant data.

The evaluation focusses on $1 \times 2$ receive diversity (see Fig. 5.7a). Here, two receive antennas, separated by the distance $d_{RX}$ are positioned at the upper frame of the TV. As

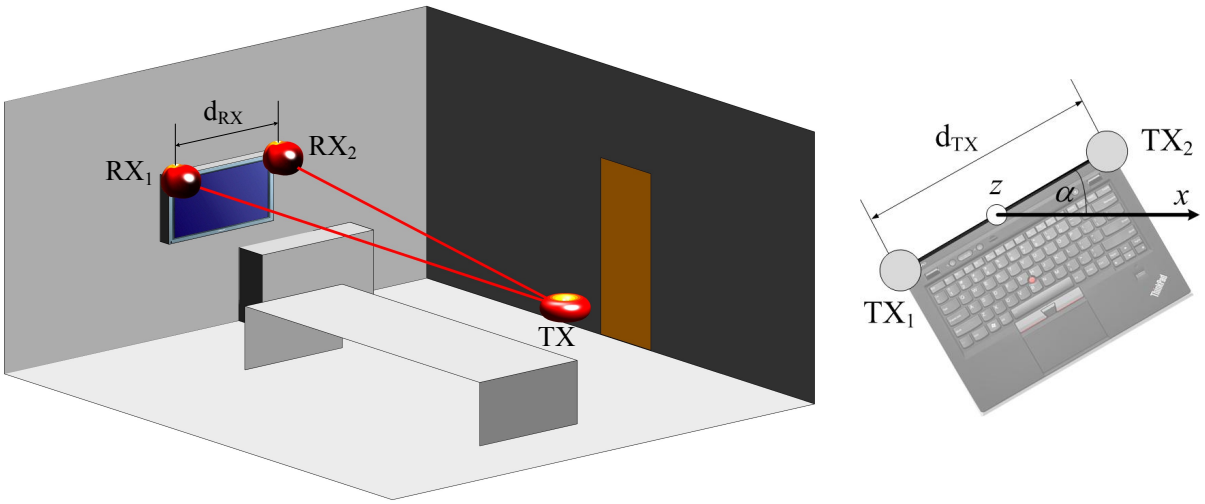


**(a)** RX diversity. **(b)** TX Diversity.

**Figure 5.7:** Illustration of the RX diversity simulation scenarios and diversity transmitter in top view.

before, the active RX antenna is selected according to the highest receive power among the two. In order to get statistically meaningful results, the TXs are distributed uniformly within the whole room at 25 different positions at a height of 1 m. This scenario reflects a situation where nomadic devices stream video data to the TV.

Additionally, chosen results are presented for $2 \times 1$ transmit diversity. In this case, the separation of the antennas ($d_{TX}$) is limited to values of 25 cm and below (see Fig. 5.7b). Higher distances are not feasible for nomadic devices like e.g. laptops, tablets or smartphones. In contrast to the fixed TV, nomadic devices can have a random angular orientation, which reduces the performance benefit. In order to take this into account in the statistics, the misalignment angle $\alpha$ is varied between 0° and 90°. Please note that, if the transmit power is distributed equally to all TX antennas and suitable signal processing techniques are applied, the TX diversity gain is the same as for RX diversity [Molis05].

At the RX, 6 dBi open-ended waveguides have been assumed. These have been already described in Section 3.2.1.2. As they are positioned close to the wall, they illuminate almost the entire room. At the TX, ideal half-wavelength dipoles (2.16 dBi) have been chosen because their omnidirectional radiation characteristics make the TX power insusceptible to antenna misalignment. With this configuration, a 4 m LOS link with a transmit power of 10 dBm would lead to a receive power of about -62 dBm. This meets the requirements of the sub-gigabit MCSs defined in the IEEE802.11ad standard for example [IEEE812]. In order to enhance the link budget to multi-gigabit data rates, higher gain in combination with beamforming is necessary. However, conventional antennas have been chosen as the goal of this study is to analyze macro diversity solely. Otherwise beamforming gain could not be separated from diversity gain.

## 5.2.2 Evaluation Results

### 5.2.2.1 Loss and Diversity Gain

In order to analyze the advantage of macro diversity statistics are compiled based on the time-varying receive power for the RX positions within the entire room. The case without diversity is taken as reference, i.e. position $RX_1$ in case of RX diversity and position $TX_1$ in case of TX diversity.

Fig. 5.8 shows the statistics of the human-induced shadow attenuation. The statistics are based on random walks of a single person. The influence of the number of persons will be analyzed later. Please note that only situations are taken into account where the signal level without diversity would drop by more than 3 dB. Hence, the CDF for this case has its minimum at exactly this value. It increases approximately linearly until it reaches 7.5 dB, which corresponds to a probability of 91%. Afterwards, the curves flattens out and reaches its maximum at 11.8 dB. In Chapter 2 and 4 it has been shown that a single MPC can experience far higher losses due to human shadowing. However, in this scenario

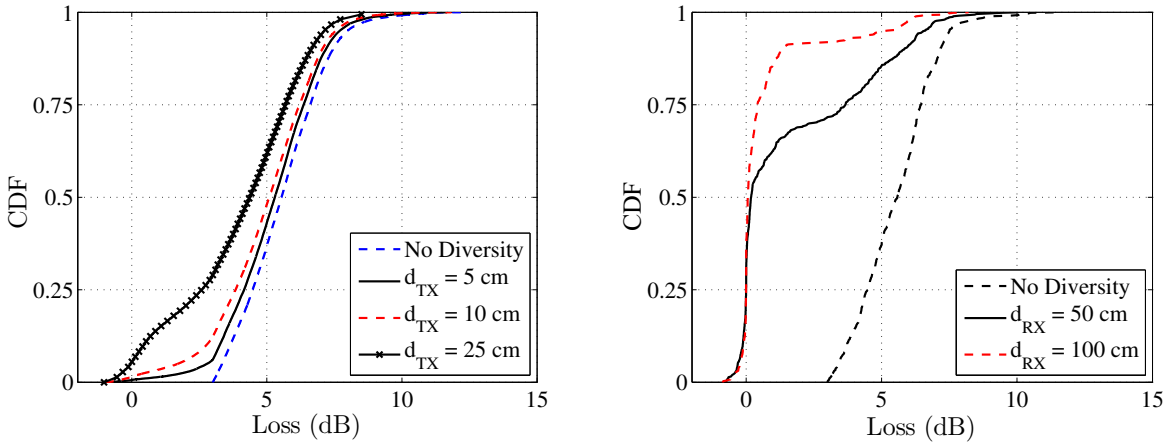


**(a)** TX diversity. **(b)** RX diversity.

**Figure 5.8:** Attenuation distribution of the losses caused by a single person.

the broad antenna beams at both ends of the communication link guarantee that power is received from MPCs, which are not affected by the person.

Transmit diversity as well as receive diversity lead to an decrease of the losses. As expected, higher antenna separations lead to lower losses. RX diversity is able to fully remove shadowing in 50% of the cases, regardless of the antenna separation. The losses are in general higher for TX diversity because of the smaller antenna separations. This is aggravated by the fact that the effective antenna separation is reduced due to the angular misalignment. Please note that for both kinds of diversity negative loss values occur, which corresponds to the situation before a shadowing event, where the reflected power from the human body adds up to the total received power.

In a next step, the diversity gain is analyzed. It is defined as the difference of the receive power with and without diversity. Statistics about the diversity gain are shown in Fig. 5.9. In general a non-zero gain can be expected in at least 50 % of the time. This can be illustrated by looking at Fig. 5.6b. The actual shadowing event for $RX_1$ starts at approximately $t = 0.6\,s$ and ends at $t = 1.2\,s$. Hence the duration amounts to about 0.6 s. Before and after this event, the receive power at $RX_1$ and $RX_2$ is not significantly different and diversity provides no gain at all. However, between $t = 0.6\,s$ and $t = 0.9\,s$ $RX_2$ provides a higher receive power than $RX_1$. Hence, diversity provides a gain in 50 % of the time. This percentage even increases with larger antenna separations. Then, the red curve is shifted to the right. In the best case, the shadowing events do not overlap, which leads to a gain in 100 % of the time. The CDF in Fig. 5.9a shows that TX diversity provides a non-zero gain in 85 % of the simulated cases respectively. However, transmit diversity with separations of 5 cm and 10 cm provides only marginal benefits. The separation of 25 cm leads to slightly better results, but also provides gains of 3 dB or more in only 20 % of the cases. Due to the higher antenna separation, the performance of RX diversity is better. In case of $d_{RX} = 100\,cm$ for instance, a non-zero gain is achieved in 96 % of the

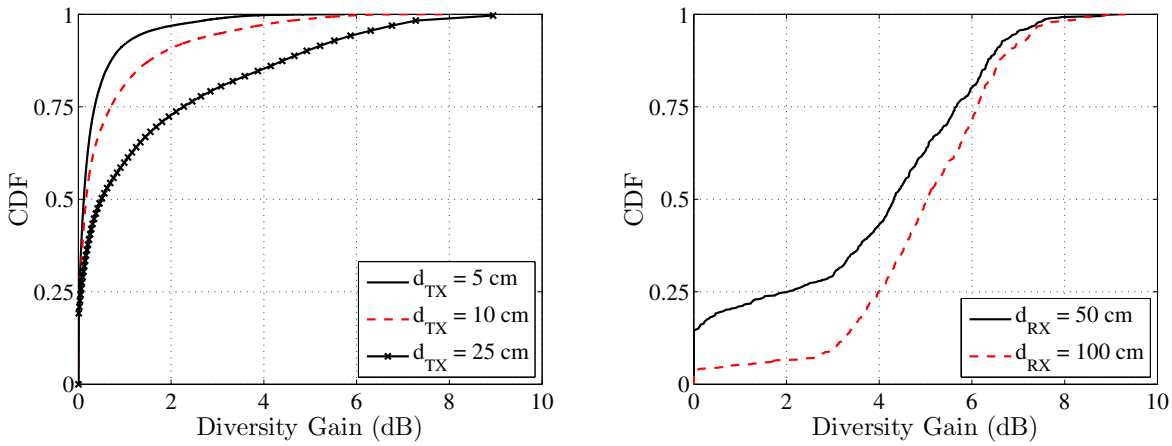


**(a)** TX diversity. **(b)** RX diversity.

**Figure 5.9:** Distribution of the diversity gain.

**Table 5.1:** Average loss and diversity gain in dB.

| | **TX Diversity** | | | **RX Diversity** | | **No Diversity** |
|---|---|---|---|---|---|---|
| | **5 cm** | **10 cm** | **25 cm** | **50 cm** | **100 cm** | |
| Loss | 5.5 | 4.8 | 3.8 | 1.7 | 0.6 | 5.6 |
| Diversity Gain | 0.3 | 0.7 | 1.5 | 3.8 | 4.9 | - |

cases and in 91 %, the gain is already higher than 3 dB. The average values of the loss and the diversity gain are summarized in Table 5.1. It is noteworthy that the benefits of diversity will increase under the assumption of directive antennas. On the one hand, the human-induced loss may become higher, which has been shown already in Section 4.2.4. This is caused by the fact that MPCs which are unaffected by the person, may be suppressed by the narrow antenna pattern. Additionally, the number of shadowing events, which are fully removed will not significantly change.

#### 5.2.2.2 Influence of the Number of Persons

The analyses above are based on simulations with one person only. Here, the dependency on the number of persons is studied. The simulations have been performed at a single TX position in the lower left part of the room. RX diversity with an antenna separation of 100 cm is assumed. In Fig. 5.10a attenuation distributions are shown under the assumption of three, six and ten persons. It can be recognized that the loss only slightly varies with the number of persons. For example, the average attenuation increases by 0.1 dB to 0.4 dB per person with and without diversity. Similar to the results with one person only, the diversity reduces the losses. This also evident in the CDF of the diversity gain which is

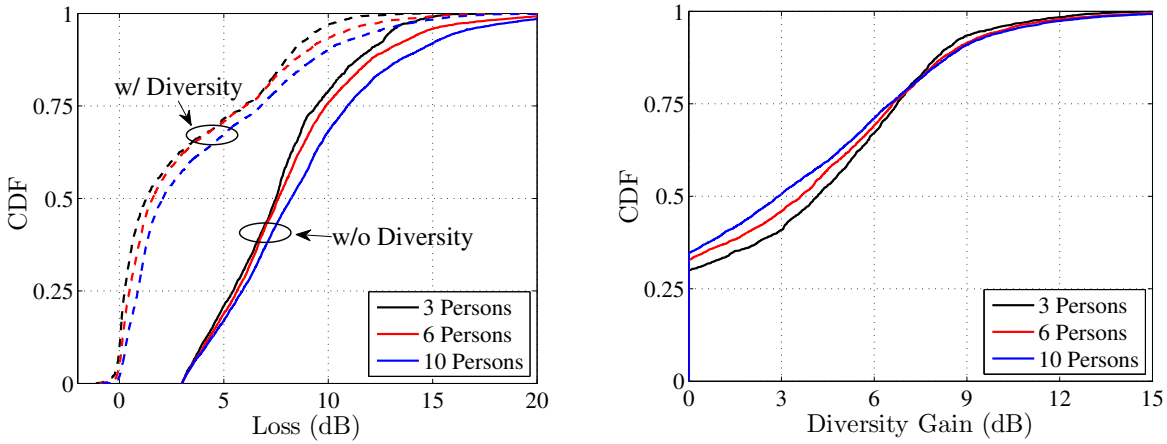


**(a)** Attenuation. **(b)** Diversity Gain.

**Figure 5.10:** Distributions of attenuation and diversity gain and the influence of the number of active persons.

shown in Fig. 5.10b. The gain is similar for all numbers of persons and amounts to 3.7 dB to 4.0 dB in average. In about 30 % of the time no gain can be achieved. Please note that these results cannot be compared directly to the ones in Fig. 5.9b as the data base is not the same.

As already shown in Chapter 4, the probability that a single MPC is attenuated strongly depends on the number of persons in a scenario. This will be discussed together with an analysis of the duration of shadowing events next. Fig. 5.11 illustrates the dependency of the relative blockage time (RBT) on the number of persons. In the investigated scenario, the proportion of time where a single link is affected by a single person amounts to 5 % only. Affection in this regard corresponds to a signal level drop of 3 dB and more. Without diversity, the RBT increases to 39 % when ten persons are active within the room. As the comparison between the RBT characteristics with and without diversity shows, a significant advantage can be achieved by macro diversity regarding the link availability. Regardless of the number of persons, the RBT is more than halved by using diversity.

Another countermeasure which could be used against time-variant human blockage, is to buffer (video) data in a higher layer. Therefore, it is interesting to know the duration of as well as the time between succeeding shadowing events. As mentioned above, a shadowing event is defined as a period of time where the loss does not fall below a value of 3 dB in this Section. CDFs for both the duration $t_{D,3dB}$ and the time between shadowing events $t_{B,3dB}$ are shown in Fig. 5.12 for three and ten active persons, respectively. The duration $t_{D,3dB}$ mostly lies between almost 0 and 3.1 s. As expected, diversity generally leads to a shortening of the shadowing events.

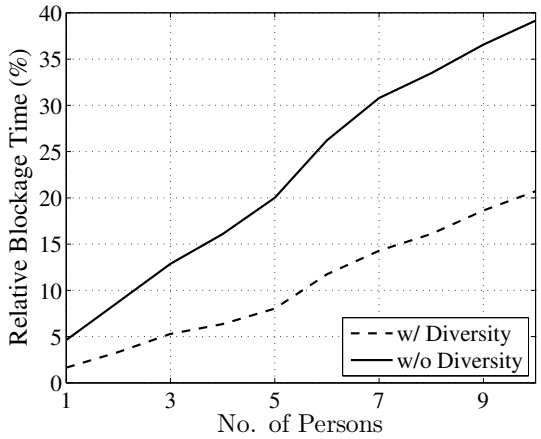


**Figure 5.11:** Relative blockage time in the scenario.

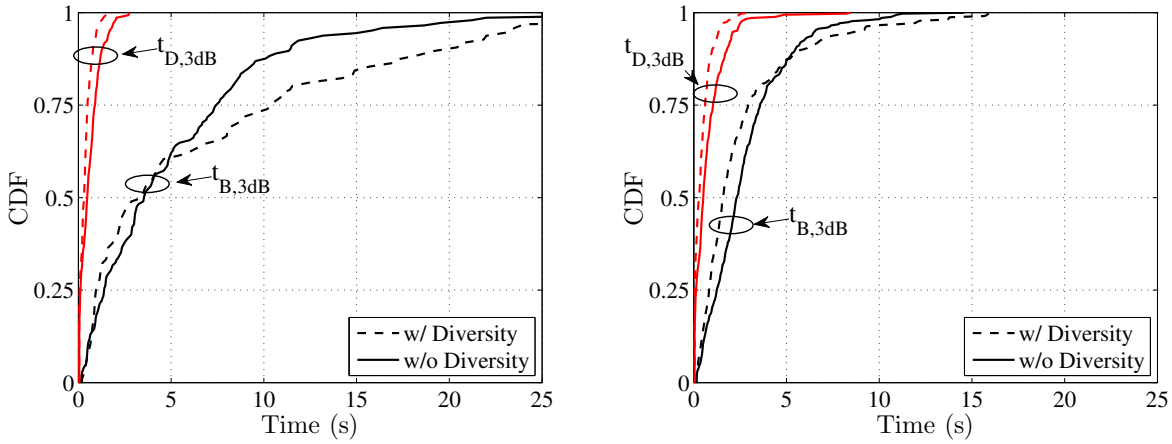


**(a)** Three persons. **(b)** Ten persons.

**Figure 5.12:** CDFs of duration $t_{D,3dB}$ and the time between shadowing events $t_{B,3dB}$.

Regarding $t_{B,3dB}$, the shape of the CDFs for the case with and without diversity differ. For example, in Fig. 5.12b, the median time between two shadowing events is slightly higher without diversity, whereas the 90%-quantile is lower. A further trend that can be observed is a slight increase of the duration with the number of persons, whereas the time between events decreases significantly.

This behavior is also clearly visible in Fig. 5.13. Here the average as well as the 90%-quantile of $t_{D,3dB}$ and $t_{B,3dB}$ are shown against the number of persons. The average duration $t_{D,3dB}$ without diversity fluctuates around 700 ms, the 90%-quantile around 1.6 seconds. Only a slight increasing trend with the number of persons can be observed. Remarkably, diversity reduces the average duration by a factor between 1.6 and 2.1 (see Fig. 5.13a).

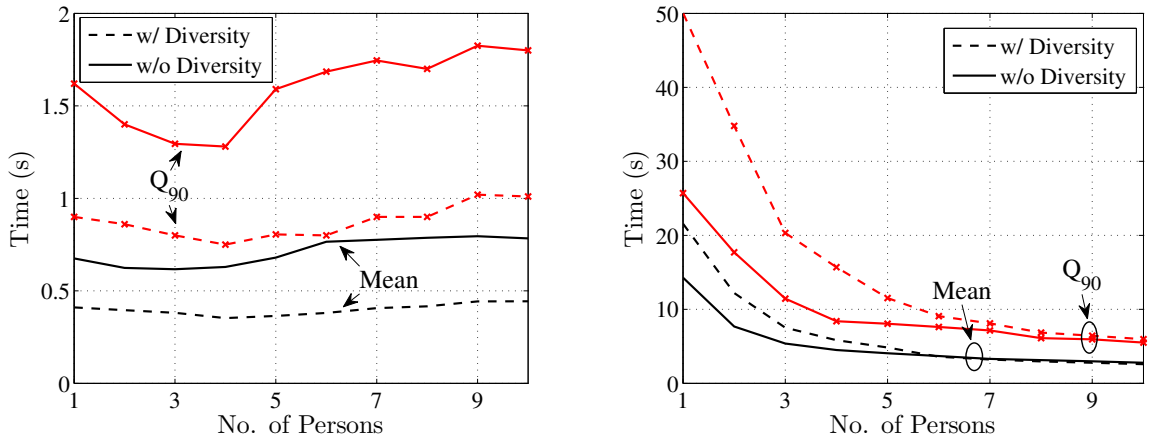


**(a)** $t_{D,3dB}$. **(b)** $t_{B,3dB}$.

**Figure 5.13:** Duration of shadowing events and time between consecutive events. The curves are shown for the mean values and the 90%-quantiles $Q_{90}$.

The time between the events decreases exponentially with the number of persons and converges to a minimum, as can be seen in Fig.5.13b. This behavior is consistent with the illustrations in Fig. 5.13a and Fig. 5.11. As $t_{D,3dB}$ only slightly decreases and the total blockage time increases, the time between the shadowing events also has to decrease with the number of persons. Interestingly, the benefits of diversity regarding $t_{B,3dB}$ vanish if more than 6 to 7 persons are active in the room. The curves start with values between 14 and 50 s and converge to values of 3 s for the average and 6 s for the 90%-quantile. Nevertheless, the shadowing events are in average always shorter than the time between them.

## 5.3 Concluding Remarks

In this chapter, two different studies have been presented, which investigate the capability of antenna diversity to overcome the problems arising from human blockage. For this purpose, the deterministic wideband model from Section 4.1 has been used, i.e. the combination of RT and the MKE model.

- ▷ In the first part of the chapter, the coverage in a living room has been investigated. The goal was to compare the performance of realistic planar 60 GHz antennas, namely a Rotman lens based beamswitching system and two types of conventional planar dipole antennas. Furthermore, an ideal half-wave dipole served as an omnidirectional reference. Regarding the planar antennas, an interesting result is that no significant difference can be observed in non-critical situations (no human blockage and no obstruction by furniture). The omnidirectional half-wave dipole antenna also provides good performance under specific circumstances, which proves that omni-

directional modes, as proposed in the 60 GHz standards, are eligible. However, in NLOS situations and the human blockage scenario the Rotman lens antenna shows its strength. The large virtual beamwidth in combination with the high antenna gain makes it possible to better cope with the human blockage compared to the other antennas. In addition, the slightly higher gain and the larger HPBW in the azimuth plane of the dipole array manifests in the slightly better coverage results in contrast to the planar dipole. Nevertheless, the coverage under the assumption of human blockage is insufficient for higher order MCSs, which are mandatory for multi-gigabit data rates, regardless of the type of antenna. This shows the necessity to max out the allowed EIRP of 40 dBm, for instance by increasing the gain further or optimizing the radiation characteristics of the antennas.

- In the second part of the chapter, the evaluation of macro diversity in a realistic conference room scenario has been presented. Here, the time-variant shadowing has been analyzed statistically by utilizing the calibrated RT tool and the MKE human blockage model. For nomadic devices such as laptops or smartphones, the diversity provide only marginal gain as practicable antenna separations are low and the arbitrary orientation further reduces the effective antenna separation. In case of higher separations, e.g. at a flat panel display a mean diversity gain of 4 to 5 dB effectively reduces the human induced loss. The gain is independent of the number of persons in the scenario. However, the loss slightly increases with the number of persons, as already shown in Chapter 4.

  In addition, the occurence rate and duration of shadowing events have been analyzed in the conference room with up to ten persons. As expected, the time, of a link being blocked increases with the number of persons. Diversity leads to a halving of the relative blockage time. The same holds true for the duration of shadowing events. The occurence rate increases with the number of persons. However, the time between succesive events is shorter than the duration itself.

# 6 Summary and Outlook

## 6.1 Summary and Contributions Beyond the State of the Art

This thesis provides a fundamental contribution to the development of multi-gigabit systems in the 60 GHz band and focusses on propagation-related research gaps. The thesis covers all areas, which are necessary for a complete description of the radio channel, namely delay dispersion, direction dispersion and Doppler dispersion. A simulation environment for the deterministic modeling of the time-variant 60 GHz indoor radio channel has been created. This unique approach which links RT with a newly developed human blockage model, accurately reproduces the mm-wave radio channel properties. Based on this, stochastic channel models have been derived and diversity techniques to overcome human shadowing have been evaluated. Beyond that, individual propagation phenomena as well as the whole radio channel have been investigated in comprehensive measurement campaigns.

Detailed conclusions have been presented already in the individual chapters. The following list condenses them and summarizes the main contributions of this dissertation in the area of wireless 60 GHz communications:

- **A methodical study about the relevance of diffraction** in indoor scenarios has been conducted, which is the first of its kind for the 60 GHz frequency range. The study comprises measurements as well as UTD and ray tracing simulations. A good agreement between theory and the experiments could be observed. Furthermore, the simulation of a typical office scenario has quantized that diffraction at stationary objects, e.g. furniture, can be neglected due to the high diffraction attenuations compared to other indirect propagation paths.
- **A geometric human shadowing model, which is based on knife-edge diffraction has been developed.** Additionally, a comparative analysis with other models, namely different circular cylinders and elliptic PEC cylinders, has been carried

out. It could be shown that in general all mentioned models are suitable to describe the interaction of human bodies and electromagnetic waves for the envisaged application in radio channel models. Based on the results of this analysis, the self-developed multiple knife edge model has been chosen for the use in the thesis because of its high computational efficiency and accuracy.

- **Comprehensive polarimetric spatio-temporal channel measurements** have been conducted, which are rare to find in literature so far. They contribute to the knowledge of the 60 GHz radio channel as they include both AoA as well as AoD characteristics. Regarding the distribution of MPCs in the AoA/AoD-domain, it has been found that in one and the same scenario diversified situations occur, reaching from moderate to high angular spreads. Besides the spatial characteristics, the measurements offer valuable information about the large- and small-scale properties of the channel within different indoor scenarios. Regarding the delay domain, the measurement results consistently show low-dispersive characteristics with very low delay spreads and excess delays. Nevertheless, without appropriate precautions, this would lead to intersymbol interferences, since the envisaged data rates are very high.

  A possible future extension to the measurement procedure is the consideration of the elevation domain. This could be realized for instance by an extension of the mechanical measurement setup or the use of antenna arrays in order to scan the elevation range. This way, e.g. the availability and the efficiency of ceiling reflections can be investigated, which may be used as an appropriate instrument to combat human shadowing.

- Additionally, the measurement data has been used for **the calibration of RT scenario data in the spatio-temporal domain**. The advantage of this new approach is that compared to conventional calibration algorithms, an unambiguous mapping between MPCs from RT and the measurements becomes possible. The RT accuracy is significantly increased after the calibration procedure. This holds even for positions in the scenario, which have not been used for the calibration. Hence, only a small number of measurements is sufficient to calibrate the entire scenario. In addition, the fact that the accuracy after the calibration does not depend on the initial assumed material parameters demonstrates the high robustness of the procedure.

- **Three different 60 GHz radio channel models have been developed, taking into account human shadowing,** namely a time-variant deterministic model, a semi-static stochastic model, and a time-variant stochastic model. The deterministic model links the calibrated RT and the MKE model and has been used for the evaluation of the antenna diversity techniques. Additionally, extensive simulations with this model provide the base for the stochastic models. These allow for a realistic emulation of the radio channel in the presence of multiple persons without the need for a deep knowledge of radio wave propagation. Especially the latter model is the first of its kind for the 60 GHz range as it includes time-variance and a CIR model.

In principle, the models can be adapted to other frequency ranges as the MKE model as well as RT is valid for higher and lower frequencies. Of course, attention has to be paid that all relevant propagation phenomena, like e.g. diffraction or scattering, are considered in the RT. A possible enhancement of the models could be the development of more realistic mobility models for the movement of the persons.

- ▷ Furthermore, the **Doppler dispersion** of MPCs reflected and diffracted at a moving human body has been investigated. This has been done based on measurements and UTD simulations. Relevant components in the Doppler spectrum are estimated to lie in the order of 1 kHz at maximum. However, for systems with highly directive antennas the impact of the Doppler effect on the data transmission is negligible as the relevant components are suppressed by the antennas.

  The quantitative impact of the Doppler shift on the data transmission can only be evaluated in further simulations, e. g. on the link level. Such simulations go beyond the scope of this thesis, but should be considered in future work. Furthermore, the focus in this thesis has been set on scenarios with nomadic TXs and RXs at fixed locations. Future research could analyze more complex scenarios by e. g. taking into account use cases with mobile devices.

- ▷ Based on the developed time-variant deterministic channel model, two studies have been conducted, which quantitatively **evaluate antenna diversity techniques to overcome the challenges of human blockage**. On the one hand, the system performance under the assumption of human shadowing has been compared for different types of antennas. It has been shown that a high-gain beamswitching antenna system outperforms conventional antennas, when the LOS path is blocked. Nevertheless, the benefit of the considered Rotman lens antenna is not as high as expected. The evaluation has also pointed out that it is necessary to utilizes the maximum allowed EIRP of 40 dBm in order to combat human shadowing at 60 GHz. On the other hand, the benefits of macro diversity in order to combat human shadowing have been investigated. Provided that the antenna separation is large enough, this technique results in an effective shortening of human-induced shadowing events. In several cases, the impact of human shadowing can be suppressed even completely. Regarding the received power, a diversity gain of several dB could be observed.

  The analyzed methods are of course not the only possible approaches to conteract human blockage problems. Future analyses may investigate further diversity techniques like e.g. maximum ratio combining or continuous beamsteering approaches. A hybrid approach of both macro diversity and beamforming would be also conceivable. For this kind of studies, the presented stochastic channel models provide appropriate tools to evaluate different approaches and support the design of smart antenna systems.

Of course, the work has been disseminated in order to increase its value for others in multiple ways as discussed in the next section.

## 6.2 Impact and Dissemination of the Work

The outcome of this thesis has been incorporated into different international research and development fora:

- ▷ All mentioned results have been presented to the scientific community in various journal and conference papers. A list with all relevant publications is given in the appendix on p. 163ff.
- ▷ A major part of the work presented in this thesis has been conducted in the framework of the European MEDEA+ project *Qstream - Ultra-high Data-rate Wireless Communication* [Qstre11]. The funding of the author had been gratefully provided by the Bundesministerium für Wirtschaft und Technologie (BMWi). In this project with about 20 scientific and industrial partners, low-cost, highly integrated, ultra-high-rate streaming applications have been addressed. The author of this thesis had the sole responsibility for 60 GHz channel modeling, which has been a central part in the conceptional phase of the project [Jacob10a, Jacob10b]. This work directly supported the development of three functional prototypes [Silig11, Herre10a, Yu09]. In particular, the developed channel models were part of a cross layer design approach linking propagation-related simulations with PHY and MAC layer simulations [Perge11].
- ▷ The author has also participated in COST2100 (Co-operation in the field of Scientific and Technical Research), which is a European network of national research projects related to the area of mobile and wireless communications. Chosen results have been presented during project meetings and made accessible to the COST2100 members in the form of technical documents. In addition, the author has been involved in writing the book chapter about channel measurements in *Pervasive Mobile and Ambient Wireless Communications* [Czink12].
- ▷ Furthermore, parts of the results have supported the development the IEEE 802.11ad standard. In this context, the author has introduced human blockage models into the official channel model document [Malts10d], which has been used for PHY layer evaluations during the standardization process [Perah10, Malts10a]. The author's work and impact in *TGad* is briefly summarized in the Appendix C.

In conclusion, this thesis provides a self-contained work covering different topics from fundamental propagation phenomena to a holistic view of the radio channel to the implications of human blockage on the system performance. Beyond that, the presented concepts and results are valuable for future work and hence have been prepared in a way that they can be directly used for the design and optimization of 60 GHz systems.

# A

# The IEEE 802.11ad 60 GHz WLAN Channel Model

For a better understanding of parts of this thesis, a basic knowledge of the *IEEE802.11ad* 60 GHz channel model [Malts10d] is required. To spare the reader the exhausting reading of the whole channel model documentation a brief overview is given in this appendix. Therefore, chosen literally excerpts of [Malts10d] are compiled in the following.

## A.1 Requirements for Channel Model

*In the beginning of the development requirements of the TGad channel model has been defined:*

- ▷ *Provide accurate space-time characteristics of the propagation channel (basic requirement) for main usage models of interest;*
- ▷ *Support beamforming with steerable directional antennas on both TX and RX sides with no limitation on the antenna technology (i.e. non-steerable antennas, sector-switching antennas, antenna arrays);*
- ▷ *Account for polarization characteristics of antennas and signals;*
- ▷ *Support non-stationary characteristics of the propagation channel arising from people motion around the area causing time-dependent channel variations.*

## A.2 General Structure of the Channel Model

*The channel model document proposes a channel structure model that provides accurate space-time characteristics and supports application of any type of directional antenna technology. The model allows for generating channel impulse responses with and without polarization characteristics support. For the sake of description simplicity, this section first*

*gives a structure of the channel model without polarization characteristics and then shows how the model is extended to account for polarization characteristics. The channel impulse response function for the channel model without polarization characteristics support may be written using a general structure as:*

$$h\left(\tau,\varphi_{RX},\theta_{RX},\varphi_{TX},\theta_{TX}\right) = \sum_{i} A^{(i)} C^{(i)}(\tau - T^{(i)}, \varphi_{RX} - \Phi_{RX}^{(i)}, \theta_{RX} - \Theta_{RX}^{(i)}, \varphi_{TX} - \Phi_{TX}^{(i)}, \theta_{TX} - \Theta_{TX}^{(i)}) \tag{A-1a}$$

$$C^{(i)}\left(\tau,\varphi_{RX},\theta_{RX},\varphi_{TX},\theta_{TX}\right) = \sum_{k} \alpha^{(i,k)} \delta(\tau - \tau^{(i,k)}) \delta(\varphi_{RX} - \varphi_{RX}^{(i,k)}) \delta(\theta_{RX} - \theta_{RX}^{(i,k)}) \delta(\varphi_{TX} - \varphi_{TX}^{(i,k)}) \delta(\theta_{TX} - \theta_{TX}^{(i,k)}) \tag{A-1b}$$

*where:*

- ▷ $h$ *is a generated channel impulse response.*
- ▷ $\tau, \varphi_{RX}, \theta_{RX}, \varphi_{TX}, \theta_{TX}$ *are time and azimuth and elevation angles at the transmitter and receiver, respectively.*
- ▷ $A^{(i)}$ *and* $C^{(i)}$ *are the gain and the channel impulse response for i-th cluster respectively.*
- ▷ $\delta(\bullet)$*- is the Dirac delta function.*
- ▷ $\tau, \Phi_{RX}, \Theta_{RX}, \Phi_{TX}, \Theta_{TX}$ *are time-angular coordinates of i-th cluster.*
- ▷ $\alpha(i,k)$ *is the amplitude of the k-th ray of i-th cluster*
- ▷ $\tau^{(i,k)}, \varphi_{RX}^{(i,k)}, \theta_{RX}^{(i,k)}, \varphi_{TX}^{(i,k)}, \theta_{TX}^{(i,k)}$ *are relative time-angular coordinates of k-th ray of i-th cluster.*

*The proposed channel model adopts the clustering approach with each cluster consisting of several rays closely spaced in time and angular domains.*

## A.3 Model Development Methodology

*As it follows from the proposed general model structure, the inter cluster and intra cluster temporal and spatial parameters need to be specified to define the channel model for some scenario. It was verified by several experimental measurements that 60 GHz propagation channel is clustered and the clusters correspond with a good accuracy to signal propagation paths predicted by ray-tracing techniques. This fact was taken into account in the used channel model development methodology.*

*The amount of experimental data was limited and to generate the inter cluster characteristics (clusters time of arrival, azimuth and elevation angles of arrival and departure)*

*ray-tracing was used. Exploitation of ray-tracing approach allowed for significant increase in available channel clusters realizations used to derive the statistical channel model parameters. For example in the conference room scenario, the application of ray tracing approach allowed to increase the number of channel realizations from about 15 experimental realizations to 100 000 ray-tracing realizations.*

*However, intra cluster parameters cannot be predicted using ray-tracing and the intra cluster structure was derived from available measurement data. The intra cluster model development was facilitated by the fact that each experimental realization includes several (typically about 10) channel clusters to average over. Special considerations are required to support polarization characteristics.*

## A.4 Usage of Channel Model in Simulations

*This section gives a brief description of the channel realization generation process that is implemented in the IEEE 802.11ad channel model. The whole process of the channel realization generation is schematically shown in Figure A.1. The generation of the channel*

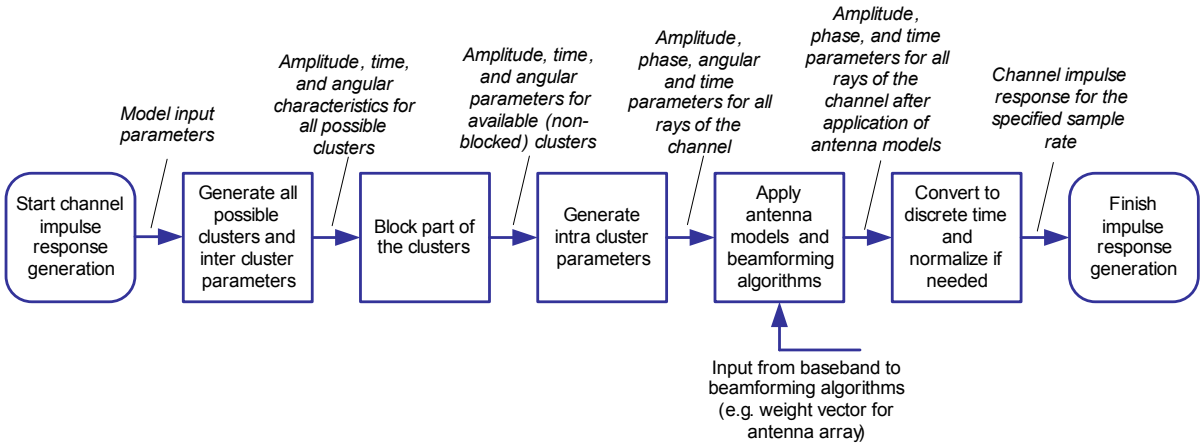


**Figure A.1:** Process of channel realization generation. Taken from [Malts10d].

*impulse response begins with selecting model input parameters. The next step is generation of all possible channel clusters between the transmitter and receiver. Amplitude, time, and angular and polarization characteristics for all clusters are generated. In a real environment not all the clusters are available for communication, some of the clusters are blocked by people, furniture, and other objects. To take this into account, a part of the clusters is blocked in the channel model. The blocked part of the clusters is selected randomly. Each cluster has an individual probability of being blocked. This probability is independent from the blockage probabilities of other clusters*[1]*. After a subset of non-blocked clusters*

[1] Please note that this part of the model is introduced by the author of this thesis. A detailed description can be found in Chapter 4

*is defined the intra cluster parameters for each non-blocked cluster are generated. Each cluster consists of multiple rays and the output of this step includes amplitude, phase, time, and angular parameters for all rays of the given channel realization. After this step the generation of channel realization is completed. But in order to be used in a simulation, antenna models must be applied to the generated realization and it must be converted from continuous to discrete time. Reference antenna models and beamforming algorithms are included, which may be applied in the next step of the channel realization generation process. The beamforming algorithms may have input from the baseband, for example, setting the weight vector of antenna array. In the last step the channel impulse is converted from continuous time to discrete time with the specified sample. After this step the generation of the discrete time channel impulse response is completed and usable in simulations. To facilitate the use of this statistical model the IEEE 802.11ad also provides MATLAB code for the generation of CIRs [Masle10].*

# B

# Implementation Aspects of the Multiple Knife Edge Model

In this appendix, implementation aspects of the multiple knife edge model (see Section 2.2.1.4) will be discussed. This is done in order to illustrate the way the model is included in the ray tracing simulations.

The main limitations of the knife edge model are the formulation as a two-dimensional problem only and the fact that it does not take into account polarization. As shown by the comparison with measurements (cf. Section 2.1.2, p.14ff), the errors caused by the neglected polarization have no significant impact in most of the practical cases.

In the knife edge theory, the plane in which transmitter and receiver lie must be perpendicular to the knife edge. Considering a three-dimensional propagation scenario, this is obviously not the general case. In order to extend the model to three dimensions, in this thesis a plane in which transmitter, receiver and the directional vector between $y_1$ and $y_2$ of a double knife edge will be considered. For this plane, all necessary geometrical param-

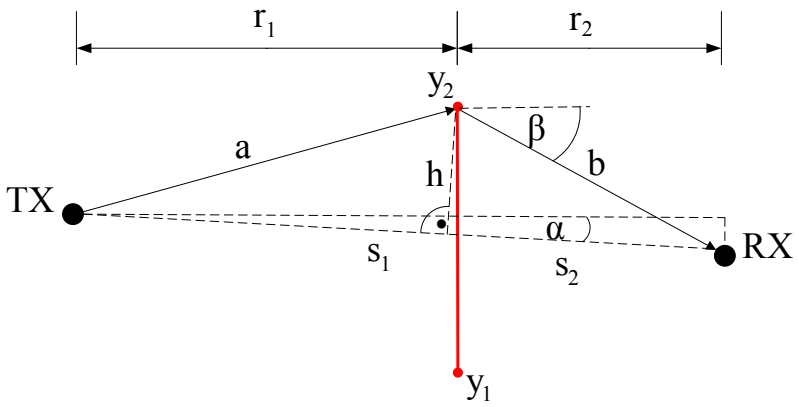


**Figure B.1:** Double knife edge with relevant geometry parameters.

eters are derived according to Fig. B.1. Compared to the three-dimensional polarimetric UTD (cf. Section 2.1.1.2) significant errors in practical relevant situations only occur in the deep shadow region and for large deviations from perpendicular incidence.

For the given three-dimensional vectors $T\vec{X}, R\vec{X}, \vec{y_1}$ and $\vec{y_2}$ the relevant relations for the diffraction at the upper edge can be derived with the help of some auxiliary quantities:

$$s = \left| R\vec{X} - T\vec{X} \right| \tag{B-1}$$

$$s = s_1 + s_2 \tag{B-2}$$

$$s = \frac{r_1 + r_2}{\sin\alpha} \tag{B-3}$$

$$a = \left| \vec{y_2} - T\vec{X} \right| \tag{B-4}$$

$$b = \left| R\vec{X} - \vec{y_2} \right| \tag{B-5}$$

$$a^2 = h^2 + s_1^2 \tag{B-6}$$

$$b^2 = h^2 + s_2^2 \tag{B-7}$$

$$r_2 = b \cdot \cos\beta \tag{B-8}$$

$$\cos\alpha = \frac{(\vec{y_2} - \vec{y_1})\left(T\vec{X} - R\vec{X}\right)}{|\vec{y_2} - \vec{y_1}| \left| T\vec{X} - R\vec{X} \right|} \tag{B-9}$$

$$\cos\beta = \frac{\pi}{2} - \frac{(\vec{y_2} - \vec{y_1})\left(\vec{y_2} - R\vec{X}\right)}{|\vec{y_2} - \vec{y_1}| \left| T\vec{X} - R\vec{X} \right|} \tag{B-10}$$

After some algebraic manipulations and together with B-8 all necessary geometry parameters are available:

$$r_1 = s \cdot \sin\alpha - b \cdot \cos\beta \tag{B-11}$$

$$s_1 = \frac{a^2 - b^2 + s^2}{2s} \tag{B-12}$$

$$s_1 = \frac{a^2 - b^2 + s^2}{2s} \tag{B-13}$$

$$s_2 = \frac{b^2 - a^2 + s^2}{2s} \tag{B-14}$$

$$h = \frac{\sqrt{2s^2\left(a^2 + b^2\right) - \left(a^2 - b^2\right)} - s^4}{2s} \tag{B-15}$$

These parameters can now be used to calculate the diffraction loss with the help of (2-1) to (2-3). In addition, the parameters have to be calculated for the lower knife edge. Therefore, only the auxiliary quantities

$$a = \left| \vec{y_1} - T\vec{X} \right| \tag{B-16}$$

$$b = \left| \vec{RX} - \vec{y_1} \right| \tag{B-17}$$

$$\cos\beta = \frac{\pi}{2} - \frac{(\vec{y_2} - \vec{y_1}) \left( \vec{RX} - \vec{y_1} \right)}{|\vec{y_2} - \vec{y_1}| \left| \vec{RX} - \vec{y_1} \right|} \tag{B-18}$$

$$\tag{B-19}$$

as well as

$$r_2 = b \cdot \sin\beta \tag{B-20}$$

have to be re-calculated.

For the total diffraction loss not all edges are taken into account. At first the intersection point between the TX-RX-connection and the rectangles building the double knife edges is calculated. If the TX-RX connection intersects with one double knife edge, only this one is taken into account (cf. Fig. 2.11a, p. 26). If the connection intersects with both rectangles, only the DKE with the lower loss is taken into account. In addition, the horizontal diffraction over the person's head is added (cf. Fig. 2.11b). The derivation of the geometry parameters for the knife edges corresponding to the diffraction over the person's head is omitted here for the sake of briefness. In principle, the procedure is the same as for the vertical knife edges.

In the case where a ray does not intersect with one of the (double) knife edges ($\nu < 0$), the distance between the ray and each edge is calculated. If the edge extends into the $n^{th}$ Fresnel zone, it is assumed to be relevant. Then, the $L_{D,KED}$ is calculated according to (2-2), whereas the height $h$ in (B-15) has to be multiplied by -1. In any other case $L_{D,KED}$ is assumed to be 0 dB. The order $n$ of the relevant Fresnel zone has been chosen to be $n = 10$, which corresponds approximately to $\nu = -5$. This has been done to reduce the computional effort, by disregarding irrelevant rays. The value $n = 10$ is sufficient because for larger distances the diffracted field is neglegible.

Finally, it should be pointed out, that the diffraction losses have to be calculated separately for each knife edge and superimposed afterwards. This is also the case if a multiply reflected ray interacts with the knife edges several times before and after the reflection process.

Based on this theoretical considerations, the functionalities have been implemented in Matlab and are used to introduce human blockage into the ray tracing simulations (cf. Chapter 4).

A complete description including the calculation of the intersection points can be found in [Prieb09].

# C

# IEEE 802.11 Standardization Work

In parallel to this thesis, a comprehensive 60 GHz channel model has been developed within the *IEEE802.11ad Task Group (TGad)* [Malts10d]. TGad has been formed in 2009 and strives for the enhancement of the current WLAN standard to achieve higher data rates. [Perah08] summarizes the goal of this group as follows: *This amendment defines standardized modifications to both the 802.11 physical layers (PHY) and the 802.11 Medium Access Control Layer (MAC) to enable operation in the 60 GHz frequency band (typically 57-66 GHz) capable of very high throughput.* In [Perah09], the initial functional requirements for 802.11ad are given. A distinction is drawn here between optional and mandatory features. The mandatory requirement are:

- ▷ Devices have to achieve a maximum PHY rate of at least 1 Gbps.
- ▷ The system provides mechanisms to ensure coexistence with other systems in the band including IEEE 802.15.3c systems.
- ▷ The TGad amendment has to maintain the network architecture and backward compatibility of the 802.11 system.

Important optional features are:

- ▷ Support of uncompressed video transmission (data rate: 3 Gbps, packet loss rate: $10^{-8}$, delay: 2 ms).
- ▷ Seamless transfer of an active session from the 60 GHz band to the 2.4/5 GHz band.
- ▷ Range of at least 10 meter at 1 Gbps at the MAC data service access point, in some NLOS PHY channel conditions.

IEEE802 standardization follows a defined procedure. At the early stage of standardization, documents describing the evaluation methodology and usage models are developed. In parallel channel and traffic models are developed to build environments for performance tests.

During this phase, the author of this thesis actively took part in the development process of the channel model. Besides other requirements, the channel model should *support non-stationarity characteristics of the propagation channel arising from people motion around the area causing time-dependent channel variations* [Malts10d]. In order to fulfill this requirement, the author proposed models for the dynamical human blockage at 60 GHz [Jacob09c, Jacob09b, Jacob09e, Jacob09g, Jacob10e]. These models are intended for system level simulations with PHY and MAC layer protocols and were completely adopted to the TGad channel model [Malts10d]. The contributions to TGad are listed in a separate bibliography on page 166. All documents are online available (https://mentor.ieee.org/802.11/documents).

# Bibliography


[Ahler12] E. Ahlers. "Chipmuster für 60-GHz-WLAN rollen an". *http://www.heise.de/netze/meldung/Chipmuster-fuer-60-GHz-WLAN-rollen-an-1650869.html*, 2012.

[AirP13] "AirPlay Homepage". *http://www.apple.com/de/airplay/*, 2013.

[Ali10] S. Ali and M. Junaid Mughal. "Narrowband Characterization of the 60 GHz Indoor Radio Channel in the Presence of Human Bodies". In: *6th International Conference on Emerging Technologies (ICET)*, pp. 226–229, 2010.

[An09] X. An, C.-S. Sum, R. Prasad, J. Wang, Z. Lan, J. Wang, R. Hekmat, H. Harada, and I. Niemegeers. "Beam Switching Support to Resolve Link-Blockage Problem in 60 GHz WPANs". In: *IEEE 20th International Symposium on Personal, Indoor and Mobile Radio Communications*, pp. 390 –394, Sept. 2009.

[Ander02] C. R. Anderson. *Design and Implementation of an Ultrabroadband Millimeter-Wavelength Vector Sliding Correlator Channel Sounder and In-Building Multipath Measurements at 2.5 & 60 GHz*. Master's thesis, Virginia Polytechnic Institue and State University, 2002.

[Balan89] C. A. Balanis. *Advanced Engineering Electromagnetics*. Wiley, 1st Ed., 1989.

[Baudr88] H. Baudrand, J. Tao, and J. Atechian. "Study of Radiating Properties of Open-Ended Rectangular Waveguides". *IEEE Transactions on Antennas and Propagation*, Vol. 36, No. 8, pp. 1071–1077, 1988.

[Bayka11] T. Baykas, C.-S. Sum, Z. Lan, J. Wang, M. Rahman, H. Harada, and S. Kato. "IEEE 802.15.3c: The First IEEE Wireless Standard for Data Rates Over 1 Gb/s". *Communications Magazine, IEEE*, Vol. 49, No. 7, pp. 114 –121, July 2011.

[Bense91] M. Bensebti, J. P. McGeehan, and M. A. Beach. "Indoor Multipath Radio Propagation Measurements and Characterisation at 60 GHz". In: *21st European Microwave Conference*, pp. 1217 –1222, Sept 1991.

[Berna04] P. Bernardi, R. Cicchetti, and O. Testa. "An Accurate UTD Model for the Analysis of Complex Indoor Radio Environments in Microwave WLAN Systems". *IEEE Transactions on Antennas and Propagation*, Vol. 52, No. 6, pp. 1509–1520, 2004.

[Bowma87] J. Bowman, T. Senior, and P. Uslenghi. *Electromagnetic and Acoustic Scattering by Simple Shapes (Revised edition)*. Hemisphere Publishing Corp., New York, 1987.

[BROAD02] BROADWAY Project. "WP1 Study: Functional System Parameters Description". Tech. Rep., iST-2001-32686, 2002.

[Bulti98] R. Bultitude, R. Hahn, and R. Davies. "Propagation Considerations for the Design of an Indoor Broadband Communications System at EHF". *IEEE Transactions on Vehicular Technology*, Vol. 47, No. 1, pp. 235–245, Feb. 1998.

[Burns83] W. Burnside and K. Burgener. "High Frequency Scattering by a Thin Lossless Dielectric Slab". *IEEE Transactions on Antennas and Propagation*, Vol. 31, No. 1, pp. 104–110, 1983.

[Butso59] P. C. Butson and G. T. Thompson. "The Effect of Flanges on the Radiation Patterns of Waveguide and Sectoral Horns". *Proceedings of the IEE - Part B: Electronic and Communication Engineering*, Vol. 106, No. 28, pp. 422–426, 1959.

[Clark68] R. H. Clarke. "A Statistical Theory of Mobile-Radio Reception". *Bell Syst. Tech. J*, Vol. 47, No. 6, pp. 957–1000, 1968.

[Coche05] Y. Cocheril, R. Vauzelle, L. Aveneau, and M. Khoudeir. "Rough Surfaces Influence on an Indoor Propagation Simulation at 60 GHz". ECPS Conference, Brest, 2005.

[Cojoc08] E. Cojocaru. "Mathieu Functions Approach to Bidimensional Scattering by Dielectric Elliptical Cylinders". *Arxiv preprint arXiv:0808.2123*, 2008.

[Cojoc13] E. Cojocaru. "Mathieu Functions Toolbox v.1.0". http://www.mathworks.com/matlabcentral/fileexchange/22081-mathieu-functions-toolbox-v-1-0, 2013.

[Collo03a] S. Collonge. *Caractérisation et Modélisation de la Propagation des Ondes Électromagnétiques à 60 GHz à l'Intérieur des Bâtiments.* PhD thesis, University of Rennes 1, 2003.

[Collo03b] S. Collonge, G. Zaharia, and G. El Zein. "Wideband and Dynamic Characterization of the 60 GHz Indoor Radio Propagation - Future Home WLAN Architectures". *Annals of Telecommunications*, Vol. 58, No. 3, pp. 417–447, 2003.

[Collo04] S. Collonge, G. Zaharia, and G. Zein. "Influence of the Human Activity on Wide-Band Characteristics of the 60 GHz Indoor Radio Channel". *IEEE Transactions on Wireless Communications*, Vol. 3, No. 6, pp. 2396–2406, 2004.

[Corde10] C. Cordeiro. "NT-12 on Beamforming (BRP), doc.: IEEE 802.11-10/0450r3". *https://mentor.ieee.org/802.11/documents*, 2010.

[Czink12] N. Czink, A. P. Garcia, K. Haneda, M. Jacob, M. Käske, J. Karedal, T. Kürner, J. Poutanen, J. Salmi, R. Thomä, and K. Witrisal. *Pervasive Mobile and Ambient Wireless Communications*, Chap. Channel Measurements. Springer, 2012.

[DLNA12] "DLNA: Technical Overview". *http://www.dlna.org/dlna-for-industry/technical-overview*, 2012.

[Dong12] K. Dong, X. Liao, and S. Zhu. "Joint Beam Adaptation in 60 GHz Interference Channel via Sequential Stochastic Approximation". In: *IEEE 75th Vehicular Technology Conference (VTC Spring)*, pp. 1–5, May 2012.

[ECMA08] ECMA. "Standard ECMA-387, High Rate 60GHz PHY, MAC and HDMI PAL". *http://www.ecma-international.org/publications/standards/Ecma-387.htm*, 2008.

[Erceg02] V. Erceg, A. Rustako Jr, and R. Roman. "Diffraction Around Corners and Its Effects on the Microcell Coverage Area in Urban and Suburban Environments at 900 MHz, 2 GHz, and 4 GHz". *IEEE Transactions on Vehicular Technology*, Vol. 43, No. 3, pp. 762–766, 2002.

[Flame00] M. Flament and M. Unbehaun. "Impact of Shadow Fading in a mm-Wave Band Wireless Network". *The 3rd Symposium on Wireless Personal Multimedia Communications,WPMC, Bangkok, Thailand*, Nov. 2000.

[Flame02] M. Flament and A. Svensson. "Diversity Benefits in 60 GHz VCN Wireless Architecture". In: *Proceedings Radiovetenskap och Kommunikations, Stockholm, Sweden*, pp. 431–435, Citeseer, 2002.

[Fleur00] B. Fleury. "First- and Second-Order Characterization of Direction Dispersion and Space Selectivity in the Radio Channel". *IEEE Transactions on Information Theory*, Vol. 46, No. 6, pp. 2027–2044, Sep. 2000.

[Garci09] A. P. Garcia, W. Kotterman, R. S. Thomä, U. Trautwein, D. Bruckner, and W. Wirnitzer. "60 GHz In-Cabin Real-Time Channel Sounding". *Fourth International Conference on Communications and Networking in China, ChinaCOM*, pp. 1–5, 2009.

[Garci10a] A. P. Garcia, , W. Kotterman, R. Zetik, M. Kmec, R. Müller, F. Wollenschläger, R. Thomä, R., and U. Trautwein. "60 GHz-Ultrawideband Real-Time Multi-Antenna Channel Sounding for Multi Giga-Bit/s Access". In: *IEEE 72nd Vehicular Technology Conference Fall (VTC-Fall)*, pp. 1 –6, Sept. 2010.

[Garci10b] A. P. Garcia, W. Kotterman, D. Brückner, and R. Thomä. "60 GHz in-Cabin Channel Characterisation and Human Body Effects". In: *4th European Conference on Antennas and Propagation, EuCAP, Barcelona Spain*, pp. 1–5, Feb. 2010.

[Garci10c] A. P. Garcia, W. Kotterman, U. Trautwein, D. Bruckner, J. Kunisch, and R. S. Thomä. "60 GHz Time-Variant Shadowing Characterization Within an Airbus 340". In: *4th European Conference on Antennas and Propagation, EuCAP, Barcelona Spain*, pp. 1–5, 2010.

[Garci11] A. P. Garcia, U. Trautwein, R. Müller, F. Wollenschläger, R. S. Thomä, J. Kunisch, I. de la Torre, R. Felbecker, M. Peter, and W. Keusgen. "60 GHz Short-Range Communications: Channel Measurements, Analysis, and Modeling 60 GHz In-Cabin Real-Time Channel Sounding". *International Journal of Microwave and Wireless Technologies*, Vol. 2, p. 201–211, 2011.

[Genc10] Z. Genc, U. Rizvi, E. Onur, and I. Niemegeers. "Robust 60 GHz Indoor Connectivity: Is It Possible With Reflections?". In: *IEEE 71st Vehicular Technology Conference (VTC-Spring)*, pp. 1–5, 2010.

[Genc12] Z. Genc, W. Thillo, A. Bourdoux, and E. Onur. "60 GHz PHY Performance Evaluation with 3D Ray Tracing under Human Shadowing". *IEEE, Wireless Communications Letters*, Vol. 1, No. 2, pp. 117 –120, April 2012.

[Geng09] S. Geng, J. Kivinen, X. Zhao, and P. Vainikainen. "Millimeter-Wave Propagation Channel Characterization for Short-Range Wireless Communications". *IEEE Transactions on Vehicular Technology*, Vol. 58, No. 1, pp. 3–13, Jan. 2009.

[Ghadd04] M. Ghaddar, L. Talbi, and T. Denidni. "Human Body Modelling for Prediction of Effect of People on Indoor Propagation Channel". *IEE Electronics Letters*, Vol. 40, No. 25, pp. 1592 – 1594, Dec. 2004.

[Ghadd07] M. Ghaddar, L. Talbi, T. Denidni, and A. Sebak. "A Conducting Cylinder for Modeling Human Body Presence in Indoor Propagation Chan-

nel". *IEEE Transactions on Antennas and Propagation*, Vol. 55, No. 11, pp. 3099 –3103, Nov. 2007.

[Giann99] F. Giannetti, M. Luise, and R. Reggiannini. "Mobile and Personal Communications in the 60 GHz Band: A Survey". *Wireless Personal Communications*, Vol. 10, No. 2, pp. 207–243, 1999.

[Green06] H. Green. "The Radiation Pattern of a Conical Horn". *Journal of Electromagnetic Waves and Applications*, Vol. 20, No. 9, pp. 1149–1160, 2006.

[Gusta12] C. Gustafson and F. Tufvesson. "Characterization of 60 GHz Shadowing by Human Bodies and Simple Phantoms". In: *6th European Conference on Antennas and Propagation (EUCAP), Prague, Czech Republic*, pp. 473–477, 2012.

[Hall03] M. Hall, L. Barclay, and M. Hewitt. *Propagation of Radiowaves*. IEE, 2nd Ed., 2003.

[Harri01] R. Harrington. *Time-Harmonic Electromagnetic Fields. IEEE Press Series on Electromagnetic Wave Theory*, IEEE Press, 2nd Ed., 2001.

[HDMI12] "HDMI Licensing, LLC: HDMI Facts". *http://www.hdmi.org/learningcenter/faq.aspx*, 2012.

[Herre09] P. Herrero, M. Jacob, and J. Schoebel. "Millimeter Wave Planar Antenna Measurement System for the 110-170 GHz Range". *Joint 5th ESA Workshop on Millimetre Wave and 31st ESA Antenna Workshop, Noordwijk, The Netherlands*, May 2009.

[Herre10a] P. Herrero. *Millimeter-Wave Systems and Technologies for Multi-Gigabit Wireless Transmission Applications*. PhD thesis, TU Braunschweig, 2010.

[Herre10b] P. Herrero and J. Schoebel. "Planar Antennas and Beamforming Devices for a Multi Gigabit 60 GHz Demonstrator with Quality of Service". *4th European Conference on Antennas and Propagation, EuCAP, Barcelona Spain*, pp. 1–5, 2010.

[Hertl07] C. Hertleer, A. Tronquo, H. Rogier, L. Vallozzi, and L. Van Langenhove. "Aperture-Coupled Patch Antenna for Integration Into Wearable Textile Systems". *IEEE Antennas and Wireless Propagation Letters*, Vol. 6, pp. 392 –395, 2007.

[HFSS13] "HFSS: High Frequency Structural Simulator". *http://www.ansys.com*, 2013.

[Hubne97] J. Hubner, S. Zeisberg, K. Koora, J. Borowski, and A. Finger. "Simple Channel Model for 60 GHz Indoor Wireless LAN Design Based on Complex Wideband Measurements". In: *IEEE 47th Vehicular Technology Conference*, pp. 1004 –1008 vol.2, May 1997.

[IEEE803] IEEE802.15 Working Group. "IEEE Standard for Information technology - Telecommunications and information exchange between systems – Local and metropolitan area networks - Specific requirements. Part 15.3: Wireless Medium Access Control (MAC) and Physical Layer (PHY) Specifications for High Rate Wireless Personal Area Networks (WPANs)". *IEEE Std 802.15.3-2003*, 2003.

[IEEE805] IEEE802.15 Working Group. "IEEE Standard for Information technology - Telecommunications and information exchange between systems - Local and metropolitan area networks - Specific requirements. Part 15.1: Wireless Medium Access Control (MAC) and Physical Layer (PHY) Specifications for High Rate Wireless Personal Area Networks (WPANs)". *IEEE Std 802.15.1-2005 (Review of IEEE Std 802.15.1-2002)*, 2005.

[IEEE809a] IEEE802.11 Working Group. "IEEE Standard for Information technology - Telecommunications and information exchange between systems - Local and metropolitan area networks - Specific requirements. Part 11: Wireless LAN medium access control (MAC) and physical layer (PHY) specifications Amendment: Enhancements for higher throughput". *IEEE Std 802.11.n-2009*, Dec. 2009.

[IEEE809b] IEEE802.15 Working Group. "IEEE Standard for Information technology - Telecommunications and information exchange between systems - Local and metropolitan area networks - Specific requirements. Part 15.3: Wireless Medium Access Control (MAC) and Physical Layer (PHY) Specifications for High Rate Wireless Personal Area Networks (WPANs) Amendment 2: Millimeter-wave-based Alternative Physical Layer Extension". *IEEE Std 802.15.3c-2009 (Amendment to IEEE Std 802.15.3-2003)*, Dec. 2009.

[IEEE809c] IEEE802.15.3c Task Group. "IEEE Standard for Information technology - Telecommunications and information exchange between systems - Local and metropolitan area networks - Specific requirements. Part 15.3: Wireless Medium Access Control (MAC) and Physical Layer (PHY) Specifications for High Rate Wireless Personal Area Networks (WPANs) Amendment 2: Millimeter-wave-based Alternative Physical Layer Extension". *IEEE, Tech. Rep*, 2009.

[IEEE812] IEEE802.11 Working Group. "IEEE Standard for Information technology - Telecommunications and information exchange between systems - Local and metropolitan area networks - Specific requirements. Part 11: Wireless LAN medium access control (MAC) and physical layer (PHY) specifications Amendment: Enhancements for Very High Throughput in the 60 GHz Band". *IEEE Std 802.11.ad-2012*, Dec 2012.

[Ingbe93] L. Ingber. "Simulated Annealing: Practice Versus Theory". *Mathematical and Computer Modelling*, Vol. 18, No. 11, pp. 29–57, 1993.

[Jacob09a] M. Jacob and T. Kürner. "Radio Channel Characteristics for Broadband WLAN Applications Between 67 and 110 GHz ". *3rd European Conference on Ant. and Prop. (EuCAP), Berlin, Germany*, pp. 1–5, 2009.

[Jacob09b] M. Jacob and T. Kürner. "Influence of Moving People on the 60 GHz Channel - a Literature Study, doc.: IEEE 802.11-09/0744r1". *https://mentor.ieee.org/802.11/documents*, 2009.

[Jacob09c] M. Jacob and T. Kürner. "Measurement Campaign at 60 GHz in the Living room Environment at TUBS, doc.: IEEE 802.11-09/0743r0". *https://mentor.ieee.org/802.11/documents*, 2009.

[Jacob09d] M. Jacob, T. Kürner, and P. Chambelin. "Deterministic Channel Modeling for 60 GHz WLAN, doc.: IEEE 802.11-09/0302r0". *https://mentor.ieee.org/802.11/documents*, 2009.

[Jacob09e] M. Jacob, C. Mbianke, and T. Kürner. "Human Body Blockage - Guidelines for TGad MAC development, doc.: IEEE 802.11-09/01169r0". *https://mentor.ieee.org/802.11/documents*, 2009.

[Jacob09f] M. Jacob, S. Priebe, C. Jastrow, T. Kleine-Ostmann, T. Schrader, and T. Kürner. "An Overview of Ongoing Activities in the Field of Channel Modeling, Spectrum Allocation and Standardization for mm-Wave and THz Indoor Communications". In: *Proceedings of IEEE Globecom, Honolulu*, 2009.

[Jacob09g] M. Jacob, S. Priebe, T. Kürner, A. Maltsev, and A. Lomayev. "Modeling the Human Induced 60 GHz Channel Dynamics, doc.: IEEE 802.11-09/1170r1". *https://mentor.ieee.org/802.11/documents*, 2009.

[Jacob10a] M. Jacob. "WP1 - Deliverable: D1.4 Preliminary Report on Channel Characterization and Models to be Used in Air Interface Design". Tech. Rep., Qstream Project, 2010.

[Jacob10b] M. Jacob. "WP1 - Deliverable: D1.5 Final Report on Channel Investigations and Models". Tech. Rep., Qstream Project, 2010.

[Jacob10c] M. Jacob, R. Geise, R. Piesiewicz, and T. Kürner. "Reflection and Transmission Properties of Building Materials in D-Band for the Modeling of Future mm-Wave Communication Systems". *4th European Conference on Ant. and Prop. (EuCAP), Barcelona, Spain*, 2010.

[Jacob10d] M. Jacob, C. Mbianke, and T. Kürner. "A Dynamic 60 GHz Radio Channel Model for System Level Simulations with MAC Protocols for IEEE 802.11 ad". In: *IEEE 14th International Symposium on Consumer Electronics (ISCE), Braunschweig*, 2010.

[Jacob10e] M. Jacob, S. Priebe, T. Kürner, A. Maltsev, and A. Lomayev. "Modeling of Dynamical Human Blockage, doc.: IEEE 802.11-10/0090r0". *https://mentor.ieee.org/802.11/documents*, 2010.

[Jacob11a] M. Jacob, S. Priebe, A. Maltsev, A. Lomayev, V. Erceg, and T. Kürner. "A Ray Tracing Based Stochastic Human Blockage Model for the IEEE 802.11ad 60 GHz Channel Model". *5th European Conference on Ant. and Prop. (EuCAP), Rome, Italy*, pp. 1–5, 2011.

[Jacob11b] M. Jacob, A. de Graauw, M. Spella, P. Herrero, S. Priebe, J. Schoebel, and T. Kürner. "Performace Evaluation of 60 GHz WLAN Antennas under Realistic Propagation Conditions with Human Shadowing". In: *XXX. URSI General Assembly, Istanbul, Turkey*, 2011.

[Jacob12] M. Jacob, S. Priebe, R. Dickhoff, T. Kleine-Ostmann, T. Schrader, and T. Kürner. "Diffraction in mm and sub-mm Wave Indoor Propagation Channels". *IEEE Transactions on Microwave Theory and Techniques*, Vol. 60, No. 3, pp. 833–844, 2012.

[Jacob13a] M. Jacob, S. Priebe, and T. Kürner. "Diversity Techniques to Overcome Human Blockage in 60 GHz WLANs". In: *13th URSI Commission F Triennial Open Symposium on Radio Wave Propagation and Remote Sensing*, Ottawa, Canada, May 2013.

[Jacob13b] M. Jacob, S. Priebe, M. Peter, M. Wisotzki, W. Keusgen, R. Felbecker, and T. Kürner. "Extension and Validation of the IEEE 802.11ad 60 GHz Human Blockage Model". *7th European Conference on Ant. and Prop. (EuCAP), Gothenburg, Sweden*, 2013.

[Jacob13c] M. Jacob, S. Priebe, M. Peter, M. Wisotzki, W. Keusgen, R. Felbecker, and T. Kürner. "Fundamental Analyses of 60 GHz Human Blockage". *7th European Conference on Ant. and Prop. (EuCAP), Gothenburg, Sweden*, 2013.

[Jemai05] J. Jemai, R. Piesiewicz, and T. Kürner. "Calibration of an Indoor Radio Propagation Prediction Model at 2.4 GHz by Measurements of the IEEE 802.11b Preamble". In: *61st IEEE Vehicular Technology Conference (VTC-Spring)*, pp. 111–115, 2005.

[Jemai09] J. Jemai, P. Eggers, G. Pedersen, and T. Kürner. "Calibration of a UWB Sub-Band Channel Model Using Simulated Annealing". *IEEE Transactions on Antennas and Propagation*, Vol. 57, No. 10, pp. 3439–3443, October 2009.

[Jones41] R. Jones. "A New Calculus for the Treatment of Optical Systems". *Journal of the Optical Society of America*, Vol. 31, No. 7, pp. 500–503, 1941.

[Khafa08] A. Khafaji, R. Saadane, J. El Abbadi, and M. Belkasmi. "Ray Tracing Technique based 60 GHz Band Propagation Modelling and Influence

of People Shadowing". *International Journal of Electrical, Computer, and Systems Engineering*, Vol. 2, No. 2, pp. 102–108, 2008.

[Klein12] T. Kleine-Ostmann, M. Jacob, S. Priebe, R. Dickhoff, T. Schrader, and T. Kürner. "Diffraction Measurements at 300 GHz for Modeling of Future THz Communication Systems". In: *37th International Conference on Infrared, Millimeter and THz Waves (IRMMW-THz)*, 2 pages (electronic), Wollongong, Australia, September 2012.

[Kobay12] A. Kobayashi. "DisplayPortTM Ver.1.2 Overview". *http://www.vesa.org/wp-content/uploads/2010/12/DisplayPort-DevCon-Presentation-DP-1.2-Dec-2010-rev-2b.pdf*, 2012.

[Kouyo74] R. Kouyoumjian and P. Pathak. "A Uniform Geometrical Theory of Diffraction for an Edge in a Perfectly Conducting Surface". *Proceedings of the IEEE*, Vol. 62, No. 11, pp. 1448–1461, 1974.

[Kürne09] T. Kürner and M. Jacob. "Application of Ray Tracing to Derive Channel Models for Future Multi-Gigabit Systems". *IEEE International Conference on Electromagnetics in Advanced Applications (ICEAA)*, pp. 517–520, 2009.

[Kunis08] J. Kunisch and J. Pamp. "Ultra-Wideband Double Vertical Knife-Edge Model for Obstruction of a Ray by a Person". In: *IEEE International Conference on Ultra-Wideband, ICUWB*, pp. 17–20, 2008.

[Kyro12] M. Kyro, K. Haneda, J. Simola, K. Takizawa, H. Hagiwara, and P. Vainikainen. "Statistical Channel Models for 60 GHz Radio Propagation in Hospital Environments". *IEEE Transactions on Antennas and Propagation*, Vol. 60, No. 3, pp. 1569 –1577, March 2012.

[Lan11] Z. Lan, L. Lu, X. Zhang, C. Pyo, and H. Harada. "A Space-Time Scheduling Assisted Cooperative Relay for mmWave WLAN/WPAN Systems with Directional Antenna". In: *IEEE Global Telecommunications Conference (GLOBECOM)*, pp. 1 –6, Dec. 2011.

[Lange02] B. Langen, G. Lober, and W. Herzig. "Reflection and Transmission Behaviour of Building Materials at 60 GHz". In: *5th IEEE International Symposium on Personal, Indoor and Mobile Radio Communications*, pp. 505–509, 2002.

[Laska07] J. Laskar, S. Pinel, D. Dawn, S. Sarkar, B. Perumana, and P. Sen. "The Next Wireless Wave is a Millimeter Wave". *Microwave Journal*, Vol. 50, No. 8, pp. 22–32, 2007.

[Ludwi66] A. Ludwig. "Radiation Pattern Synthesis for Circular Aperture Horn Antennas". *IEEE Transactions on Antennas and Propagation*, Vol. 14, No. 4, pp. 434 – 440, Jul 1966.

[Luo12] J. Luo. *Enabling Techniques for Future Broadband High Speed Wireless Communications*. PhD thesis, TU Berlin, 2012.

[Malko08] A. Malko, M. Jacob, and R. Piesiewicz. "W-Band Measurements for Common Buildings Materials". In: *International Students and Young Scientists Workshop on Photonics and Microsystems, Wroclaw, Poland*, pp. 47–49, 2008.

[Malts09] A. Maltsev, R. Maslennikov, A. Sevastyanov, A. Khoryaev, and A. Lomayev. "Experimental Investigations of 60 GHz WLAN Systems in Office Environment". *IEEE Journal on Selected Areas in Communications*, Vol. 27, No. 8, pp. 1488 –1499, Oct. 2009.

[Malts10a] A. Maltsev, R. Maslennikov, A. Lomayev, and A. Sevastyanov. "PHY Performance Evaluation with 60 GHz WLAN Channel Models, doc.: IEEE 802.11-10/0489r1". *https://mentor.ieee.org/802.11/documents*, 2010.

[Malts10b] A. Maltsev, R. Maslennikov, A. Sevastyanov, A. Lomayev, A. Khoryaev, A. Davydov, and V. Ssorin. "Characteristics of Indoor Millimeter-Wave Channel at 60 GHz in Application to Perspective WLAN System". In: *4th European Conference on Antennas and Propagation (EuCAP)*, 5 pages (electronic), Barcelona, April 2010.

[Malts10c] A. Maltsev, E. Perahia, R. Maslennikov, A. Sevastyanov, A. Lomayev, and A. Khoryaev. "Impact of Polarization Characteristics on 60-GHz Indoor Radio Communication Systems". *IEEE Antennas and Wireless Propagation Letters*, Vol. 9, pp. 413–416, 2010.

[Malts10d] A. Maltsev, V. Erceg, E. Perahia, C. Hansen, R. Maslennikov, A. Lomayev, A. Sevastyanov, A. Khoryaev, G. Morozov, M. Jacob, S. Priebe, T. Kürner, S. Kato, H. Sawada, K. Sato, and H. Harada. "Channel Models for 60 GHz WLAN Systems, doc.: IEEE 802.11-09/0334r8". *https://mentor.ieee.org/802.11/documents*, 2010.

[Manab95] T. Manabe, K. Sato, H. Masuzawa, K. Taira, T. Ihara, Y. Kasashima, and K. Yamaki. "Polarization Dependence of Multipath Propagation and High-Speed Transmission Characteristics of Indoor Millimeter-Wave Channel at 60 GHz". *IEEE Transactions on Vehicular Technology*, Vol. 44, No. 2, pp. 268–274, 1995.

[Manab96] T. Manabe, Y. Miura, and T. Ihara. "Effects of Antenna Directivity and Polarization on Indoor Multipath Propagation Characteristics at 60 GHz". *IEEE Journal on Selected Areas in Communications*, Vol. 14, No. 3, pp. 441–448, 1996.

[Masle10] R. Maslennikov and A. Lomayev. "Implementation of 60 GHz WLAN Channel Model, doc.: IEEE 802.11-10/0854r3". *https://mentor.ieee.org/802.11/documents*, 2010.

[Mbian10] C. Mbianke Ngatat. "Vergleich des mm-Wellen Funkkanals in verschiedenen Umgebungen". Diplomarbeit, TU Braunschweig, Institut für Nachrichtentechnik, 2010.

[McNam90] D. McNamara, C. Pistorius, and J. Malherbe. *Introduction to the Uniform Geometrical Theory of Diffraction.* Artech House, 1990.

[Milli99] T. Milligan. "More Applications of Euler Rotation Angles". *IEEE Antennas and Propagation Magazine*, Vol. 41, No. 4, pp. 78–83, 1999.

[Molis05] A. Molisch. *Wireless Communications.* Wiley, 2005.

[Morai04] N. Moraitis and P. Constantinou. "Indoor Channel Measurements and Characterization at 60 GHz for Wireless Local Area Network Applications". *IEEE Transactions on Antennas and Propagation*, Vol. 52, No. 12, pp. 3180 – 3189, Dec. 2004.

[Morai10] N. Moraitis, P. Constantinou, and D. Vouyioukas. "Power Angle Profile Measurements and Capacity Evaluation of a SIMO System at 60 GHz". In: *IEEE 21st International Symposium on Personal Indoor and Mobile Radio Communications (PIMRC)*, pp. 1027 –1031, Sept. 2010.

[Nguye11] T. Nguyen, E. Masry, and L. Milstein. "Channel Model and Performance Analysis of QAM Multiple Antenna Systems at 60-GHz in the Presence of Human Activity". In: *IEEE Global Telecommunications Conference (GLOBECOM)*, pp. 1 –6, Dec. 2011.

[Nicol10] M. L. Nicolás, M. Jacob, and T. Kürner. "Physical Layer Simulation Results for IEEE 802.15.3c with Different Channel Models". In: *Proceedings of URSI Kleinheubacher Tagung, Miltenberg, Germany, (5 pages)*, 2010.

[Nucke11] J. Nuckelt, M. Schack, and T. Kürner. "Deterministic and Stochastic Channel Models Implemented In a Physical Layer Simulator for Car-to-X Communications". *Advances in Radio Science*, Vol. 9, pp. 165–171, 2011.

[Obaya98] S. Obayashi and J. Zander. "A Body-Shadowing Model for Indoor Radio Communication Environments". *IEEE Transactions on Antennas and Propagation*, Vol. 46, No. 6, pp. 920–927, 1998.

[O'Kee10] W. O'Keefe Coburn, T. Anthony, and A. Zaghloul. "Open-Ended Waveguide Radiation Characteristics - Full-Wave Simulation Versus Analytical Solutions". In: *IEEE Antennas and Propagation Society International Symposium (APS-URSI)*, pp. 1 –4, July 2010.

[Owen46] A. R. G. Owen and L. Reynolds. "The Effect of Flanges on the Radiation Patterns of Small Horns". *Journal of the Institution of Electrical Engineers - Part IIIA: Radiolocation*, Vol. 93, No. 10, pp. 1528–1530, 1946.

[Pagan06] P. Pagani and P. Pajusco. "Modeling the Space-and Time-Variant Ultra-Wideband Propagation Channel". In: *IEEE International Conference on Ultra-Wideband (ICUWB)*, pp. 201—-206, Waltham, USA, 2006.

[Pan10] H. Pan and M. Park. "Enhancing Gigabit Throughput Wireless Communication Performance Using Spatial-Diversity Approach With Slot-Loop mm-Wave Antenna Arrays". In: *IEEE Antennas and Propagation Society International Symposium (APS-URSI)*, pp. 1 –4, July 2010.

[Papou02] A. Papoulis and S. Pillai. *Probability, Random Variables, and Stochastic Processes*. McGraw-Hill New York, 4th Ed., 2002.

[Park12] M. Park and H. K. Pan. "A Spatial Diversity Technique for IEEE 802.11ad WLAN in 60 GHz Band". *IEEE Communications Letters*, Vol. 16, No. 8, pp. 1260 –1262, August 2012.

[Patha80] P. Pathak, W. Burnside, and R. Marhefka. "A Uniform GTD Analysis of the Diffraction of Electromagnetic Waves by a Smooth Convex Surface". *IEEE Transactions on Antennas and Propagation*, Vol. 28, No. 5, pp. 631–642, 1980.

[Perah08] E. Perahia. "VHT 60 GHz PAR plus 5C's, doc.: IEEE 802.11-08/0806r6". *https://mentor.ieee.org/802.11/documents*, 2008.

[Perah09] E. Perahia. "TGad Functional Requirements, doc.: IEEE 802.11-09/0228r3". *https://mentor.ieee.org/802.11/documents*, 2009.

[Perah10] E. Perahia. "VTGad Evaluation Methodology, doc.: IEEE 802.11-10/0296r16". *https://mentor.ieee.org/802.11/documents*, 2010.

[Perge11] F. Perget, D. Dragomirescu, M. Jacob, T. Kürner, C. Vaucher, and R. Plana. "Performance Evaluation of Beamforming Solutions for mmWave Wireless Systems". In: *IEEE Global Telecommunications Conference (GLOBECOM)*, pp. 1–5, 2011.

[Peter07] W. Peter, W. Keusgen, and R. Felbecker. "Measurement and Ray-Tracing Simulation of the 60 GHz Indoor Broadband Channel: Model Accuracy and Parameterization". In: *2nd European Conference on Antennas and Propagation, Edinburgh, Scotland*, pp. 1 –8, Nov. 2007.

[Peter12] M. Peter, M. Wisotzki, M. Raceala-Motoc, W. Keusgen, R. Felbecker, M. Jacob, S. Priebe, and T. Kürner. "Analyzing Human Body Shadowing at 60 GHz: Systematic Wideband MIMO Measurements and Modeling Approaches". *6th European Conference on Ant. and Prop. (EuCAP), Prague, Czech Republic*, 2012.

[Piesi07] R. Piesiewicz, C. Jansen, D. Mittleman, T. Kleine-Ostmann, M. Koch, and T. Kürner. "Scattering Analysis for the Modeling of

THz Communication Systems". *IEEE Transactions on Antennas and Propagation*, Vol. 55, No. 11 Part 1, pp. 3002–3009, 2007.

[Piesi08] R. Piesiewicz, R. Geise, M. Jacob, J. Jemai, and T. Kürner. "Indoor Channel Measurements of Point-to-Point Ultra Broadband Short Range Links Between 75 GHz and 110 GHz". In: *IEEE Antennas and Propagation Society International Symposium (APS-URSI)*, pp. 1–4, 2008.

[Pollo09] A. Pollock. *Multi Antenna Techniques for Millimetre Wave Radios*. PhD thesis, University of South Australia, 2009.

[Prieb09] S. Priebe. "Ray Tracing-basierte Untersuchung von Abschattungs- und Beugungsphänomenen bei 60 GHz in Hinblick auf Beamforming". Studienarbeit, TU Braunschweig, Institut für Nachrichtentechnik, 2009.

[Prieb12] S. Priebe, M. Jacob, and T. Kürner. "Calibrated Broadband Ray Tracing for the Simulation of Wave Propagation in mm and Sub-mm Wave Indoor Communication Channels". *European Wireless, Poznan, Poland*, 2012.

[Prieb13a] S. Priebe, M. Kannicht, M. Jacob, and T. Kürner. "Ultra Broadband Indoor Channel Measurements and Calibrated Ray Tracing Propagation Modeling at THz Frequencies". *Submitted to IEEE Transactions on Antennas and Propagation*, 2013.

[Prieb13b] S. Priebe. *Towards THz Communications: Propagation Studies, Indoor Channel Modeling and Interference Investigations*. PhD thesis, TU Braunschweig, Institut für Nachrichtentechnik, 2013.

[Qstre11] Qstream. "Ultra-high Data-rate Wireless Communication". *http://www.qstream-60ghz.org/*, 2011.

[Rao09] S. Rao. *Engineering Optimization: Theory and Practice*. Wiley, 2009.

[Rappa11] T. Rappaport, J. Murdock, and F. Gutierrez. "State of the Art in 60-GHz Integrated Circuits and Systems for Wireless Communications". *Proceedings of the IEEE*, Vol. 99, No. 8, pp. 1390 –1436, Aug. 2011.

[Rappa96] T. Rappaport. *Wireless Communications: Principles and Practice*. IEEE Press Piscataway, NJ, USA, 1996.

[Saada09] R. Saadane, A. Khafaji, J. El Abbadi, and M. Belkasmi. *Recent Advances in Technologies*, Chap. The Influence of People Shadowing on the Modelling of 60 GHz Band Propagation, pp. 275–290. www.intechopen.com, 2009.

[Sadri07] A. Sadri. "802.15.3c Usage Model Document (UMD), Draft, doc: 15-06-0055-22-003c". *https://mentor.ieee.org/802.15/documents*, 2007.

[Saleh87] A. Saleh and R. Valenzuela. "A Statistical Model for Indoor Multipath Propagation". *IEEE Journal on Selected Areas in Communications*, Vol. 5, No. 2, pp. 128–137, 1987.

[Sarri07] I. Sarris and A. Nix. "Power Azimuth Spectrum Measurements in Home and Office Environments at 62.4 GHz". In: *IEEE 18th International Symposium on Personal, Indoor and Mobile Radio Communications (PIMRC)*, pp. 1–4, Sept. 2007.

[Sato07] K. Sato, H. Sawada, Y. Shoji, C.-S. Choi, R. Funada, H. Harada, S. Kato, and M. Umehira. "A New LOS Kiosk Channel Model Based on TSV Model, IEEE P802.15-07-0607-01-003c". *https://mentor.ieee.org/802.15/documents*, 2007.

[Sato97] K. Sato, T. Manabe, T. Ihara, H. Saito, S. Ito, T. Tanaka, K. Sugai, N. Ohmi, Y. Murakami, and M. Shibayama. "Measurements of Reflection and Transmission Characteristics of Interior Structures of Office Building in the 60-GHz Band". *IEEE Transactions on Antennas and Propagation*, Vol. 45, No. 12, pp. 1783–1792, 1997.

[Sato98] K. Sato and T. Manabe. "Estimation of Propagation-Path Visibility for Indoor Wireless LAN Systems Under Shadowing Condition by Human Bodies". *48th IEEE Vehicular Technology Conference (VTC)*, Vol. 3, 1998.

[Saund07] S. Saunders and A. Aragon-Zavala. *Antennas and Propagation for Wireless Communication Systems*. Wiley, 2nd Ed., 2007.

[Sawad09] H. Sawada, H. Nakase, S. Kato, M. Umehira, K. Sato, and H. Harada. "Polarization Dependence in Double Directional Propagation Channel at 60GHz". In: *IEEE 20th International Symposium on Personal, Indoor and Mobile Radio Communications (PIMRC)*, pp. 3010 –3014, Sept. 2009.

[Sawad12] H. Sawada, S. Takahashi, and S. Kato. "Disconnection Probability Improvement by Using Artificial Multi Reflectors for Millimeter-Wave Indoor Wireless Communications". In: *IEEE 75th Vehicular Technology Conference (VTC Spring)*, pp. 1 –5, May 2012.

[Schac12] M. Schack. *Integrated Simulation of Communication Applications in Vehicular Environments*. PhD thesis, TU Braunschweig, Institut für Nachrichtentechnik, 2012.

[Schra11] T. Schrader, K. Kuhlmann, R. Dickhoff, J. Dittmer, and M. Hiebel. "Verification of Scattering Parameter Measurements in Waveguides up to 325 GHz Including Highly-Reflective Devices". *Advances in Radio Science*, Vol. 9, pp. 9–17, 2011.

[Schul11] B. Schulte, M. Peter, R. Felbecker, W. Keusgen, R. Steffen, H. Schumacher, M. Hellfeld, A. Barghouthi, S. Krone, F. Gude-

rian, *et al.* "60 GHz WLAN Applications and Implementation Aspects". *International Journal of Microwave and Wireless Technologies*, Vol. 2, pp. 213–221, March 2011.

[Seide94] S. Seidel and T. Rappaport. "Site-Specific Propagation Prediction for Wireless In-Building Personal Communication System Design". *IEEE Transactions onVehicular Technology*, Vol. 43, No. 4, pp. 879–891, 1994.

[Silig11] A. Siligaris, O. Richard, B. Martineau, C. Mounet, F. Chaix, R. Ferragut, C. Dehos, J. Lanteri, L. Dussopt, S. Yamamoto, R. Pilard, P. Busson, A. Cathelin, D. Belot, and P. Vincent. "A 65 nm CMOS Fully Integrated Transceiver Module for 60GHz Wireless HD Applications". In: *IEEE International Solid-State Circuits Conference Digest of Technical Papers (ISSCC), 2011 IEEE International*, pp. 162 –164, Feb. 2011.

[Simon05] M. Simon and M. Alouini. *Digital Communication Over Fading Channels*. John Wiley & Sons, Hoboken, New Jersey, 2nd Ed., 2005.

[Singh09] S. Singh, F. Ziliotto, U. Madhow, E. Belding, and M. Rodwell. "Blockage and Directivity in 60 GHz Wireless Personal Area Networks: From Cross-Layer Model to Multihop MAC Design". *IEEE Journal on Selected Areas in Communications*, Vol. 27, No. 8, pp. 1400 –1413, October 2009.

[Sket13] "SketchUp Homepage". *http:/www.sketchup.com*, 2013.

[Smith98] J. Smith. "Fock Functions". http://www.arrows.demon.co.uk/fock/, November 1998.

[Smuld09] P. Smulders. "Statistical Characterization of 60-GHz Indoor Radio Channels". *IEEE Transactions on Antennas and Propagation*, Vol. 57, No. 10, pp. 2820 –2829, Oct. 2009.

[Smuld94] P. Smulders. "Deterministic Modelling of Indoor Radio Propagation at 40–60 GHz". *Wireless Personal Communications*, Vol. 1, No. 2, pp. 127–135, 1994.

[Smuld95] P. Smulders. *Broadband wireless LANs: a feasibility study.* PhD thesis, Technische Universiteit Eindhoven, 1995.

[Smuld97] P. Smulders and L. Correia. "Characterisation of Propagation in 60 GHz Radio Channels". *Electronics Communication Engineering Journal*, Vol. 9, No. 2, pp. 73 –80, Apr. 1997.

[Spell12] M. Spella and A. de Graauw. "A Low-Cost High-Efficiency Broadband Integrated Antenna for 60-GHz Transceiver Modules". In: *6th European Conference on Antennas and Propagation (EUCAP), Prague, Czech Republic*, pp. 1271–1275, March 2012.

[Stein01] M. Steinbauer, A. Molisch, and E. Bonek. "The Double-Directional Radio Channel". *Antennas and Propagation Magazine, IEEE*, Vol. 43, No. 4, pp. 51 –63, Aug. 2001.

[Strat41] J. Stratton. *Electromagnetic Theory.* McGraw-Hill New York, 1941.

[Tang57] C. Tang. "Backscattering from Dielectric-Coated Infinite Cylindrical Obstacles". *Journal of Applied Physics*, Vol. 28, No. 5, pp. 628–633, 1957.

[Thare88] A. Tharek and J. McGeehan. "Propagation and Bit Error Rate Measurements Within Buildings in The Millimeter Wave Band About 60 GHz". In: *Conference Proceedings on Area Communication, EUROCON*, pp. 318 –321, Jun. 1988.

[Tsang11a] Y. Tsang and A. Poon. "Detecting Human Blockage and Device Movement in mmWave Communication System". In: *IEEE Global Telecommunications Conference (GLOBECOM)*, pp. 1 –6, Dec. 2011.

[Tsang11b] Y. Tsang and A. Poon. "Successive AoA Estimation: Revealing the Second Path for 60 GHz Communication System". In: *49th Annual Allerton Conference on Communication, Control, and Computing, Allerton*, pp. 508 –515, Sept. 2011.

[Tsang11c] Y. Tsang, A. Poon, and S. Addepalli. "Coding the Beams: Improving Beamforming Training in mmWave Communication System". In: *IEEE Global Telecommunications Conference (GLOBECOM)*, pp. 1 –6, Dec. 2011.

[Ucci13] G. Ucci, R. Consulting, and T. Reznor. *Infantile Humor in Engineering.* Willie John & Daughters, Boston, 6th Ed., 2013.

[Van B07] J. Van Bladel. *Electromagnetic fields.* Wiley, 2nd Ed., 2007.

[Vaugh03] R. Vaughan and J. Andersen. *Channels, Propagation and Antennas for Mobile Communications.* IET, 2003.

[Villa00] F. Villanese, N. Evans, and W. Scanlon. "Pedestrian-induced fading for indoor channels at 2.45, 5.7 and 62 GHz". In: *52nd Vehicular Technology Conference (VTS-Fal)*, pp. 43–48, 2000.

[Wait59] J. Wait. *Electromagnetic Radiation From Cylindrical Structures.* Pergamon Press, 1959.

[WiFi12] "WiFi Display Technical Specification v1.0.0". *https://www.wi-fi.org/wi-fi-display-technical-specification-v100*, 2012.

[WiGig12] WiGig Alliance. *http://wirelessgigabitalliance.org*, October 2012.

[Wirel07] WirelessHD Consortium. "WirelessHD Specification Version 1.0". *http://www.wirelesshd.org*, 2007.

[Wirel10] WirelessHD Consortium. "WirelessHD Specification Version 1.1". *http://www.wirelesshd.org*, 2010.

[Xu02] H. Xu, V. Kukshya, and T. Rappaport. "Spatial and Temporal Characteristics of 60-GHz Indoor Channels". *IEEE Journal on Selected Areas in Communications*, Vol. 20, No. 3, pp. 620–630, 2002.

[Yang07] H. Yang, P. Smulders, and M. Herben. "Channel Characteristics and Transmission Performance for Various Channel Configurations at 60 GHz". *EURASIP Journal on Wireless Communications and Networking*, Vol. 2007, No. 1, pp. 43–43, 2007.

[Yang08a] H. Yang, M. Herben, I. Akkermans, and P. Smulders. "Impact Analysis of Directional Antennas and Multiantenna Beamformers on Radio Transmission". *IEEE Trans. on Vehicular Technology*, Vol. 57, No. 3, pp. 1695–1707, 2008.

[Yang08b] H. Yang. *Towards Low-Cost Gigabit Wireless Systems at 60 GHz: Channel Modelling and Baseband Design*. PhD thesis, Eindhoven University of Technology, 2008.

[Yıldı08] F. Yildirim, A. Sadri, and H. Liu. "Polarization Effects for Indoor Wireless Communications at 60 GHz". *IEEE Communications Letters*, Vol. 12, No. 9, 2008.

[Yong06] S. Yong *et al.* "TG3c Channel Modeling Sub-Committee Final Report". *IEEE802. 15-06-0195-07-003c*, 2006.

[Yong11] S.-K. Yong, P. Xia, and A. V. Garcia. *60 GHz Technology for Gbps WLAN and WPAN: From Theory to Practice*. Wiley, 2011.

[Yoshi94] K. Yoshitomi and H. Sharobim. "Radiation From a Rectangular Waveguide With a Lossy Flange". *IEEE Transactions on Antennas and Propagation*, Vol. 42, No. 10, pp. 1398–1403, 1994.

[Young00] D. Young and N. Beaulieu. "The generation of correlated Rayleigh random variates by inverse discrete Fourier transform". *Communications, IEEE Transactions on*, Vol. 48, No. 7, pp. 1114–1127, 2000.

[Youss94] A. Youssef, J. Mon, O. Meynard, H. Nkwawo, S. Meyer, and J. Leost. "Indoor Wireless Data Systems Channel at 60 GHz Modeling by a Ray-Tracing Method". In: *44th Vehicular Technology Conference (VTC)*, pp. 914–918, 1994.

[Yu09] Y. Yu, P. Baltus, A. van Roermund, A. de Graauw, E. van der Heijden, M. Collados, and C. Vaucher. "A 60 GHz Digitally Controlled RF-Beamforming Receiver Front-End in 65nm CMOS". In: *IEEE Radio Frequency Integrated Circuits Symposium (RFIC)*, pp. 211 –214, June 2009.

[Zhado11] M. Zhadobov, N. Chahat, R. Sauleau, C. Le Quement, and Y. Le Drean. "Millimeter-Wave Interactions with the Human Body: State of Knowledge and Recent Advances". *International Journal of Microwave and Wireless Technologies*, Vol. 3, No. 2, pp. 237–247, 2011.

[Zhao03] X. Zhao, S. Geng, L. Vuokko, J. Kivinen, and P. Vainikainen. "Polarization Behaviours at 2, 5 and 60 GHz for Indoor Mobile Communications". *Wireless Personal Communications*, Vol. 27, No. 2, pp. 99–115, 2003.

[Zhao11] D. Zhao, Y. He, L. Li, D. Joos, W. Philibert, and P. Reynaert. "A 60 GHz 14 dBm Power Amplifier with a Transformer-Based Power Combiner in 65 nm CMOS". *International Journal of Microwave and Wireless Technologies*, Vol. 3, No. 02, pp. 99–105, 2011.

[Zwick02] T. Zwick, C. Fischer, and W. Wiesbeck. "A Stochastic Multipath Channel Model Including Path Directions for Indoor Environments". *IEEE Journal on Selected Areas in Communications*, Vol. 20, No. 6, p. 1178–1192, 2002.

[Zwick05] T. Zwick, T. Beukema, and H. Nam. "Wideband Channel Sounder With Measurements and Model for the 60 GHz Indoor Radio Channel". *IEEE Transactions on Vehicular Technology*, Vol. 54, No. 4, pp. 1266–1277, 2005.

# Author's Relevant Publications

## Book Chapter

1. N. Czink, A. P. Garcia, K. Haneda, M. Jacob, M. Käske, J. Karedal, T. Kürner, J. Poutanen, J. Salmi, R. Thomä, and K. Witrisal, *Pervasive Mobile and Ambient Wireless Communications*. Springer, 2012, ch. Channel Measurements.

## Journal Papers

1. M. Jacob, S. Priebe, R. Dickhoff, T. Kleine-Ostmann, T. Schrader, and T. Kürner, "Diffraction in mm and sub-mm Wave Indoor Propagation Channels," *IEEE Transactions on Microwave Theory and Techniques*, vol. 60, no. 3, pp. 833–844, 2012.
2. S. Priebe, M. Kannicht, M. Jacob, and T. Kürner, "Ultra Broadband Indoor Channel Measurements and Calibrated Ray Tracing Propagation Modeling at THz Frequencies," *Submitted to IEEE Transactions on Antennas and Propagation*, 2013.

## Conference Papers

1. R. Piesiewicz, R. Geise, M. Jacob, J. Jemai, and T. Kürner, "Indoor Channel Measurements of Point-to-Point Ultra Broadband Short Range Links Between 75 GHz and 110 GHz," in *IEEE Antennas and Propagation Society International Symposium (APS-URSI)*, 2008, pp. 1–4.
2. A. Malko, M. Jacob, and R. Piesiewicz, "W-Band Measurements for Common Buildings Materials," in *International Students and Young Scientists Workshop on Photonics and Microsystems, Wroclaw, Poland*, 2008, pp. 47–49.


3. M. Jacob and T. Kürner, "Radio Channel Characteristics for Broadband WLAN Applications Between 67 and 110 GHz ," *3rd European Conference on Ant. and Prop. (EuCAP), Berlin, Germany*, pp. 1–5, 2009.

4. P. Herrero, M. Jacob, and J. Schoebel, "Millimeter Wave Planar Antenna Measurement System for the 110-170 GHz Range," *Joint 5th ESA Workshop on Millimetre Wave and 31st ESA Antenna Workshop, Noordwijk, The Netherlands*, May 2009.

5. T. Kürner and M. Jacob, "Application of Ray Tracing to Derive Channel Models for Future Multi-Gigabit Systems," *IEEE International Conference on Electromagnetics in Advanced Applications (ICEAA)*, pp. 517–520, 2009.

6. M. Jacob, S. Priebe, C. Jastrow, T. Kleine-Ostmann, T. Schrader, and T. Kürner, "An Overview of Ongoing Activities in the Field of Channel Modeling, Spectrum Allocation and Standardization for mm-Wave and THz Indoor Communications," in *Proceedings of IEEE Globecom, Honolulu*, 2009.

7. M. Jacob, R. Geise, R. Piesiewicz, and T. Kürner, "Reflection and Transmission Properties of Building Materials in D-Band for the Modeling of Future mm-Wave Communication Systems," *4th European Conference on Ant. and Prop. (EuCAP), Barcelona, Spain*, 2010.

8. M. Schack, M. Jacob, and T. Kürner, "Comparison of In-Car UWB and 60 GHz Channel Measurements," in *4th European Conference on Ant. and Prop. (EuCAP), Barcelona, Spain*, April 2010, pp. 1 –5.

9. M. Jacob, C. Mbianke, and T. Kürner, "A Dynamic 60 GHz Radio Channel Model for System Level Simulations with MAC Protocols for IEEE 802.11 ad," in *IEEE 14th International Symposium on Consumer Electronics (ISCE), Braunschweig*, 2010.

10. M. L. Nicolás, M. Jacob, and T. Kürner, "Physical Layer Simulation Results for IEEE 802.15.3c with Different Channel Models," in *Proceedings of URSI Kleinheubacher Tagung, Miltenberg, Germany, (5 pages)*, 2010.

11. M. Jacob, S. Priebe, A. Maltsev, A. Lomayev, V. Erceg, and T. Kürner, "A Ray Tracing Based Stochastic Human Blockage Model for the IEEE 802.11ad 60 GHz Channel Model," *5th European Conference on Ant. and Prop. (EuCAP), Rome, Italy*, pp. 1–5, 2011.

12. M. Jacob, A. de Graauw, M. Spella, P. Herrero, S. Priebe, J. Schoebel, and T. Kürner, "Performace Evaluation of 60 GHz WLAN Antennas under Realistic Propagation Conditions with Human Shadowing," in *XXX. URSI General Assembly, Istanbul, Turkey*, 2011.

13. T. Kürner, M. Jacob, and S. Priebe, "Channel Modeling – Exploring the Impact of Human Blocking ," *International Wireless Industry Consortium (IWPC) Workshop: 60 GHz Short Range Wireless – What is the Future?, Berlin, Germany*, 2011.

14. F. Perget, D. Dragomirescu, M. Jacob, T. Kürner, C. Vaucher, and R. Plana, "Performance Evaluation of Beamforming Solutions for mmWave Wireless Systems," in *IEEE Global Telecommunications Conference (GLOBECOM)*, 2011, pp. 1–5.

15. S. Priebe, M. Jacob, and T. Kürner, "Affection of THz indoor communication links by antenna misalignment," in *6th European Conference on Antennas and Propagation (EUCAP), Prague, Czech Republic*, March 2012, pp. 483 –487.

16. ——, "The Impact of Antenna Directivities on THz Indoor Channel Characteristics," in *6th European Conference on Antennas and Propagation (EUCAP), Prague, Czech Republic*, March 2012, pp. 478 –482.

17. M. Peter, M. Wisotzki, M. Raceala-Motoc, W. Keusgen, R. Felbecker, M. Jacob, S. Priebe, and T. Kürner, "Analyzing Human Body Shadowing at 60 GHz: Systematic Wideband MIMO Measurements and Modeling Approaches," *6th European Conference on Ant. and Prop. (EuCAP), Prague, Czech Republic*, 2012.

18. S. Priebe, M. Jacob, and T. Kürner, "Calibrated Broadband Ray Tracing for the Simulation of Wave Propagation in mm and Sub-mm Wave Indoor Communication Channels," *European Wireless, Poznan, Poland*, 2012.

19. T. Kleine-Ostmann, M. Jacob, S. Priebe, R. Dickhoff, T. Schrader, and T. Kürner, "Diffraction Measurements at 300 GHz for Modeling of Future THz Communication Systems," in *37th International Conference on Infrared, Millimeter and THz Waves (IRMMW-THz)*, 2 pages (electronic), Wollongong, Australia, September 2012.

20. M. Jacob, S. Priebe, M. Peter, M. Wisotzki, W. Keusgen, R. Felbecker, and T. Kürner, "Fundamental Analyses of 60 GHz Human Blockage," *7th European Conference on Ant. and Prop. (EuCAP), Gothenburg, Sweden*, 2013.

21. ——, "Extension and Validation of the IEEE 802.11ad 60 GHz Human Blockage Model," *7th European Conference on Ant. and Prop. (EuCAP), Gothenburg, Sweden*, 2013.

## Contributions to IEEE 802.11ad

1. M. Jacob, T. Kürner, and P. Chambelin, "Deterministic Channel Modeling for 60 GHz WLAN, doc.: IEEE 802.11-09/0302r0," *https://mentor.ieee.org/802.11/documents*, 2009.

2. M. Jacob and T. Kürner, "Measurement Campaign at 60 GHz in the Living room Environment at TUBS, doc.: IEEE 802.11-09/0743r0," *https://mentor.ieee.org/802.11/documents*, 2009.

3. ——, "Influence of Moving People on the 60 GHz Channel - a Literature Study, doc.: IEEE 802.11-09/0744r1," *https://mentor.ieee.org/802.11/documents*, 2009.

4. M. Jacob, C. Mbianke, and T. Kürner, "Human Body Blockage - Guidelines for TGad MAC development, doc.: IEEE 802.11-09/01169r0," *https://mentor.ieee.org/802.11/documents*, 2009.

5. M. Jacob, S. Priebe, T. Kürner, A. Maltsev, and A. Lomayev, "Modeling the Human Induced 60 GHz Channel Dynamics, doc.: IEEE 802.11-09/1170r1," *https://mentor.ieee.org/802.11/documents*, 2009.

6. ——, "Modeling of Dynamical Human Blockage, doc.: IEEE 802.11-10/0090r0," *https://mentor.ieee.org/802.11/documents*, 2010.

7. A. Maltsev, V. Erceg, E. Perahia, C. Hansen, R. Maslennikov, A. Lomayev, A. Sevastyanov, A. Khoryaev, G. Morozov, M. Jacob, S. Priebe, T. Kürner, S. Kato, H. Sawada, K. Sato, and H. Harada, "Channel Models for 60 GHz WLAN Systems, doc.: IEEE 802.11-09/0334r8," *https://mentor.ieee.org/802.11/documents*, 2010.

# Acronyms

| | |
|---|---|
| AoA | Angle of Arrival. |
| AoD | Angle of Departure. |
| AP | Access Point. |
| APP | Angular Power Profile. |
| AWGN | Additive White Gaussian Noise. |
| BER | Bit Error Rate. |
| BMWi | Bundesministerium für Wirtschaft und Technologie. |
| BPSK | Binary Phase Shift Keying. |
| CDF | Cumulative Distribution Function. |
| CIR | Channel Impulse Response. |
| COST | Co-operation in the Field of Scientific and Technical Research. |
| DKE | Double Knife Edge (Diffraction). |
| DLNA | Digital Living Network Alliance. |
| DUT | Device under Test. |
| Ecma | European Computer Manufacturers Association. |
| EIRP | Equivalent Isotropically Radiated Power. |
| FEC | Forward Error Correction. |
| FFT | Fast Fourier Transform. |

GMM Gaussian Mixture Model.
GPIB General Purpose Interface Bus.

HDMI High-Definition Multimedia Interface.
HFSS High Frequency Structural Simulator.
HHI Heinrich-Hertz-Institut.
HPBW Half Power Beamwidth.

IEEE Institute of Electrical and Electronics Engineers.
IFFT Inverse Fast Fourier Transform.
IHF Institut für Hochfrequenztechnik.

KED Knife Edge Diffraction.

LDPC Low-Density Parity-Check Coding.
LOS Line-of-Sight.

MAC Medium Access Control.
MCS Modulation and Coding Scheme.
MED Maximum Excess Delay.
MKE Multiple Knife Edge (Diffraction).
MPC Multipath Component.

NLOS Non-Line-of-Sight.

OFDM Orthogonal Frequency Division Multiplexing.

PAL Protocol Adaptation Layer.
PDF Probability Density Function.
PDP Power Delay Profile.
PEC Perfectly Electric Conducting.
PHY Physical Layer.
PVC Poly Vinyl Chloride.

QAM Quadrature Amplitude Modulation.
QPSK Quadrature Phase Shift Keying.

RBT Relative Blockage Time.
RDS RMS Delay Spread.
RMS Root Mean Square.

| | |
|---|---|
| RT | Ray Tracing. |
| RX | Receiver. |
| SC | Single Carrier. |
| SC-FDE | Single Carrier with Frequency Domain Equalization. |
| SGH | Standard Gain Horn. |
| SNR | Signal-to-Noise-Ratio. |
| STA | Stationary Device. |
| TE | Transverse Electric. |
| TG3c | IEEE802.15.3c Task Group. |
| TGad | IEEE802.11ad Task Group. |
| TM | Transverse Magnetic. |
| ToA | Time of Arrival. |
| TX | Transmitter. |
| UTD | Uniform Theory of Diffraction. |
| VNA | Vector Network Analyzer. |
| WiGig | Wireless Gigabit Alliance. |
| WLAN | Wireless Local Area Network. |
| WPAN | Wireless Personal Area Network. |
| WR | Waveguide Rectangular. |